Manipulation of biomimetic objects in acoustic levitation

Angelica Castro

▶ **To cite this version:**

Angelica Castro. Manipulation of biomimetic objects in acoustic levitation. Acoustics [physics.class-ph]. Université Pierre et Marie Curie - Paris VI, 2013. English. NNT : . pastel-00938546

HAL Id: pastel-00938546
https://pastel.hal.science/pastel-00938546

Submitted on 29 Jan 2014

HAL is a multi-disciplinary open access archive for the deposit and dissemination of scientific research documents, whether they are published or not. The documents may come from teaching and research institutions in France or abroad, or from public or private research centers.

L'archive ouverte pluridisciplinaire **HAL**, est destinée au dépôt et à la diffusion de documents scientifiques de niveau recherche, publiés ou non, émanant des établissements d'enseignement et de recherche français ou étrangers, des laboratoires publics ou privés.

THESE DE DOCTORAT DE
L'UNIVERSITE PIERRE ET MARIE CURIE

Ecole Doctorale 388
Chimie Physique et Chimie Analytique de Paris Centre

Présentée par
Luz Angélica CASTRO CAMACHO

Pour obtenir le grade de
DOCTEUR de l'UNIVERSITÉ PIERRE ET MARIE CURIE

Manipulation of biomimetic objects in acoustic levitation

Dirigé par Mauricio Hoyos

Soutenue le 18 Décembre 2013

Devant le jury composé de :

Mme. Catia Contado	Rapporteur
Mme. Itziar González Gómez	Rapporteur
M. Mauricio Hoyos	Directeur de thèse
M. Dominique Salin	Examinateur
M. Bernard Zappoli	Examinateur

Summary

The main goal of this thesis is to explore the possibilities given by the acoustic levitation for manipulating micron sized rigid and elastic particles in parallel plate resonators. In order to perform high throughput separations and biotests of a big number of objects, we conceived, design and built all the resonators we used and developed new methodologies we shall show in this experimental work.

Particle manipulation has potential applications in bioengineering, pharmaceutical industry, chemical engineering, material engineering, in which particles are collected, concentrated, separated and transported. Non-contact techniques are required in areas such as biotechnology i.e., cell manipulation of blood constituents. Levitation is a promising tool for contactless processing of materials, contactless guiding and levitated rotors, non toxic manipultation and handling, positioning, orientation and transfer of systems.

Ultrasonic standing waves (USW) can be used to trap, to move and spatially localize micron-scale objects such as particles and cells, particularly well suited for manipulate them in microfluidic scale devices. Another possibility is that particles can be moved by using two or more transducers to modulate the standing wave field.

When a big number of particles undergo an USW in a parallel plate resonator, levitation occurs and the aggregation process is established. The aggregation process in microfluidic resonators concern a few particles thus very small aggregates are produced. In our study we are dealing with aggregates composed of hundreds or thousands of particles, generating 2D or 3D structures.

We studied the aggregation process and the acoustic streaming. One of the originalities of this work is the introduction of pulse mode acoustics. The acoustic mode employed plays a role in the control of the aggregate morphology, shape, size and configuration and allowed to highly reduce the acoustic streaming.

The first stage of the aggregation process is related to interparticles interactions called secondary Bjerknes force. We introduced a methodology for measuring this short range force (one or two particle diameters range) and values of $\sim 10^{-13}$ N. In addition, we measured the Bjerknes force in microgravity conditions.

Usually in an acoustic resonator an USW can trap species bigger than 1μm such as micron-sized particles, cells and even bacteria. However, when species becomes smaller than this size, particle manipulation is challenging. This complexity is due the influence of the acoustic streaming that modifies the particle behavior. In fact, studies of the acoustic streaming sustain that the limit size able to manipulate particles by radiation forces is 2μm. Because of the acoustic streaming is a recurrent problem in acoustophoresis, special care has been taken in our study for better understand a control of the manipulation process of particles in acoustic resonators.

We used the programmed acoustic for separating particles in the Hydrodynamic Acoustic Continuous Sorter - HACS device or acoustic step-SPLITT fractionator. We barely study applications to bacteria and catalytic micro rods manipulated by acoustics. This work generated four patents.

Keywords: acoustic resonator, ultrasonic standing waves, continuous mode, pulse mode, aggregates, acoustic streaming, Bjerknes forces, microgravity, s-SPLITT, separation, self-acoustophoresis, bacteria, liposomes, boundary layer, acoustic separation, sub-micron size particles, HACS.

Acknowledgements

I would like to acknowledge the finantial support for this thesis given by the Centre National de la Recherche Scientific -**CNRS**- and the Centre National des Etudes Spaciales -**CNES**-.

My sincere gratitude to my supervisor, Dr Mauricio Hoyos, for his continuous guidance, patience and knowledge in all the stages of this thesis. His confidance and friendship no matter latitude or longitude, encouraged me to move forward in my scientific growing for which I am extremely grateful. Thanks to Dr Veronica Raspa for her invaluable help with simulations and her "ever living Argentina" (and remembrances of dulce de leche-milk candy).

Dr Tom Mallouk, Wei Wang and Suzanne Ahmed of Penn State College for the growing enthusiasm and fruitful discusions of "self-acoustophoresis" effect. Dr Despina Bazou for a very nice 2D or 3D co-operation aggregated between Dublin and Boston. Dr Marcela Camacho at CIF, Universidad Nacional de Colombia and her students to their invaluable effort with cell culture and interest in acoustic manipulation. Dr Eric Clement and his group for their enjoyment for results and bacteria bath.

This project was carried out at the Physique et Mécanique des Milieux Heterogènes -**PMMH**- laboratory at the **ESPCI**. I would like to thanks to people of the **PMMH**, for sharing and help during these three years (2010-2013): Philippe Petitjeans (Director), Frederique Auger, Claudette Barez, Amina Mialet, Xavier Benoit-Gonan and the guys of machine shop.

To Anna Garcia-Sabaté, Eunhye Cho, Ludovic Keiser and Esteban Montenegro for their enthusiam and valuable contributions for the experiments that make part of this work.

My family that have given me their unequivocal support throughout, as always, for which my mere expression of thanks likewise does not suffice.

Last, but by no means least, I thank my friends in France, USA, England and elsewhere for their support, care and joy throughout (mainly in hard moments). Everywhere I could have the opportunity to stay, each one of you have become a second family.

Contents

List of Tables

List of Figures

List of Symbols

Symbol	Description and unit
r	Particle radius (m)
n	Number of nodes of the acoustic wave
w	Thickness of the acoustic resonator (HACS, s-SPLITT device) (μm)
G	Acoustic contrast factor
A, V_0, U_0	Amplitude of the acoustic wave (V)
ISP	Inlet splitting plane
OSP	Outlet splitting plane
USW	Ultrasonic standing wave
Qa'	Flow of the sample at the inlet a' (ml/min)
Qa	Flow at the outlet a (ml/min)
Qb'	Flow of the vector liquid at the inlet b' (ml/min)
Qb	Flow at the outlet b (ml/min)
Q	Total flow (ml/min)
λ	Wavelenght (m)
f	Frequency of the acoustic wave (s^{-1})
$k = \frac{2\pi}{\lambda}$	Acoustic wavenumber (m^{-1})
ω	Angular frequency (s^{-1})
V	Volume of the particle (m^3)
d_c	Critical distance (m)
δ	Viscous boundary layer (μm)
τ	Relaxation time (s)
g	Gravitational acceleration (m/s^2)
ν	Kinematic viscosity (m^2/s)
η	Dynamic viscosity (Kg/m s or N s/m^2)
ϕ	Potential function
β_f	Compressibility of the fluid
ρ_f	Density of the fluid (Kg/m^3)
p_{ac}	Acoustic pressure (Pa)
c_p	Speed of sound of the particle (m/s)
β_p	Compressibility of the particle (Pa^{-1})
ρ_p	Particle density (Kg/m^3)

c_f	Speed of sound of the fluid (m/s)
$Z = c * \rho$	Acoustic impedance (Kg/s m^2)
u_s	Streaming velocity (μm/s)
$\langle v_2 \rangle$	Steady acoustic streaming velocity (m/s^{-1})
$\mathbf{U}$	Fluid velocity vector (m/s)
$\bar{U}$	Average flow velocity (m/s)
$\mathbf{v}$	Particle velocity vector (m/s)
$\mathbf{F}_{\mathrm{ac}}$	Acoustic radiation force (N)
$\mathbf{F}_{\mathrm{z}}$	Primary radiation force (N)
$\mathbf{F}_{\mathrm{xy}}$	Transverse radiation force (N)
$\mathbf{F}_{\mathrm{PB}}$	Primary Bjerknes force (N)
$\mathbf{F}_{\mathrm{SB}}$	Secondary Bjerknes force (N)
$\mathbf{F}_{\mathrm{p}}$	Interparticle attractive or repulsive force (N)
$\mathbf{F}_{\mathrm{b}}$	Buoyancy (N)
$\mathbf{F}_{\mathrm{Drag}}$	Drag force (N)
$\langle Eac \rangle$	Acoustic energy density (J/m^3)

Chapter 1

General Introduction

The main goal of this thesis is to explore the possibilities given by the acoustic levitation of micron sized rigid and elastic particles such as biological and biomimetic objects in parallel plate resonators. In order to perform high throughput separations and biotests of a high number of objects, we designed resonators and we developed the methodologies we shall show in this experimental work. In this introductory part we evoke the theoretical bases and concepts we shall use along this thesis.

Particle manipulation has potential applications in bioengineering, pharmaceutical industry, chemical engineering, material engineering, in which particles are collected, concentrated, separated and transported [3]. Non-contact techniques are required in areas such as biotechnology i.e., cell manipulation of blood constituents. Levitation is a promising tool for contactless processing of materials, contactless guiding and levitated rotors, non toxic manipultation and handling, positioning, orientation and transfer of systems [4].

Different types of particle manipulation

- Magnetic: the levitation comes from a magnetic field generated by permanent, electromagnetic or superconducting magnets.
- Optical: particles can be freely suspended and accelerated by the forces of radiation pressure from visible laser light.
- Electric: used to directly manipulate several kinds of particles such as conductive, semiconductive and dielectric materials.
- Aerodynamic: uses a flow of gas or liquid to apply a force. According to the flow direction, two different approaches can be considered: air cushion or Bernoulli levitation.

- Acoustic: uses acoustic waves to apply forces on the part to be manipulated. Two configurations can be found: standing waves and near-field levitation.

By acoustic manipulation we mean the generation of relative displacements between particles and the surrounding fluid of relative displacements between particles themselves under the action of ultrasonic radiation forces in order to induce separations, segregations, aggregations or other transport processes. Particle manipulation technology with ultrasonic standing waves has emerged as a powerful tool for handling micron-sized particles in microfluidics devices; ultrasonic standing waves can be used to trap, to move and spatially localize micron-scale objects such as particles and cells, particularly well suited. Another possibility is that particles can be moved by using two or more transducers to modulate the standing wave field [5].

In this thesis, we are mainly concerned by these concepts: acoustic radiation force, acoustic streaming, acoustophoresis, and separation.

Separation is the classification or sorting of material into their original constituents. Our work group studied separation with field-flow fractionation technique (FFF) that consist in the application of an axial field force to a ribbon-like channel such as thermal, electric, magnetic or sedimentation fields [6] for analytical purposes. Splitt fractionation was also used for continuous separations reached the characterization and the study of non-ideal effects such as lift forces and shear induced diffusion [7]. Following by the development of a mini SPLITT device or step-SPLITT patented and validated with digital holographic microscopy [8] where the coupling between the hydrodynamic focusing in the s-SPLITT device and a field force: magnetic or acoustic field allow the separation of species. In a previous work [9, 10], the coupling of the hydrodynamic and an acoustic field (generated by two transducers near by) create a programmed acoustic field. This programmed acoustic field in the s-SPLITT device, leads the HACS device (Hydrodynamic Acoustic Continuous Sorter).

In Europe, other research groups works in microfluidics mainly with silicon chip devices exploiting USW forces and acoustic streaming to manipulate cells, bacteria, particles, among others.

In this chapter we are going to evoke the theorical elements that are employed in the manipulation process of species in acoustic resonators.

1.1 Physics of ultrasonic particle manipulation

Particle manipulation by ultrasonic standing waves is done in an acoustic resonator, a cavity where one of their walls a piezoceramic transducer is incorporated; their opposing wall serve as passive reflector. The ultrasonic wave generated is reflected and the wave superposition is known as a standing wave. Ultrasonic waves are mechanical waves that require a physical medium to propagate. When an acoustic wave is introduced in a fluid, the generation of pressure gradients may trigger different effects such as the radiation force and the acoustic streaming; both are related to progressive waves, however the effect is

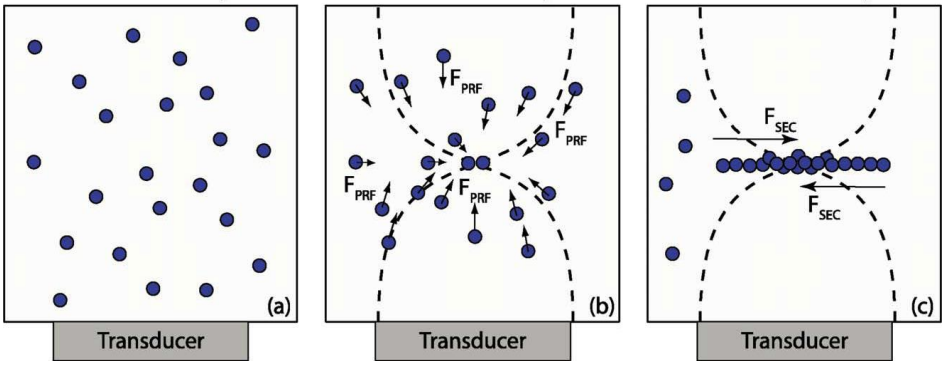

Figure 1.1 General scheme of acoustic forces in an acoustic resonator. a) Suspended particles in the ultrasonic resonator. b) The pressure profile is represented by dashed lines where the **PRF** pulls particles to the node. c) Transverse radiation force **TPRF** and secondary forces leads to particle aggregation. Taken from [11].

much stronger when ultrasonic standing waves (USW) are applied.

In the resonator, by carefully tuning the resonance frequency and/or the wave amplitude, particles in a suspension (Figure 1.1 a) interact with acoustic forces. Also, according to their nature, particles go towards the node or to the antinode. In our resonators, particles displaces from the plate to an equilibrium position in which the acoustic force and the gravitational force are balanced; that is given by the interaction between particles and the primary radiation force (**PRF**) also known as acoustic levitation (Figure 1.1 b). Once at the equilibrium position or levitation, other forces start to interact leading particle aggregation.

The resonance frequency of an acoustic resonator is achieved by reaching the following condition: $w = n.\frac{\lambda}{2}$, where w is the width or the thickness of the device [1], n is the number of pressure nodes of the standing wave and λ the wavelength is equal to $(\frac{c_f}{f})$ where c_f is the speed of sound in the water (1482 m/s) and f is the acoustic frequency [11]. The acoustic force is proportional to the frequency and hence by reducing the resonator dimension to a half wavelength resonance condition, the frequency will have to be increased. An incremented frequency yields a higher magnitude of the manipulating acoustic force, which thus increases to a level where strong forces enable manipulation of micron-sized objects in continuous flow based systems [12].

In a liquid, acoustic waves are longitudinal waves which means that the fluid particles are displaced along the wave giving as result the compression and rarefaction of the particles in the medium. Particles are subjected to pressure fluctuations arising from the displacement of the molecules of the medium. An acoustic wave is commonly described as [13]:

$$\mathbf{F}_z = A\cos\left(\frac{2\pi x}{\lambda} + \frac{\varphi}{2}\right)\sin\left(\frac{2\pi t}{T} + \frac{\varphi}{2}\right). \tag{1.1}$$

The displacement z of a point in the standing wave corresponding to a certain position

[1] we work with acoustic levitation, then in our devices w is the thickness of the resonator

(x) and time (t), depends on the amplitude of the standing wave (A), the time for one full period (T) and the phase difference between the two traveling waves (φ). For USW, the equation 1.1 can be rewritten in terms of pressure: $p = p_0 \sin(kx)\cos(\omega t)$ where $k = (\frac{2\pi}{\lambda})$ and $\omega = \frac{2\pi}{T}$ [13].

1.1.1 Acoustic Radiation force

Foreign inclusions in a fluid (gas bubbles, liquid drops, solid particles, among others), are irradiated axially by a sound field. The suspended particles experience steady time-averaged hydrodynamic forces, which may be large enough to drive them towards the local pressure node or antinode planes to aggregate or cluster them at a certain space points. These forces are called acoustic radiation pressure or acoustic radiation forces [14]. The acoustic radiation can be produced due to various physical effects [15]

- Change in the density of energy of the propagating wave due to absorption and scattering;
- Spatial variations of the energy density in the standing wave;
- Reflection from inclusions, walls or other interfaces.

Acoustic forces are found in a variety of scientific and technical applications such as acoustic levitation, calibration of sound transducers, acoustic coagulation of aerosols, biomedical ultrasonics, among others and play an important role in many other acoustic phenomena, such as sonoluminiscence and acoustic cavitation [14].

First described by Kundt and Lehman in 1866, particle manipulation was tested by an experiment on dust particles. The action of the acoustic force organized the particles in a series of bands at the nodes of the USW; a distance corresponding to half the wavelength of the sound wave separate each band. King [16] in 1934, proposed an expression for the acoustic radiation force, considering particles as rigid spheres freely suspended in a non-viscous fluid exposed to a plane traveling and standing waves . Yosioka and Kawasima in 1955, extended King's theory for compressible spheres finding a good agreement between theoric and experimental data [17]. Gorkov proposed in 1962, an alternative formulation for the acoustic radiation force, based on the energy stored in a one-dimensional plane standing wave [18].

The determination of the acoustic force proposed by Gor'Kov [18] have been explained by Bruus [19] and Andersen [1]. Considering the governing equations of particle manipulation: the thermodynamic equation of state that express pressure p and density ρ and the kinematic continuity equation for ρ, for an isothermal and incompressible Newtonian fluid

$$p = p(\rho), \tag{1.2}$$

$$\partial_t \rho = -\nabla \cdot (\rho \mathbf{v}), \tag{1.3}$$

$$\rho \partial_t \mathbf{v} + (\mathbf{v} \cdot \nabla)\mathbf{v} = -\nabla p + \eta \nabla^2 \mathbf{v} + \beta \eta \nabla(\nabla \cdot \mathbf{v}) + \vec{F_{body}}. \tag{1.4}$$

If the external forces are absent and using the Eulerian field description, these equations becomes a set of non-linear coupled partial differential equations that are hard to solve analytically and numerically. Solutions can be found by using the perturbation method.

$$p = p_0 + p_1 + p_2,$$
$$\rho = \rho_0 + \rho_1 + \rho_2,$$
$$\mathbf{v} = \mathbf{v_0} + \mathbf{v_1} + \mathbf{v_2}.$$

The perturbations of zeroth order, consider a fluid in quiescent state which before the presence of any acoustic wave: the density ρ_f and the pressure p_f are constants and the zero velocity of the fluid $\mathbf{v_0} = \mathbf{0}$. The pressure p_0 corresponds to the internal energy per volume in the fluid.

$$p = p(\rho_0) = p_0, \tag{1.5}$$
$$\partial t \rho_0 = 0, \tag{1.6}$$
$$0 = -\nabla p_0. \tag{1.7}$$

The presence of the acoustic wave generates tiny perturbations in the fields of density, pressure and velocity. The oscillation generated by the transducer (in the order of nanometers) perturbe the system (the acoustic wave travels in the liquid with the amplitude of the oscillation), leading the first order perturbation. The acoustic oscillation is an isentropic process. Then, if we introduce the speed of sound in the fluid, c_f

$$c_f^2 \equiv \left(\frac{\partial p}{\partial \rho}\right)_s \tag{1.8}$$

Then, the fields p_1, ρ_1, and $\mathbf{v_1}$ are time-dependent and describes the fundamental acoustic wave. The expressions of for the perturbations of first order are:

$$p_1 = c_f^2 \rho_1, \tag{1.9}$$
$$\partial_t \rho_1 = -\rho_0 \nabla \cdot \mathbf{v_1}, \tag{1.10}$$
$$\rho_0 \partial_t \mathbf{v}_1 = -c_f^2 \nabla \rho_1 + \eta \nabla^2 \mathbf{v}_1. \tag{1.11}$$

The time derivative expression of first order of the Navier-Stokes and the pressure equations, lead the following expression:

$$\frac{1}{c_f^2}\partial_t^2 p_1 = \left[1 - \frac{(1+\beta)\eta}{\rho c_f^2}\partial_t\right] \nabla^2 p_1 \tag{1.12}$$

thus the invicid case can be reduced to lead the wave equation:

$$\nabla^2 \phi = \frac{1}{c_f^2}\partial_t^2 \phi. \tag{1.13}$$

The potential function (ϕ) can be used to know the pressure at a certain point, or if the derivate is done in the space it is possible to know the velocity of the fluid at that point.

The invicid consideration ($\mathbf{v_1}$ to being irrotational) makes the gradient of a potential $\mathbf{v_1} \equiv \nabla\phi$, useful to determine the velocity by knowing the pressure field.

$$p_1 = -\rho_0 \partial_t \phi_1, \tag{1.14}$$

$$\mathbf{0} = \nabla \times \mathbf{v}_1, \tag{1.15}$$

$$\mathbf{v_1} = \nabla\phi_1. \tag{1.16}$$

The perturbation is harmonic where the average of the force is zero, the same as $\langle p_{in} \rangle = 0$ and $\langle \mathbf{v_{in}} \rangle = 0$. Therefore, the radiation force must be a second-order effect for which the time average does not vanish $\left\langle \cos^2(\omega t) \right\rangle = 1/2$ [20]. Then, the expressions of second order of the equations are

$$p_2 = c_f^2 \rho_2 + \frac{1}{2}\partial_\rho (c_f^2)(\rho_1^2), \tag{1.17}$$

$$\partial_t \rho_2 = -\rho_0 \nabla \cdot \mathbf{v_2} - \nabla(\rho_1 \dot{\mathbf{v}}_\mathbf{1}), \tag{1.18}$$

$$-\nabla p = \rho_1 \partial_t \mathbf{v_1} + \rho_0 \partial_t \mathbf{v_2} + \rho_0 (\mathbf{v_1} \cdot \nabla)\mathbf{v_1}. \tag{1.19}$$

Non-linear effects means that the effects of a perturbation (at MHz frequencies) are determined only by integrating in one period of time because is useful to know what happen during one oscillation period. The average of linear terms (harmonic perturbations) are zero (means in the force). Second order effects means small forces. Second-order perturbations fields lead to time-independent effects such as the acoustic force and the acoustic streaming.

The particle suspensions are dilute enough that particle-particle interactions are negligible and thus only single-particle effects are relevant. The particle-wave scattering and the viscous drag force from the acoustic streaming flow are time-averaged second-order effects arising from products of the first order fields. The drag force from the acoustic streaming dominates the motion of small particles, while the motion of larger particles are dominated by the acoustic radiation force [21].

Primary radiation force, PRF In a plane harmonic standing wave, this radiation force $\mathbf{F}_z$ acts in the axial direction (sense of force actuation) driving the particles of volume V (considering the wavelength bigger than the particle radius), normal to the node or the antinode plan [22]. The primary force is sensitive to the size of the particles as well as to the density and the compressibility of both the solids and the suspending fluid [23]. This force appears as a second order of the Navier-Stokes equation. The order of magnitude of the acoustic force is ($\approx 10^{-9}$ N) high enough for influencing micron sized particles [24, 25], cells [26], lipids [9] or even bacteria [27].

The radiation force arises due any discontinuity in the propagating phase (a particle, cell, droplet or bubble) acquiring a position-dependent acoustic potential energy by virtue of being in the sound field (Figure 1.2). Suspended particles tend to move towards and concentrate at positions of minimum acoustic potential energy. This force is sensitive to the size of the particles as well as to the density and compressibility of the particles and the suspending fluid.

At the pressure nodes, the levitation force is zero while everywhere else levitation forces act in the direction of the nearest pressure node. Then, suspended particles will be

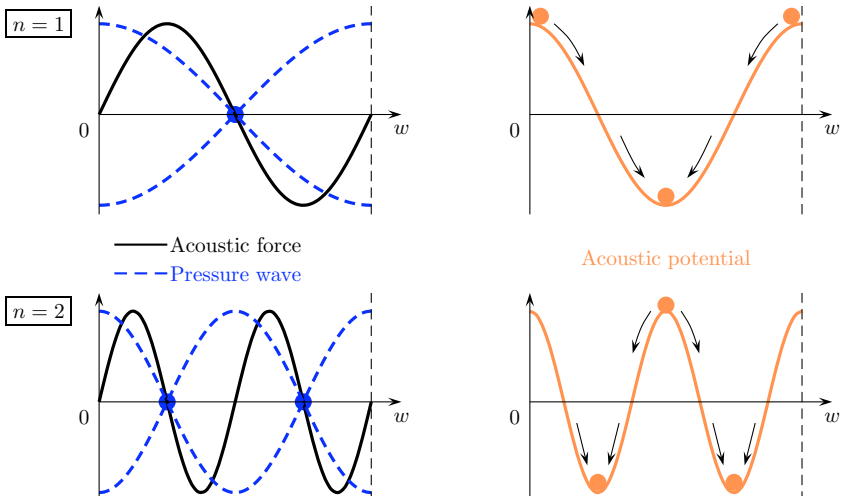

Figure 1.2 Left: graph of the acoustic force and the corresponding pressure field for one ($n = 1$) and two-nodes ($n = 2$). The number of nodes follows the relationship: $w = n(\lambda/2)$ with λ the wavelength. Right: acoustic potential from which the force derivate for the same values of n. Minima of potential, which are stable equilibrium positions, have the same position as the pressure nodes: particles are attracted toward these nodes. Taken from [10].

positioned below the pressure node and stabilized by the levitation force originating the anti-symmetric part of the acoustic radiation pressure. Then, the acoustic force can be expressed in terms of the potential field as $\mathbf{F}_{\text{ac}} = -\nabla\phi$, where ϕ is the force potential field, expressed by

$$\phi = \frac{4\pi r^3}{3}\left[f_1 \langle PE\rangle - \frac{3}{2} f_2 \langle KE\rangle\right]. \tag{1.20}$$

Where r is the particle radius, $\langle PE\rangle$ and $\langle KE\rangle$ are the average potential energy (fluid compression) and kinetic energy (particle motion) density respectively, described as

$$\langle KE\rangle = \frac{\rho_f}{2}\langle u^2\rangle, \tag{1.21}$$

$$\langle PE\rangle = \frac{\beta_f}{2}\langle p_f^2\rangle. \tag{1.22}$$

The factors f_1 and f_2 are defined by the expressions

$$f_1 = 1 - \frac{\rho_f c_f^2}{\rho_p c_p^2}, \tag{1.23}$$

$$f_2 = \frac{3(\rho_p - \rho_f)}{(2\rho_p + \rho_f)} \tag{1.24}$$

If the factors f_1 and f_2 are both positive, the particle is attracted to regions where the kinetic energy is large and the potential energy is small; then, the sphere goes to the velocity antinode. However, if f_1 and f_2 are both negative, the sphere is attracted to regions where the potential energy is large and the kinetic energy is small, that is to pressure antinodes [28]. Suspended particles tend therefore to move towards and concentrate at positions of minimum acoustic potential energy [29].

The acoustic force can be written as:

$$\mathbf{F}_{\text{ac}} = V\langle E_{ac}\rangle k G \sin(2kz) \tag{1.25}$$

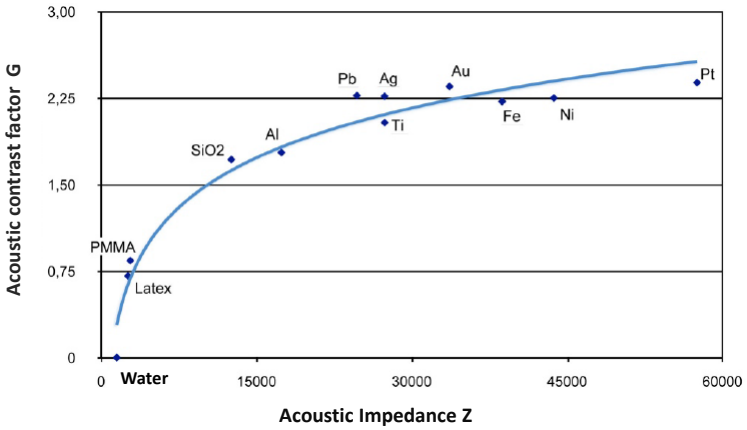

Figure 1.3 Relationship of the factor G and the acoustic impedance. Silica-latex particles are able to separate, however in the case of metal particles such as gold-iron this separation would be difficult to obtain.

where the $\langle E_{ac} \rangle$ is the average acoustic energy density, V is the particle volume, z is the distance from the wall to the nodal or antinodal plane, $k = \frac{2\pi}{\lambda}$ is the wave number and G is the acoustic contrast factor, defined by the expression

$$G = \frac{3\rho_p + 2(\rho_p - \rho_f)}{2\rho_p + \rho_f} - \frac{c_f^2 \rho_f}{c_p^2 \rho_p} \tag{1.26}$$

The factor G can be useful to compare with the acoustic impedance $\mathbf{Z}$ (where $\mathbf{Z} = \mathrm{c}\ \rho$ of particles or the fluid), as shown in Figure 1.3 in which it can be possible to determine if particles can be fractionated according to their properties (density and compressibility).

1.1.2 Transverse radiation force

The acoustic radiation force has a weak transverse component, result of the geometrical imperfections of the resonator: the parallelism of the resonator walls, the lateral walls vibrations and the imperfection of the energy field provided by the transducer. Once particles reach the nodal plane, the axial force is zero and the transverse force becomes important driving the particles in the x-y plane pushing them towards the zones of maximum acoustic energy. This transverse component is two orders of magnitude smaller than the resulting axial force.

First derived by Whitworth et al. [25], who considered a cylindrical waveguide and a pseudo standing wave field to calculate the speed at which particles can be transported. Finally the mathematical expression of the force was finally proposed by Woodside et al. [30], considering the acoustic field as the sum of two, equal amplitude and oppositely directed traveling waves of slightly different frequency. The acoustic pressure field is given by the following expression (and following in this part the the notation of Whitworth et al.

[25]):

$$p_{(R,z,t)} = p_{(R)} \left[\frac{\cos(k_1 z - \omega_1 t) + \cos(k_2 z + \omega_2 t)}{2} \right].$$

Where k_1 and k_2, are the wavenumbers, ω_1 and ω_2 are the angular frequencies of the waves. The acoustic pressure amplitude $p_{(R)}$ (described as a Bessel function) depend on the radial position R. By using the trigonometric identity:

$$\cos a + \cos b = 2 \cos \left(\frac{a+b}{2} \right) \cos \left(\frac{a-b}{2} \right). \tag{1.27}$$

The equation can be put in the form

$$p_{(R,z,t)} = p_{(R)} \cos \left[\frac{(k_1 + k_2)z}{2} - \frac{(\omega_1 - \omega_2)t}{2} \right] \times \cos \left[\frac{(k_1 - k_2)z}{2} - \frac{(\omega_1 + \omega_2)t}{2} \right]. \tag{1.28}$$

The acoustic force on a small particle is

$$\mathbf{F}_{\mathrm{ac}} = VB\nabla \langle KE \rangle - V \left[1 - \frac{\beta_p}{\beta_f} \right] \nabla \langle PE \rangle . \tag{1.29}$$

The term B, is the relative motion between the particle and the surrounding fluid. For a spherical particle this term is small compared to a wavelength. Thus, B is given by the expression:

$$B = \frac{3(\rho_p - \rho_f)E}{2\rho_p + \rho_f}. \tag{1.30}$$

with E is a viscous correction factor.

The temporal average potential energy density can be related to the acoustic pressure field by the equation

$$\langle PE \rangle = \left\langle \frac{p^2_{(r,z,t)}\beta}{2} \right\rangle. \tag{1.31}$$

The time period T must be equal to an integral number of acoustic periods. The calculation of the radiation force on slowly moving particles, T must also be chosen to be smaller than the time required for the particle to move at an appreciable distance:

$$\frac{4\pi}{(\omega_1 - \omega_2)} \gg \mathrm{T} \gg \frac{4\pi}{(\omega_1 + \omega_2)}. \tag{1.32}$$

Introducing the potential energy equation

$$\left\langle \frac{2PE}{\beta} \right\rangle = p^2_{(r)} \cos^2 \left[\frac{(k_1 + k_2)z}{2} \cup \frac{(\omega_1 - \omega_2)t}{2} \right] \times \cos^2 \left[\frac{(k_1 - k_2)z}{2} \cup \frac{(\omega_1 + \omega_2)t}{2} \right]. \tag{1.33}$$

Considering dispersionless the acoustic field that can be approximated to

$$\nabla p_{(R,z,t)} = \left[\frac{\partial p_{(R,z,t)}}{dz} \vec{z} \right] \tag{1.34}$$

where the potential and kinetic acoustic energies are

$$\langle PE\rangle = \frac{p_{(R)}^2\beta}{4} - \frac{p_{(R)}^2\beta\cos^2\left[(k_1-k_2)z-(\omega_1-\omega_2)t\right]}{4}, \tag{1.35}$$

$$\langle KE\rangle = \frac{p_{(R)}^2\beta}{4} - \langle PE\rangle\,. \tag{1.36}$$

Once determined the potential and kinetic energies, the transverse force is

$$\mathbf{F}_{\mathrm{xy}} = VB\nabla\langle KE\rangle - V\left(1-\frac{\beta^*}{\beta}\right)\nabla\langle PE\rangle\,. \tag{1.37}$$

Where the acoustic energy is

$$Eac = \frac{p_{(R)}^2\beta}{4}. \tag{1.38}$$

The trigonometric relation $1-\cos^2\alpha = \sin^2\alpha$ then, the transverse component of the **PRF** is

$$\mathbf{F}_{\mathrm{xy}} = V\nabla Eac\left[B\sin^2(kx)\right] - \cos^2(kz)\left[1-\frac{\beta^*}{\beta}\right]. \tag{1.39}$$

1.1.3 Secondary radiation force

When particles are close enough each other, secondary forces start to act. This force is the result of the scattering between particles. These forces are two orders of magnitude smaller than PRF and are the main responsible of the aggregation process. When the interaction occurs in multiple particles in the suspension, they will not only experience the primary acoustic force, but also the secondary forces caused by waves scattered by other particles. These interparticle forces are called Bjerknes forces [31]. Primary Bjerknes force has been related to the interaction between an individual bubble and the acoustic force. However, when two or more bubbles or particles interacts the secondary Bjeknes force acts [32].

1.2 Acoustic energy density

The acoustic energy density **Eac** is a measure of the energy residing in a wave field. Can be used to indicate the strength of the acoustic fields of an acoustic resonator and to characterize the loss of the acoustic energy due to viscous damping and radiation forces.

The acoustic energy is an essential parameter in particle manipulation because it sets the scale for the acoustic radiation forces and streaming flows. The energy transported with acoustic waves is composed by the kinetic energy of the moving fluid elements and the potential energy of the compressed fluid [33].

$$\langle KE\rangle = \frac{1}{2}\rho_f v_1^2 = \frac{1}{2}\rho_f(\nabla\phi_1)^2, \tag{1.40}$$

$$\langle PE\rangle = \frac{1}{2}\beta_f p_1^2. \tag{1.41}$$

Then, the total time-averaged acoustic energy density becomes [1]:

$$E_{ac} = \frac{1}{4}\left(\rho_f v_1^2 + \beta_f p_1^2\right) = \frac{1}{4}\rho_f V_0^2. \tag{1.42}$$

where V_0^2 is the amplitude of the standing wave. By the relation E_{ac} is proportional to p^2.

1.3 Resonance

Ultrasound acoustics in the low MHz range are well suited for applications in microfluidics, because at these frequencies combined with the speed of sound in water at room temperature, leads to wavelengths ($\lambda \approx .,1\text{mm}$) which may fit into submillimeter-sized cavities or microfluidic systems and form a standing pressure wave, known as resonance. Appliying ultrasounds to an experimental microfluidic setup requires the use of a piezo electric transducer, driven at MHz frequency by an AC voltage. The transducer initially vibrates with a time-harmonic acceleration, leading to a time-harmonic varying pressure field in the resonator [34]. Resonance occurs when at a certain frecuency there is a maximum of energy stored in the resonator. For several reasons it is often advantageous to operate an acoustic resonator at these resonance modes: they are usually both stable and reproducible, their spatial patterns are controlled by the geometry of the device and at the resonance a maximum of acoustic power is delivered from the transducer to where it is needed in the system in the form of radiation force on suspended particles or acoustic streaming of the solvent [35].

In practice, a piezoelectric transducer has a nominal resonance frequency. Nevertheless, when the transducer is glued to the surface (wall), acoustic dispersion occurs slighly modifying the resonance frequency. By using the condition $w = \frac{2\pi}{\lambda}$, the real resonance of the cavity (driving frequency) is not the same as the nominal frequency of the transducer. The resonance frequency needs to be carefully determined for each resonator. In a standing wave when n= 1 and the walls are rigids the node of the USW is placed at the middle of the resonator thickness and the antinodes are at the walls, and this case is ours. If the walls are elastic, other configurations may happen.

1.4 Acoustic streaming

Acoustic streaming is a viscosity effect, leading to time independent second-order velocity terms [1]. The creation of a Reynolds stress in the fluid [36] results in the attenuation of the acoustic wave [37]. In addition to the forces on suspended particles, acoustic streaming is induced in the suspending phase. Streaming exerts a drag on a particle that would be expected to modify particle behavior; streaming arises because energy dissipation mechanisms in the bulk phase due to energy absorption in the fluid and energy dissipation at the interfaces between the fluid and solid surfaces.

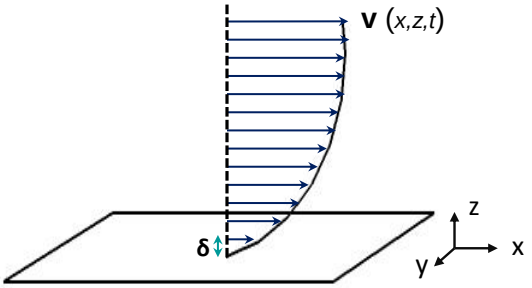

Figure 1.4 Scheme of the boundary layer in the device.

The acoustic streaming flows was described and studied by Rayleigh in 1884 [38], who treated the case of standing waves between parallel walls; he also studied three cases of streaming observed by Faraday and Dvorak. The fist two cases are related to the observations made by Faraday on the patterns assumed by sand and fine powders on Chladni's vibrating plates. The third case relate to the observations made by Dvorak on the circulation of air currents in a Kundt's tube [39].

According to the scale of the streaming, different authors had classified in three main types [40, 39]:

- Eckart streaming ($\gg \lambda$). Also known as large-scale streaming. Generated in a non-uniform free sound field, whose scale is much larger than the acoustic wavelength. This streaming and thermal convection can drive particles out of desired positions or disrupt particle aggregates.
- Rayleigh streaming ($= \lambda$). Vortex-flow streaming generated outside the boundary layer at the bulk fluid (in a standing wave field).
- Schlichting streaming ($\ll \lambda$) or boundary layer streaming. This micro-streaming is a vortex flow inside the thin boundary layer at a solid-liquid interface. Boundary effects at the solid wall and the viscosity of the fluid near the boundary leads to a time-independent flow near the boundary.

Considering the boundary between a potential flow in the x direction and a solid wall placed in the x-y plane, invariant in the y direction. Appliying a non-slip boundary condition there is a change in the velocity from the full flow far away from the boundary to zero velocity in a boundary layer of thickness δ, as depicted in Figure 1.4. It is found to be:

$$\delta = \sqrt{\frac{2\eta}{\rho_f \omega}} \tag{1.43}$$

The boundary layer is much smaller than the wavelength of the acoustic wave i.e for a resonance frequency of 2.85MHz, $\delta = 0.35\mu$m and $\lambda = 520\mu$m; however high frecuency means a reduction of δ i.e: for a resonance frequency of 4.115MHz, $\delta = 0.295\mu$m with $\lambda = 360\mu$m. Considering the fluid as incompressible in the boundary layer, denoting the constant density $\rho = \rho_f$ and leading to the condition $\nabla \cdot \mathbf{v} = \mathbf{0}$ the problem here is $\lambda \gg L_0 \gg \delta$.

The fluid in the resonator is a potential flow, that is, at rest at the wall and outside the boundary layer there is flow at x-direction. According to the Figure 1.4, the velocity changes from the velocity far from the boundary layer δ to zero. Close to the solid wall it is not possible to neglet the viscosity, thus the derivation of the equation of motion for the fluid in the boundary layer takes into account the perturbations of first-order in pressure and velocity of the viscid Navier-Stokes equation. By following the approach of [19, 1], at x-direction

$$\partial_t \mathbf{v_{(1,x)}} = -\frac{\mathbf{1}}{\rho_\mathbf{f}} \partial_\mathbf{x} \mathbf{p_1} + \nu \partial_\mathbf{z}^\mathbf{2} \mathbf{v_{(1,x)}}. \tag{1.44}$$

First order terms describe the oscillating portion of the variables related to the acoustic field and their time averages are equal to zero. The second order terms describe time independent contributions of pressure, density and velocity developed as a result of streaming [37]. Considering the second order of this equation:

$$\partial_t \mathbf{v_{(2,x)}} + \left(\mathbf{v_{(1,x)}} \partial_\mathbf{x} + \mathbf{v_{(1,z)}} \partial_\mathbf{z}\right) \mathbf{v_{(1,x)}} = -\frac{\mathbf{1}}{\rho_\mathbf{f}} \partial_\mathbf{x} \mathbf{p_2} + \nu \partial_\mathbf{z}^\mathbf{2} \mathbf{v_{(2,x)}}. \tag{1.45}$$

where $\nu = \frac{\eta}{\rho}$

Because the flow in the z-direction is small compared with the flow at the x-direction, the pressure gradient is small in z-direction and can be neglected. However, this gradient must be the same in the boundary layer and the main stream. Using the Bernoulli equation to express $\partial_x p$ to the flow outside the boundary layer:

$$\begin{aligned} f(t) &= \partial_t \phi + \frac{1}{2} |\nabla \phi|^2 + \frac{1}{\rho} p, \\ 0 &= \partial_x \partial_t \phi + \frac{1}{2} \partial_x |\nabla \phi|^2 + \frac{1}{\rho} p, \\ \frac{1}{\rho} \partial_x p &= -\partial_t U_{1,(x)} - U_{1,(x)} \partial_t U_{1,(x)}. \end{aligned}$$

Here, $U_{1,(x)}$ is the first order velocity field outside the boundary layer. Now the equations 1.44 and 1.45 becomes:

$$\frac{1}{\rho} \partial_x p_1 = -\partial_t U_{1,(x)}, \tag{1.46}$$

$$\frac{1}{\rho} \partial_x p_2 = -U_{1,(x)} \partial_t U_{1,(x)}. \tag{1.47}$$

These equations with 1.44 and 1.45 becomes:

$$\partial_t \mathbf{v_{(2,x)}} + \left(\mathbf{v_{(1,x)}} \partial_\mathbf{x} + \mathbf{v_{(1,z)}} \partial_\mathbf{z}\right) \mathbf{v_{(1,x)}} - \nu \partial_\mathbf{z}^\mathbf{2} \mathbf{v_{(2,x)}} = \mathbf{U_{1,(x)}} \partial_\mathbf{t} \mathbf{U_{1,(x)}}.$$

A simplification of the second order equation of motion is to consider time-averaged values (the time average of a periodic varying derivative can be vanish). Then, the second order becomes:

$$\nu \left\langle \partial_z^2 v_{(2,x)} \right\rangle = \left\langle \mathbf{v_{(1,x)}} \partial_\mathbf{x} \mathbf{v_{(1,x)}} \right\rangle + \left\langle \mathbf{v_{(1,z)}} \mathbf{v_{(1,x)}} \right\rangle - \left\langle U_{1,(x)} \partial_x U_{1,(x)} \right\rangle. \tag{1.48}$$

Where the solution of equation 1.48 is possible by solving the equation velocity 1.44. As the flow is potential in the x-direction, outside the boundary layer a standing wave with amplitude U_0 and wavenumber k, give to the first order expression:

$$U_{1,(x)} = U_0 \cos(kx) e^{-i\omega t}. \tag{1.49}$$

The solution for the second-order time-averaged velocity far from the boundary solid at z$\rightarrow \infty$ is

$$\left\langle v_{(2,x)} \right\rangle = \frac{1}{8} \frac{U_0^2}{c_f} \sin(2kx). \tag{1.50}$$

The acoustic streaming rises to a velocity in which oscillates at twice the frequency of the standing wave. However, the acoustic streaming velocity is independent of the viscosity even though it was an effect created by the viscosity at the boundary.

The primary disadvantage of fluid manipulation through acoustic streaming is the inefficiency of the phenomenon. Although all microfluidic devices are inefficient compared to large-scale devices. As streaming is a second order, non-linear phenomenon only a small fraction of the acoustic energy is transferred to steady fluid momentum [37].

1.5 Conclusion

In this introduction we evoked some theoretical background and the concepts that we used along the thesis. Particularly the fact the radiation force and the acoustic streaming are second order effects in the pressure.

1.6 Thesis outline

This thesis is composed of 10 chapters.

Chapter 2: Controlling the aggregation process. In this chapter we introduce pulse mode acoustics to study and to control the aggregation process and the morphology of the aggregates.

Chapter 3: Determination of secondary Bjerknes forces. In this chapter we developed an experimental methodology to determine the secondary Bjerknes forces. This determination was done for particles of different sizes and cells.

Chapter 4: Determination of the secondary Bjerknes force in microgravity. By following the methodology introduced in the last chapter, we presented the secondary Bjerknes forces determined in micro gravity product of two parabolic flights campaigns.

Chapter 5: Programmed acoustic separation device. In this chapter, we present the s-SPLITT device that combines hydrodynamic focusing and a programmed acoustic field. The separation of 7 and 12 μ was improved by the use of the acoustic field.

Chapter 6: Controlling the acoustic streaming. In this chapter, we introduce pulse mode acoustics as strategy to manipulate sub-micron sized particles. Also, we study the potential of pulse mode in the control of the acoustic streaming for some resonator geometries and sizes of particles.

Chapter 7: Applications in bacteria and metallic micro rods.

Chapter 8: Perspectives.

Chapter 9: Résumé de la thèse. French summary of the thesis.

Chapter 10: Conclusions and outlook. This chapter presents the main conclusions and future contributions of this work.

1.7 Publications during the PhD thesis

- Despina Bazou, Angelica Castro, Mauricio Hoyos. *Controlled cell aggregation in a pulsed acoustic field.* Ultrasonics, (2012) 52, 7, 842–850 (Annex A).
- Mauricio Hoyos, Angelica Castro. *Controlling the acoustic streaming by pulsed ultrasound.* Ultrasonics, (2013), 53, 1, 70–76 (Annex D).
- Anna Garcia –Sabate, Angelica Castro, Mauricio Hoyos, Ricard Gonzalez. *Experimental study of inter-particle acoustic forces.* Journal of the Acoustical Society of America, 2013 submitted (Annex B).
- Wei Wang, Angelica Castro, Mauricio Hoyos, Thomas Mallouk. *Autonomous motion of metallic micro-rods propelled by ultrasound.* ACS Nano, (2012) 6 (7), 6122–6132 (Annex E).
- Suzanne Ahmed, Wei Wang, Lamar O.Mair, Robert D. Fraleigh, Angelica Castro, Mauricio Hoyos and Thomas E. Mallouk. *Steering Acoustically Propelled Nanowire Motors towards Cells in a Biologically Compatible Environment using Magnetic Fields.* Langmuir, 2013 submitted and accepted (Annex F).

1.7.1 Patents

Based on the work of the group and mainly on the patent of the s-SPLITT device:

1 Dispositif de Séparation Fluidique « STEP-SPLITT » developped by Mauricio HOYOS, Pascal KUROWSKI, Natacha CALLENS. FR 0550645 11 march 2005 CNRS-UPMC.

During the course of this PhD thesis, we could developed other patents such as

1 **Method of forming a multilayer aggregate of objects « Multilévitation »**. Mauricio HOYOS, Angelica CASTRO and Despina BAZOU. European patent: EP12154125.4 6 february 2012 CNRS ESPCI and CNES.

2 **Method of forming an aggregate of objects: Pulsed acoustic field**. Mauricio HOYOS, Angelica CASTRO. International patent: PCT/FR2012/050403. 27 february 2012. CNRS, ESPCI and CNES.

3 **A method of manipulating objects « Acoustic streaming»**. Mauricio HOYOS, Angelica CASTRO. US patent: 13489555 6 june 2012 CNRS, ESPCI and CNES.

Chapter 2

Controlling the aggregation process

When a big number of particles undergo an USW in a parallel plate resonator, levitation occurs and the aggregation process is established. The aggregation process in microfluidic devices concern a few particles thus very small aggregates. In our study we are dealing with aggregates composed of hundreds or thousands of particles, generating 2D or 3D structures as showed the article (Annexe A).

In this chapter, we are going to study the aggregation process that we control. The originality of this first study is the introduction of pulse mode acoustics. The acoustic mode employed plays a role in the control of the aggregate morphology, shape, size and configuration.

2.1 Particle aggregation

At the levitation plane, the transverse component of **PRF**, **TPRF**, drives particles toward the point of maximum energy. Once particles are close each other the acoustic scattering generated by them, gives rise to the interaction force called secondary Bjerknes force that is attractive for particles placed at a plane perpendicular to the wave propagation. The Bjerknes force consolidates the aggregate[1].

Since the terms *Aggregation and Trapping* have not being clearly defined in literature, some papers refer as the same process; either, there is not difference between the numbers of particles involved. Then, acoustic trapping is the process where the **PRF** acts on particles to immobilize them at the equilibrium position. Later, transverse and secondary forces lead to particle aggregation.

[1] Aggregate: clump, cluster or agglomerate

Regardless these processes, applications deal with concentration, separation and manipulation of particles and cells. Some examples are studies of the morphology of micron-sized particles aggregates [41], retention of yeast cells [42] and also the influence of the medium concentration ($CaCl_2$) on the structure the aggregate [26]. Separation of suspended particles deals with filtering of liquids from sized particles in a plane parallel resonator[43, 30, 44, 9]; separation of oil emulsions from porous media, where oil droplets are positioned at the wave antinodes guided by USW [45]. Noncontact, non-toxic, non-damage effects of USW have been reported for cells (neural stem cells, human B cells, HepG2 cells, natural killer cells) and the potential showed by the acoustic as manipulation technique [46, 47, 48, 49] and in studies of cell-cell interactions and formation of 3D structures [50, 51]. Ultrasound can enhance the interaction of functionalized particles in suspension[29].

2.1.1 Phenomenology

Usually researches in acoustofluidics, employ microfluidic devices to manipulate single particles. An example is the device depicted in Figure 2.1a and b that correspond to a transversal resonator. In this device, the standing wave goes perpendicular to the incident direction of actuation [12]. In contrast, our devices are parallel plate resonators where the standing wave goes parallel to the direction of actuation. The **PRF**leads the acoustic levitation of the species. As depicted in Figure 2.1 c, Hele-Shaw cells lead us to manipulate particles with or without flow. The scale allows us to increase the amount of particles to manipulate with respect to microfluidic devices.

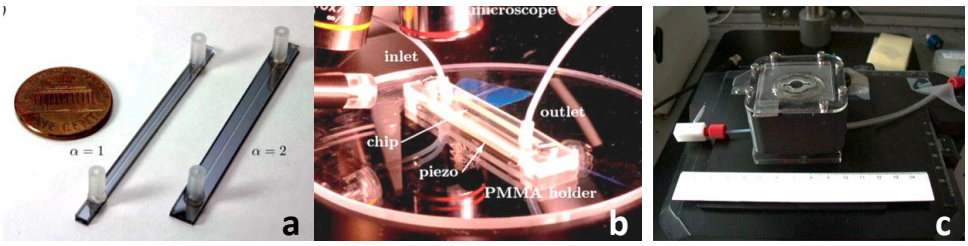

Figure 2.1 Some microfluidic devices employed by research groups: a) Scale of microfluidic devices. b) General view of the set-up; taken from [52]. c) Acoustic resonator of our group.

Our devices are parallel plate resonators that means, a device composed of different layers: the transducer generates the sound and is followed by the coupling layer (glue). Then, the transmission layer forms the bottom of the resonator followed by the fluid layer that contains the suspension; at the other end, the reflector layer is responsible for reflecting the incident wave back into the fluid layer, producing the standing wave [12].

The nominal frequency of the transducer does not correspond to the same value of the driving frequency. At these frequencies, we observe multiple aggregates in levitation: particles levitate and the aggregation process is carried out at low speed. By carefully tuning the frequency, it is possible to obtain the value adapted to forming a big aggregate; meanwhile, we observe the displacement of the aggregate by some μm in the x-y direction

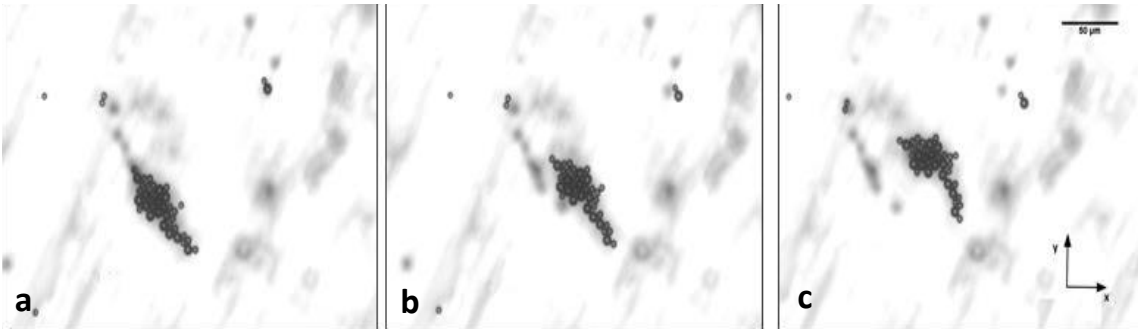

Figure 2.2 By tuning the frequency of the resonator, an aggregate of 15μm latex beads is observed for different frequencies at a) $f = 2.8885$ MHz. b) $f = 2.911$MHz. c) $f = 2.9475$MHz. Scale bar = 50μm, 5X magnification

that differs to the initial aggregation point, as depicted in Figure 2.2. The shape of the aggregate may vary due to rearrangements originated from the displacement in the transverse direction. The driving frequency produces faster migration, particle aggregation and also an homogeneous aggregate.

2.2 Acoustic modes

Usually, the frequency and the wave amplitude are associated as the acoustic parameters employed in particle manipulation. By acoustic mode we mean continuous and pulse wave emission. The latter is used in biological applications for targeting tissues with high energy ultrasound.

2.2.1 Aggregation in continuous mode

In our experimens the acoustic wave in continuous mode is delivered till the moment where the aggregation process finishes [2]. The aggregates obtained by this mode, are characterized by their tridimensional morphology [48, 53]. Also, 3D structures are obtained when the particle density is higher than 10^6 particles/ml [26]. This morphology is the result of the superposition of particle layers that generates non-homogeneous structures.

For cells, the aggregates obtained are also tridimensional, characteristic of mammalian tissues. Nevertheless, the observation under microscope of 3D aggregates makes difficult the study of cell-cell interactions for biological or pharmacological applications [48, 51].

[2] most part of the particles are aggregated and just ones rest at the levitation plane

2.2.2 Aggregation in pulse mode

Once fixing the driving frequency and the wave amplitude in continuous mode, we tuned the wave generator to burst function. Pulse mode, as depicted in Figure 2.3, consists in sending a group of pulses (Np) or periods separated by a certain time Then, we consider two parameters in pulse mode: the time of pulses Tp and the repetition time Tt.

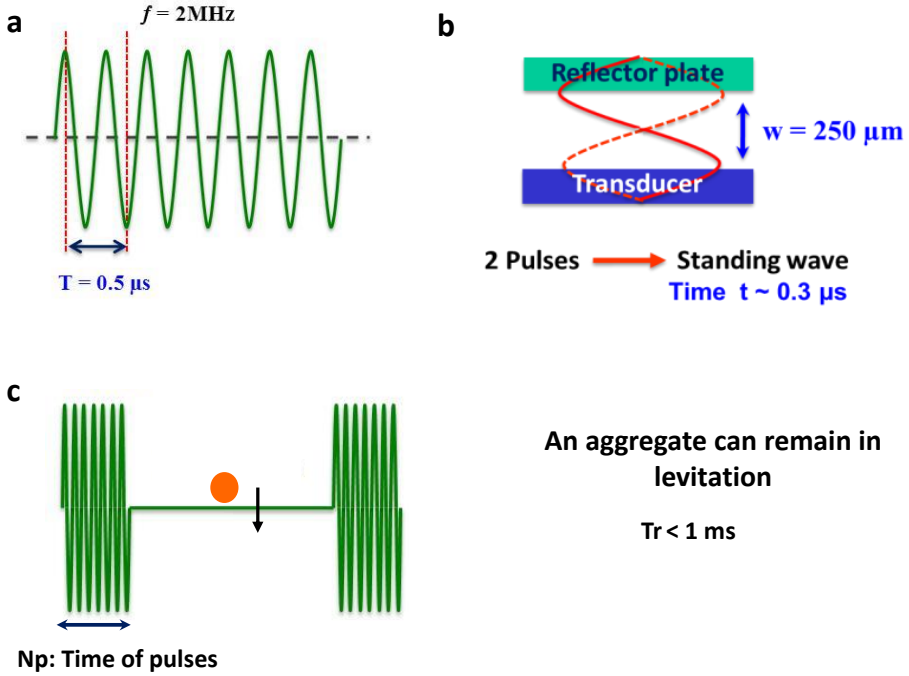

Figure 2.3 a) An USW of $f = 2$MHz emitted in continuous mode. The period of the wave is 0.5μs. b) Pulse mode means sending several packages of pulses (same frequency) separated by the repetition time. The pulses should be strong enough to remain particles or aggregates in levitation and the repetition time should be short enough to avoid particle settle down. Experimentally, Tt was determined as 1ms. c)For a resonator of 250μm thickness, an ultrasonic standing wave lasts 300 ns. Then, to form an USW it is necessary 2 pulses.

2.2.2.1 Time of pulses Tp

Given by the number of pulses Np multiplied by the time of one pulse at the resonance frequency. Is the time when the ultrasound is "on". It should be high enough for generating a standing wave, which lasts sufficiently for particles to reach their terminal velocity, given by the expression:

$$u_t = u_0 \left[1 - e^{(-t/\tau)}\right]. \tag{2.1}$$

Where u_0 is the terminal velocity, the relaxation time τ can be obtained by solving the equation of motion:

$$\mathbf{F}_{\mathrm{xy}} + \mathbf{F}_{\mathrm{s}} = \rho_p V \frac{du}{dt}. \tag{2.2}$$

Material	Particle size (μm)	Density (Kg/m^{-3})	Relaxation time (s)
Latex beads*	3	1050	0.52 μs
Latex beads*	10	1050	5.8 μs
Latex beads*	15	1050	13.1 μs
Silica beads*	10	1800	10 μs
Red blood cells**	2.62	1096	1.54 μs

Table 2.1 Relaxation time calculated for different particles. *Micromod particles, ** taken from [1]

However, the value of the force $\mathbf{F}_{\text{xy}}$ in unknown and there is no relationship that consider the complex coupling between the transverse acoustic force implied in the aggregation process. By solving the motion equation for the ratio $[u_t/u_0]$ the relaxation time can be determined. Table 2.1 shows the determination of this parameter for different particles where that does not depend on the field force using the following expression:

$$\tau = \frac{\rho_p d^2}{18\eta} \tag{2.3}$$

Therefore, we can neglect the relaxation time when a minimum of 10 pulses is emitted thereby reducing transient and retardation effects. We shall then consider that when the acoustic field is on, particles immediately move with constant velocity. When the acoustic field is off, particles instantly stop traveling.

2.2.2.2 Repetition time Tt

Is the time between the transducer is "off". It is important that Tt should be short enough, in order to prevent the sedimentation of particles or aggregates i.e., to a given number of pulses $Np = 100$, $t_{on} = 0.5$ms when the frequency is 2MHz. If each package is separated with a repetition time of 1kHz i.e: $t_{off} = 1$ms. We shall consider the limit of the allowed settling distance as one particles radius. For example, the sedimentation velocity of 10 μm latex is $\backsim 3\mu$m/s thus Tt should not be less than $1.67s^{-1}$. However an aggregate of particles settles down faster than a single particle. Experimentally, we have determined that the maximum repetition frequency for preventing particle or an aggregate to settle down is about $R_f = 1$ kHz: 1ms.

Generally speaking, for an experiment lasting 1 min, each on-off cycle lasts $t_{cycle} = 1.05$ ms, leading approximately 57143 on-off cycles during the experiment. Then, the total time at which the force is "on" will then be $\backsim 2.86$ seconds, $\backsim 5$ % of the total time.

2.3 Controlling the aggregation process

By using the resonator depicted in Figure 2.4 lend by Despina Bazou (Trinity College of Dublin) experiments were done to study the influence of continuous and pulse acoustic

modes in the aggregation process. The thickness of this resonator is established by the condition: $w = \frac{n\lambda}{2}$ where λ is the wavelength and n is the number of nodes.

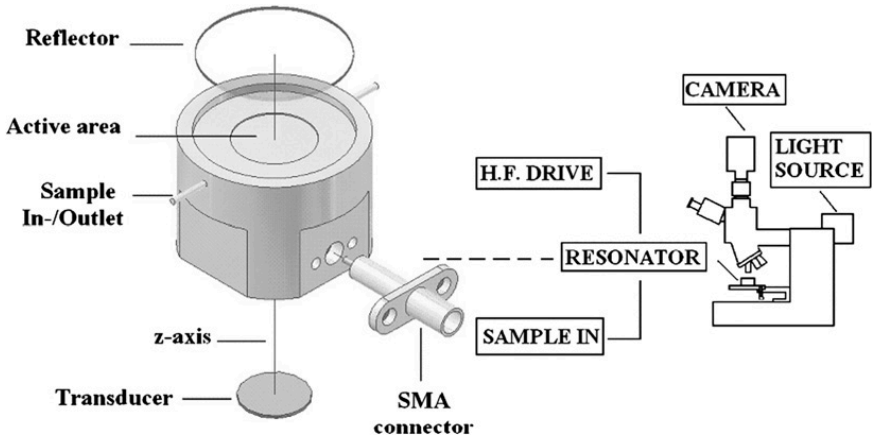

Figure 2.4 Schematic view of the ultrasonic resonator employed and the scheme of the epifluorescence observation. Quartz like reflector layer provides optical access from above. The back electrode was etched to give a single central aggregate in a single half-wavelength. This resonator has 250μm thickness and uses a transducer of 3MHz (Ferroperm, Denmark) [50].

Particle suspensions of 10 and 15 μm diameter [3] respectively supplied at 10% suspension of solids by, where aliquots were diluted to 20 ml to give about 0.11% solids in deionized water.

For cells, by following the protocol of cellular culture described in the article (Annexe A), we employed concentrations of 5×10^5 and 3×10^6 cells/ml of CaCO2 cells (colon adenocarcinoma).

The sample was injected in the resonator filling homogeneously their volume (45 μl). After one minute, particles settled down and the acoustic field was switch on. The initial conditions: the driving frequency, the transducer voltage for particles and cells as mentioned in Table 2.2.

	Driving frequency (MHz)	**Wave amplitude (Vp-p)**
10 μm latex beads	2.134	14.4
15 μm latex beads	2.132	16
CaCO2 cells	2.148	10

Table 2.2 Experimental conditions employed.

Once the driving frequency was established, we noted fast levitation as showed in Figure 2.5. Starting with a driving frequency of 2.15 MHz, in continuous mode we founded better results by sweeping the resonance frequency at the second or third decimal. By fixing the new frequency, we changed to pulse mode. In pulse mode, our first aim was to

[3] Micromod® polystyrene latex, density 1.056 kg/m^3

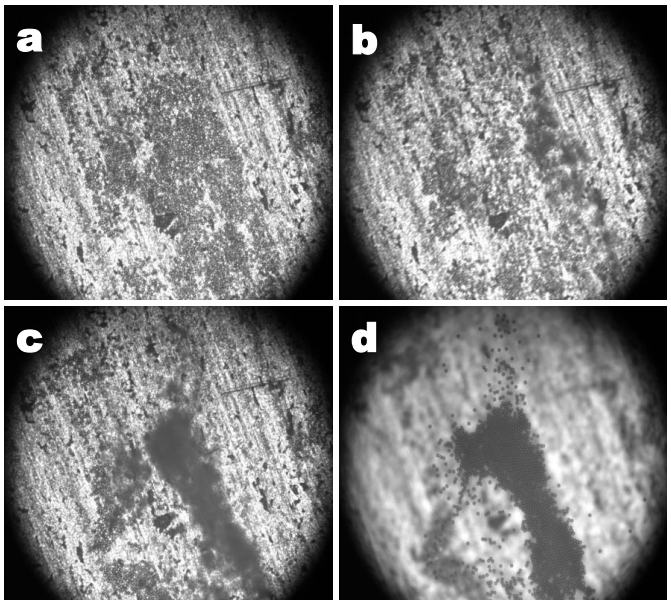

Figure 2.5 Levitation process observed for 10μm particles at 5X magnification. a) At t = 0, particles are settled down (metal plate is clearly distinguishable). b) At t = 4s, particles start to move towards the levitation plane. c) In the levitation plane particles aggregates them, t = 14s. d) At t = 30s, and at the levitation plane, particles aggregates.

determine the number of pulses needed to keep an aggregate unchanged in levitation. For single particles, a minimum of 100 pulses can keep them just in levitation. Lower number of pulses produces disaggregation and sedimentation; the same effect was also observed for repetition time smaller than 1 kHz irrespective of the number of pulses employed. In contrast for cells, the minimum number of pulses required for aggregation was 50 and a $Tt = 1$ kHz. Therefore, in all experiments we aimed at forming aggregates of similar sizes (maximum diameter $\backsim$2 mm).

2.4 Results

Usually, aggregates are formed by single particles, doublets, triplets or even small aggregates already formed at other points of the levitation plane. The aggregation process is faster in continuous mode than in pulse mode. Figure 2.6, illustrates the aggregation process in continuous mode for 10μm latex particles.

Then, the formation of an aggregate like a layer is obtained, however, single particles still aggregate. At the border of the aggregate there is particle reorganization. The overlapping of particle layers were generated by the increasing pressure of incoming particles, thus determining the change of the aggregate configuration from 2D to 3D aggregates. Tridimensional structures are shown in Figure 2.7, where 3D structures can be visible as darker zones at the center of the aggregate.

Films were analyzed employing the software ImageJ. By drawing the aggregate at the time using the free-hand software tool during the aggregation process, the area of the aggregate was determined (Figure 2.8). Then, we could determine the increment of the aggregate area.

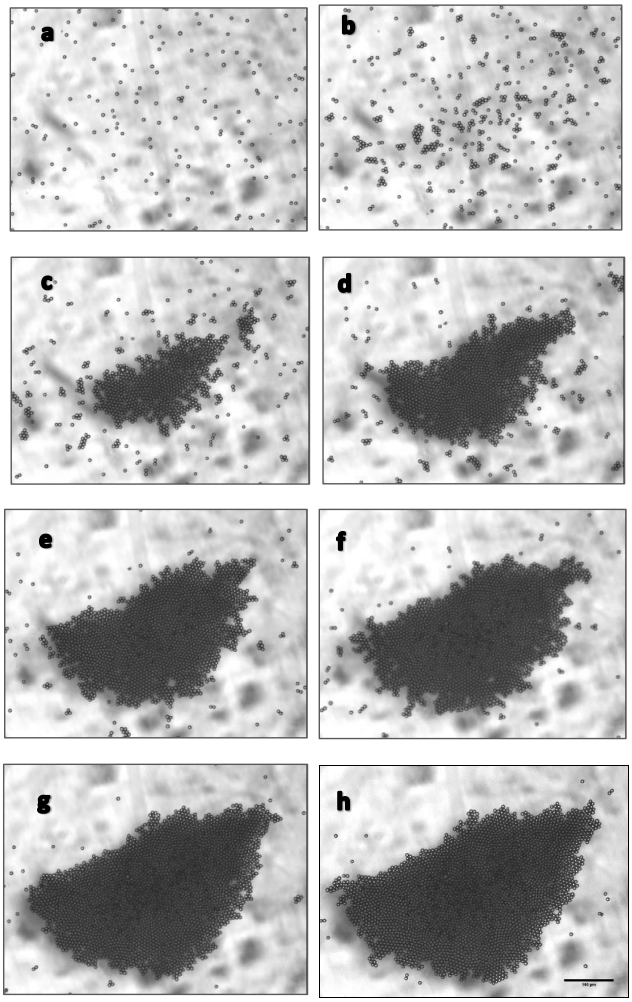

Figure 2.6 Aggregates obtained in continuous mode for 10μm particles. a) Particle levitation. b) One second later, doublets and single particles reach the aggregation point. c-d) The aggregate is formed by particles that arrive at their boundary and starts to reorganize. e-h) Particle overlapping generates 3D structures, observed as dark zones at the central part of the aggregate. The aggregation process was completed in 300 s and the aggregate reached a diameter of 2 mm. Scale bar = 100μm.

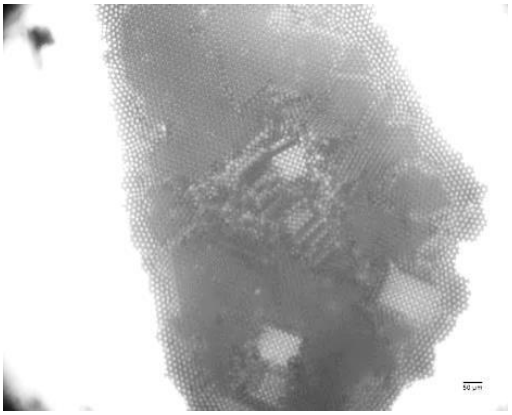

Figure 2.7 15μm latex particles aggregate. Tridimensional structures can be seen as dark regions, mainly at the central part of the aggregate. Scale bar = 50μm.

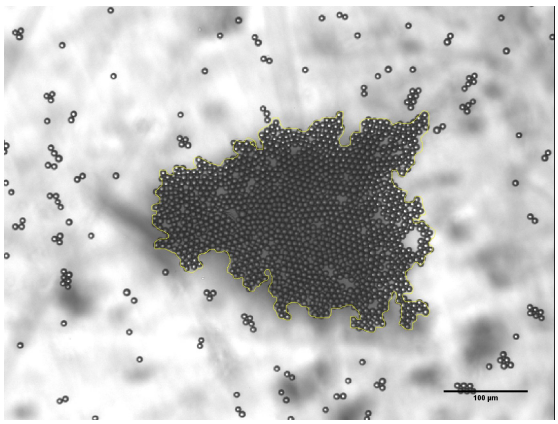

Figure 2.8 For the area determination, the aggregate contour is drawed (yellow line) in ImageJ software. Scale bar = 100μm.

The aggregation rate was estimated by measuring the area growth over time for each aggregate as shown equation 2.4 where the normalized aggregate area was quantified as

$$\text{Aggregate normalized} = \frac{\text{Aggregate area at time t}}{\text{Final aggregate area}}. \tag{2.4}$$

2.5 Particle aggregates

In Figure 2.9a, the curve for 10μm particles in continuous mode show a rapid increase until 4s to finally becoming more linear. These increments are the effect of particle rearrangements: particles arrives to the aggregate and reorganize at the periphery or push the other ones towards the center of the aggregate, leading 3D structures. The effect of these rearrangements is more evident in Figure 2.9 b, where the peaks represents the transitions from a 2D aggregate to 3D by particle overlapping. However, in pulse mode (Figures 2.9 c and d) during the aggregation process we do not appreciate in both curves these variations. The rearrangements are smooth and at slow velocity due the aggregation process where remains a 2D aggregate.

Figure 2.10 shows the aggregation process in pulse mode. Roughly at t = 1s there are some doublets already formed going to the levitation point. The aggregate produced is 2D particle layer.

Similar tendencies we observe in the cases of 15μm particles in continuous and pulse mode. In continuous mode, we observe more variations (Figs 2.11 a and b) in the formation of the aggregate also in their transition to 3D structures than in the case of 10μm. In pulsed mode the growth rate was linear (Fig.2.11 c) and the fluctuations were smaller than those observed in continuous mode. The normalized area growth rate shows transitions less than 0.1, due particle rearrangement is small compared to that observed in continuous mode (Fig. 2.11 d).

Now, the aggregation process in pulsed mode is slower than in continuous mode, do not imply that lower growth rates entail a higher probability to obtain 2D than 3D aggregates; in fact, the initial particle or cell concentration also need to be taken in consideration. It is worth noting that the aggregation process in continuous mode, the most part of the particles reached the node already aggregated (some doublets and triplets) and only

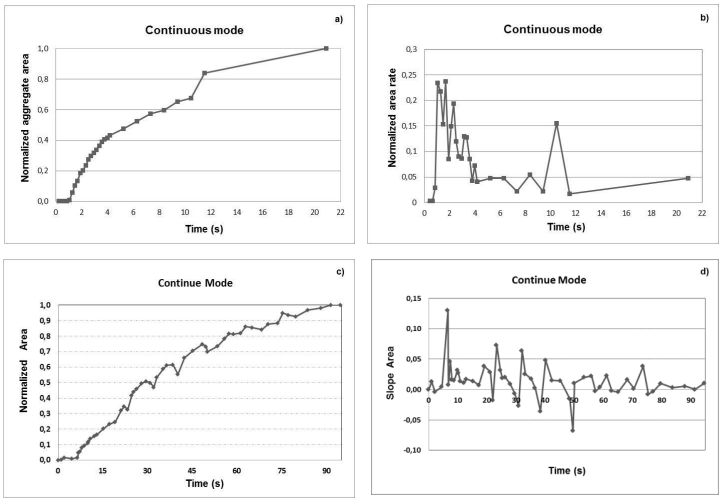

Figure 2.9 a and c) Normalized aggregate area, b and d) normalized area rate, for 10μm particles produced in continuous mode and pulse mode.

a few single particles joined the aggregate from the bottom of the resonator, and their contribution to the 3D structure was negligible, whereas in pulsed mode all particles started to aggregate by reaching the node.

2.6 Cell aggregates

Ultrasonic frequencies are preferred for cell manipulation, where high pressure amplitudes do not induce ultrasonic cavitation, usually associated with vigorous order-disrupting bubble activity [54], leading cell damage or lissis.

The aggregation process in cells was done at a driving frequency of 2.13 MHz, where after 10s of ultrasounds the aggregate reached its maximum size. Representative 3D and 2D cell aggregates are shown in Fig.2.12 a and b, obtained in continuous and pulse mode respectively. Experiments in continuous mode with particles clearly showed layer overlapping (Fig 2.7), while cell aggregates showed rather darker layers (Fig.2.12 a).

It is important to note that cells are more elastic than particles, thus initially, compaction of the aggregates occurred by increasing the pressure prior to the formation of cell layers.

The curve of the growth rate variation in continuous ultrasound is depicted in Fig.2.13 a. When cells are employed, the aggregate does not grow linearly with time. The elastic properties of the cells as well as their polydispersity could account for this effect. In continuous mode, the cell aggregate growth rate followed the same pattern as that for 10μm particle aggregates; a rapid increase of the area in the first second followed by a linear growth. In contrast, in pulsed mode the growth rate was slower and followed by a linear pattern. This holds true for all the pulse modes conditions used here. The growth rate fluctuations in continuous mode showed an initial peak and then decreased

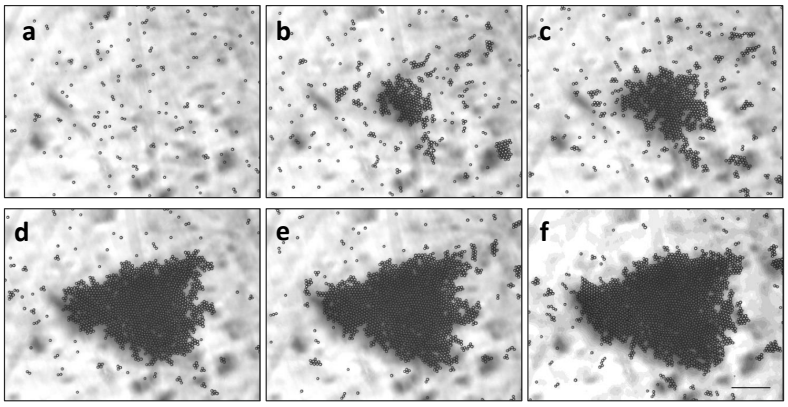

Figure 2.10 Aggregation process in pulse mode for 10μm latex particles; generated at 100 pulses and 4kHz as repetition frequency. This process lasts 3min.

to converge with the curves obtained for the different pulse mode conditions; peaks in pulse mode curves were rarely observed and were still much smaller than those observed in continuous mode.

We have to note that the resonator is a closed system thereby the aggregate is in batch sedimentation. Hydrodynamic lubrication interactions can keep particles in relatively close contact, therefore sedimentation of the disrupted aggregate occurs much faster than that of a single particle. Cell aggregate sedimentation is more unpredictable as cells are not rigid; they have physiological interactions and in many cases they are polydisperse. When the acoustic force is switched off, the sedimentation rate of a cell aggregate is very low, much slower than that of an equivalent aggregate of particles. Furthermore, the cell aggregate does not fall as a consolidated regular shaped body due to the cell-cell interactions, but more like a folded sheet. Cells are denser and less compressible than the suspending phase; they migrate under the influence of **PRF** to the pressure nodes separated by half an acoustic wavelength. During this process, there is no detectable increase in the resonator temperature over 1 h of continuous ultrasound that could change the driving frequency, as previously shown by Bazou et al. [26].

Finally, we estimate the transverse acoustic force responsible for aggregation in continuous and in pulse mode. By measuring the migration velocity for particles and cells at the levitation plane [4] and the transverse force, as show Table 2.3.

	Continuous mode		**Pulse mode**	
	v_{xy} (m/s)	$\mathbf{F}_{\mathrm{xy}}$ (N)	v_{xy} (m/s)	$\mathbf{F}_{\mathrm{xy}}$ (N)
10 μm latex	2×10^{-5}	1.8×10^{-12}	4×10^{-6}	4×10^{-13}
15 μm latex	1.3×10^{-5}	2×10^{-11}	3.5×10^{-6}	2×10^{-13}
CaCO2 cells	2.23×10^{-4}	12×10^{-11}	1.47×10^{-4}	5.5×10^{-11}

Table 2.3 Transverse forces and velocities determined for particles and cells in pulse and continuous mode. The average cell diameter is 20μm.

[4] Using the free software Tracker http://www.cabrillo.edu/ dbrown/tracker/

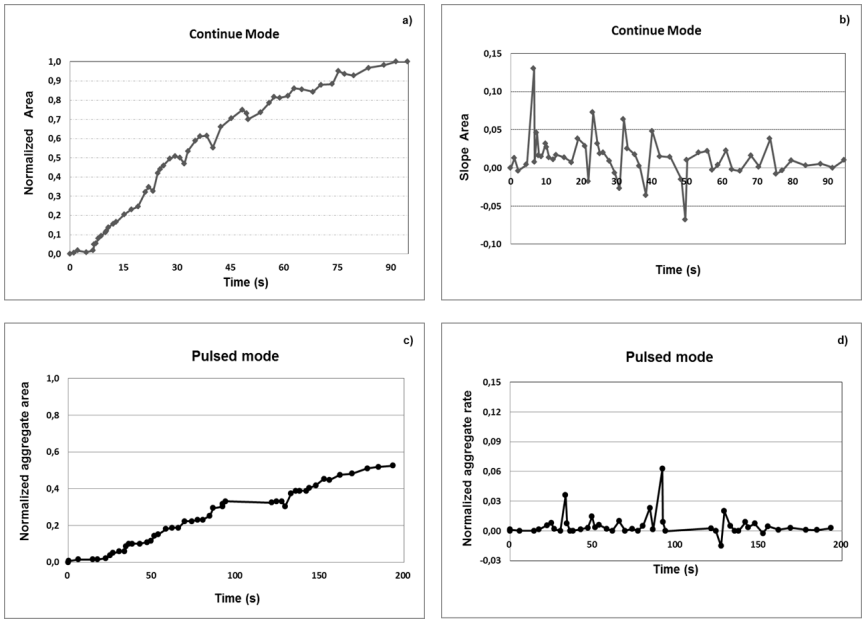

Figure 2.11 a and c) Normalized aggregate area, b and d) normalized area rate, for 10μm and 15μm particles respectively produced in pulse mode. Pulsed mode was employed for 15μm particles at 250 pulses and 2 kHz as repetition frequency.

Pulse mode can control particle and cell aggregation. The aggregation rate is reduced when pulse mode is employed. By considering that particles have a constant transverse velocity and by taking into account that the drag force is proportional to the velocity, we can compare the velocity ratio: $u_{pulsed}/u_{continuous}$, being 0.24 for 15 μm and 0.2 for 10μm particles. We note that the considerations made here concern typical velocities; an analytical statistical study that determines the velocity distributions would be required for thoroughly exploiting the aggregation process in pulse mode.

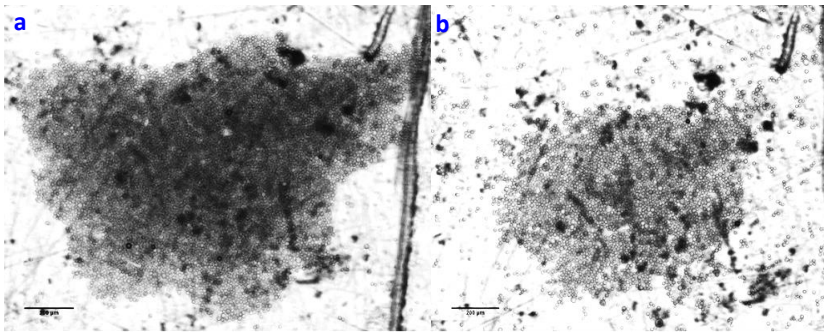

Figure 2.12 Aggregates of cancer cells, observed at 5X magnification. Aggregates obtained in a) continuous mode and in b) pulse mode. Scale bar = 200μm.

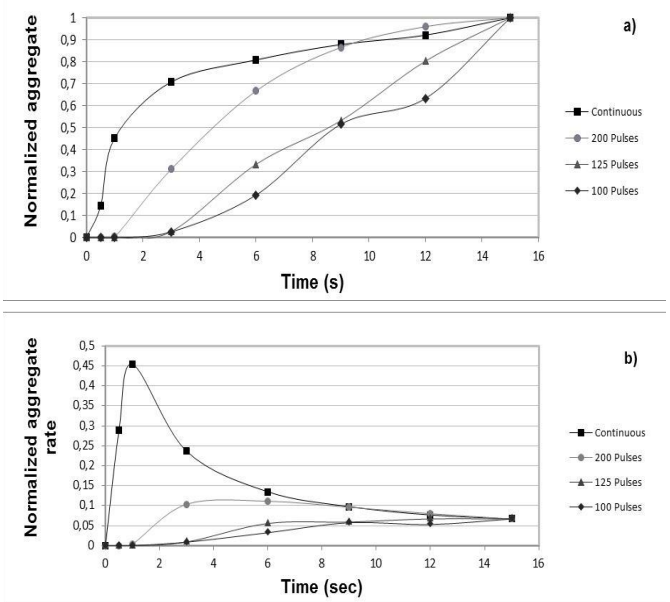

Figure 2.13 a) Normalized aggregate area and b) Normalized aggregate rate obtained to CaCO2 cells in ultrasonic resonator in continuous and different pulse modes (100, 125, 200 pulses).

2.7 Aggregation by modifying the wave amplitude

Another possibility of generating 2D aggregates is by reducing the amplitude of the acoustic wave i.e., by reducing the voltage. Lower amplitude implies weak acoustic forces; the transverse velocity does not change significantly.

Experiments were done with 15 μm latex particles (0.1 of solids diluted in water) by reducing the amplitude of the acoustic wave from the maximum amplitude (16 Vp-p), as show Figure 2.14. The aggregates obtained at 30 and 40%, shows several 3D structures at the center (Figure 2.14 a and b respectively). At 60%, Figure 2.14c shows an aggregate mostly 2D but at the center it is possible to appreciate a concave shape.

However, at a threshold amplitude, **PRF** is not enough to maintain the aggregate in levitation and particles settle down i.e., the amplitude threshold for levitation of 10μm latex beads is 8 Vp-p whereas for silica beads of the same size is important to consider minimum of 15 Vp-p. Usually, we employ the maximum value, where the process is faster and also aggregates are at least homogeneous. Then, we compared these aggregates to those obtained in pulse mode. The aggregation process takes more time than at the 60% amplitude reduction. Hence, a 2D aggregate was obtained, as depicted in Figure 2.15a.

A careful observation allowed us to precise that at central part of the aggregate start to present a concavity. Figures 2.15 b and c, shows a careful particle reorganization at this zone. By comparing the aggregates obtained in both cases, we can see that pulse mode allows the generation of 2D aggregates.

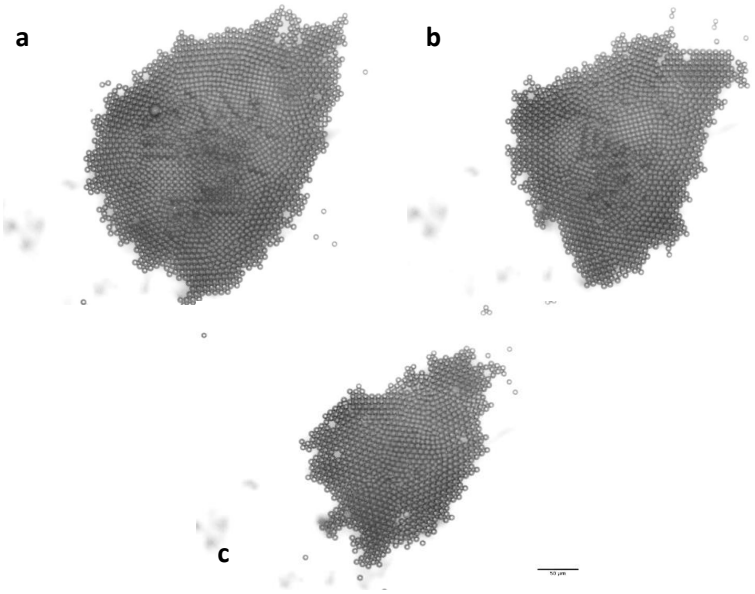

Figure 2.14 Aggregates of 15μm latex beads obtained by reducing the wave amplitude to a) 30, b) 40 and c) 60% from the maxima of 16 Vp-p. We observed a proportional increment of the time of aggregation: at 30% the experiment lasts 6 min, at 40% 8,3min and at 60% 10,5min. Experiments done at lower amplitudes just produced particle levitation and doublets formation. Scale bar = 100μm.

2.8 Conclusions

Pulse mode acoustics is a new way of controlling the aggregation process and aggregate morphology. Throughout experiments made in continuous mode for particles and cells, we observed 3D structures generally at the center of the aggregates obtained; these 3D structures are not homogeneous. Meanwhile, by modifying pulse mode parameters such as the time of pulses and the repetition time a 2D structure can be obtained in acoustic levitation. By doing several observations at the microscope we could identify these structures obtained as homogeneous layers.

The use of pulse mode offers several advantages as respect to continuous mode. The possibility of increasing the acoustic force through employment of a minimum number of pulses resulting in rapid yet controlled particle or cell aggregation without adversely affecting the cells, reduced liquid/cell media heating maintaining constant the thermodynamic and physicochemical properties of the suspension and the architecture of the resultant aggregate can be modified irrespective of the initial particle or cell concentration.

Finally, based on these observations we consider that by reducing the amplitude to control the aggregation process is not worth, in fact is difficult to find the precise amplitude to generate the optimum or required 2D aggregate.

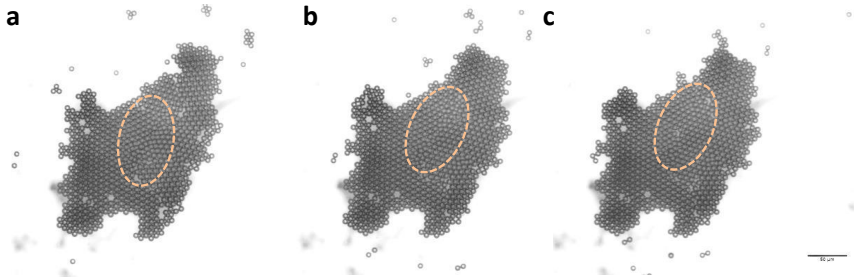

Figure 2.15 Aggregates of 15μm latex beads obtained at pulse mode where the oval in dot lines show a) a part of the aggreggate that star to folding. b) However, pulse mode allow to the aggregate to remain their 2D structure; there is particle reorganization and c) the aggregate can remain with an homogeneous morphology. Scale bar = 100μm.

Chapter 3

Determination of secondary Bjerknes forces

The study of acoustic forces on different media has become important in late years because of the increasing number of applications taking advantage of acoustic manipulation of objects: acoustic levitation or contactless positioning and manipulation of drops and bubbles and management of fluids in low gravity. Furthermore, many authors have experimentally and theoretically studied the secondary Bjerknes force acting mainly on bubbles not on rigid particles. Even though scientific articles have been written about secondary forces in particles, as far as we know, none of them has experimentally determined the magnitude of these forces [55] (see Annexe B).

The goal and the originality of this study is to present an experimental method to determine the secondary Bjerknes force in the aggregation process of rigid particles and cells. This study leads us a better understanding of the interparticle interaction during the aggregation process.

In a previous work of our group, films made of the aggregation process in particles, showed interparticle interactions taking place. Carefully regarding frame by frame the cases obtained as depicted in Figure 3.1, we identified a critical distance at which there is a slight vibration of one or both particles indicating that they start to undergo the interaction; we assume to be the secondary Bjerknes interaction. After the critical distance, particles approach till being in contact forming a stable doublet that is the first stage of the aggregation process.

3.1 Secondary Bjerknes force

In 1904, two Norwegian scientists C.A. Bjerknes and his son V.F.K. Bjerknes carried out a mathematical analysis of pulsating air bubbles in a stationary acoustic field. They took

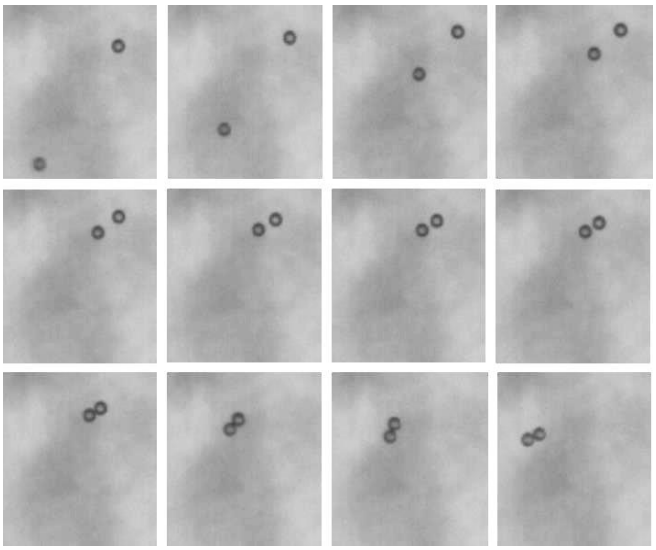

Figure 3.1 10μm latex beads at the levitation plane. Once particles reach the critical distance, both start to interact leading particle aggregation. Magnification 20X.

into account assumptions such as: the surrounding liquid is inviscid and incompressible, the separation distance between two bubbles is much larger than their radii, bubbles keep their spherical shape during pulsations, and the amplitude of the pulsations is small enough that nonlinear effects can be negligible. Therefore, the force exerted by the primary radiation force (**PRF**) on one air bubble is known as the primary Bjerknes force. The mutual attraction or repulsion force between two air bubbles when the wavelength is assumed to be much greater than the radii and spacing of the bubbles is known as the secondary Bjerknes force.

In a sound field, an object will scatter the incident wave and experience the acoustic radiation force which is a nonlinear time-average effect associated with nonlinear properties of the wave motion in a continuous media. The radiation force arises as the result of second-order effects of the primary and the scattered wave fields. Then, when two objects are present in a sound field, in addition to the **PRF**, the total acoustic radiation force on either object will also include the effect due to the scattered field of the primary wave by the other object [55]. In such situations the forces between objects can be calculated simply by using the following equation

$$F_{1-2} = -\langle V_2(t)\nabla p_1(r,t)\rangle\,. \tag{3.1}$$

where F_{1-2} is the force acting on sphere 2 by sphere 1, V_2 is the volume of the sphere 2, p_1 is the scattered pressure field of the primary incident wave by sphere 1 at the location of sphere 2. There is no dependence of the force on the incident direction. The pressure gradient generates the secondary Bjerknes force. This calculation is only valid when the wavelength is greater than the distance between the two objects. Otherwise the re-scattering of the radiated field by the other object has to be taken into account to give a better representation of the total field. The integration of the total pressure field over the surface of the object has to be performed to calculate the total radiation force on the object [56].

Weiser et al. [57] in 1984 studied the acoustic forces for particles where they found interparticle interactions. This study was the first one to take into account the secondary Bjerknes force between two compressible spheres. By taking into account the compressibilities of the spheres the expression derived can be written as follows [58].

$$\mathbf{F}_{\mathrm{SB}} = -\frac{2\pi\rho_f}{9}(\beta_f\omega P_a)^2\left(1-\frac{\beta_1}{\beta_f}\right)\left(1-\frac{\beta_2}{\beta_f}\right)\frac{r_1^3 r_2^3}{d^2} \tag{3.2}$$

where d is the inter-particle distance. These forces are defined specifically for particles and they can be explained as the attraction or repulsion forces between two particles that oscillates in a standing wave. According with the references, the magnitude of the force between rigid spheres depends strongly on the interparticle distance d.

Also, Weiser et al. [57] gave two expressions depending on the angle formed between the lining of the two particles and the direction of the propagating field. Hence, when analyzing two equal spheres aligned in the direction of propagation of the sound field we shall use

$$\mathbf{F}_{\mathrm{p}} = \frac{4\pi(\rho_p-\rho_f)^2 v_{ac}^2 r^6}{3\rho_f d^4} \tag{3.3}$$

where v_{ac} is the velocity amplitude of the incident acoustic wave. In this equation (3.3), the force will be repulsive. When particles are aligned perpendicularly to the direction of propagation, the force will be attractive.

$$\mathbf{F}_{\mathrm{p}} = -\frac{2\pi(\rho_p-\rho_f)^2 v_{ac}^2 r^6}{3\rho_f d^4} \tag{3.4}$$

The Table 3.1, presents a summary of the different forces that interacts in an ultrasonic resonator. Considering a frequency of 2.83MHz, the same acoustic energy in $\mathbf{F}_{\mathrm{xy}}$ and $\mathbf{F}_{\mathrm{z}}$, and the same particles size (10 μm latex beads) the magnitude of $\mathbf{F}_{\mathrm{SB}}$ and $\mathbf{F}_{\mathrm{p}}$ has been determined. The value of v_{ac} is calculated by using the expression: $E_{ac} = (\rho_f v_{ac})/2$ that is of the order of 3.6 cm/s [55].

	Force	Plane of Action	Described for	Magnitude (N)
Primary Acoustic Field	Axial Acoustic Force $\mathbf{F}_{\mathrm{z}}$	Axial	Particles	10^{-11}
	Primary Bjerknes Force $\mathbf{F}_{\mathrm{PB}}$	Axial	Bubbles	10^{-5}
	Transverse Acoustic Force $\mathbf{F}_{\mathrm{xy}}$	Transverse	Particles	10^{-13}
Secondary Acoustic Field	Secondary Bjerknes Force $\mathbf{F}_{\mathrm{SB}}$	Transverse	Particles and Bubbles	$10^{-13}/10^{-5}$
	Force Between Two Rigid Spheres $\mathbf{F}_{\mathrm{p}}$	Transverse	Particles	10^{-15}

Table 3.1 Summary of the acoustic forces in an acoustic resonator for $r = 10\mu$m latex particles at an approximate distance of 20 μm. These orders of magnitude takes into account polystyrene particles in water. Acoustic axial and transverse forces have been considered as in [30], i.e. $E_{ac} = 18$ J/m^3.

Secondary forces are two orders of magnitude smaller and are even effective at very short distances between particles [31].

According to [1] the acoustic pressure can be expressed in terms of the average acoustic energy $\langle E_{ac} \rangle$ as

$$|p_{ac}| = c_f \sqrt{4\rho_f \langle E_{ac} \rangle} \tag{3.5}$$

3.2 Experimental determination of secondary Bjerknes force

The secondary Bjerknes force cannot be determined directly because single measurements of the acoustic pressure inside the channel cannot be made. Since the Reynolds number in the channel is small, Stokes' drag can be considered:

$$\mathbf{F}_{\text{Drag}} = -6\pi\eta r\mathbf{v}, \tag{3.6}$$

An indirect method based on the balance of forces acting on a particle in the levitation plane was considered. The force balance can be expressed as:

$$\left(\rho_p V + \frac{\rho_f V}{2}\right) \frac{d\vec{v}}{dt} = \mathbf{F}_{\text{xy}} + \mathbf{F}_{\text{Drag}} + \mathbf{F}_{\text{SB}}. \tag{3.7}$$

where V is the static particle volume, $\vec{v}$ is the particle velocity.

The equation 3.7 contains two unknown terms, $\mathbf{F}_{\text{xy}}$ and $\mathbf{F}_{\text{SB}}$. In order to determine these forces, it is necessary to identify the regions where each force is acting. This identification can be carried out from the analysis of the evolution of the velocity of the particle in the time. As depicted in Figure 3.2 at the levitation plane, particle A moves due the transverse force ($\mathbf{F}_{\text{xy}}$) at a transverse velocity (v_{xy}). When particle A is close to particle B, there is a critical distance d_c in which particles start to interact and the mutual attraction was observed. At the critical distance, we consider the interaction of the transverse and the secondary Bjerknes force.

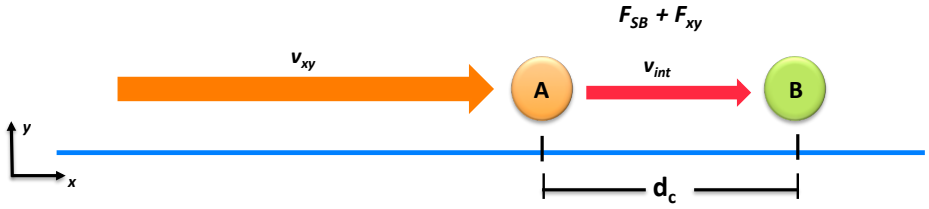

Figure 3.2 Schema of experimental determination of the secondary Bjerknes forces. Particle A travels at the levitation plane due the influence of the **TPRF**. When particle A is enough close to Particle B at d_c, both start to interact. Then, the mutual attraction between particles takes place.

Just before d_c, by tracking the particle A we can determine the transverse velocity v_{xy} (a mean velocity) to determine the transverse force. As the value of the acoustic pressure is unknown, we can consider $\mathbf{F}_{\text{xy}} = \mathbf{F}_{\text{Drag}}$. Considering that $\mathbf{F}_{\text{xy}}$ does not change significantly after particles reach d_c, $\mathbf{F}_{\text{SB}}$ can be determined from the difference of the $\mathbf{F}_{\text{xy}}$ and the force of interaction (we obtained a velocity of interaction (by measuring the distance and time of interaction). Once $\mathbf{F}_{\text{SB}}$ is known, p_{ac} can be calculated from Eq. 3.5.

3.2.1 Transverse approach

Experiments were done employing the resonator depicted in Figure 3.3. The details of the experimental set-up employed in this chapter had been described in the article (Annexe B).

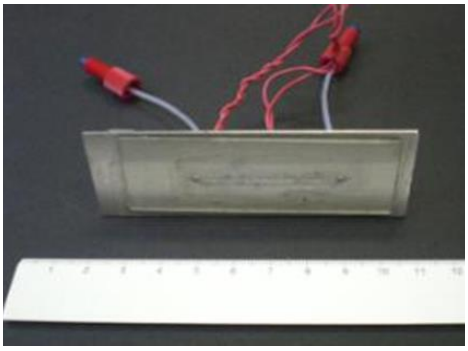

Figure 3.3 Ultrasonic resonator one inlet-one outlet, allow flow throughout the resonator. The device is composed by a stainless steel plate with a PZ-27 transducer of 2.5MHz as nominal frequency (Ferroperm, Denmark), glued behind the metal plate. The dimensions of the resonator are: 4cm length, 250μm thickness and 1cm width. As reflector plate we use a glass plate. We employed a driving frequency of 2.63MHz.

A two ways valve was placed at the cell outlet to ensure stationary conditions inside the cell for the experiments and to flush the suspension to a waste flask after each test.

The different suspensions were injected by means of a syringe. Once particles were injected, the valve was closed and particles were let to sediment for one minute. Afterwards, the ultrasound system was turned on at the driving frequency and films were recorded. These cases where processed by means of the open-source software Fiji (ImageJ). The position of the particles at each frame was obtained by using the plug-in MTrack2 in which the protocol for image treatment is described in the Annexe B.

More than 100 films were recorded, 9 of which contained 17 analyzable cases. These cases consist of two single particles in the levitation plane approaching each other due to effects of the transverse force and the secondary Bjerknes force. Instead the big amount of films done, we obtained a low number of analyzable cases. This can be due by the limited field of view of the microscope through which the channel was observed, the change of particles position due their interaction with the acoustic energy. Among the analyzable cases we have for a driving frequency of 2.83MHz latex particles of 5μm, 7.5μm and one case between 3.5 and 5μm and for a driving frequency of 2.866MHz another case for 5μm particles. The particle position and its velocity can be obtained at each video frame (Figure 3.4).

The different values of the acoustic pressure and acoustic energy in the analyzed cases can be explained by the fact that each case was carried out under different experimental conditions; the particle attraction and aggregation occurred in different zones of the levitation plane, which had different values of the acoustic energy density. The range

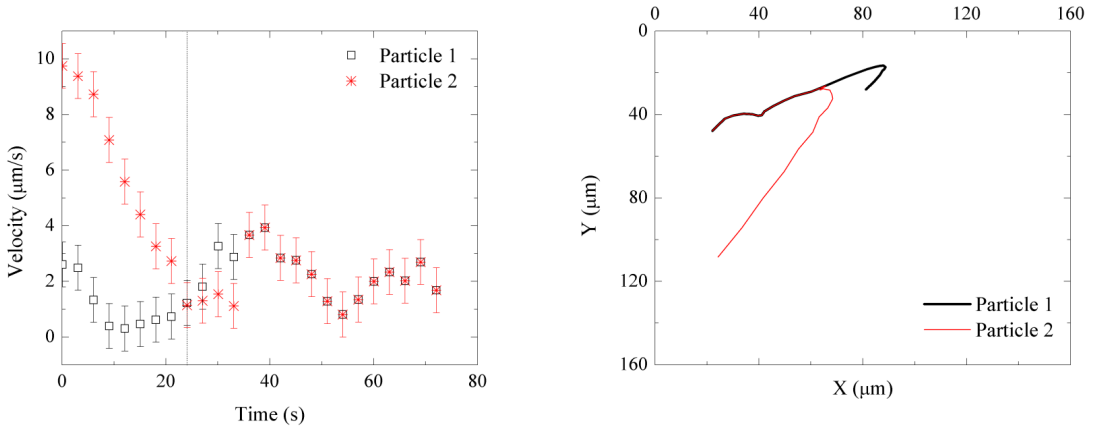

Figure 3.4 (a) Trajectories, and (b) velocity profile of two 5μm particles at 2.83MHz. Dashed line shows the time at which d_c is reached.

Particle size	d_c (μ/m)	$\mathbf{F}_{xy}$ (N)	$\mathbf{F}_{SB}$ (N)	p_f (Pa)	Eac (J/m^3)
5μm	24.1	4.75×10^{-14}	6.78×10^{-14}	3.92×10^{5}	17.10
7.5μm	39.2	5.75×10^{-14}	7.02×10^{-14}	1.92×10^{5}	4.09
5μm	24.4	1.01×10^{-13}	5.07×10^{-14}	3.38×10^{5}	12.70
5μm - 3.5μm	23.1	4.90×10^{-14}	2.49×10^{-14}	3.88×10^{5}	16.70

Table 3.2 Secondary Bjerknes forces, critical distance, acoustic pressure and acoustic energy density determined for these cases.

of values of the acoustic energy obtained are very close to those reported by [30] (13-18 J/m^3). It can be observed that the secondary Bjerknes force is slightly larger for 7.5μm particles, especially taking into account that the calculated Eac is approximately three times smaller than in the rest of the cases. The case with two different size particles shows the smallest value of secondary Bjerknes force, which is in agreement with the theoretical predictions.

3.2.2 Tracking both particles

Now, we consider more complex cases: two particles traveling at the levitation plane leading interparticle interaction to produce a doublet. Here due the easiness of manipulation, we employ Tracker software [1] to determine the mean transverse velocity. Instead to consider the angle between particles and the component of the velocity, we consider the magnitude of the resultant. A careful observation lead the determination of the critical distance and the time of interaction (in which the interparticle interaction is produced till the formation of the doublet).

Then, monodisperse suspensions of latex beads of 5, 7, 10, 12 and 15μm were diluted in

[1] using the free software Tracker http://www.cabrillo.edu/ dbrown/tracker/

distilled water at 10% of solids. However, in this part we employed a circular resonator depicted in Figure 3.5.

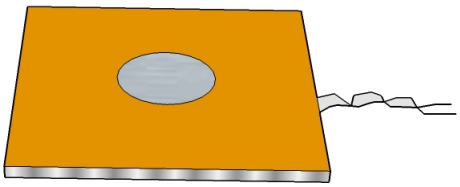

Figure 3.5 Circular resonator composed of a stainless steel plate of 2mm thickness where a circular PZ-26 transducer (Ferroperm, Denmark) of 4.2MHz of nominal frequency is glued behind (Chemtronics conductive epoxy). At the other side of the plate, polyimide Kapton® tape was employed to build the resonator. A cover slip was used like reflector plate.

Once the sample was put on the resonator, we left to sediment for one minute. Afterwards, the ultrasound system was turned on at the driving frequency for particles levitation and aggregation. The weak concentration of suspensions and the knowledge of the development of experiments allowed us an easy identification of the cases. Then, we recorded 15 films, 3 made for each particle size in which we obtained approximately 3 or 4 analyzable cases. Figure 3.6 shows the $\mathbf{F}_{\mathrm{SB}}$ for different particle sizes. This force increases with the increase of the particle size.

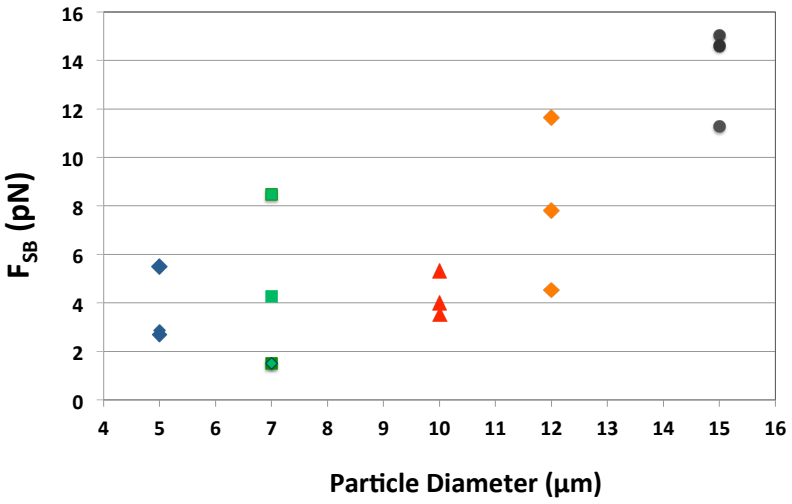

Figure 3.6 Secondary Bjerknes forces measured in the resonator for different aggregation process of particles of the same diameter. Each point is an experiment.

Graphically, the relationship between the critical distance and the particle size, Figure 3.7a, shows an increment of d_c with the critical distance, as 3.7. However, in figure 3.7b, there is a relationship at least 2 ± 0.5 of diameter particle.

At the critical distance one particle accelerates; this acceleration is faster that sometimes difficult to determine. A mean velocity was determined to directly calculate $\mathbf{F}_{\mathrm{SB}}$ even

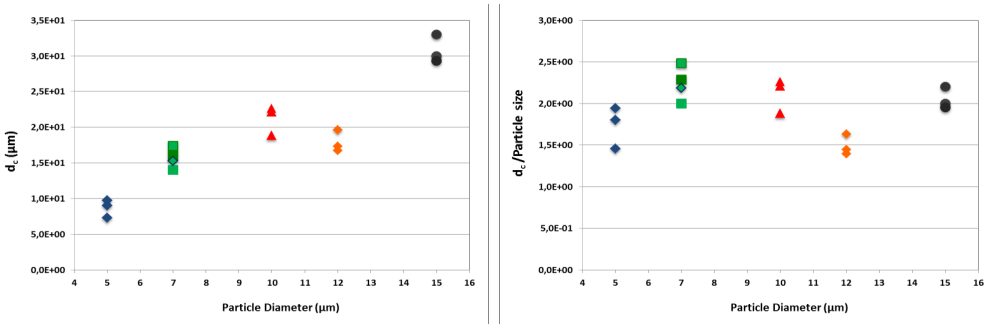

Figure 3.7 a) Critical distance versus particle diameter. b) Ratio of the critical distance and the particle diameter versus particle diameter. Each point corresponds to an experiment.

Particle diameter	dc (μm)	$\mathbf{F}_{\text{xy}}$ (N)	$\mathbf{F}_{\text{SB}}$ (N)	p_{ac} (Pa)	Eac (J/m^3)
5 (μm)	9	2.58×10^{-13}	2.9×10^{-13}	1.5×10^{6}	258.1
	17.3	1.57×10^{-13}	2.7×10^{-13}	2.8×10^{6}	889
	9.7	1.73×10^{-13}	5.5×10^{-13}	2.25×10^{6}	573.5
7 (μm)	17.4	3.5×10^{-13}	1.18×10^{-12}	2.15×10^{6}	527.4
	16	3.18×10^{-13}	3.3×10^{-13}	1.04×10^{6}	123.8
	15.3	2.49×10^{-13}	2.1×10^{-13}	8×10^{5}	71.8
10 (μm)	18.8	6.46×10^{-13}	1.06×10^{-12}	7.6×10^{5}	65.1
	22.7	2.5×10^{-13}	7.1×10^{-13}	7.45×10^{5}	63.1
	22.1	2.26×10^{-13}	8×10^{-13}	7.71×10^{5}	67.5
12 (μm)	26.7	5.7×10^{-13}	2.8×10^{-12}	1.01×10^{6}	115.3
	17.3	4.7×10^{-13}	1.08×10^{-12}	4.07×10^{5}	18.8
	19.6	3.9×10^{-13}	4.14×10^{-13}	6.05×10^{5}	41.6
15 (μm)	30	1.87×10^{-12}	3.39×10^{-12}	6.4×10^{5}	46.3
	33	4.05×10^{-13}	4.5×10^{-12}	8.1×10^{5}	74.6
	29.3	4.4×10^{-13}	4.38×10^{-12}	9.7×10^{5}	57.1

Table 3.3 Results for the different particles sizes.

by regarding the films frame by frame (adquired with a Thorlabs high resolution CCD camera). For this, we determined a velocity of interaction, we means to obtain the time in which the interaction lasts and the interaction distance center to center.

By using this method, the values presented in 3.3 are at least one order of magnitude bigger than those presented in 3.2. Roughly speaking the methodology could be the same, as we will show in section 6.4.1 there is an influence on particles behavior due the geometry of the resonator: Figs (3.3 and 3.5). Probably there is an interaction or a threshold between the secondary Bjerknes forces and the acoustic streaming for Figure 3.5 due the variability of the cases obtained: short interparticle distances, some times accelerated probably to the interaction of the acoustic energy distribution at the levitation plane. These variations leads these results in agreement with theoretical values obtained by Barnkob et al. [52].

3.2.3 Bjerknes force determination in cell-cell aggregation

At a frequency of 3MHz and the resonator employed in the last chapter (Figure 2.4), we measured the secondary Bjerknes force for the aggregation process of cancer cells (CaCO2 colon adenocarcinoma). Cellular concentrations of 2×10^5 cell/ml was employed in the experiments where we observed acoustic cell-cell interactions as show Figure 3.8; Bjerknes forces lead cellular aggregation.

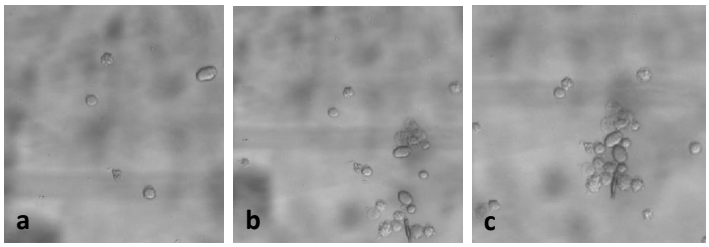

Figure 3.8 Cancer cells aggregation (CaCO2 cells). a) Cells travel due the transverse force towards the aggregate. b) Inter-cellular interaction. c) Cell aggregation. Once the doublet is formed, this travel toward the aggregate.

The observed cases were analyzed according to the second methodology proposed. Due cell polydispersity, each case was studied separately. Results obtained are shown in 3.4.

Case	Cell diameter* (μm)	dc (μm)	$\mathbf{F}_{\text{xy}}$ (N)	$\mathbf{F}_{\text{SB}}$ (N)	p_{ac} (Pa)	Eac (J/m^3)
1	9.35	21.8	4.4×10^{-12}	2.2×10^{-12}	1.54×10^6	268.3
2	10.7	30	2.72×10^{-12}	2.04×10^{-12}	1.37×10^6	213.5
3	11.2	29.1	1.06×10^{-12}	3.3×10^{-13}	4.7×10^5	24.6
4	11	18	2.8×10^{-12}	3.8×10^{-12}	1.06×10^6	126.6
5	10.6	28.5	4.08×10^{-12}	2.1×10^{-12}	1.3×10^6	188.2
6	12.4	36.2	3.35×10^{-12}	6.75×10^{-12}	1.95×10^6	431.5
7	9.15	27.2	5.14×10^{-12}	1.76×10^{-12}	1.84×10^6	385.3
8	12.7	29.6	8.47×10^{-12}	7.5×10^{-12}	1.55×10^6	271.5
9	10.5	22.5	4.6×10^{-12}	2.32×10^{-12}	1.16×10^6	152
10	14.3	36	6.18×10^{-12}	4.7×10^{-12}	1.05×10^6	125.8

Table 3.4 Results for cells, where * means average cell diameter.

These results show us that contrarily to particles, secondary Bjerknes forces in cells are one order of magnitude bigger than those of particles, due their bigger compressibility and also their sizes. However, the results of the acoustic energy and the acoustic pressure, takes our attention to the influence of the geometry of the resonator, due the similar orders of magnitude obtained in both cases.

3.3 Conclusion

We measured the secondary Bjerknes force for several particle diameters. We obtained a qualitative agreement with the theory that the Bjerknes force increase with the particle

size. Is the first time that Bjerknes force has been determined for rigid particles and cells. Any other data exist in literature. We could not precisely compare theoretical and experimental values, because we don't have the acoustic pressure and the acoustic energy for each case, for each experiemental point. Nevertheless the order of magnitude of the forces is in agreement with the theory (10^{-12} -10^{-13} N).

We found a critical distance of approximately 2± 0.5 particle diameters for the cases. Also in the case of cells, the Bjerknes forces determined are one order of magnitude higher than in the case of particles. This is probably due to their elasticity.

Chapter 4

Determination of the secondary Bjerknes force in microgravity

We consider that acoustic levitation as an analog of gravity. Then, it could be possible to manipulate species using acoustics in weightlessness conditions. In order to test the capabilities of ultrasound to operate in weightlessness conditions we performed experiments in microgravity in the airbus A300-zero G (Novespace, Bordeaux-France). This work opens the possibility of performing cell culture in space because of the capability of ultrasound for generating cell aggregates in contactless conditions. In this chapter we present experimental measurements of the secondary Bjerknes forces for particles of different sizes by following the methodology presented in the last chapter.

Figure 4.1 shows the alternatives to achieve microgravity conditions.

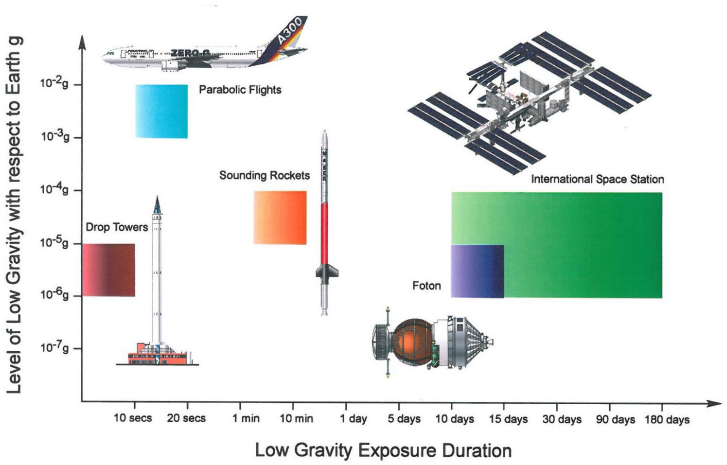

Figure 4.1 Several microgravity conditions.

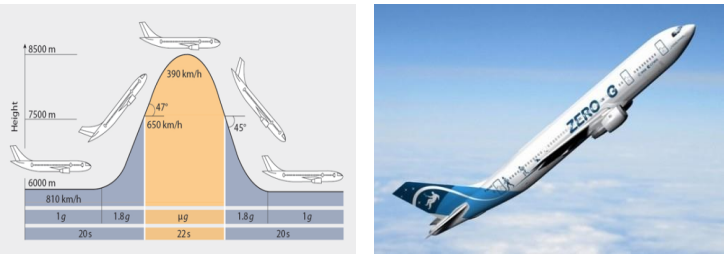

Figure 4.2 a) Parabolic flight scheme describing the hypergravity (1.5-1.8g) and microgravity periods, each one lasts 20s. The flight starts at 6000m and describes a parabol. During the first hypergravity phase, the aircraft is currently nosed up at 47°. The next twenty seconds there is microgravity conditions characterized by the weightlessness period (the same like in the space). Afterwards, the aircraft is now pointing 45° down again to the period of hypergravity, to finally arrive to a 1g period. The aim of the initial hypergravity stage is to gain sufficient velocity and altitude so as to produce a lengthy period of microgravity. b) View of the aircraft (A300 zero-G) during the hypergravity phase, just before the microgravity period.

Experiments at the parabolic flight at the airbus A300-zero G, allow to simulate free fall conditions that is, the conditions that allow to simulate the microgravity. In the aircrat, the microgravity reached values of 10^{-2} - 10^{-3}g. Figure 4.2 shows the trajectory that the aircraft follow.

In a previous work of our group [10], the interest was to determine the acoustic energy in an acoustic resonator. However, the results of the observation *in situ* of the resonator, indicated that the particles displaces to the real position of the node in microgravity, as depicted in Figure 4.3. In our case, as acoustic forces depends on the acoustic energy, we

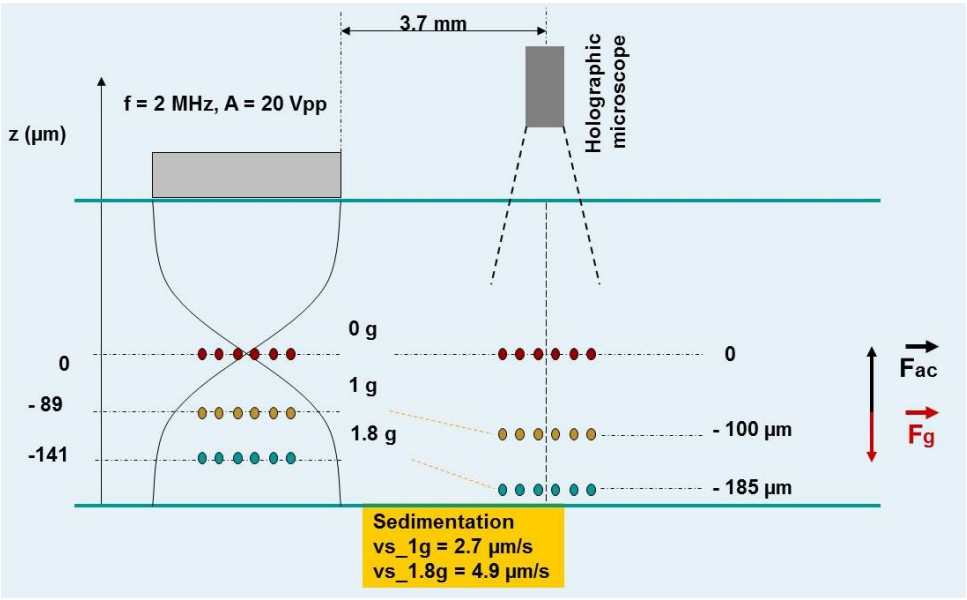

Figure 4.3 Scheme of the determination of the acoustic node position at microgravity, 1g and 1.8g in an acoustic resonator by the observation *in situ* by digital holographic microscopy.

can consider that this reduction can be affected in the same order for secondary forces.

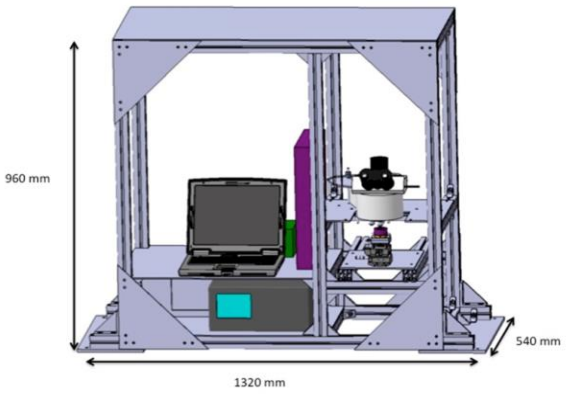

Figure 4.4 Set-up employed at the aircraft. There is the zone for particle focusing comprised by the resonator and the microscope. At the left side of the set-up, there is the zone of ultrasound generation and film registration. Ultrasounds are generated by a function generator and amplified by a signal amplifier, connected by BNC wires. In order to avoid accidents, the set-up during the campaign is covered by plastic foam.

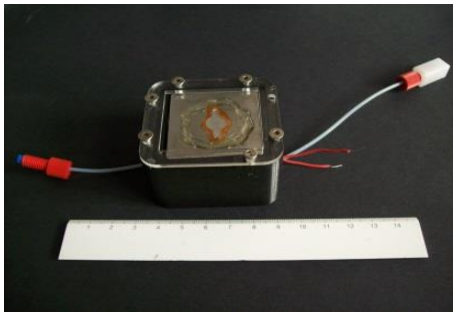

Figure 4.5 Ultrasonic resonator employed in the parabolic flight campaigns. The inlet and outlet of the device is connected to a valve that allows particle injection to the resonator and cleaning. The transducer employed is a PZ26 (4.2MHz as nominal frequency) of 3.843MHz as driving frequency.

Theoretically, the secondary Bjerknes forces reach their maximum at the node. If there is an unbalance in the forces (gravitational and acoustic forces), that would mean the direct dependency of secondary forces on **PRF**.

4.1 Experiments

The set-up employed in the flight for particle observation and equipment functioning during 1.8 and μ-g conditions is depicted in Figure 4.4. We determine the secondary Bjerknes forces of the films obtained during the 96^{th} and 102^{nd} parabolic flights campaigns (2012-2013 respectively). Aided by a reflection microscope, we observe *in situ* the particles position after switched on the ultrasounds. Microscope observations were filmed with the objective to observe the position of particles and the aggregation process after switch on the acoustic.

There, we can determine the particle position and the aggregation process by modifying the concentration of the suspension and the particle size of the suspensions. The circular resonator of Figure 4.5 of 180μm thickness and 8mm diameter was employed. Samples concentration of 0.1 – 0.5% in volume of 7, 10, 12 and 15μm latex beads was employed.

Particles were injected at 1g phase using a 5ml syringe. In order to avoid the particles stack on the metal plate, they remained in flow (aided by a little flow produced with the syringe). At the μ-g phase, the acoustic was switched on and particles react immediately to the ultrasounds. The aggregation process last on average 17s to 15μm, 23s to 12μm and 31s to 10μm particles.

4.2 Results

Films started during the first phase of hypergravity and finished at the second hypergravity phase (all the aggregation process). From a total of 120 possible experiments, we filmed 92 cases where 68 where analyzed. However, due the vibrations of the aircraft, the determination of the critical distance (dc) was done by regarding carefully the films frame by frame to appreciate the point in which there is the modification of the particle speed. This change indicated the interaction of the secondary Bjerknes forces leading to particle aggregation. Other factor that affected us, was the use of 0.5% solids (high concentration suspension) because the interactions were observed far away from the aggregation point, also Bjerknes interactions could not be filmed to this concentration, just the aggregation process in doublets, triplets and little aggregates.

For each particle size, we determined the secondary Bjerknes forces in microgravity and we obtained the results depicted in Figure 4.6. Contrarily in 1g, in microgravity there is an increment of the secondary Bjerknes forces with the particle size. There is a difference of one order of magnitude bigger for microgravity that the cases determined on earth gravity.

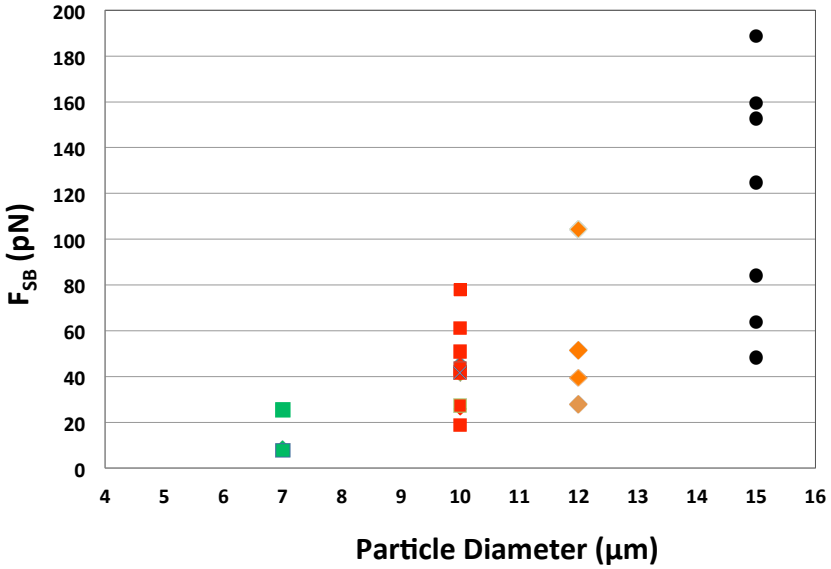

Figure 4.6 Secondary Bjerknes forces obtained for several particle sizes in microgravity. Each point corresponds to one experiment.

Comparing the results obtained in this section with those obtained in the last chapter, in Figure 4.7a there is an increment in this critical distance according to the increment of the particle size. However, the ratio between the critical distance and the particle diameter (Figure 4.7b) show a relationship at least 2 ± 0.5 of diameter particle, similar to the results obtained on ground.

For a little amount of cases, we could determine the secondary Bjerknes force at 1.8g, as Figure 4.8 presents. Comparing the results obtained for secondary Bjerknes forces on

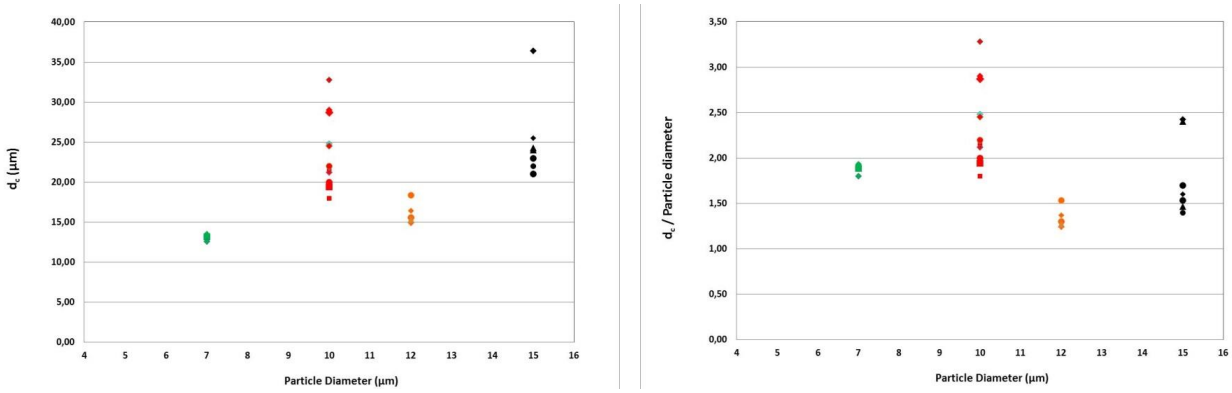

Figure 4.7 a) Critical distance vs., particle diameter. b) Ratio of the critical distance and the particle diameter vs., particle diameter. Each point corresponds to an experiment.

ground, μ-g and 1.8g for 10μm particles there is a difference of one order of magnitude higher in μ-g and 1.8g (instead the small amount of results obtained for hypergravity conditions) than those obtained on ground. The aggregation process at 1.8g could be

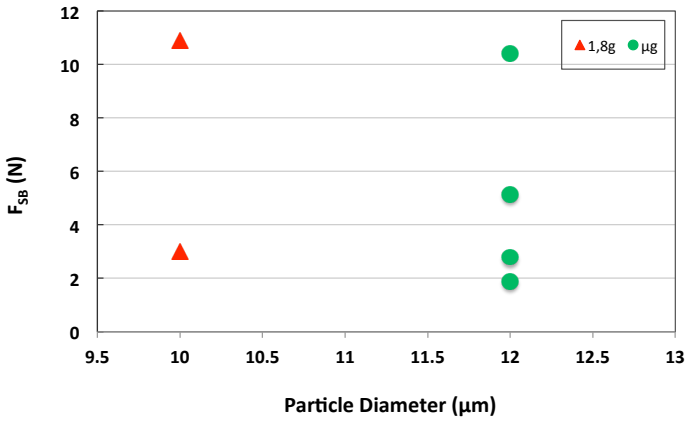

Figure 4.8 Secondary Bjerknes forces obtained for 10 and 12μm latex beads at 1.8-g and μ-g respectively.

obtained after the μ-g phase. However, films were difficult to obtain due the vibrations and the modification of the focus of the microscope. Even though, the ratio of the critical distance for each particle size is roughly 2 particle diameters (evidence not clear for 15μ-m particles).

The results presented in Table 4.1 for determinations at μ-g conditions.

During the aggregation process at the μ-g phase, we switched off the ultrasounds. The aggregate remain in levitation and consolidated as show Figure 4.9.

The same experiment was done at 1g and 1.8g, but the result shows that the without ultrasound the aggregate settles down much faster at 1.8g than at 1g. Nevertheless we had to refocus the plane during the μ-g and 1.8g, due little variations of the microscope (that

Particle diameter	dc (μm)	$\mathbf{F}_{xy}$ (N)	$\mathbf{F}_{SB}$ (N)	p_{ac} (Pa)	Eac (J/m^3)
7 (μm)	12.6	2.92×10^{-12}	7.7×10^{-13}	1.3×10^{5}	1.8
	13.2	2.33×10^{-12}	2.6×10^{-12}	2.4×10^{5}	6.5
	13.5	1.03×10^{-12}	9.74×10^{-13}	1.52×10^{5}	2.6
10 (μm)	24.8	2.48×10^{-12}	4.34×10^{-12}	5.9×10^{5}	39.2
	21.2	3.05×10^{-12}	7.8×10^{-12}	6.73×10^{5}	51.5
	19.4	2.33×10^{-12}	4.4×10^{-12}	4.63×10^{5}	24.4
	21.6	3.5×10^{-12}	6.11×10^{-12}	6.1×10^{5}	42
12 (μm)	15.3	1.4×10^{-12}	1.87×10^{-12}	2.38×10^{5}	6.43
	15.6	1.9×10^{-12}	2.8×10^{-12}	2.96×10^{5}	9.98
	16.4	6.2×10^{-12}	1.04×10^{-11}	6×10^{5}	41.24
	15	3.3×10^{-12}	5.13×10^{-12}	3.85×10^{5}	16.87
15 (μm)	36.03	1.7×10^{-11}	3.11×10^{-11}	2.29×10^{6}	594.4
	21	8.05×10^{-12}	1.89×10^{-11}	1.04×10^{6}	122.4
	22	6.3×10^{-12}	1.5×10^{-11}	9.8×10^{5}	108.7
	24.3	7×10^{-12}	1.25×10^{-11}	9.7×10^{5}	108.3

Table 4.1 Results of experiments done at μ-g conditions.

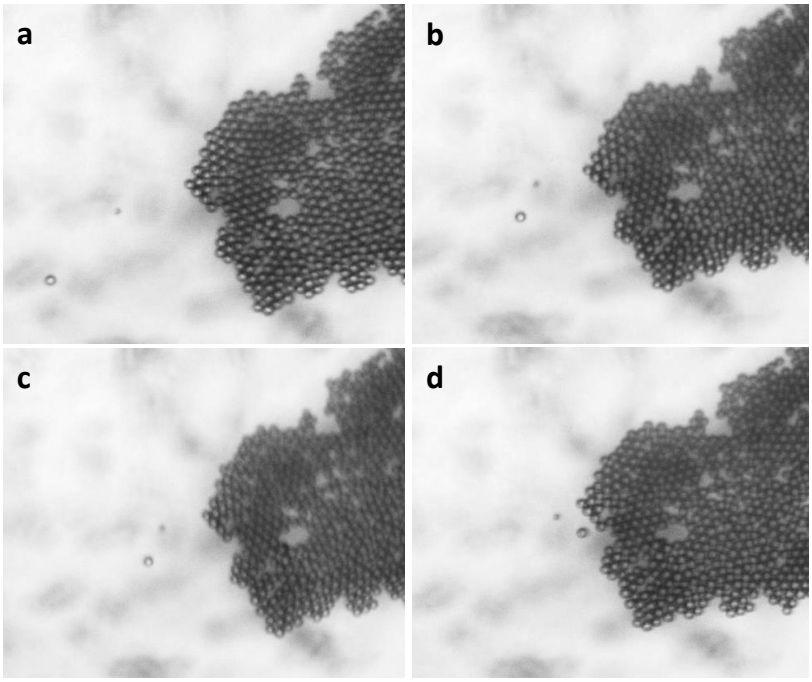

Figure 4.9 Aggregation process in μ-g conditions. a) Particles in levitation. b - c) The acoustics is stoped. Then, it is possible to appreciate that the aggregate remain consolidated; there is a difference of 5s between these pictures (at 1g, this time is too long for particle sedimentation). d) Ultrasounds are activated again and the aggregation process continues in μ-g conditions.

made some deviations of the determination of the total aggregation time process). This determination can give us a better understanding of the role of gravity in the aggregation process.

4.3 Conclusions

The secondary Bjerknes force was determined in microgravity conditions for several particle sizes. The forces determined are one order of magnitude higher that the forces determined on ground. This is due the influence of the micrograity that can place exactly the particles at the nodal plane where pressure is zero as well as **PRF**and **TPRF**. In that case, only Bjerknes force are acting upon particles and they are not veiled by other forces.

The critical distance found in the cases seem the same like those found on ground.

Chapter 5

Acoustic particle separation

Separation and isolation of particulate materials according to their mass are often crucial steps in sample characterization and preparation for a multitude of applications involving living cells, macromolecules, industrial colloids and particles, synthetic polymers, pharmaceutical emulsions and liposomes and environmental materials. The widespread need for mass-dependent separation with high selectivity and resolution has driven the development of separation techniques such as centrifugation, field flow fractionation (FFF), split-flow thin fractionation (SPLITT), elutriation, capillary electrophoresis, size-exclusion chromatography and hydrodynamic chromatography [59].

In this chapter we present the use of the acoustic field coupled to the s-SPLITT device to produce particle separations. However in [10], the disposition of one transducer near another one can improve the separation of the species in this device.

5.1 Split-flow thin cell fractionation SPLITT

The preparative technique of split-flow thin fractionation (SPLITT) and the technique of field flow fractionation (FFF) belong to the separation family of methods which use a ribbon-like channel where the species are transported by a laminar flow and axially transported and transversally driven by an external field force. The field force could be of different natures: thermal, dielectrophoretic, electric, magnetic, gravitational, acoustic [60, 61].

Developed in 1985 by Calvin Giddings, SPLITT can be used for discrete or continuous separations of cells, macromolecules and particles. Splitters are generally aligned at both ends of the flow cell dividing the incoming and outcoming flow streams into an adjacent thin lamina [59]. The separation in this device, is produced in their thickness Figure 5.1.

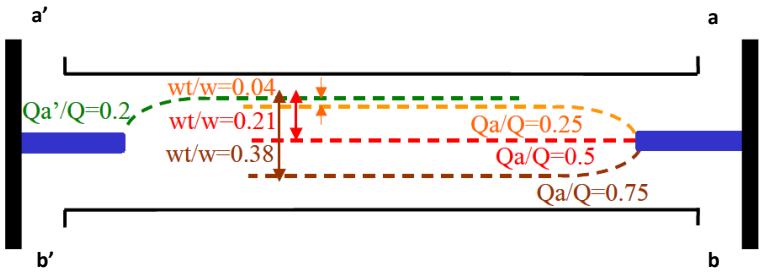

Figure 5.1 SPLITT device. The sample is input at the inlet a' adjacent to wall A, and the carrier fluid (an inert fluid) is input at inlet b'. In blue, are represented the flow splitters; these occupy about one third of the channel thickness w, one-fifth of the channel length L and the entire channel width b (direction perpendicular to the plane)

SPLITT fractionation is a fast and easy way to achieve preparative or semi preparative sorting without using filters or dialysis membranes [60].

Such the flow is divided inside the channel, there are two virtual fluid boundaries:

- ISP – inlet splitting plane. The position $w_{a'}$ depends of the injection flow Qa' and divides the inlet sample and the vector fluid **b'**.
- OSP – oulet splitting plane. Separate outlet **a** of the fluid layer that is going to exit in **b**, so the position **wa** depends on the outlet flow Qa.

These planes lie at a distance $w_{a'}$ (at the inlet) and w_a (at the outlet). Then, the following relation relates the flow rates to the ISP position

$$\frac{Q_{a'}}{Q} = 3\left(\frac{w_{a'}}{w}\right)^2 - 2\left(\frac{w_{a'}}{w}\right)^3 \tag{5.1}$$

With the total flow rate Q as $Q = Qa + Qb = Qa' + Qb'$. By regulate the flows at the inlets or at the outlets, the position of the ISP and the OSP can be modifyed. A common parameter in SPLITT fractionation, required for studying selectivity and resolution, is the cutoff diameter d_c [61]:

$$d_c = \sqrt{\frac{18\eta(Q_a - Q_{a'})}{Lbg\Delta\rho}} \tag{5.2}$$

5.2 Step Splitt device, s-Splitt

This device is a modification of the SPLITT channel, where the splitters were replaced by steps, as show Figure 5.2. The s-SPLITT channels yield high velocities at relatively low flow rates, generating enrichment through hydrodynamic effects such as inertial lift forces and shear induced diffusion [62].

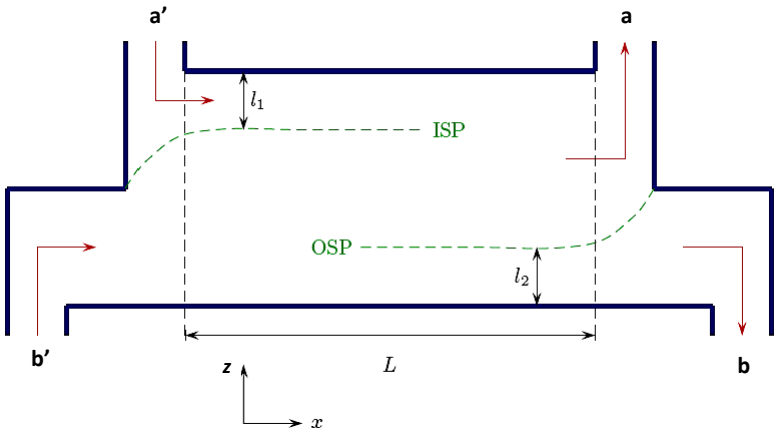

Figure 5.2 s-SPLITT device.

However, their functionning and theoretical treatment of this device is the same as done for a classical SPLITT.

5.3 HACS - Hydrodynamic acoustic continuous sorter device for programmed separation

The manipulation of particles in USW offers the possibility of separate particle mixtures. The patented s-SPLITT technology allow the coupling of an acoustic field. The hydrodynamic forces can focuse layers of particles as shown in Annexe C and composed one of the versions of the HACS device (Hydrodynamic Acoustic Continuous Sorter) 5.3. It is also a high throughput device.

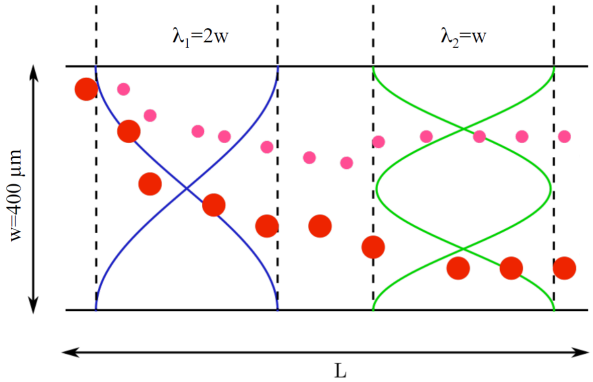

Figure 5.3 Acoustic SPLITT fractionation principle. Two transducers with different frequencies are placed closely along the channel and generate USW.

The first transducer generates a single-node wave, inducing a pre-separation through the difference in relaxation time of the different species. In the gap between the two transducers, particles are freely settling. Particles with the smaller relaxation time end

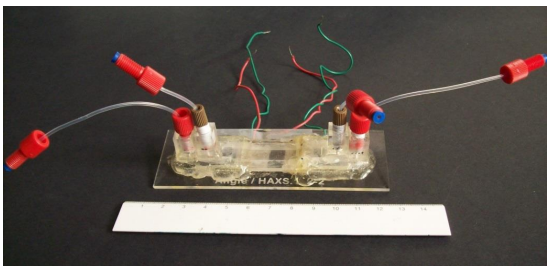

Figure 5.4 HACS device of two inlets and two outlets. The channel of $50 \times 10 \times 0.4 = 200mm^3$, has been built by using one plate in plastic material and the other a glass plate; in between, Mylar spacers have been inserted. The inlet and outlet part of the s-SPLITT channel are similar to the classic SPLITT device but the splitters are replaced by steps. Ultrasonic transducers (Ferroperm, Denmark) of surface $5 \times 10 = 50mm^2$ of 1 and 3 MHz of nominal resonance frequency were used. Each transducer was glued to an aluminium plate (epoxy conductive) and then glued to the plastic plate. The driving resonance frequency were 1.56 and 3.75 MHz. Transducers were placed at 10mm away from the inlet step.

up in the lower half of the channel while those having the bigger relaxation time will remain in the upper half. The second transducer, by generating a two-node wave, drives the separated species to the nodes while keeping them far from the walls. Particles in the lower half are guided toward the lower outlet, while particles in the upper half are guided toward the upper outlet. We will refer to this configuration of acoustic waves as the (1-2) configuration. Many other configurations are possible in our acoustic programming technique, in function of separations required [9].

5.3.1 Experiments

The device is composed of a home made step-SPITT channel comprising two inlets and two outlets (Fig. 5.4). The determination of the resonance frequency of the transducers was verified by observing *in situ* the particle focusing by microscopy (observation of particle levitation) as shown Figure 5.5.

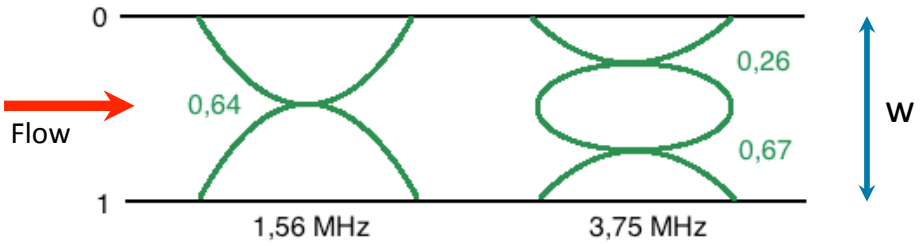

Figure 5.5 Acoustic configuration of the device. The position of the nodes was verified with a reflexion microscope, indicating a fraction of the channel thickness.

The diluted sample was composed a mixture of 7 and 12 μm latex beads [1] suspended in deionized water; the volume fraction was around 0.1%. Flow injection at b' was performed by using syringe pumps KDS Scientific. At the outlets, a and b, the sample was withdrawn

[1] Micromod

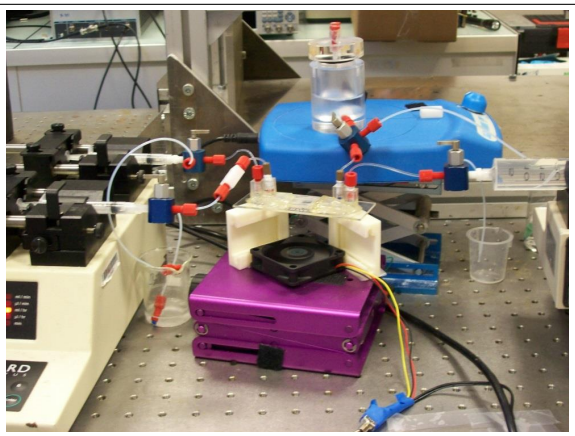

Figure 5.6 Experimental Set-up. A small fan was placed under the device to prevent transducers heating (both operated in continuous mode).

by a Harvard pump (two ways pump33, Holliston MA, USA). The set-up is indicated in Figure 5.6.

Many experiments were done with the aim to separate 7-12 μm latex particles. The experimental procedure was as follow: the particle mixture was injected at the inlet a' at a flow rate $Q_{a'}$= 3 mL/h; the carrier (deionized water), was injected at the inlet b' at $Q_{b'}$= 18.6 mL/h for a total flow rate $Q = Q_{a'} + Q_{b'}$= 21.6 mL/h. The postion of the ISP =0.23w = 92 μm. However, the best separation of these particles was obtained at OSP =0.59w = 236 μm. Results are in Table 5.1, where the recovery is the ratio between the inlet and outlet concentration and the purity is the ratio between the specific concentration of each species.

	Gravitational		**Acoustic**	
	7 μm	12 μm	7 μm	12 μm
Purity in a	98%	2%	96%	4%
Purity in b	93%	7%	88%	12%
Recovery	80%	90%	60%	90%

Table 5.1 Purity and recovery of 7 and 12 μm particles separated with and without acoustics, for ISP=0.23 and OPS=0.59.

From an initial concentration for 7 and 12 μm particles was 50-50% and the initial purity. We could enrich in 7μm particles in a. With respect to the initial fraction the acoustic help us to improve the separation with a good recovery.

5.3.2 Particle trajectories calculation

During the acoustic separation process, particles in a SPLITT channel (Fig 5.3) experience several forces and hydrodynamic interactions: the acoustic force, the drag force, the buoyancy force, particle-particle and particle-wall interactions. However as we work with

dilute suspensions, particle-particle interactions will be neglected. For the sake of clarity, we will recall the expression of drag force, buoyancy and the acoustic force.

Drag force The expression of the drag force is:

$$\mathbf{F}_{\text{Drag}} = 6\pi\eta r\vec{U}. \tag{5.3}$$

where η is the dynamic viscosity of the fluid, $\vec{U}$ the fluid velocity and $\vec{v}$ the particle velocity. A Poiseuille flow is established in the channel, with a parabolic profile given by:

$$\vec{U} = 6\bar{U}\frac{x}{w}\left(1-\frac{x}{w}\right)\vec{e_x}. \tag{5.4}$$

where $\bar{U}$ is the average flow velocity. The horizontal velocity of each particle is driven only by the x component of that force, and will therefore be always close to the fluid velocity. The x component of the drag force constitutes a friction force and is expressed as: $-6\pi\eta r\ \vec{v}_x$.

Buoyancy The net force resulting from buoyancy and particle weight reads:

$$\mathbf{F}_{\text{b}} = \frac{4}{3}\pi r^3 g(\rho_f - \rho_p)\vec{e_z}\ , \tag{5.5}$$

where g is the standard gravity.

Acoustic force The principal effect of the acoustic force is to drag injected species toward the nodes of the pressure field. These nodes move in the case of a progressive wave, but remain fixed in the case of a standing wave. The intensity of the acoustic force upon a particle depends on its volume and its acoustic impedance. It is thus possible to generate selectivity based on those physico-chemical parameters. We note that the acoustic impedance becomes here a new selectivity parameter in SPLITT-like separation methods.

When acoustic and gravitational fields are coupled, the main effect of buoyancy is to shift particles underneath the equilibrium positions. Both forces scale as r^3. This implies that the equilibrium positions, given by $\mathbf{F}_{\text{ac}} + \mathbf{F}_{\text{b}} = \vec{0}$, do not depend on particle size. Thus the use of an acoustic standing wave does not allow realizing particle separation in size once the species have reached their equilibrium position.

In contrast, the characteristic time or relaxation time, taken by particles to reach their equilibrium positions depends on the particle size as it results from the competition between the acoustic and drag forces. It scales by $\eta z/(r^2 kG\bar{E}ac)$, where z is the distance between the node and the initial particle position. By considering the relaxation time as the product of an average transverse velocity and the particle initial distance to the node. Our separation scheme is based on this dependence of the relaxation time on the particle size: by properly choosing the residence time, the magnitude of the acoustic field and frequencies, particles can be efficiently separated across the channel thickness. To compute the particle trajectories during their migration through the channel, were used

MATLAB with the **ODE45** tool. This routine uses a Runge Kutta method to solve differential equations, where integrate numerically equations of motion:

$$\frac{\mathrm{d}\vec{v}}{\mathrm{d}t} = \frac{1}{m}\left(\mathbf{F}_{\mathrm{ac}} + \mathbf{F}_{\mathrm{b}} + \mathbf{F}_{\mathrm{d}}\right) \ . \tag{5.6}$$

where F is a known function of $\vec{v}$ and t. We thus reformulate Newton's law in the following manner:

$$\frac{\mathrm{d}}{\mathrm{d}t}\begin{bmatrix} \vec{x} \\ \vec{v} \end{bmatrix} = \begin{bmatrix} \vec{v} \\ (\mathbf{F}_{\mathrm{ac}} + \mathbf{F}_{\mathrm{b}} + \mathbf{F}_{\mathrm{d}})/m \end{bmatrix} \ . \tag{5.7}$$

Relaxation to the equilibrium position We solve first the equations to determine the relaxation to the equilibrium position. Calculations have been performed for both acoustic modes: continuous and pulse. As depicted in Figure 5.7, shows the relaxation distance from the top-wall as a function of time. There are four curves: two in continuous mode with and without gravity. Without gravity correspond to the trajectory already treated in literature but using the following analytical expression for microfluidic devices [33]

$$z_{(zo,t)} = \frac{1}{k_z}\arctan\left\{\tan\left[k_z\left(z_0 + \frac{w}{2}\right)\right]\exp\left(\frac{t}{t^*}\right)\right\} - \frac{w}{2}. \tag{5.8}$$

where the relaxation time t^* is

$$t^* = \frac{3\eta}{4G\left(k_y r\right)^2 Eac}. \tag{5.9}$$

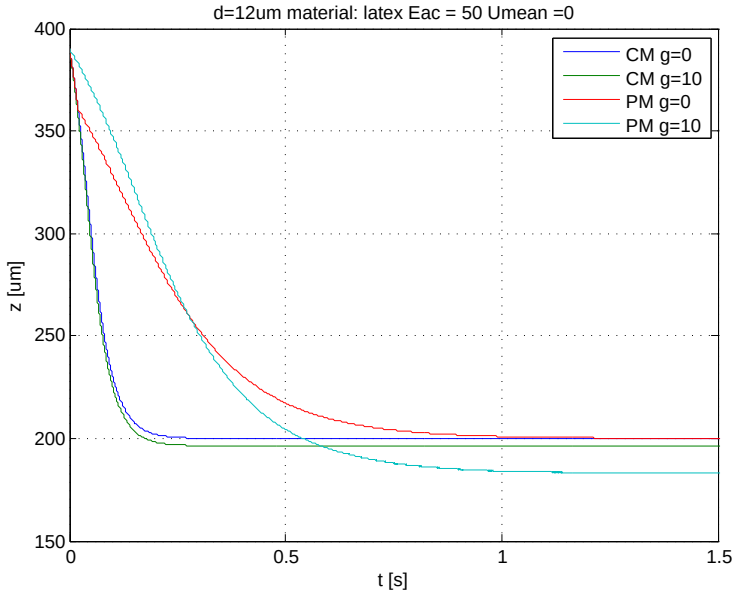

Figure 5.7 Particle relaxation to the equilibrium position in continuous (CM) and pulse mode (PM) with Duty cycle = 0.2, for 12 μm latex beads, with and without gravity, g. In pulse mode the relaxation is slower than in continuous mode, equivalent to have smaller acoustic energy (will see in chapter 6, that Duty cycle factor here is 5).

Here, we include in our calculations the gravity. In pulse mode, the small energy and the equilibrium position is lower. In pulse mode the relaxation is takes more time than in continuous mode because of is analogous to use smaller energy.

Relaxation with flow and separation - HACS We compute the trajectories for different particles sizes and for the same size of different acoustic impedance in order to test the perfomance of the separation. As accelerations of particles could be high, it is necessary to use a short time step, of the order of 10μs. However, once particles have converged, their accelerations are much smaller. In addition, we have made the following assumptions:

- the acoustic waves are perfect stationary waves so that we can use the expression of the acoustic force;
- the divergence of the acoustic fields is not taken into account, so that the waves have a square-shaped transverse profile;
- the flow has a parabolic profile all along the channel.

The separation obtained confirms the predictions made by the model, even though the resolution is lower than predicted. In fact, the model predicts that all particles should be focused at the two nodes, without any significant broadening in thickness distribution (Figure 5.8). It is apparent that this situation did not happen in real experiments. Besides that fact, other nonidealities have to be considered for explaining the broad distributions observed in the real experiment. Firstly in a real channel it will not be possible to set up a perfect standing wave. This is due to the several interfaces that will be present on the path of the wave through the channel. It will result in a displacement of the nodes and in a reduction of the acoustic force intensity.

However the general features of the acoustic force will remain the same (particles will be driven to the nodes with a relaxation time having the same dependence on their size), and thus the separation principle does not change. Secondly, the transverse profile of the waves is not square-shaped. This will also result in a change of the relaxation times, as the amplitude of the force will vary across the width of the acoustic wave. But with the transducer geometry used the divergence of the beam is only a few degrees, and this effect can be neglected.

Figure 5.9, shows the particles trajectories calculated for a separation of latex-silica particles of the same size. This demonstrates the capability of the acoustics to use the acoustic impedance as physicochemical parameter to separate.

5.4 Conclusions

Many experiments had been performed. However, we couldn't have the expected results because of the separator need be to improved.

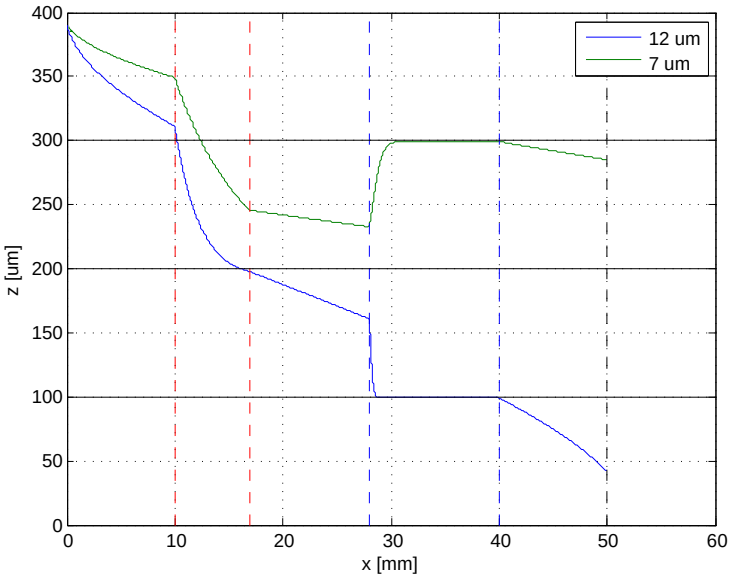

Figure 5.8 Separation in HACS separator of 7 and 12μm latex beads. The initial position is close to the top wall. Configuration one-two nodes. The first node is depicted in red-dot lines while the second transducer is indicated by the blue-dot lines. Theoretically we demonstrate that it is possible to separate these two species as we will obtain experimentally. Average velocity.

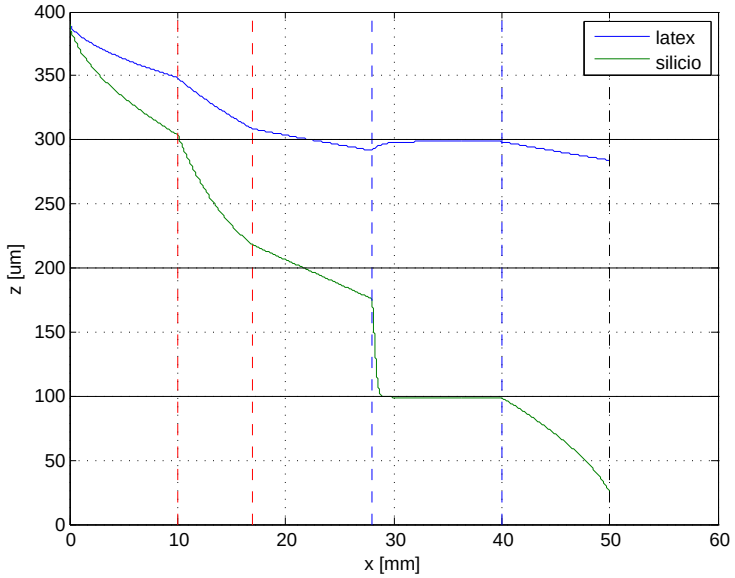

Figure 5.9 Separation in HACS separator of 10μm particle and silica latex beads. The initial position is close to the top wall. Configuration one-two nodes. The first node is depicted in red-dot lines while the second transducer is indicated by the blue-dot lines. Theoretically we demonstrate that it is possible to separate these two species as we will obtain experimentally. Average velocity.

We performed calculations of relaxation and trajectories that for further experiments will helps us to improve the separation.

Chapter 6

Controlling the Acoustic Streaming

Usually in an acoustic resonator an USW can trap species bigger than 1μm such as micron-sized particles, cells and even bacteria. However, when species becomes smaller than this size particle manipulation is challenging. This complexity is due the influence of the acoustic streaming that modifies the particle behavior. In fact, studies of the acoustic streaming sustain that the limit size able to manipulate particles by radiation forces is 2μm [20, 33]. Because of the acoustic streaming is a recurrent problem in acoustophoresis, special care has been taken in our study for better understand a control of the manipulation process of particles in acoustic resonators.

Therefore, as we presented in chapter 2, pulse mode acoustics can control the morphology of an aggregate regardless the time of ultrasound application. In this chapter, we introduce the use of pulse mode acoustics as an alternative for controlling and/or reducing the acoustic streaming. This is the originality of this study. Our goal is to demonstrate the capability of manipulating sub-micron sized particles.

6.1 Generalities

Acoustic streaming is a steady fluid flow, generated by the viscous attenuation of high amplitude acoustic waves. Part of the energy lost through acoustic dissipation is imparted to the fluid as steady momentum by means of nonlinear hydrodynamic coupling. Streaming flows strongly varies depending on the mechanism behind the attenuation of the acoustic wave, the streaming velocity [1], the length scale and the geometry of the flow [37].

[1]The velocity of the acoustic streaming decreases by increasing the fluid viscosity and increases by increasing the frequency and the pressure amplitude.

The acoustic streaming (AS), is present when the primary radiation force **PRF**is generated by the USW. The forces implied in the acoustic streaming are very small compared to **PRF**. Generally veiled by main flows or neglected when micron-size species are manipulated [2], AS becomes visible when the suspension is composed of sub-micron-size particles; species are focused close to a nodal plane generating a steady concentration profile. The flow velocity generated by the streaming spanning from tenths to hundreds of μm/s [63, 64], high enough for dragging out the particles.

Acoustic streaming is applied in the enhancement of heat and mass transfer and metal electro deposition [40, 65]. In microfluidics, acoustic streaming has been employed to mixing and pumping of fluids [29, 66]. Cavitation microstreaming generates a whole scale flows to the generation of highly targeted flows, micromixing and cell membrane poration. Pumping can be possible through this method no matter the chemic-ionic composition of the fluid, either the complexity of the channel geometries. On the cellular membrane, microstreaming flows in biological cells may result in significant physiological effects such as increase in cell metabolism, cellular differentiation, elongation of endothelial cells and cellular membrane poration; microstreaming generated by air bubbles can also generate hemolysis of erythrocytes [66]. The existence of streaming can be used to enhancing the interaction of cells and retroviruses, agglomerating cells in droplets and the removal of non-specifically bound proteins from surfaces [67]. *In vitro*, the acoustic streaming can be useful in medical diagnosis: to help to distinguish small cysts from solid lesions, because small cysts often contain internal echoes. AS could determine cyst viscosity content based on AS velocity [68].

6.2 Pulse mode acoustics

As we presented in chapter 2, by modifying parameters of pulse mode such as the time of pulses Tp and the repetition time Tt, is possible to control the morphology of the aggregates (2D or 3D). In this chapter, we consider the parameter Duty cycle in the normalization of the total time of an on-off cycle: $Tp+Tt$ by Duty cycle $= Tp/(Tp+Tt)$. Therefore when acoustic is off, Duty cycle $= 0$, otherwise in continuous mode Duty cycle $= 1$.

6.2.1 Observations of the acoustic streaming

Firstly, the nodal plane was determined by using 15μm particles in levitation; this help us, to fix the focus of the microscope. Fluorescent carboxylate beads of 883nm (Polysciences Inc, Warrington PA, USA) of concentration less than 0.1% were used in the experiments.

When the sample was placed in the resonator under the absence of acoustics, particles exhibit Brownian motion. Once the acoustics was switched on, their displacement is different to Brownian motion due the influence of the drag generated by the acoustic forces. In continuous mode, particles react to the ultrasounds with an average relaxation

[2]manipulation is generate relative displacements between particles and the surrounding fluid under the action of ultrasonic radiation forces in order to induce separations, aggregation or other transport processes

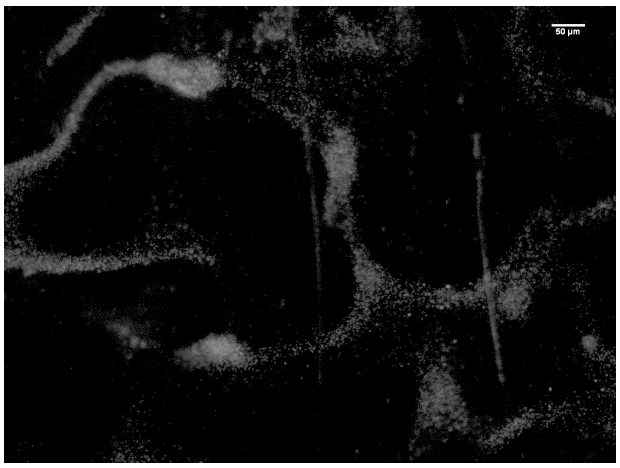

Figure 6.1 Acoustic streaming patterns at the levitation plane for 883nm particles in continuous mode. Scale bar = 50μm, magnification 20X.

time of 35s [3]. Once at the levitation plane, particles and little aggregates (of diameter roughly 1-10μm) form a layer of some μm thickness. We observe that the superior and inferior part of that layer describes a vortex throughout the transverse direction in which their superior and inferior parts have opposite directions (clockwise or counter-clockwise).

After one minute at the equilibrium position, the interaction between the particles and the acoustic energy leads the formation of clumps or agglutinates, as depicted in Figure 6.1. However, the position of the agglutinates at the transverse position vary in the time with the acoustic energy that pulls them toward other positions of the levitation plane. Let's note that when ultrasounds are turned off, the flow stops instantly and particles settle down.

The recirculation of the agglutinates or patterns in the resonator had been reported by Mitome [64], as the result of the non-uniformity of the energy distribution in the resonator and other resonances produced by geometrical factors. For 1μm particles in a cylindrical resonator, the AS reported by Kuznetsova and Coakley [40] describes at the nodal plane Rayleigh vortices (whose planes of circulation are perpendicular to the transducer plane) and circulate parallel to the transducer plane. Visualizations of the AS by following the streamlines using particle image velocimetry (PIV) for sub-micron particles as seeds, show that particles are concentrated forming clumps, leading to configurations that may depend on the acoustic energy distribution and by the competition between radiation forces and diffusion [64, 63, 40, 69, 70].

When pulse mode acoustics was probed, we observed particle levitation and the organization of a layer of particles of some micron thickness. There is still a relaxation time of 35 s in which particles reach the levitation plane. However, there is not vortex formation where particles travel in the transverse direction as shown Figure 6.2. When ultrasounds are switched off, the little aggregates settle down and most part of individual particles gets unfocused; for some, sedimentation is a long process that takes place in roughly 2 minutes.

[3] relaxation time is the time taken by particles for reaching the equilibrium profile or a stable distribution around the nodal plane

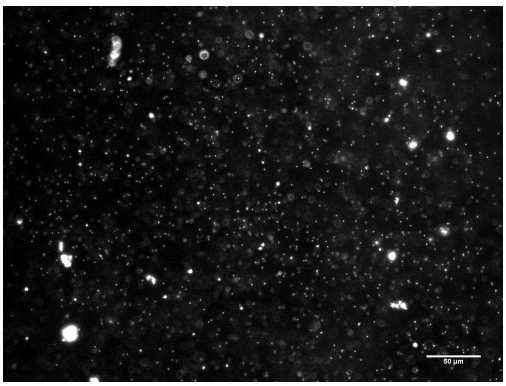

Figure 6.2 AS observed for 883nm fluorescent particles in pulse mode at 4.3 kHz and 300 pulses. Scale bar= 50μm, magnification 10X.

6.2.2 Differences between the acoustic modes employed on the AS

Due the influence of the AS, the manipulation of sub-micron particles by USW is challenging. Usually, in continuous mode the control of the acoustic streaming for sub-micron particles has been reported as the reduction of the wave amplitude. Pulse mode is introduced here as an alternative to reduce it by remaining the radiation forces.

In the rectangular resonator depicted in Figure 3.3, experiments were done in continuous and pulse mode with 883nm fluorescent particles. In continuous mode we systematically reduced the wave amplitude to observe the behavior of 883nm particles and the characteristics of the AS. The details of the experimental set-up employed had been described in the paper (Annexe D).

In the field of view, individual fluorescent particles were tracking to estimate a characteristic streaming velocity of AS. However, we need to find common variables in order to compare the streaming velocities in both modes. Due the proportionality of the streaming velocity to the acoustic energy according to the relationship (eq. 1.50):

$$\vec{v}_s = \left(\frac{3\pi V_0^2 f}{32 c_f^2} \right) z \tag{6.1}$$

where z is the distance to the levitation plane from the bottom wall of the resonator, V_0 is the amplitude of the ultrasonic velocity related to the acoustic energy density by the expression [42].

$$\langle E_{ac} \rangle = \left(\frac{1}{2} \right) \rho_f V_0^2. \tag{6.2}$$

Therefore the streaming velocity $\vec{v}_s$ becomes proportional to the average energy density. The maximum streaming velocity $\vec{v}_{smax}$, is the velocity at the maximum voltage applied and proportional to the maximum energy density $\langle E_{ac,max} \rangle$. It follows that

$$\frac{\vec{v}_s}{\vec{v}_{s,max}} = \frac{E_{ac}}{E_{ac,max}} = \left(\frac{V_{p-p}}{V_{p-p,max}} \right)^2. \tag{6.3}$$

In pulse mode, we can make the hypothesis that the average particle velocity during one cycle is

$$\vec{v}_s = \vec{v}_{s,max} \frac{Tp}{(Tp + Tt)}. \tag{6.4}$$

proportional to the streaming velocity. Then, Duty cycle becomes proportional to the mean energy density $\langle Eac \rangle$. Thus,

$$\frac{\vec{v}_s}{\vec{v}_{s,max}} = \frac{E_{ac}}{E_{ac,max}} = \left[\frac{\text{Duty cycle}}{\text{Duty cycle}_{max}} \right]. \tag{6.5}$$

Where $\text{Duty cycle}_{max} = 1$

The streaming velocity obtained in pulse and continuous modes is represented in Figure 6.3. At continuous mode, at the maximum voltage applied the average streaming velocity is $\vec{v}_{s,max} = 15\mu$m/s, but for little aggregates (some of approx., 10μm diameter) these moves at least 30% less than the AS velocity of the bulk fluid. In pulse mode, the modification of Tp and Tt gives lesser velocities that the obtained at continuous mode; at the minimum Duty cycle, particles attain an AS velocity of 2.5 μm/s. As we expected, the higher the amplitude of the acoustic wave, the higher the streaming velocity. However, the curve that should be linear according to the assumptions made before is rather close to a power law.

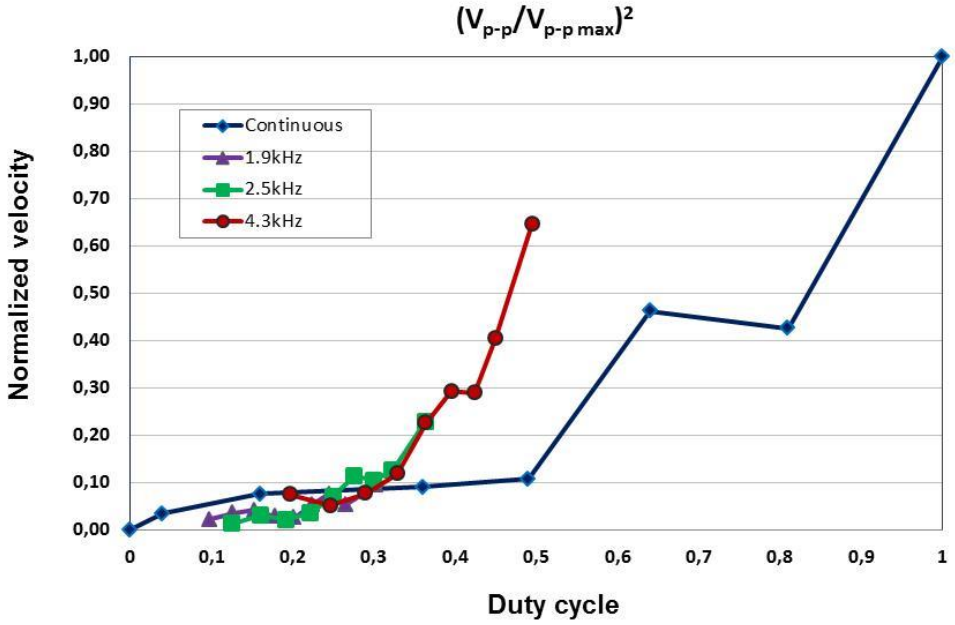

Figure 6.3 Normalized velocity streaming in pulse and continuous mode determined for 883nm fluorescent particles. In continuous mode was determined by reducing the wave amplitude. At pulse mode, by remaining three different repetition times constant the number of pulses was modifyed. When acoustic is off remaining currents such as other thermal effects and Brownian motion produces a particles velocity of 2.14 μm/s that for all the measurements this value had been subtracted. This value is higher than the characteristic velocity related to Brownian motion estimated to 1μm/s, obtained by calculating the diffusion coefficient $D = (kT/3\pi nl)$ approx., $5.5^9 cm^2/s$, where d= 800nm, k is the Boltzmann constant, T is the absolute temperature and the diffusion length l in a time t=1s given by $l = (2Dt)^1/2$ approx., 1μm.

The divergence in the behavior between pulse and continuous modes, shows that for generating the same acoustic streaming velocity is necessary less energy in pulse mode than in continuous mode. Less energy also implies less heat dissipation that is a good advantage

when ultrasounds need to be applied for long periods. This remarkable result indicates that pulse mode seems to be an efficient way to applying ultrasound in resonators.

6.3 Acoustic streaming threshold

Taking as a reference the particles behavior observed in continuous mode, to the same experimental conditions in this time we systematically modified the pulse mode parameters (Tp and Tt) allowing the reduction of the AS to a minimum. Then, we could identify a threshold where the velocity of streaming is reduced till a point in which most amount of particles leave the vortex. This threshold is represented in Figure 6.4, showing the regimes where there is and there is not acoustic streaming.

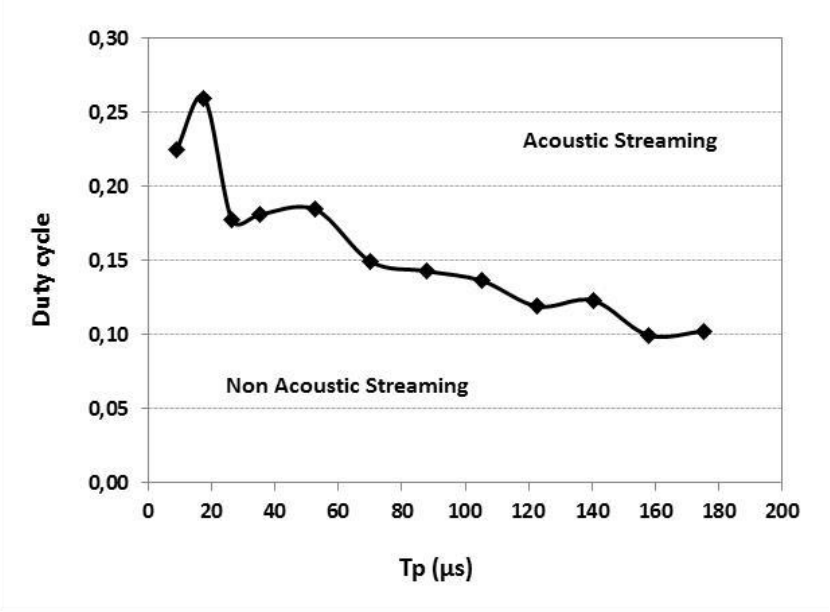

Figure 6.4 Threshold of the acoustic streaming.

The curve presents a maximum of Duty cycle in 25 pulses. This point could indicate the onset of the acoustic streaming as Pigott and Strum [2] found. In their experiment, they obtained an empirical correlation to the streaming velocity $v = bt^p$ where t is the time of the acoustic streaming, b is a factor that depends on:

$$b = \beta \frac{I}{I_{max}}^{\mu}. \tag{6.6}$$

β is a factor sensitive to the viscosity and the geometry and I is the intensity applied to the system. The development of the streaming could be larger or smaller by the scaling factor b that depends on the geometry of the vessel, the location of measurement, the viscosity of the liquid and the acoustic power absorbed [2].

In our case (Figure 6.4), we obtained a potential adjust from the maximum point till the

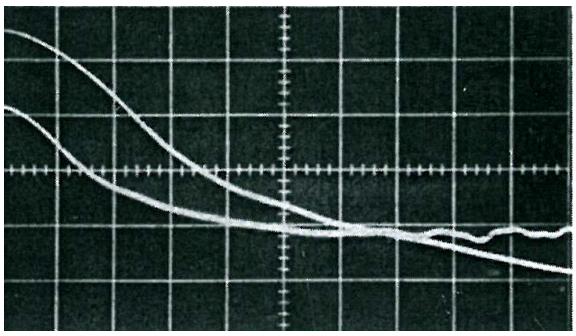

Figure 6.5 Photograph of two oscilloscope deflections, proportional to the streaming velocity. One vertical division corresponds to $0.64 cm/s$ and one horizontal position to 1s. These deflections show the onset of the acoustic streaming of their experimental system. Taken from [2].

last one, that gives the expression:

$$v = 0.667 t^{-0.355}. \tag{6.7}$$

where $r^2 = 0.912$. The identification of the pulse mode parameters that generate AS allows us the manipulation of sub-micron particles.

6.3.1 Pulse mode and radiation forces

Pulse mode acoustics allow us to reduce the velocity streaming without affect neither the primary forces nor the secondary radiation forces. A mixture of 883 nm and 15 μm latex particles (Coulter standard L15 Beckman Coulter Inc, Miami, USA) was employed to test the ability of pulse mode to keep primary and secondary radiation forces strong enough for generating particle levitation and aggregation.

In the circular resonator (Figure 3.5), for a driving frequency of 4.12 MHz, big particles reach first the levitation plane and afterwards they form an aggregate (Figure 6.6a). Slowly, little ones reach the levitation plane and once there, the acoustic streaming is generated (Figure 6.6b-d). A careful observation allows us to highlight that the aggregate tend to turn (some μm) clockwise or counter-clock wise in the nodal plane due the acoustic streaming.

In pulse mode, as soon as acoustics in switched on in the system big particles reach the levitation plane. Little particles act immediately to the acoustics but they are going to spend more time to reach the levitation plane. Figures 6.7a and 6.7b show a 15μm aggregate surrounded by a stable cloud of little particles. Particles in continuous and pulse mode were focused at the same plane (of the resonator).

Analog experiments were performed in continuous mode by reducing the amplitude where the relaxation time for 15μm particles lasts at least more than one second and the aggregate did not levitate consolidated as was observed in pulse mode. The **PRF**is stronger in pulse mode than in continuous mode at the threshold as previously stated based on particle layer thickness.

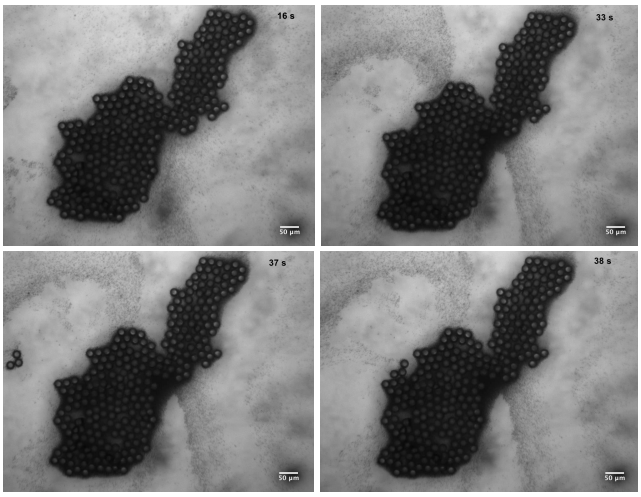

Figure 6.6 Mixture of 15μm and 883nm particles, at the levitation plane in continuous mode. a) Little particles surround the aggregate. b) Pattern of sub-micron particles arrives to the aggregate. c and d) the little aggregate reach the big one. Scale bar= 50μm, 10X magnification.

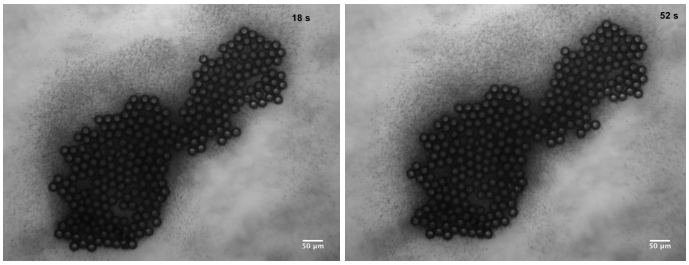

Figure 6.7 Mixture of 15μm and 883nm particles in pulse mode using 100 pulses and 6.5 kHz. a) An aggregate of 15μm is formed at the levitation plane. Little particles form a cloud around the aggregate. b)Then, 34s after there is a stable cloud of little particles around the big aggregate. Scale bar= 50μm, 10X magnification.

6.4 Influence of other parameters in the acoustic streaming

The reduction or control of the acoustic streaming in pulse mode acoustic was tested by modifying other factors such as the resonator geometry, the particle size and the thickness of the particle layer. Based on these modifications, we could obtain other AS thresholds.

6.4.1 The resonator geometry

In pulse mode, the behavior of the AS for 883nm particles was compared for different resonator geometries: circular, squared and oval as depicted in Figure 6.8. Each resonator was done by putting several layers of Kapton® tape to obtain a thickness of roughly 180μm.

According to the shape of the resonator employed, the threshold of the AS was obtained

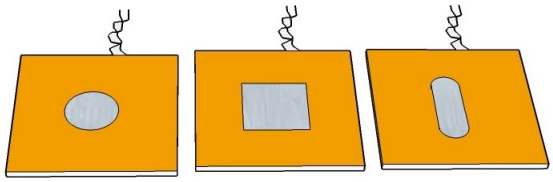

Figure 6.8 Each resonator is composed of a stainless steel plate of 2mm thickness where a circular PZ26 transducer of 4.2MHz of nominal frequency is glued behind (Chemtronics®, conductive epoxy). At the other side of the plate polyimide Kapton® tape was employed to build the resonator. A cover slip was used like reflector plate. The circular resonator has 6mm diameter; the squared 8mm lengh.

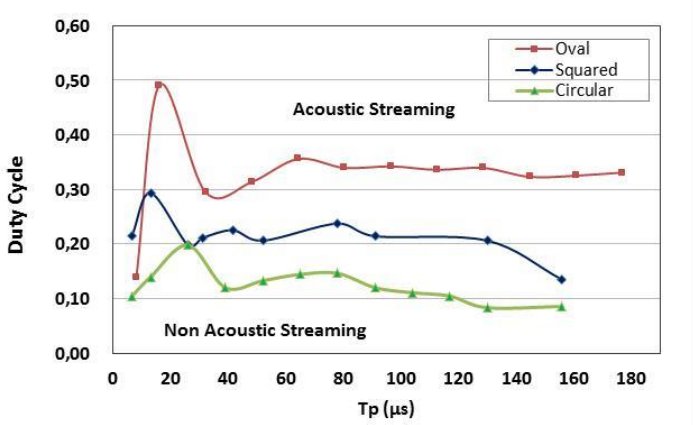

Figure 6.9 Threshold of the acoustic streaming for the different resonators employed.

by modifying pulse mode parameters as show Figure 6.9.

The oval resonator allows more energy by keeping the stability of the manipulation; Duty cycle obtained for oval resonator was higher for higher times of pulses. The oval geometry was proposed geometry obtained as a solution in our group to reduce the instability at the levitation plane for aggregates conformed of a mixture of silica and latex beads. Contrarily, for the circular resonator the figure indicate that less energy is necessary for manipulating particles. However, experiments showed a transition at the transverse direction; particles tend to the edges of the resonator and therefore travel towards middle points. Similar results were observed in the squared resonator where the instability of the agglomerates is reduced.

6.4.2 Particle size

The particle size was another factor in the AS behavior. Then, taking the circular resonator (Fig. 6.8), we employed particles of different sizes: 500nm, 1μm, 3μm and 5μm (sicastar-green F plain, micromod particles); 883nm carboxylate particles were also employed. Monodisperse particle suspensions were done, with a concentration of 0.1% in

deionized water. At each experiment, 30μl of suspension was put in the resonator. The modification of pulse mode parameters leads an AS threshold observed in Figure 6.10, for each particle size employed.

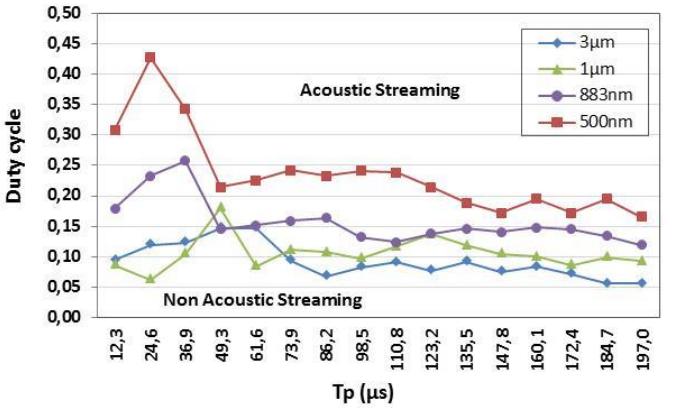

Figure 6.10 Threshold of the acoustic streaming determined for the different particles sizes tested.

There is a relationship between the acoustic energy and the particle sizes employed. Extracting the maxima points of the Figure 6.10, as depicted in Figure 6.11 it is possible to observe that smaller particles need more energy to manipulate them in an acoustic resonator.

6.4.2.1 Observations of the acoustic streaming for size particle

- 500 nm. At a driving frequency of 4.04MHz, the relaxation time is 1min. At the levitation plane, particles form a layer. Figure 6.12a-c, show the effect of the drag generated for the AS producing a fast agglutination, patterns and their translation at the transverse direction.

- 883 nm. We observed particles levitation at a driving frequency of 4.115MHz. Furthermore, their relaxation time is 35s with layer organization at the levitation plane. Figure 6.12d-e, shows the influence of the AS in the particle agglutination, patterns formation and their translation.

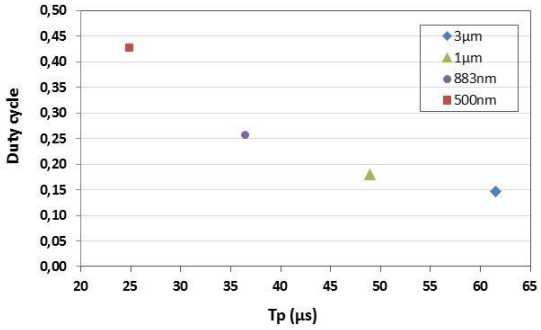

Figure 6.11 Maxima point for duty cycle reached according to the particle size tested. For 500nm, the maximum point corresponds at 100 pulses; at 883nm for 150 pulses. At 1μm for 200 pulses and for 3μm was reached at 250 pulses.

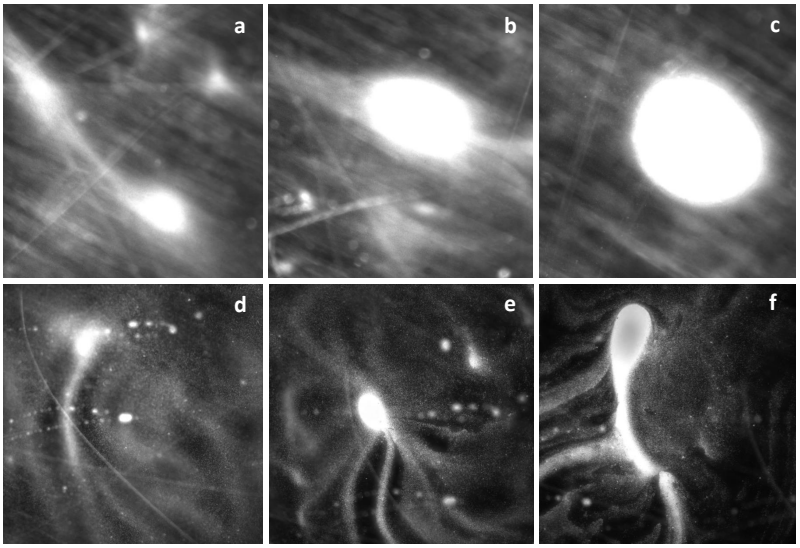

Figure 6.12 Observation of the acoustic streaming for 500nm and 883nm particles made in dark field. For 500nm particles at a)1min, b) 3 min and c) after 5min of the experiment. Magnification 5X. For 883nm particles at d) at 1min, at e) 3 min and f) after 5min of the experiment. Magnification 10X.

- 1μm. At a driving frequency of 4.083MHz, there is a fast particle levitation. Once at the levitation plane, there is aggregation of single particles and little aggregates (composed of tenth of particles) that travels due **TPRF**, till the point of maxima energy to form a big aggregate. Presumably there should be a critical size of the aggregate, because a careful observation showed us an aggregate with several layers–multilayers, as depicted in Figure 6.13b.

Furthermore, the AS observed in these aggregates is the slow displacements of individual layers (vortex) and/or by the rotation of the particles at the central part of the layers. However, there is not currents or patterns formation. In pulse mode, there is the reduction of the particles rotation. At the periphery of the aggregate, particles can be seen close each other (Figure 6.13d), but not like continuous mode case where the aggregate periphery is more compacted Figure 6.13c. The contribution of pulse mode in this case, is that the spinning particles at the middle part are stopped and at the periphery it is possible to appreciate them.

Usually latex or carboxylate particles arrives at the levitation plane. Once there, they start to aggregate and/or follow the patterns (circles). Instead of the behavior described for latex or carboxylate particles, the AS experienced by silica particles is another interaction at the middle part of the aggregate. Then, experiments in the circular resonator for particles of 1μm latex and silica (monodisperse suspensions) were done to evaluate differences in the AS according to the material of the particle. Threfore, Figure 6.14 indicate no significative differences.

- 3μm. At a driving frequency of 4.06MHz there is an immediate levitation and interaction of the acoustic streaming which drag single particles throughout the levitation plane. There is particle aggregation.

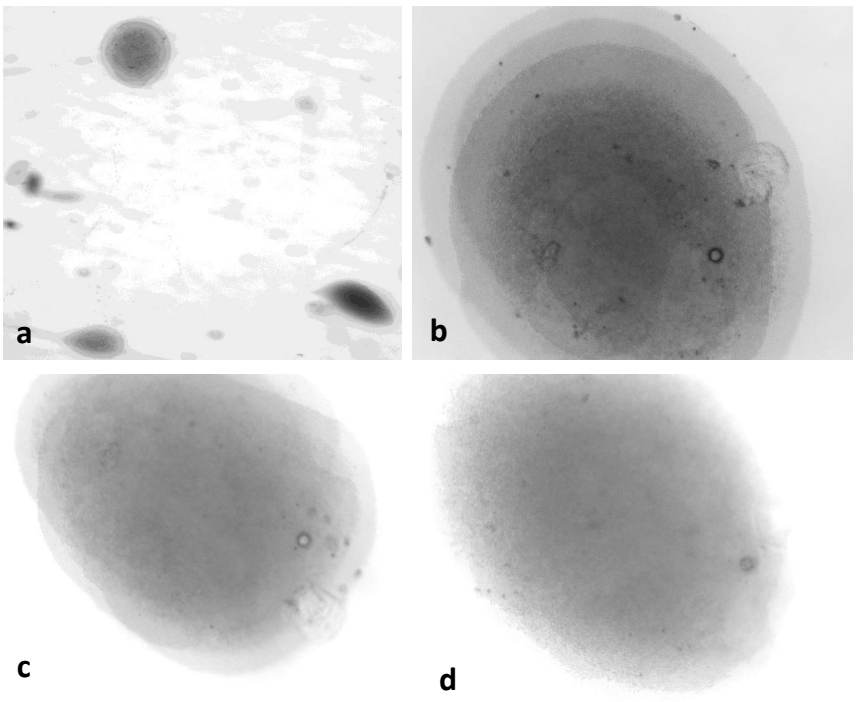

Figure 6.13 Observation of the acoustic streaming for 1μm particles a) at 1min, b) after 5min of the experiment. The same aggregate at the levitation plane in c) continuous mode and d) in pulse mode. Magnification 10X.

6.4.3 Layer thickness

In order to estimate the capacity of the acoustic mode employed to keep the particles layer focused at the levitation plane, experiments were done in continuous and pulse mode. By using monodisperse suspensions of 500nm, 883nm, 1μm and 3μm, and by using the circular resonator we measured the layer thickness at the levitation plane.

Each experiment started in continuous mode. After one minute, by turning to pulse mode at the threshold (Tp and Tt). The particles layer was measured with the microscope by fixing the positions of the firsts and the last particles. These measurements were done after the first minute time in which most part of particles reach the node and after one minute under the same conditions, as reported in Figure 6.16.

The values of the thickness layer are bigger in pulse mode than in continuous mode. It is considered that the **PRF**at the nodal plane could be weaker in pulse mode than in continuous mode. However, for 3μm particles these values have a tendency to reduce. In detail, the changes of the layer thickness of 1 and 3μm were actually unsystematic at each experiment; we observed in both cases the larger thickness in pulse mode such as 500 and 883nm particles and the smaller thickness in pulse mode. It could be defined that the acoustic mode employed do not have an influence any more on the force to focus the particles when their size is such (bigger), larger than 1μm.

A second experiment was done. From the beginning of the experiment, in pulse mode

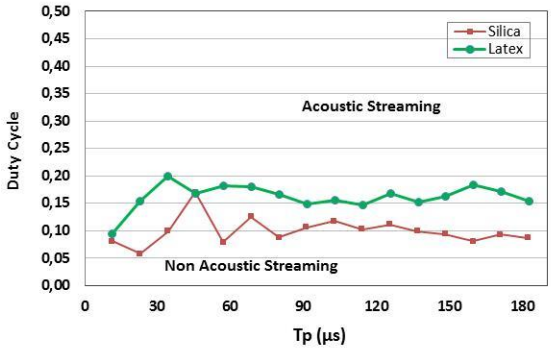

Figure 6.14 Acoustic streaming threshold for particles of 1μm but different material: latex and silica.

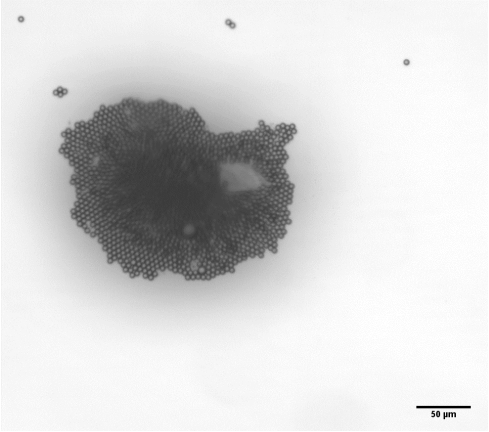

Figure 6.15 For 3μm latex beads, there is a fast particle levitation and aggregation. However, the AS is still evident in this particle size, because particles moves according to the acoustic energy distribution at the levitation plane. After 5min of the experiment, aggregates remain in levitation. Scale bar= 50μm, magnification 10X.

we measured the layer thickness after 1, 5 and 10 minutes (Figure 6.17). The object of this study was not only to find an efficient way of controlling the AS but also to be able to reduce it by keeping the primary and secondary radiation forces strong enough to manipulate sub-micron-sized particles.

6.5 Conclusions

In this experimental work we wanted to demonstrate the possibility of controlling the acoustic streaming in an USW fluidic resonator by using a pulsed ultrasound technique. Acoustic streaming can be reduced and likely controlled in pulse mode by adequately adjusting the number of pulses and the repetition time.

According to the results, sub-micron particles (smaller than 2μm, as the references) can be manipulated in an USW fluidic resonator. A calibration curve showed that the control parameter could be used for determining a streaming threshold. Pulse mode opens new perspectives for manipulating colloids by USW. The major finding in this work was that the characteristic transverse streaming velocity has been systematically modified by using pulsed ultrasound, keeping particles concentrated at the nodal plane without switching off the primary radiation force undergoing by particles.

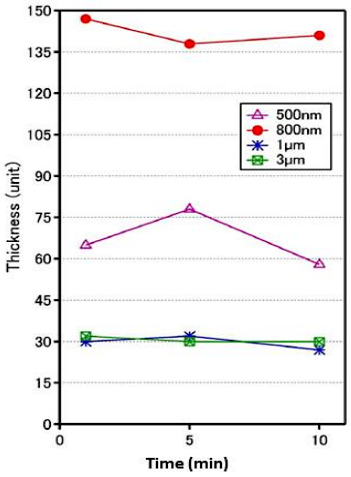

Figure 6.16 Layer thickness for particles of a) 500nm, b) 883nm, c) 1μm and d) 3μm obtained by acoustic levitation.

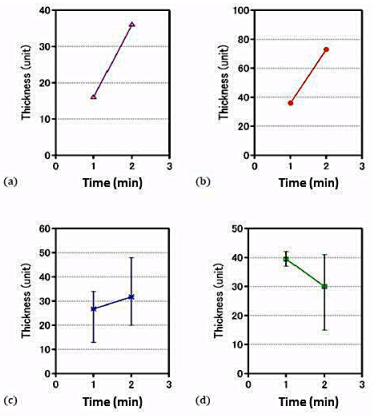

Figure 6.17 Measurement of the variation of the layer thickness on time, for the different particles size employed: a) 500nm, b) 883nm, c) 1μm and d) 3μm.

We found that the acoustic streaming could be reduced by adequately adjusting the number of pulses and the repetition frequency. The acoustic energy can be determined and controlled using the pulsed ultrasound technique. We'd seen that this phenomenon is also function on time.

Chapter 7

Applications for bacteria and metallic micro rods

We demonstrated the capability of our resonators to manipulate particles and cells. Other potential applications such as living organisms like bacteria and inert particles like metallic micro objects, could be interesting. In this chapter we present a preliminary work on *E. coli* bacteria and catalitic micro rods.

7.1 Bacteria

In previous work in collaboration with Eric Clément's group PMMH, *Escherichia coli* bacteria were studied. By studying the hyper-diffusive character and hydrodynamic components of the bacteria bath, wall effects modify bacteria diffusivity [71]. Then, by taking bacteria away from the walls it should be possible determine the real effect without lubrication generated by walls. In doing so, we used the strategy of USW to pull bacteria away from the walls.

In literature, bacteria suspensions had been clarified in an acoustic filter in batch or in flow operation modes by clump collection through electronic phase of frequency modulation of the sound field. Hawkes et al. [72], reported the removal of 80% of bacteria *E. coli* in an USW filter with a continuous through-flow of 0.3 ml/min. These applications did not generate a biofilm structure. By acoustically manipulating bacteria in microfluidic devices, biofilm-like structures have been obtained in tunable vertical flows. The mechanism used is known as "cavitation microstreaming", where oscillations of a microbubble trapped at a horseshoe structure exposed to acoustic waves at 30 kHz and 12Vp-p. Bacteria *E. coli* start to collect within the vortices of the microbubble. Several minutes are needed to bacterial collection in the vertical flow: microbial colonies similar to biofilms streamers are reached; the collection is faster and intense for bacteria with higher motility. Typical sizes after 2-3min appeared in the vortex reach a size of approximately 40μm [73].

In our case, by testing bacteria bath in the resonator, the bath reacts immediately to the ultrasounds (Figure 7.1 a). Concentrations of 2.8×10^8 till 4.8×10^8 ml^{-1} in MMA culture media diluted 10 and/or 20 times were employed. Instead bacteria levitation, their aggregation was also observed as the formation of film-like structures. Experiments were done using the circular resonator (Figure 3.5), to better identify this formation and the bacteria behavior under the action of USW. Transverse and secondary forces increases the contact between bacterium leading a film-like structure generation. By measuring the thickness of the obtained film (with the aid of the microscope) we obtained a structure of some micron thickness.

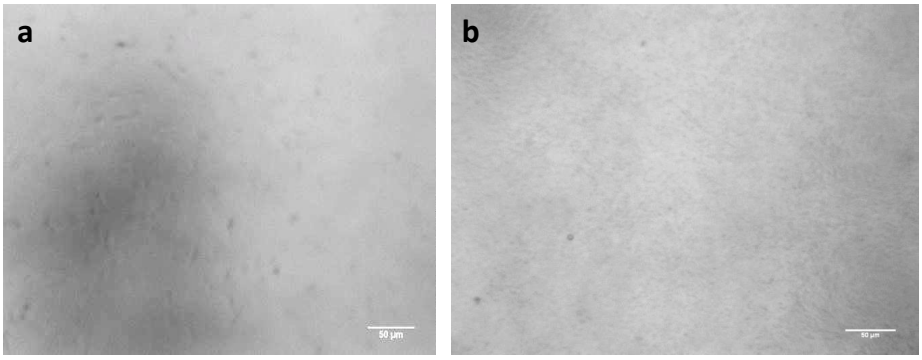

Figure 7.1 a) Bacteria are observed as little black points, observed in the resonator with 50X magnification. b) In continuous mode with a driving frequency of 4.130MHz and $18V_{p-p}$, we obtained a film-like structure in acoustic levitation. Scale bar = 50μm.

After 5 minutes of the experiment in levitation, the acoustic is switched off as show Figure 7.2a where the film obtained settles down. Afterwards, we switched-on the ultrasounds. The levitation of the film allow us to appreciate the elasticity of the generated structure as Figure 7.2b shows. Finally the film reach their flat appearance at the levitation plane (Fig. 7.2c).

Due to difficulties in the observation of the phenomenon, latex particles of 15 μm were used as tracers (Figure 7.3a). Contrarily to particles aggregates, is possible to appreciate

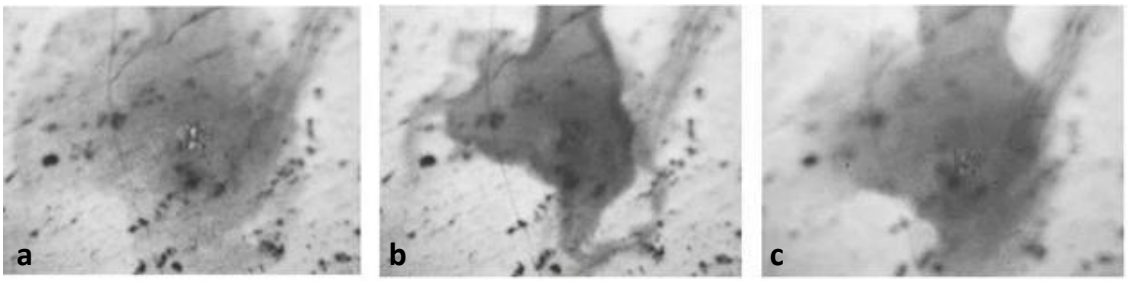

Figure 7.2 a) Film on the metal plate "acoustic-off". b) Film levitation. The central part of the film goes faster towards the levitation plane than the periphery. c) Film in levitation at the equilibrium position. Magnification 10X.

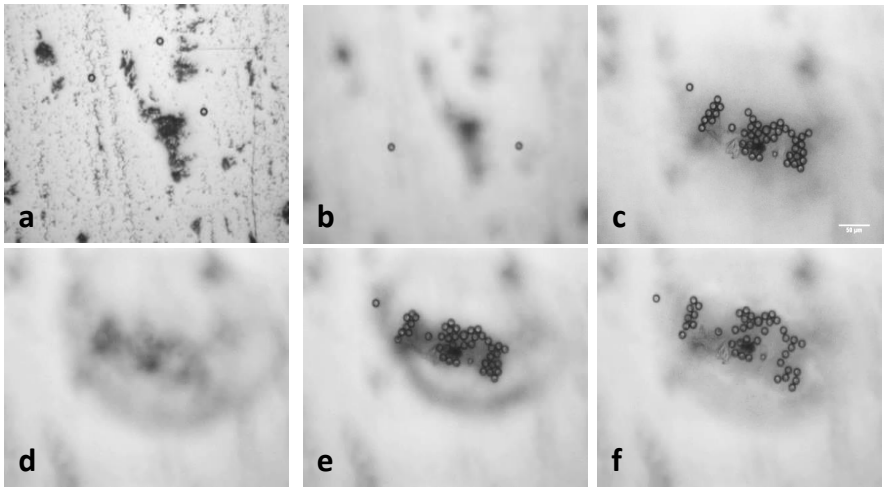

Figure 7.3 a) Bacteria bath and 15μm latex beads like tracers. b) Levitation and aggregation of the bacteria bath and the particles. c) Film and aggregate reorganization. d) The absence of the acoustic settles-down the film generated. e) Particles levitate faster that the film. f) Film at the equilibrium position. Magnification 20X, scale bar= 50μm.

that bacteria and/or their bio products generate an extra drag in the aggregation process (Figure 7.3d). By switching on the acoustics, the film already placed at the plate, levitate where particle levitation is faster than the biofilm (Figures 7.3e-f).

By increasing the magnification of observation, it is possible to appreciate the tracers immersed of bacteria film, as depicted in the Figure 7.4.

The formation of the film was tested in the time for continuous and pulse modes. In both acoustic modes, we could observe the change in bacteria-film concentration-activity to establish the configuration as shown Figure 7.5. In pulse mode by using 250 pulses at 1 kHz as repetition frequency, we observe the same behavior than in continuous mode where the process lasts at least 10 minutes. However, the minimum conditions in which the film levitates was reached in continuous mode by reducing the wave amplitude at 6Vp-p; in pulse mode, levitation was reached at 10 pulses and 1 kHz (at 14Vp-p).

In the time, there is a concentration zone where the film started to consolidate reducing the activity between bacterium generating a solid-elastic zone:

- High activity but also low concentration stable zone is formed where bacteria movement is random and fast. In this stable zone, bacteria seem in interaction forming somehow a liquid-like phase.
- The film is formed by a third zone where the concentration is low and bacteria don't seem in interaction. This zone is gas-like phase.

A great number of experiments had been done showing these novel structures and further we need to demonstrate that the structures are true biofilms.

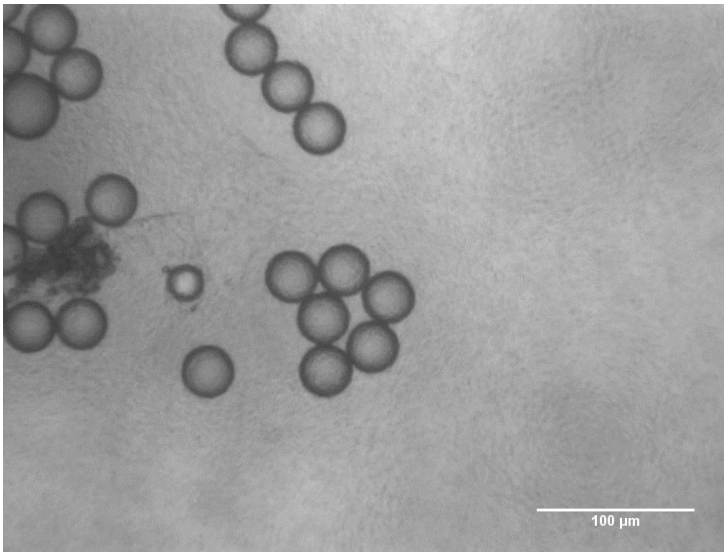

Figure 7.4 Latex 15μm tracers beads immersed in the film. Magnification 20X, scale bar=100μm.

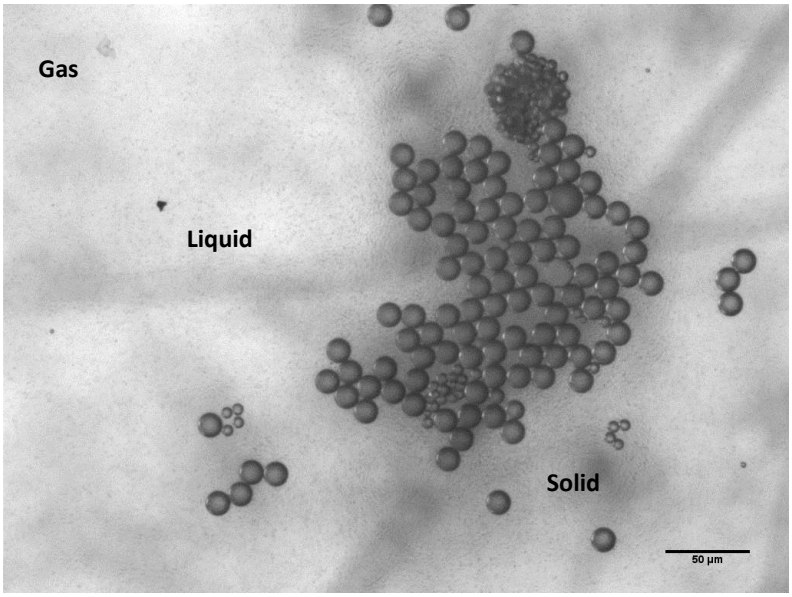

Figure 7.5 Configuration of the film. These configurations are in close relationship with bacteria activity. Magnification 20X, scale bar=50μm.

Figure 7.6 FESEM images of metal rods: gold-ruthenium (AuRu).

7.2 Metallic micro rods

Metallic rods act as autonomous micromotors displaying biomimetic behavior (bacteria-like motion) that includes transport of cargo, chemotaxis, swarming, and predator-prey interactions. However, their autonomous motion in biological environments relies on the use of toxic hydrogen peroxide (H_2O_2) or hydrazine derivatives as fuel which difficult their use in biological models. Another strategies of autonomous motion includes the use of an external electric and magnetic fields to drive micro-objects in biological media where the resulting motion is not autonomous.

Self-propelled rods are also active fluids. Their movement is hyper diffusive in hydrogen peroxide, biomimetic to bacteria [71]. Due their high density they are also close to the walls of the recipient. The rods are made of a single metal component (Au, Ru or Pt) or axially segmented (AuRu) are typically 1 to 3 μm long and 300 nm in diameter, as depicted in Figure 7.6.

Similar in the case of bacteria, we test metallic rods in our resonators to allow the pure diffusive effect. Experiments were done in the circular resonator (Figure 3.5), at 4.150MHz as driving frequency and 18Vp-p. Observations revealed that ultrasonic standing waves lead levitation and propulsion of metallic rods in axial and directional motion as well as in fast in-plane rotation.

Without acoustics, metallic rods describe Brownian motion. When the acoustic is switch on, metallic rods levitate and are dragged by the acoustic streaming leading the aggregation and the formation of patterns. However, we observe the rotation of the rods (at their axis) and the spindle axis of the rod-shaped aggregates, respectively as is illustrated in Figure 7.7a. The vortices generated by the metal rods lead to the self-assembly of the rods into chains (Figures 7.7a and 7.7d). The metallic rods showed axial directional motion (Figure 7.7b) with speeds as high as $\sim 200\mu$m/s. Directional motion of metal rods occurred even where rods were aggregated into patterns (Figure 7.7 c and e), where it can be observed their propulsion in the acoustic field i.e., the aggregation of the rods into patterns did not stop their directional motion or change their directions. Additionally, the metallic rods not only form a dense ring pattern; also populated the inside of the ring, forming many concentric and less dense rings in which chains of rods orbited the center where a smaller number of metal rods showing reduced directional motion (Figure 7.7e).

Consider two metal rods close to each other, which are cruising along the ring or streak patterns. Each one is subject to several forces: the repulsive hydrodynamic drag force

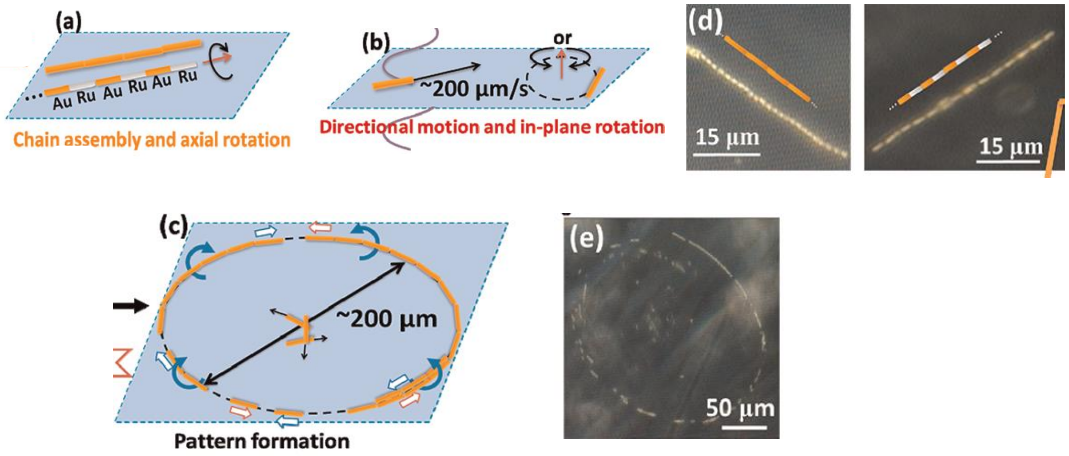

Figure 7.7 Directional motion and chain assembly axial rotation of metal rods at the levitation plane. Even where rods were aggregated into ring or streak patterns. Observations at the microscope were done at dark field due the facilities to distinguish the single components of metal and bimetallic rods, where the Ru end appears silvery. The directional motion, observed in the case of AuRu rods, the Ru side was always leading. Once two metal rods align, they continue to assemble with other rods or chains trying to form long chains. Interestingly, when two chains (or rods) traveling in opposite directions meet each other, they do not interfere with each other's motion or assemble into growing chains. Instead, they spiral around each other and continue in their original direction of motion; these directions are opposite along the chain axis because all the rods are confined by the vortex drag force.

from the vortex induced by the other rods, the secondary Bjerknes force as well as the attractive van der Waals force when the rods are close to each other, and the driving force propelling the rod along its axis. Under the effect of these forces, the rods adjust their positions until the total energy is minimized, which occurs when two rods are aligned in the axial direction on the nodal line. By modifying the amplitude of the acoustic wave the spinning speed of the rod can increase or reduce. It is important to note that even a slight deviation (a few kHz, or around 1% of the frequency) away from the resonance frequency dramatically decreased the intensity of the rod motion.

Figure 7.8 shows the self-assembly interactions of chains formed by metal rods. Each polar rod in these chains points in the same direction so that the chain has an AuRu|AuRu|AuRu structure. This head-to-tail assembly is not particularly surprising considering that the bimetallic rods always move with the same end forward (e.g. the Ru end for AuRu rods), and only rods moving in the same direction can align into chains. As noted above, chains moving in opposite directions eventually pass each other without coalescing into a single chain.

Among the kinds of motion described, axial propulsion is particularly interesting because it opens up the possibility of powering autonomous movement in a variety of media that are compatible with ultrasound. Metallic rods behave differently in acoustic fields than polymer spheres or rods. Shape asymmetry drives motion along the axis of the metallic rod, a mechanism we tentatively call "self-acoustophoresis".

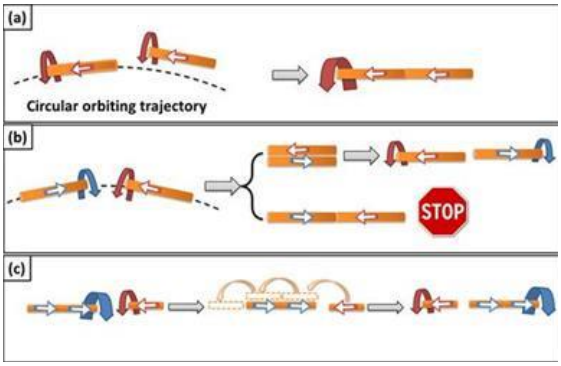

Figure 7.8 Illustration of chain assembly and directional motion of metal rods along the chains: (a) two metal rods moving in the same direction along the ring interacts and form a spinning doublet. (b) two metal rods moving in opposite directions either brush against each other or meet each other head-to-head; (c) when a metal micro-rod meets a chain moving in the opposite direction, the rod brushes against the chain and the two parties continue separately. The presence of metallic rods at the edge of the ring or streak patterns on the nodal plane generates vortices in the fluid, which cause the rods to spin and induces their self-assembly into chains.

7.2.1 Ultrasonic propulsion in pulse mode

In pulse mode, experiments were done using the same frequency and amplitude as in continuous mode. By choosing several combinations of Tt and Tp, it is possible to tune the activity of the metal rods. For example high Duty cycles, means a larger Tp and smaller Tr where rods levitate and show strong rotation. We found the threshold for levitating rods at the onset of rotating motion at a Duty cycle of 0.04, that means 1 kHz repetition time and $Np = 150$ pulses. However when Duty cycle is lowered, the activity of the rods decreased until the threshold Duty cycle, where the rods maintain levitation but show little rotation. A Duty cycle below this threshold results in destabilization and sinking of the rods back to the bottom of the cell.

The results from the pulse mode experiments help to quantify the forces at work in the different motions of the metal rods. First, the acoustic radiation force levitates the rods. Below of the threshold, Duty cycle of 0.04, metal rods were no longer levitated and began to sink. At this power, the levitation force balances the gravitational force, which is approximately 0.027 pN for 2μm $\times$300 nm gold rods. Therefore, for experiments carried out in continuous mode at the same instantaneous power, the levitation force can be estimated to be $1/0.04 \times 0.027$ pN $= 0.75$ pN.

At low Reynolds numbers ($\sim 10^{-4} - 10^{-5}$ for microrods moving at a few μm/s), this force is equal to the hydrodynamic drag force:

$$\mathbf{F}_{\text{Drag}} = \left(\frac{2\pi\eta l}{In\frac{2l}{d} - 0.72} \right) v. \tag{7.1}$$

where l is the length of the rods (2 μm), d is their diameter (150 nm), and v is the velocity of the rods that are being pushed to the nodal lines, which is $\sim 5\mu$m/s. From equation 7.1, the drag force is ~ 0.025 pN, which is equal to the lateral force. This force is about 2 orders of magnitude stronger than the $\mathbf{F}_{\text{xy}}$ and is comparable to the acoustic force. This suggests that self-acoustophoresis arises primarily from scattering of acoustic waves traveling in the z-direction. The transverse force $\mathbf{F}_{\text{xy}}$ acting on the rods pushes them into nodal lines and forms the streak and ring patterns at the levitation plane.

7.3 Conclusions

Applications of these objects in our devices shows us potential uses to improve and to test better parameters, resonator configurations and other factors that could generate the control of the species tested. For Bacteria, a new application of this methodology can produce in short time (roughly in seconds) a bacteria-like film that in other conditions requires hours, days and also weeks. Also, we observe that the production of the film in acoustics is linked with the time of application of ultrasound and the mobility of bacteria. However, it is necessary to test the phase formation in pulse mode. Acoustic energy could stimulate the secretion of a metabolite (primary or secondary) to give cohesion between each bacterium or is probable another interaction of the flagella.

Acoustic waves can induce rods propulsion and directional motion, include under fluids such as the former do not show fast chemically powered movement in 5% H_2O_2 solution whereas the latter do or by modifying the salt concentration in the media (which tend to inhibit the self-electrophoretic movement of catalytic micromotors in H_2O_2). The locally induced pressure gradient propels the metal rods in a similar way as the acoustic pressure gradient moves particles, a phenomenon sometimes called acoustophoresis. The pressure gradient is generated locally and affects only the individual rods we use the term self-acoustophoresis to describe this mechanism.

We have demonstrated that MHz frequency acoustic waves can propel, align, rotate and assemble metallic micro-rods in water. Control experiments with polymer particles and metal spheres lend support to the hypothesis that shape and material play a critical role in the directional motion and the generation of strong vortices along the axis of aligned metal rods. Based on observations with template-grown homogeneous and bimetallic nanorods, it is likely that shape asymmetry, specifically the curvature at the ends of the micro-rods, leads to the directional motion by a self-acoustophoresis mechanism. The significance of this finding lies in the possibility of driving and controlling micromachines in biologically relevant environments using ultrasound. Ultrasonic guidance of nanorods is probably the future in the field of drug delivering [74].

Chapter 8

Perspectives

This work open new perspectives to other applications to different biological materials: liposomes, cells and collagen.

8.1 Liposomes

Liposomes are sub-micron sized, self-assembled lipid structures. They can act as a biomimetic compartments with a membrane that resembles that of living cells, encapsulated materials such as DNA, proteins, drugs or other chemicals. Vesicles have been made using different surfantants besides phospholipids [75]. Applications such as remotion of toxic drugs, drug delivery requires the use of monodisperse samples. However, the preparation methods generates polydisperse liposomes thus separation is an important step. The application of USW to separate polydisperse samples of liposomes in our resonators as depicted in Figure 8.1.

8.2 Cells

Cells offer us a great number of applications. Due the character of non-toxic, non-invasive of USW, the frequencies employed do not damage the cells (MHz frequencies). One of them is to generate selective aggregates of cancer cells, in order to detect rare cells.

Applications in neuronal cells (schwan cells), macrophages infected with malaria, separation of platelets from blood cells among others.

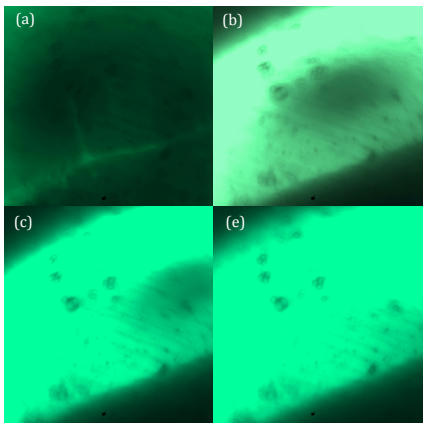

Figure 8.1 a) 500nm silica particles and liposomes in the resonator, acoustic-off. b-c) Acoustic-on, where there is acoustic levitation and aggregation of the species at two different levels of a n=2 resonator. There is a special emphasis in the liposomes aggregate that can be flushed out the resonator by using a low flow.

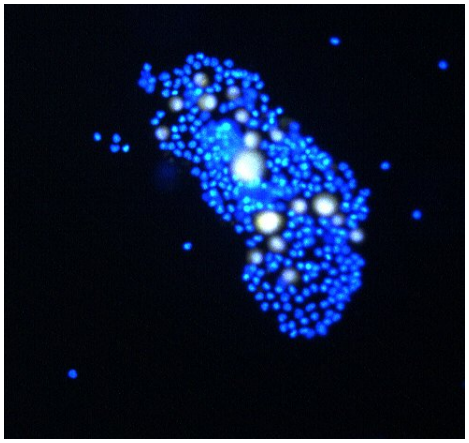

Figure 8.2 Aggregate of cancer cells obtained in acoustic levitation.

8.3 Collagen

In our work is possible to develop collagen films in levitation that can be used as scaffolds to cell culture. By following the protocol to obtain collagen gel, this is introduced in the resonator, where USW levitates the structure.

8.4 Drug delivering with metallic micro rods

The self-acoustophoresis mechanism presented in the last chapter, open new possibilities of drug delivering by non-invasive methods, as Wang and Gao [76] reported

Another potential for drug delivery is the presented in the annexe F by the coupling

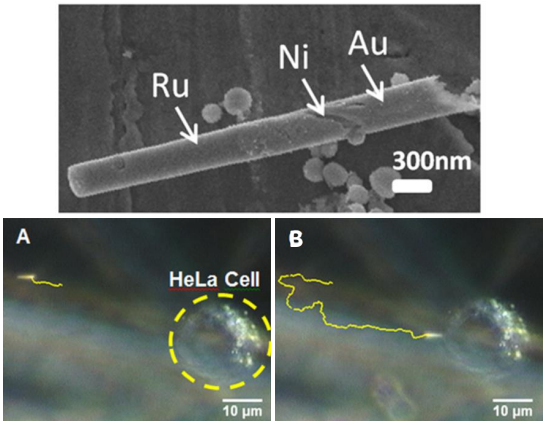

Figure 8.3 Catalytic micro cylindres acoustically and magnetically guided towards a HeLa cell.

between magnetic and acoustic forces to guide rods towards cells to vaccination.

Chapitre 9

Résumé de la thèse

L'objectif principal de cette thèse est d'explorer les possibilités offertes par la lévitation acoustique pour manipuler des particules élastiques et rigides de taille micrométrique ainsi que des objets biologiques et biomimétiques dans des résonateurs composées des plaques parallèles. Afin d'effectuer des séparations et biotests d'un grand nombre d'objets à haut rendement, nous avons conçu et construit tous les résonateurs que nous avons utilisés, et nous avons développé des nouvelles méthodologies que nous allons montrer dans ce travail expérimental.

Applications potentielles dans le domaine de la bio-ingénierie, de la industrie pharmaceutique, du génie chimique, du génie des matériaux, dont la collection des particules a besoin des méthodologies pour les collecter, concentrer, séparer et transporter [3]. Des techniques sans-contact sont nécessaires dans des domaines comme la biotechnologie, pour manipuler des cellules sanguines sans risques de contamination. Donc, la lévitation acoustique a des applications potentielles [4].

Dans cette thèse, nous sommes concernés par les concepts suivants : force de radiation acoustique, l'acoustic streaming (courrants acoustiques), acoustophorèse et séparation. Ce travail a généré quatre brevets.

Nous entendons par manipulation acoustique, la génération de déplacements relatifs entre les particules et le fluid, ainsi que les déplacements relatifs entre les particules sous l'action de forces de radiation acoustique afin d'induire des séparations, ségrégations, agrégations ou d'autres processus de transport.

Les ondes stationnaires ultrasonores (ultrasonic standing waves USW), sont souvent utilisés pour piéger, déplacer et localiser spatialement des objets micrométriques : comme des particules et des cellules en particulier, bien adaptés à l'échelle des dispositifs microfluidiques. Une autre possibilité est que les particules peuvent être déplacées à l'aide de deux ou plusieurs transducteurs qui modulent le champ acoustique [5].

La manipulation des particules par USW, se fait dans un résonateur acoustique qui est une cavité où l'un des parois est collé un transducteur piezo céramique ; la paroi opposée serve de réflecteur passif. L' onde ultrasonore générée est réfléchie et la superposition des ondes est connue comme une onde ultrasonore stationnaire. Les ondes ultrasonores sont des ondes mécaniques qui ont besoin d'un milieu physique pour se propager. Quand une onde acoustique est introduit dans un fluide, des gradients de présion génerés peuvent déclencher différents effets comment la force de radiation acoustique et l'acoustic streaming, les deux effects liés à des ondes progressives, mais son effet est beaucoup plus fort lorsqu'on utilise des ondes ultrasonores stationnaires.

Dans un résonateur, quand on établi la fréquence de résonance et/ou l'amplitude de l'onde acoustique, les particules dans suspension (9.1 a) sont affectés. Selon la nature des particules, elles seront placés vers le noeud ou vers le ventre de l'onde. Le déplacement des particules va dès la plaque d'en bas jusqu'à la position d'équilibre, là où la force acoustique et la force de gravité sont équilibrées. Ce position d'équilibre, aussi connue sous le nom de plan de lévitation acoustique (Fig. 9.1b) dont il y a l'interaction entre les particules et la force de radiation primaire (**PRF**). Une fois en lévitation, d'autres forces aparaissent et génèrent l'agrégation des particules : la composant transversal de la force primaire **PRF**, **TPRF**que pousse les particules vers les zones d'energie maximal. Quand les particules sont proches l'une d'autre, la diffusion acoustique donnent lieu à une force d'interaction nommé force secondaire de Bjerknes. Cette force-ci est attractive pour les particules sur un plan perpendiculaire à la propagation de l'onde. La force de Bjerknes conforme l'agrégat [1].

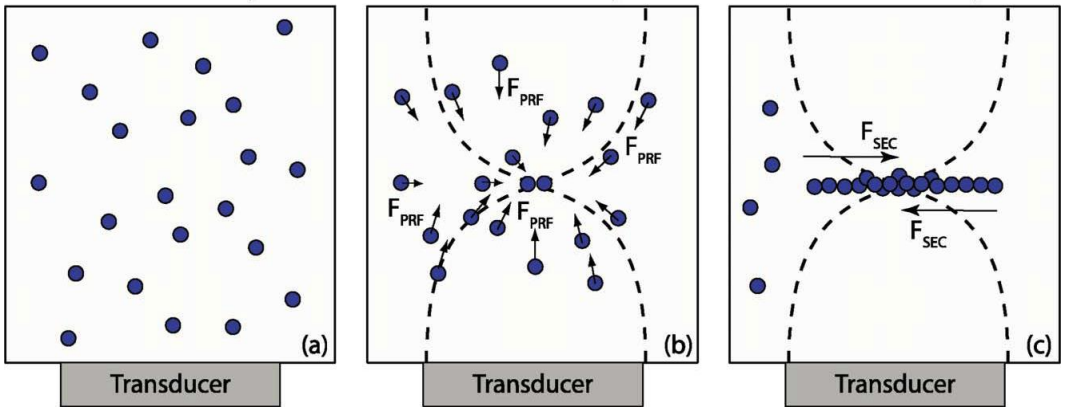

FIGURE 9.1 Schema géneral des forces acoustiques dans un résonateur acoustique a) Particules suspendues. b) Le profil de pression, répresenté par les lignes pointues, montre que la force **PRF** amène les particules vers le noeud de l'onde. c) La compossant transversal de la force primaire **TPRF** et la force acoustique sécondaire génèrent la agrégation des particules. Pris de [11].

Nos dispositifs sont des résonateurs de plaques parallèles composées des différents couches ou plaques : le transducetur qui génère l'onde acoustique, suivie par une plaque de couplage que forme le fond du résonateur. Ensuite, la couche ou plaque de fluide qui contient la suspension et à l'autre extréme, la plaque réflectrice responsable de la réflexion de l'onde incidente dans la couche de fluide, qui permet la production de l'onde stationnaire [12].

[1] Agrégat : clump, cluster ou aglomerat

Dans un résonateur acoustique la fréquence de résonance est obtenue avec la condition : $w = n\frac{\lambda}{2}$, où w est la largeur ou la hauteur du résonateur, n est le nombre de noeuds de pression de l'onde stationnaire et λ est la longueur d'onde égale à $(\frac{c_f}{f})$ où c_f est la vitesse du son dans l'eau 1482 = m /s et f est la fréquence acoustique [11]. La force acoustique est proportionnelle à la fréquence et si en réduisant la dimension du résonateur à la condition de résonance (la motié de la longueur d'onde), la fréquence devra augmenter. L'incrément de la fréquence donne une majeur force acoustique qui permet manipuler objets de taille micrométriques dans systèmes continus en flux [12].

Chapitre 2 : Contrôl du processus d'agrégation

Quand un grand nombre de particules subissent une USW dans un résonateur à plaques parallèles, la lévitation se produit et le processus d'agrégation s'établi. Le processus d'agrégation dans résonateurs microfluidiques permet la manipulation de juste quelques particules et par conséquent la obtention des petits agrégats. Dans notre étude, nous avons produit des agrégats composés de centaines ou de milliers de particules, générant des structures 2D ou 3D (voir Anexe A).

La fréquence nominale de l'onde ne correspond pas à la même valeur de la fréquence de résonance. La plus part des cas, la fréquence nominal génère la lévitation des particules, mais le processus d'agrégation s'effectue lentement. L'ajustement de la fréquence (en quelques decimals) permet la formation rapide d'un agrégat de gros taille. On a pu observer que la variation de la fréquence déplace l'agrégat quelques μm dans la direction x-y de son point d'agrégation initiale (voir Figure 2.2). Donc, il y a une variation dans la forme de l'agrégat en raison des réarrangements qui produit son déplacement dans la direction transversale.

La fréquence de résonance et l'amplitude de l'onde acoustique sont les paramètres normalement le plus utilisées pour manipuler des particules avec USW. Maintenant, nous proposons le mode acoustique pulsé, plus utilisé dans des applications biologiques pour cibler des tissus avec des ultrasons à haute énergie.

Agrégation en mode continu

L'onde acoustique en mode continu est apliquée jusqu'au moment où le processus d'agrégation fini. Les agrégats obtenus par ce mode, sont caracterisés par leur morphologie 3D [48, 53] ou lorsque la densité des particules est supérieur à 10^6 particules/ml [26]. Cette morphologie est résultat de la superposition de couches de particules qui génère des structures non homogènes.

Pour les cellules, les agrégats obtenus sont également tridimensionnelles, caractéristiques de tissus de mammifères. Néanmoins, l'observation au microscope des agrégats 3D rend difficile les études sur l'interaction entre les cellules, pour des applications biologiques ou pharmacologiques [48, 51].

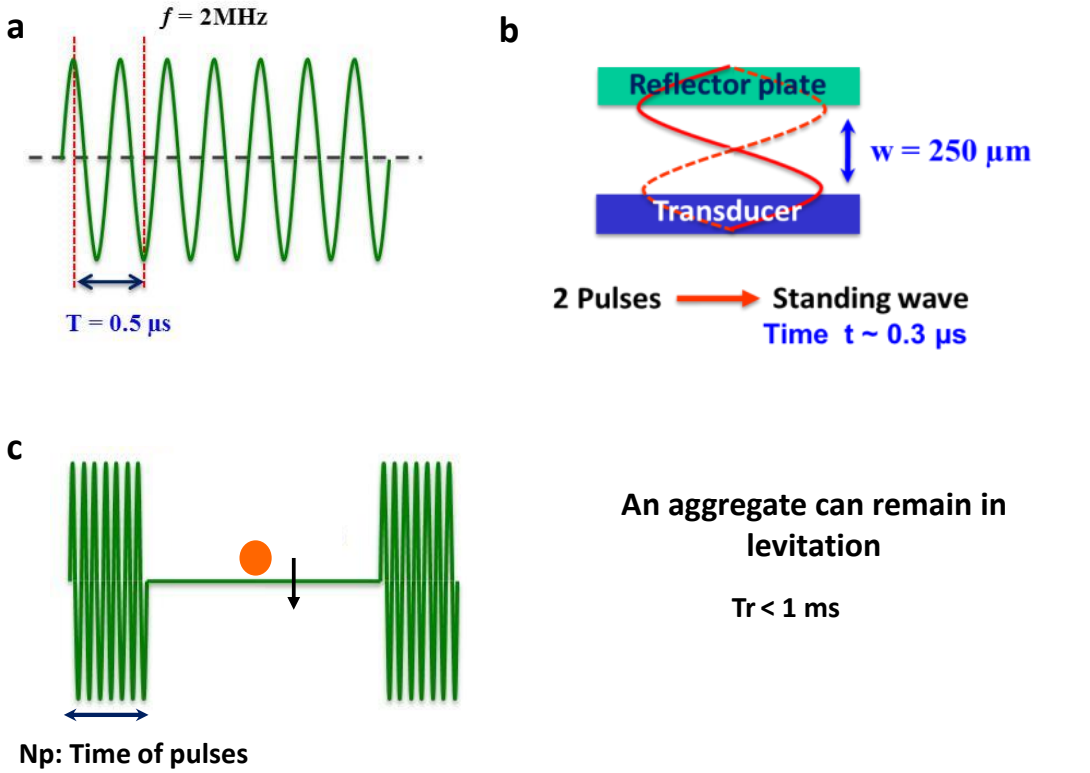

FIGURE 9.2 a) Onde USW de $f = 2$MHz en mode continu. b) Pour un résonateur de 250μm d'épaiseur, une USW tard 300 ns. c) Quand on envoie plusieurs pulses (à la même fréquence) séparées par un temps de répétition sufisant pour empêcher la sédimentation des particules ou des agrégats en lévitation. Ce temps-là a été determiné comme d'un 1ms.

Agrégation en mode pulsé

Une fois la fréquence de résonance est établie, ainsi que l'amplitude de l'onde acoustique, on met le générateur d'onde en fonction "burst". Le mode acoustique pulsé, comme montre la Figure 9.2, consiste à envoyer un groupe des pulses (Np) ou des périodes séparées par une certaine temps [2]. Ensuite, nous considérons deux paramètres en mode pulsé : le temps des pulses et le temps de répétition.

Temps des pulses Tp

C'est le nombre des pulses Np multiplié par le temps d'un pulse à la frequence de résonance. C'est le temps dont le transducteur est allumé ("on"). Il doive être le plus haut pour générer une onde stationaire et pour que les particules puissent attenidre sa vitesse terminal qui est donné par l'expression du chapitre 2.

[2] deux pulses sont nécessaires pour établir un USW

La vitesse de rélaxation peut être obtenue l'exprésion suivante :

$$\mathbf{F}_{\mathrm{xy}} + \mathbf{F}_{\mathrm{s}} = \rho_p V \frac{du}{dt}. \tag{9.1}$$

Neanmoins, la valeur de la force $\mathbf{F}_{\mathrm{xy}}$ est inconue et il n'a pas une rélation que considère la rélation complexe entre la force transversal acoustique dans le processus d'agrégation. Donc, l'écuation est résolu avec la rélation $[u_t/u_0]$ du temps de rélaxation.

Temps de répétition Tr

Est le temps dont le transducteur est "off". Il est important que Tt soit assez court, afin de empêcher la sédimentation des particules ou des agrégats, pour un nombre des pulses $Np = 100$ ce qui signifie $t_{on} = 0.5$ ms lorsque la fréquence est 2 MHz. Si chaque paquet d'ondes est séparé avec un temps de répétition de 1kHz c'est-à-dire : $t_{off} = 1$ ms. On considère une distance limite de sédimentation de un rayon de particule par exemple, la vitesse de sédimentation de une particule de 10 μm latex est $\backsim 3\mu$m/s, donc Tt ne devrait pas être moins de $1.67s^{-1}$. Cependant, on observe que la sédimentation d'un agrégat des particules est beaucoup plus rapide que celle d'une particule unique. Expérimentalement, nous avons déterminé que la fréquence limite de répétition est d'environ R_f = 1kHz : 1ms.

De manière générale, pour une expérience d'une durée de 1 min chaque cycle on-off dure $t_{cycle} = 1.05$ ms, environ 57143 cycles on-off pendant l'expérience. Puis, le temps total où la force est «on» sera alors $\backsim$ 2,86 secondes et $\backsim$ 5 % du temps total.

Contrôl de l'agrégation

En collaboration avec Despina Bazou (Trinity College de Dublin), nous utilisons le résonateur illustré dans la Figure 2.4. Nous avons effectué des expériences en mode acoustique continu et pulsé pour des particules de latex de 10 et 15 μm et pour des cellules cancereuses (le protocol de culture cellulaire est décrit dans l'article (anexe A), et nous avons employé des concentrations entre 5×10^5 et 3×10^6 cellules/ml de CaCO2 cellules-colon adenocarcinoma).

Avec les conditions expérimentals (dans la Table 2.2) on a mésuré l'évolution de l'agrégat en fonction du temps :

$$\text{Aggregate normalized} = \frac{\text{Aggregate area at time t}}{\text{Final aggregate area}}. \tag{9.2}$$

On a pu constater que le processus d'agrégation en mode continu génère des estructures 3D. Les particules se agrégent et avec le temps, il y a des réarrangements dans la péripherie des particules qu'arrivent, ce que produit le chevauchement des couches des particules et ensuite le changement de la configuration globale. Le chevauchement est généré par la pression croissante des particules incidentes, déterminant ainsi le passage des structures 2D à 3D. Structures tridimensionnelles sont présentés dans la figure 2.7, où les structures 3D peuvent sont visibles comme des zones sombres au centre de l'ensemble.

Le mode acoustique pulsé est une nouvelle façon de contrôler le processus d'agrégation et sa morphologie. Tout au long des expériences effectuées en mode continu avec des particules et des cellules, nous avons observé des structures 3D généralement obtenues au centre des agrégats ; ces structures 3D ne sont pas homogènes. Pendant ce temps, en modifiant les paramètres de mode pulsé tels que le nombre des pulses ou/et le temps de répétition, on a pu générer une structure 2D en lévitation acoustique. On a mésuré la vitesse transversal des particules pendant le procesus d'agrégation pour les deux processus (Table 2.3).

L'utilisation du mode acoustique pulsé offre plusieurs avantages par rapport au mode continu : la possibilité d'augmenter la force acoustique grâce à l'emploi d'un nombre des pulses minimum qui permet l'agrégation des particules ou des cellules sans les endomager, réduit le rechaufement du liquide et des transducteurs ce qui permet maintenir constants les propriétés thermodynamiques et physico-chimiques de la suspension. L'architecture de l'agrégat résultant peut être modifié indépendamment de la concentration initiale des particules ou des cellules.

Chapitre 3 : Détermination de la force secondaire de Bjerknes

L'étude des forces acoustiques dans différents millieux est devenue importante ces dernières années en raison du nombre croissant d'applications qui profitent de la manipulation d'objets sous acoustique : lévitation acoustique pour positionnement et contact, manipulation de gouttes et de bulles et la manipulation des fluides en microgravité. En outre, de nombreux auteurs ont étudié expérimentalement et théoriquement la force secondaire de Bjerknes principalement pour des bulles, non sur particules rigides. Des articles scientifiques ont été écrits sur les forces secondaires en particules, autant que nous le savons, aucun d'entre eux les a déterminé expérimentalement [55].

L'objectif et l'originalité de cette étude est de présenter une méthode expérimentale pour déterminer la force secondaire de Bjerknes dans le processus d'agrégation des particules rigides et des cellules. Cette étude a conduit à une meilleure compréhension de l'interaction entre les particules dans le processus d'agrégation. Nous avons mis en place une méthodologie pour mesurer cette force de courte portée (entre une ou deux particules de diamètre) et nous avons trouvé les valeurs de 10^{-13} N (voir anexe B).

Dans un travail précédent de notre groupe, les films réalisés du processus d'agrégation des particules, nous ont montré les interactions interparticulaires. En regardant attentivement les cas, image par image, comme est représenté sur la figure 9.3, nous avons identifié une distance à laquelle il y a une légère perturbation entre une ou les deux particules indiquant qu'ils commencent à subir l'interaction. Donc, nous supposons qui il peut s'agir de l'action de la force sécondaire de Bjerknes. Après cette distance, les particules se rapprochent jusqu'à être en contact dont il y a la formation d'un doublet stable, première étape du processus d'agrégation.

Nous avons mesuré la force secondaire de Bjerknes pour plusieurs diamètres de particules et pour des cellules cancereuses, selon le schema de la Figure 9.4.

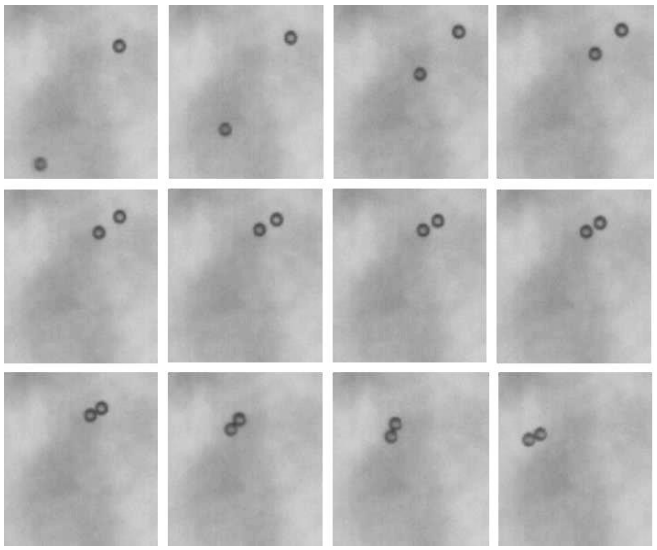

FIGURE 9.3 10μm particules de latex dans le plan de lévitation.

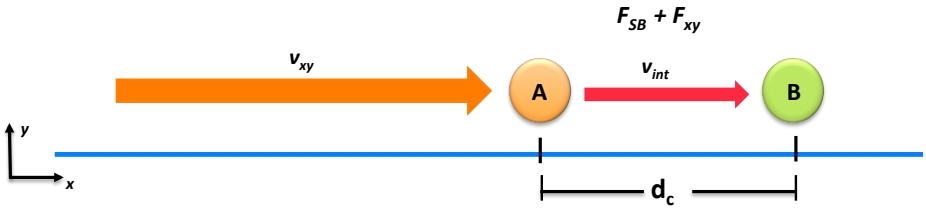

FIGURE 9.4 Schema de la détermination expérimental de la force secondaire de Bjerknes. Une particule dans le plan de lévitation est sous l'influence de la force **TPRF**. Quand la particule est proche de une autre à une distance d_c, commence l'interaction. Donc, l'atirance entre les deux particules a lieu.

Nous avons obtenu un accord qualitatif avec la théorie selon laquelle la force de Bjerknes, augmente avec la taille des particules. C'est la première fois que cette force a été déterminée pour les particules rigides et des cellules. Neanmoins, nous n'avons pas pu comparer précisément les valeurs théoriques et expérimentales, parce que nous n'avons pas les valeurs expérimental de la pression acoustique ni de l'énergie acoustique pour chaque cas, ni pour chaque point. Les ordres de grandeur des forces est en accord avec la théorie (10^{-12} - 10^{-13} N, voir résultats pags 38, 40 et 41 pour les cas des cellules).

Chapitre 4 : Détermination de la force secondaire de Bjerknes en micropesanteur

Il pourrait être possible de manipuler les espèces en utilisant l'acoustique dans les conditions d'apesanteur. Nous avons effectué des expériences en microgravité dans l'Airbus A300-zéro G (Novespace, Bordeaux-France). Ce travail ouvre la possibilité d'effectuer des

cultures des cellules dans l'espace en raison de la capacité des ultrasons à générer des agrégats de cellules dans des conditions sans contact. En suivant la méthodologie proposée au chapitre 3, dans ce chapitre-ci nous présentons des mesures expérimentales des forces secondaires de Bjerknes pour des particules de tailles différentes en conditions de micropesanteur.

Le travail de Ratier [10], pour la détermination de l'énergie acoustique dans un résonateur acoustique a permis de trouver la position d'équilibre (plan de lévitation) selon des observations *in situ* dans le résonateur. Donc, les résultats ont indiqué le déplacement des particules à la position réelle du nœud en microgravité, comme le montre la Figure 9.5.

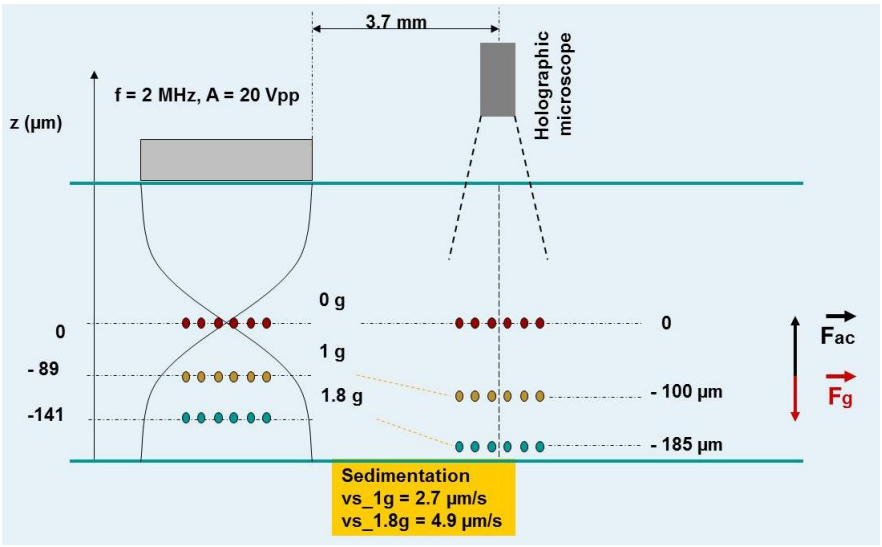

FIGURE 9.5 Schema de l'observation *in situ* de la position du nœud acoustique en microgravité, 1g et 1.8g dans un résonateur acoustique.

La force seconadaire de Bjerknes a été déterminée dans des conditions de microgravité pour plusieurs tailles de particules. Les forces déterminées en micropesanteur sont un ordre de grandeur plus élevé que les forces déterminées sous sol. L'influence de la microgravité peut placer les particules exactement dans le plan nodal, là où la pression est nulle ainsi que **PRF** et **TPRF**.

Dans ce cas, la force de Bjerknes agit directement sur les particules et ils ne sont pas voilée par d'autres forces. La distance critique trouvée dans les cas semblent même comme ceux qu'on trouve sur sol.

Chapitre 5 : Séparation acoustique des particules

La séparation et l'isolement de materiaux particulaires en fonction de leur masse sont souvent des étapes cruciales dans la caractérisation d'un échantillon et l'étape précendant pour une multitude d'applications impliquant des cellules vivantes, des macromolécules, des colloïdes industrielles et des particules, des polymères synthétiques, des émulsions

pharmaceutiques et des liposomes et des matériaux environnementaux. Le besoin généralisé de la séparation dépendant de la masse avec une grande sélectivité et la résolution a entraîné le développement des techniques de séparation telles que la centrifugation, le field flow fractionation (FFF), le split-thin flow fractionation (SPLITT), l'élutriation, l'électrophorèse capillaire, la chromatographie d'exclusion et l'hydrodynamique chromatographie [59].

Nous avons utilisé l'acoustique programmé pour faire le tri des particules avec des forces hydrodynamiques sous écoulement en continu. Le couplage de la séparation hydrodynamique avec le champs acoustique dans le dispositif s-SPLITT a géneré le dispositif HACS -Hydrodynamic Acoustic Continuous Sorter- lequel a des étapes de fractionnement selon les transducteurs qui ont été mis en place pour améliorer la séparation comment l'indique la Figure 9.6. Comment l'a démontré Ratier [10], la disposition d'un transducteur près de l'autre permet améliorer la séparation des espèces dans ce dispositif. De nombreuses expé-

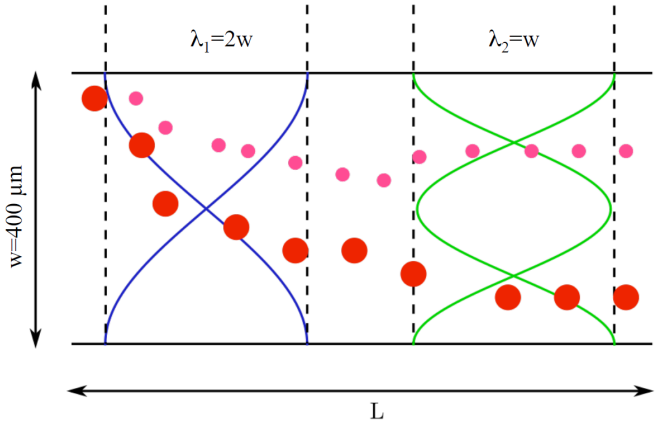

FIGURE 9.6 Principe de la séparation acoustique programmé. Deux transducteurs de fréquences différents sont placés au long du résonateur. Ce résonateur fonctionne sous flux.

riences ont été réalisées dans un nouvel dispositif pour séparer une mélange des particules de 7 et 12 μm.

Trajectoires des particules

Au cours du processus de séparation acoustique, les particules dans un canal subissent plusieurs forces et interactions hydrodynamiques : la force acoustique, la force de traînée, la force de flottabilité entre particules et les interactions particules-paroi. Cependant, comme nous travaillons avec une suspension diluée, les interactions entre particules seront négligés.

Nous avons effectué des calculs des trajectoires des particules dans une modèle qu'on a esaié ; pour les expériences nous permettra améliorer la séparation. La séparation obtenue confirme les prédictions faites par le modèle, même si la résolution est inférieure à la prédite. En fait, le modèle prévoit que toutes les particules doivent se concentrer au niveau des deux noeuds, sans aucun élargissement significatif de la distribution dans l'épaisseur.

Tout d'abord dans un canal réel, il ne sera pas possible de mettre en place une onde stationnaire parfait, cela est dû à plusieurs interfaces qui seront présents sur le trajet de l'onde à travers le canal. Il se traduira par un déplacement des nœuds et par une réduction de l'intensité de la force acoustique. Toutefois, les caractéristiques générales de la force acoustique resteront les mêmes (les particules seront amenés à les nœuds avec un temps de relaxation ayant la même dépendance de leur taille), et donc le principe de séparation ne change pas. Deuxièmement, le profil transversal des ondes n'est pas de forme carrée. Ceci entraîne également une modification des temps de relaxation.

Plusieurs expériences ont été faites. Cependant, nous ne pourrions pas avoir les résultats escomptés en raison que le dispositif doit être amélioré.

Chapitre 6 : Contrôl de l'acoustic streaming

Habituellement, un résonateur acoustique peut piéger des espèces de taille supérieur à 1μm : comme des particules, des cellules de taille micrométrique et même des bactéries. Cependant, quand les espèces deviennent plus petites de cette taille, la manipulation acoustique est un défi. Cette complexité est due l'influence de l'acoustic streaming qui modifie le comportement des particules. En fait, études théoriques sur l'acoustique streaming ont établi que la taille limite pour manipuler des particules est de 2μm [20, 33].

L'une des originalités de ce travail est la mise en place du mode acoustique pulsé. Les modes acoustiques employés jouent un rôle dans le contrôle de la morphologie globale des agrégats, la forme, la taille et la configuration. Par conséquent, comme nous l'avons présenté dans le chapitre 2, le mode acoustique pulsé peut contrôler la morphologie d'un agrégat, donc, dans ce chapitre nous présentons l'utilisation du mode pulsé comme alternative pour le contrôle et/ou réduir l'acoustic streaming quand on ajuste ses paramètres : nombre des pulses et le temps de répétition. Notre objectif est démontrer la capacité de manipuler les particules de taille plus petit à 1μm.

L'acoustic streaming est un flux de fluide stable, produite par l'atténuation visqueuse de haute amplitude des ondes acoustiques. Le streaming varie fortement en fonction du mécanisme d'atténuation de l'onde acoustique, la diffusion en continu la vitesse [3], l'échelle de longueur et la géométrie du résonateur [37].

L'acoustic streaming (AS), est présent lors que la force de radiation primaire **PRF** est généré par USW. Les forces impliquées dans AS sont très petites par rapport à **PRF**. Généralement voilé par les flux principaux ou négligé lorsque les espèces de taille micrométrique sont manipulés [4]. Quand la suspension est composée de particules inférieures au 1μm, l'AS devient visible ; les espèces sont concentrés à la proximité du nœud pour générer un profil de concentration en équilibre. La vitesse du streaming peut varier de dizaimes à des centaines de μm/s [63, 64], suffisamment élevée pour faire bouger les particules.

[3] La vitesse de l'acoustique streaming diminue si la viscosité du fluide augmente et augmente en fonction d'un augmentation de la fréquence et l'amplitude de l'onde.

[4] manipulation est la génération des déplacements relatifs entre les particules et le fluide environnant sous l'action de forces de radiation acoustique afin d'inciter les séparations, l'agrégation ou d'autres processus de transport.

Différences entre les modes acoustiques employées sur l'AS

Normalement, quand le mode continu est utilisé, les particules de 883nm vont vers le nœud de l'onde acoustique, mais dans le plan de lévitation. Elles forment une nappe de quelques micromètres d'épaiseur. Ensuite, il y a la récirculation entre les particules de la couche supérieur et inférieur de la nappe. Par contre, quand on allume les ultrasons en mode pulsé, les particules forment une nappe, mais il n'a pas de formation de vortex. Les particules sont en lévitation.

Dans un résonateur rectangulaire (Figure 3.3), on a fait des expériences en mode continu et mode pulsé : en mode continu on a réduit l'amplitude de l'onde acoustique et en mode pulsé, on a varié le temps de répetition et le nombre des pulses Tp et Tt pour particules fluorescentes de 883nm. Les paramèters du mode pulsé Tp et Tt, peuvent contrôler la morphologie des agrégats (2D ou 3D). Dans ce chapitre on considère le paramètre Duty cycle comme la normalization d'un cycle total on-off : $Tp + Tt$ et Duty cycle $= Tp/(Tp + Tt)$. Donc, si l'acoustic est éteinte, Duty cycle $= 0$, autrement en mode continu Duty cycle $= 1$. Les détails de l'expérience sont dans l'article à voir dans l'anexe D. Chaque expérience on l'a enregistré et mésuré la vitesse du streaming avec le software Tracking.

Pour comparer les vitesses obtenues dans les deux modes acoustiques, nous avons trouvé une rélation qui permet faire ce comparaison :

$$\frac{\vec{v}_s}{\vec{v}_{s,max}} = \frac{E_{ac}}{E_{ac,max}} = \left(\frac{Vp - p}{V_{p-p,max}}\right)^2 . \tag{9.3}$$

La vitesse du streaming obtenue pour les deux modes acoustiques est représentée dans la Figure 9.7. En mode continu, au voltage maximale appliquée la vitesse du streaming moyenne est $\vec{v}_{s,max} = 15\mu$m/s. En mode pulsé, la modification de Tp et Tt a donné des vitesses plus petites que les obtenues en mode continu ; un Duty cycle minimum dont les particules peuvent atteindre une vitesse AS de 2,5 μm/ s. Comme on s'y attendait en mode continu, plus l'amplitude de l'onde acoustique est élevée, plus la vitesse du streaming augmente. Cependant, la courbe qui doit être linéaire selon les hypothèses formulées avant, est assez proche d'une loi de puissance.

La différence entre le comportement des particules en mode continu et en mode pulsé, montre que la même vitesse de streaming en continu est produit en mode pulsé malgre une mineur énergie acoustique. Moins d'énergie acoustique implique également moins de dissipation thermique qui est un bon avantage quand le transducteur doit être appliqué pendant longues périodes. Ce résultat indique que le mode pulsé peut être un moyen efficace pour appliquer des ultrasons dans les résonateurs. Nous avons constaté que l'énergie acoustique peut être déterminée et contrôlée à l'aide du mode acoustique pulsé.

Seuil de l'acoustic streaming

Les paramètres du mode pulsé peuvent être utilisés pour réduir la vitesse du streaming jusqu'àu minimum, comme on peut voir dans la Figure 6.4, dont on peut identifier les régions où il y a et il y n'a pas de streaming.

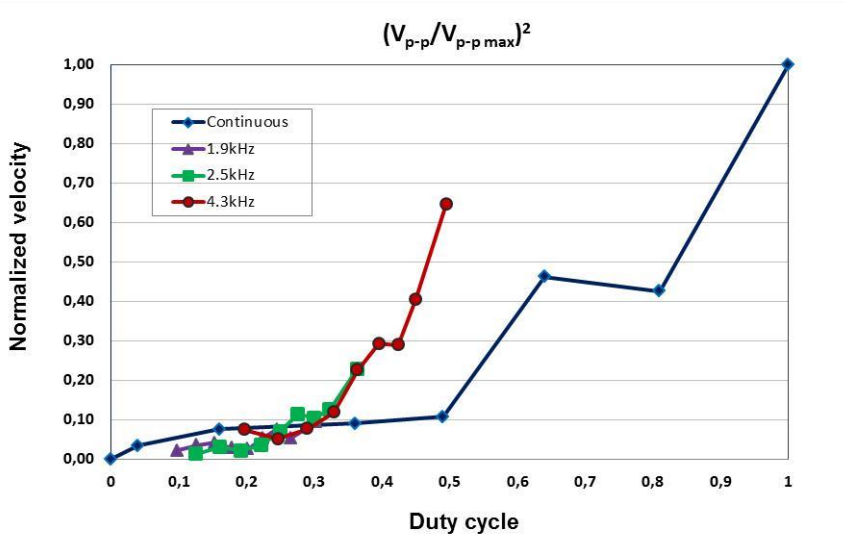

FIGURE 9.7 Vitesse de l'acoustic streaming normalisé en mode continu et mode pulsé pour particules de 883nm. En mode continu cette vitesse a été mésuré par la réduction de l'amplitude de l'onde acoustique et sous mode pulsé par la modification du nombre des pulses si on mantient le temps de répetition constant. Quand le système est éteint, il y a des courrant rémanantes comment des éffects thermiques et le mouvement Brownien dont les particules peuvent atteindre une vitesse de 2.14 μm/s qui a été soustrait des toutes les valeurs obtenues. Cet valeur est plus grand que la vitesse characteristique du mouvement Brownien 1μm/s, obtenu pour le calcule du coeficient de diffusion $D = (kT/3\pi nl)$ approx., $5.5^9 cm^2/s$, où d= 800nm, k c'est la constante de Boltzmann, T est la temperature absolute et la longueur de diffusion length l en le temps t=1s donné par $l = (2Dt)^1/2$ approx., 1μm.

On a déterminé le seuil de l'acoustic streaming quand'on a modifié des paramètres tels que : la taille des particules (500nm, 883nm, 1μm et 3μm) et la forme du résonateur (ovale, circulaire et carré) et on a vu l'influence de l'AS dans chaque paramètres. Les résultats ont permis de démontrer des nouvelles perspectives pour la manipulation des colloïdes par ondes ultrasonores stationnaires .

Mode pulsé et les forces de radiation acoustiques

Cependant, la réduction de l'acoustic streaming par le mode pulsé, ne signifie pas la réduction des forces primaire et secondaire. Expériences ont été faites en ces modes acoustiques pour un mélange des particules de 15μm et 883nm.

Sous le mode continu, les gros particules levitent et s'agrégent et les petites particules une fois dans le plan de lévitation sont influencés par l'acoustic streaming et on peut voir que petit à petit quelques unes arrivent à la péripherie de l'agrégat. Contrairement au mode continu, en mode pulsé les grosses particules atteignent lentement le plan de lévitation. Les petites particules agissent immédiatement à l'acoustique mais prennent plus de temps pour atteindre le plan de lévitation. Bien que les petites particules sont dans le plan de lévitation, elles ne sont pas pris par l'acoustic streaming comme le montre les Figures 6.7 a et 6.7 b, dont l'agrégat est entouré par un nuage de petites particules.

On a effectué des expériences similaires en mode continu par réduction de l'amplitude. Cependant, ce ne pas possible de contrôler l'acoustic streaming non plus la capacité de focalisation des particules (couche).

Chapitre 7 : Aplications pour les bacteries et des micro cylindres métaliques

Nous avons démontré la capacité de nos résonateurs à manipuler des particules et des cellules. D'autres applications potentielles telles que les organismes comme les bactéries et particules inertes comme des micro cylindres métalliques, pourrait être intéressante.

Bactérie

Pour les bactéries, une nouvelle application de cette méthodologie peut produire en peu de temps (à peu près en secondes) d'un film de bactéries que dans d'autres conditions nécessiterai des heures, des jours ou jusqu'à des semaines pour se former.

En outre, on observe que la production du film en acoustique est liée à la durée d'application de l'acoustique et de la mobilité des bactéries. Les forces transversal et secondaire aident avec le contact entre bactéries menant la génération du film. En mesurant l'épaisseur du film (avec l'aide du microscope), nous avons obtenu une structure de quelques micromètres d'épaisseur.

La formation du film a été ésayé dans le temps pour les modes continu et pulsé. Dans les deux modes acoustiques nous avons pu observer le changement dans les bactéries film concentration-activité pour établir la configuration comme on peut voir dans la Figure 9.8. En mode pulsé avec un nombre de pulses de 250 et 1 kHz comme fréquence de répétition. Nous obtenons le même comportement que dans le mode continu, où le processus dure au moins 10 minutes.

Il existe une zone de concentration, où le film se consolide et il y a une réduction de l'activité entre bactéries, ce qui génère une zone solide-élastique :

- Forte activité et également une zone stable à faible concentration est formé où le mouvement des bactéries est aléatoire et rapide. Dans cette zone stable, les bactéries semblent en interaction formant en quelque sorte une phase de type liquide.

- Le film est formée par une troisième zone où la concentration est faible et que les bactéries ne semblent pas en interaction. Cette zone est la phase comme gaz.

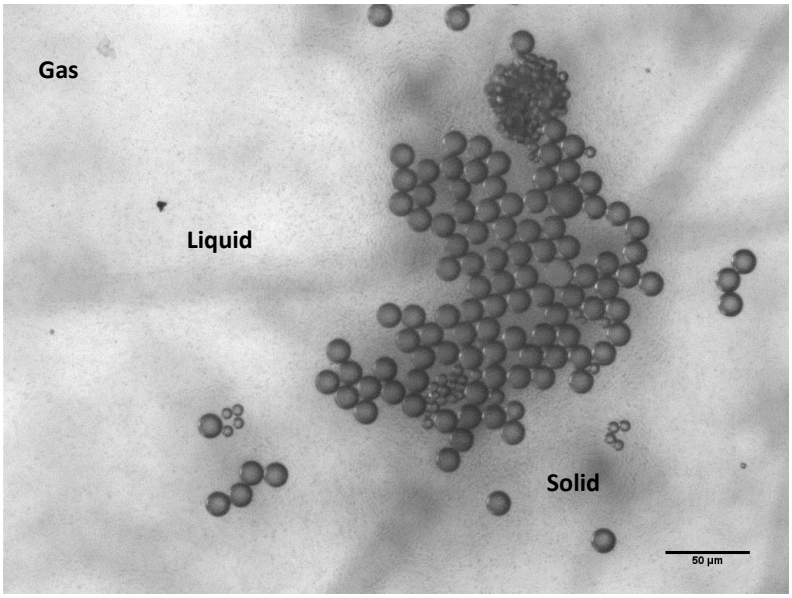

FIGURE 9.8 Configuration du film. Scale bar=50μm.

Micro cylindres métalliques

Normalement, les micro cylindres métalliques agissent comme micromoteurs autonomes dont ils ont un comportement biomimétique qui comprend le transport, la chimiotaxis, et les interactions prédateur-proie. Cependant, leur mouvement autonome dans des environnements biologiques repose sur l'utilisation de peroxyde d'hydrogène (H_2O_2) et de l'hydrazine, substracts toxiques (en tant que combustible), ce qui difficulte leur utilisation dans des systèmes biologiques. Autres stratégies de mouvement autonome comprend l'utilisation de champs électriques et magnétiques externes pour conduire les micro-objets dans les milieux biologiques où le mouvement résultant n'est pas autonome. Les micro cylindres métalliques sont également fluides actifs. Leur mouvement est hyper diffusive en peroxyde d'hydrogène, biomimétique comme des bactéries [71]. En raison de leur densité élevé, ils sont également à proximité des parois du récipient. Les micro cylindres métalliques sont faites d'un composant métallique unique (Au, Ru ou Pt) ou axialement segmentées (AuRu), typiquement de 1 à 3 μm de longueur et de 300 nm de diamètre, comme est représenté sur la Figure 7.6.

Sans acoustique, les micro cylindres décrivent le mouvement brownien. Lorsque l' acoustique est allumé, les cylindres vont vers le plan de lévitation et sont pris par l'acoustic streaming qui les conduisent à l'agrégation et à la formation de motifs. Cependant, on observe la rotation des micro cylindres (à leur axe), et l'axe des aiguilles formées, respectivement comme est illustré sur la Figure 7.7 a. Les tourbillons générés par les aiguilles métalliques conduisent à un auto-assemblage dans motifs en forme des chaînes (figures 7.7 a et 7.7 d). Les aiguilles métalliques ont montré un mouvement directionnel axial (figure 7.7 b) avec des vitesses aussi élevées que $\sim 200\mu$m/ s.

La Figure 9.9 montre les interactions d'auto-assemblage de chaînes formées par les aiguilles métalliques. Chaque clindre (fait du metal polaire) points dans la même direction de sorte que la chaîne a une estructure tel que la direction est : AuRu| AuRu|... AuRu. Cet ensemble tête-à-queue n'est pas particulièrement surprenant étant donné que les aiguilles

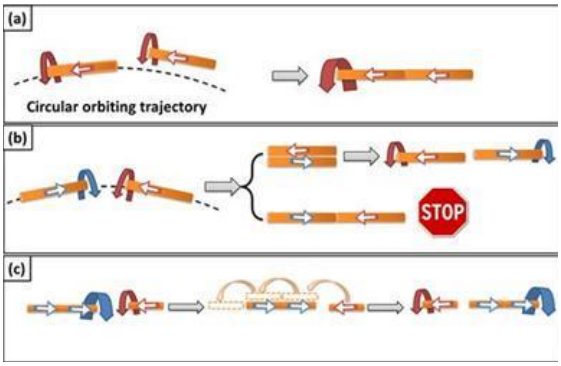

FIGURE 9.9 Illustration de l'assemblage des aiguilles et le mouvement directionel des cylindres métalliques : (a) deux cylindres métalliques qui se déplacent dans la même direction interagissent avec autres et forment un binôme (doublet). (b) Deux cylindres métalliques se déplacent dans des directions opposées, soit brosse contre l'autre ou se rencontrer l'un l'autre en tête-à-tête.

bimétalliques se déplacent toujours avec la même extrémité avant (par exemple à l'extrémité des aiguilles pour Ru AuRu), et seulement se peuvent aligner du même sens. Ces aiguilles se déplacent en directions opposées et par la suite, se croisent sans coalescence en une seule chaîne.

Nous avons démontré que les ondes acoustiques de fréquences de MHz peuvent propulser, aligner, tourner micro cylindres catalytiques et former aiguilles métalliques dans l'eau. Des expériences de contrôle avec des particules polymèriques et des sphères de métal viennent étayer l' hypothèse selon laquelle la forme et le matérial jouent un rôle critique dans la trajectoire et la génération des aiguilles solides, alignées au long de l'axe des cylindres métalliques.

Des observations avec des micro cylindres métalliques mono et bimétalliques, indique la probable influence de l'asymétrie de sa forme en particulier la courbure au niveau de ces extrémités qui entraîne le mouvement directionnel, mécanisme que nous avons nommé self-acoustophorèse. L' importance de cette découverte réside dans la possibilité de contrôler les micro cylindres métalliques dans des environnements biologiques en utilisant des ultrasons.

Chapitre 8 : Perspectives

Lors des aplications que nous avons trouvé dans nos résonateurs, nombreaux expériments nous permet d'envisager d'autres applications comment ce le cas pour des liposomes, autres cellules et pour l'utilisation des cylindres métalliques pour faire la delibrance des medicaments avec des ultrasons, comme une manière sans contact et non invasive.

Un gran spectrum des applications avec des cellules nous offre le caracter no toxique, no invasive des ultrasons et des fréquences que nous utilisons. Applications avec macrophages infectés avec malaria, et du génie tissulaire. french

Chapter 10

Conclusions

- One of the main apports of this work is the introduction of pulse mode acoustic for controlling the aggregation process and the acoustic streaming. The 2D or 3D structures could be controlled by using pulse mode acoustics.
- Acoustic streaming has been highly reduced open up the possibility of manipulating sub-micron sized particles (liposomes, cell organels, and colloids).
- For the first time, we determined experimentally the secondary Bjerknes forces for particles and we set-up a technique for that. Also, we determined Bjerknes force in microgravity where we observe the possibility of manipulating by acoustics particulate materials in weightlessness conditions, as analog of artificial gravity.
- We discovered self-acoustophoresis for micro rods manipulation open up the possibility to drug delivering by non invasive methods.
- By manipulating *E. coli* bacteria in our devices, we could form a film-like structures in acoustic levitation.
- Perspectives in liposomes, cell manipulation, drug delivering and tissue engineering are readily open.

Appendix A

Controlled Cell Aggregation in a Pulsed Acoustic Field

Ultrasonics 52 (2012) 842–850

Contents lists available at SciVerse ScienceDirect

Ultrasonics

journal homepage: www.elsevier.com/locate/ultras

Controlled cell aggregation in a pulsed acoustic field

Despina Bazou [a,b,1], Angélica Castro [c], Mauricio Hoyos [c,*]

[a] Centre for Research on Adaptive Nanostructures and Nanodevices (CRANN), Trinity College, Dublin, Ireland
[b] School of Pharmacy and Pharmaceutical Sciences, Trinity College, Dublin, Ireland
[c] Laboratoire de Physique et Mécanique des Milieux Hétérogènes, Ecole Supérieure de Physique et Chimie Industrielles, Paris, France

ARTICLE INFO

Article history:
Received 7 October 2011
Received in revised form 16 January 2012
Accepted 16 January 2012
Available online 3 March 2012

Keywords:
Aggregation
Pulsed ultrasounds
Standing waves
Cells
Particles

ABSTRACT

Cell aggregation in ultrasonic resonators can be obtained in a few seconds. Hundreds even thousands of cells can be levitated in suspension and generate 2D or 3D aggregates. Nevertheless, the aggregation rate and the 2D or 3D configurations of the resultant aggregates are very difficult to control. This work reports on a novel way of generating and controlling particle and cell aggregates using pulsed ultrasound. This technique specifically explores (in addition to the ultrasound wave, frequency and amplitude) the time of ultrasound application, i.e. the number of pulses as well as the pulse repetition frequency. We demonstrate that with pulsed ultrasound, particles and/or cells levitate in suspension, as with continuous ultrasound, and the aggregation rate can be modified in a controlled manner. By carefully tuning the number of pulses and the repetition frequency, the 3-D and 2-D configurations of the aggregates can be selectively generated. In addition, pulsed ultrasound limits transducer heating, thus allowing for higher acoustic energies than those currently employed with continuous ultrasound.

© 2012 Elsevier B.V. All rights reserved.

1. Introduction

Cell manipulation techniques are important in many areas of research including cell biology, molecular genetics, biotechnological production, clinical diagnostics and therapeutics. Physical methods of manipulating suspended cells at single-particle microscopic resolution include hydrodynamic [1], optical [2,3], dielectrophoretic [4,5], magnetic [6,7] and ultrasonic [8–10] cell trapping.

Of the above-mentioned methods, ultrasound trapping has been less extensively exploited. Compared to other methods, ultrasonic cell manipulation is an inexpensive non-contact technique that allows simultaneous and synchronous manipulation of a large number of cells in a very short time [8]. It is simple in both set-up and operation, and is non-invasive, chemically inert (non-toxic) and physically non-destructive [11]. Taking into account its high efficiency and reliability and the fact that it can be used with the majority of cell types, this technique holds great promise in cell manipulation techniques for a variety of applications.

We have previously reported [8] on an ultrasound standing wave trap (USWT) capable of holding >10,000 cells at the focal plane of a microscope. The USWT is an ultrasound resonator where the acoustic path-length in the cell suspension is a single half wavelength. The resonator has a pressure node plane half way through the cell suspension and parallel to the transducer [8,12]. The cell trap exploits the fact that cells experience an axial direct acoustic radiation force when in an ultrasound standing wave field [8,12]. This force drives them towards a node plane. They then move, within that plane, to accumulate at the centre of the field, i.e. at the nodal plane [13]. The USWT has been used to synchronously and rapidly (within 10 s of seconds) form and levitate 2-D [8,12,13] and 3-D [14,15] cell aggregates in suspension away from the influence of solid substrata. At low cell concentrations ($\leqslant 5 \times 10^5$/ml), aggregates are 2-D, while at concentrations of $\geqslant 10^6$/ml, 3-D aggregates are generated [15]. This presents a relatively narrow particle/cell concentration margin over which 2-D aggregates can be formed. While, undoubtedly 3-D aggregates are more tissue-mimetic, there is still great interest in the 2-D form of the aggregate as this facilitates light microscope resolution of the interaction processes occurring between cells.

Here, we present a novel approach to form and levitate 2-D particle and cell aggregates in the USWT using pulsed ultrasound. Our results show that introducing pulses of ultrasound (as opposed to continuous ultrasound) provides a more controlled aggregation mechanism, allowing for the formation of 2-D versus 3-D aggregates as per experimental requirements.

2. Materials and methods

2.1. Ultrasound trap

The in-house constructed trap employed in the present work (Fig. 1) had four layers; a transducer (PZ26 Ferroperm, Kvistgard,

* Corresponding author.
E-mail address: hoyos@pmmh.espci.fr (M. Hoyos).
[1] Present address: Edwin L. Steele Lab, Harvard Medical School and Massachusetts General Hospital, Charlestown, Boston, USA.

0041-624X/$ - see front matter © 2012 Elsevier B.V. All rights reserved.
http://dx.doi.org/10.1016/j.ultras.2012.01.005

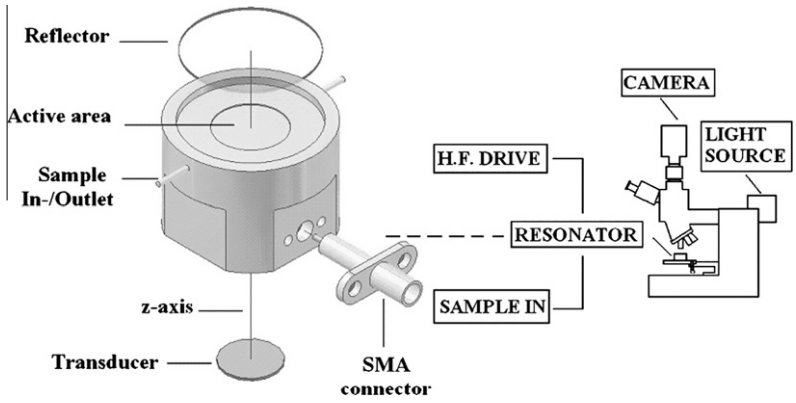

Fig. 1. Schematic diagram of the ultrasound trap, epi-microscope, sample loading and ultrasound generation.

Denmark) nominally resonant in the thickness mode at 3 MHz and mounted in a radially symmetric housing, a steel layer coupling the ultrasound to a one half wavelength ($\lambda/2$ or 0.25 mm depth, where λ is the wavelength of sound in water at 3 MHz) aqueous layer and a quartz acoustic reflector that provided optical access from above [8]. The outer diameter of the cylindrical steel body was 35 mm. The 'sample-containing' active area had a diameter of 18 mm. The disk transducer (12 mm diameter) was driven at 2.13 MHz. We note that the nominal resonance frequency of the transducer (3 MHz) is different than the nominal resonance frequency of the resonator (2.13 MHz) due to the steel-coupling layer. Its back electrode was etched to a 6 mm diameter circle so as to give a single central aggregate in a single half-wavelength chamber. The quartz glass acoustic reflector had a thickness of 0.5 mm ($\lambda/4$) so as to locate the single pressure node plane half way through the sample volume. The piezoceramic transducer was driven by a 100 MHz dual channel arbitrary wave generator (5062 Tabor Electronics, Israel) and the signal was amplified by a dual differential wide band 100 MHz amplifier (9250 Tabor Electronics, Israel). The signal was visualized with a digital storage oscilloscope (IDS 8064 60 MHz ISOTECh, Hanan–Israel). In experiments with continuous and pulsed ultrasound, amplitudes of 5–15 $V_{p\text{-}p}$ were employed, the number of pulses varied between 25 and 250 and the pulse repetition frequency from 1 to 5 kHz.

2.2. Optical system

A fast, high-resolution XM10 (Soft Imaging System, SIS, GmbH) mounted on an Olympus BX51 M reflection epi-fluorescence microscope allowed observation in the direction of sound propagation (negative z-axis). Images were captured by a standard PC equipped with the Cell-D image acquisition and processing software (Soft Imaging System, SIS, GmbH).

2.3. Polystyrene latex beads suspensions

We used 15 and 10 μm diameter polystyrene latex particles (density 1056 kg/m^3) supplied as a 10% suspension of solids by Micromod (Rostock, Germany). Aliquots were diluted here to 20 ml to give about 0.11% solids in deionized water.

2.4. Cell culture

Caco2 (human epithelial colorectal adenocarcinoma) cells were a kind gift of Prof. M Radomski (School of Pharmacy and Pharmaceutical Sciences, Trinity College Dublin, Ireland). Cells were maintained as a replicative culture at 37 °C under an atmosphere of 95% air and 5% CO_2. Caco2 cells were cultured in Modified Eagle Medium (MEM) supplemented with 100 μg/ml penicillin-streptomycin solution, 0.05 g/l sodium pyruvate and 10% foetal calf serum (FCS). At confluence, cells were treated with Trypsin/EDTA solution (1×), for 10 min to release cells from the culture flask surface. Cells were filtered through a 40 μm Nitex cell strainer (FALCON) to ensure a single cell suspension. Cells were then pelleted by centrifugation at 2000 rpm for 5 min, resuspended in fresh serum-free MEM medium (containing all of the aforementioned supplements), counted and finally diluted to concentrations of 5×10^5/ml and 3×10^6/ml.

2.5. Experimental procedure

A Gilson minipuls3 peristaltic pump (Gilson, Inc. Middleton, USA) was used to pump the sample into the USWT. The microscope was pre-focused on the central plane of the trap at the axial region. The pump was switched off and the ultrasound exposure was immediately initiated. The aggregation process was observed using 5x, 10x and 20x objectives.

2.6. Measurements of the aggregate area

Measurements of the cell and particle aggregate areas were carried out using the Cell P (Soft Imaging System, SIS, GmbH) and Image J image processing softwares respectively. Films at a rate of 24 images/s were recorded, and the area of the aggregate was determined using the free-hand software tool; the contour of the aggregate was delineated at different times during the aggregation process and the aggregate area (in pixels) was automatically calculated. The normalized aggregate area was quantified by dividing the aggregate area at specific time points during the aggregation process over the aggregate area when the aggregate growth was complete i.e. when no single particles or cells were joining the already formed aggregate (still some particles remained at a distance from the central aggregate without moving or moving at extremely low velocities). Finally, the aggregation rate was estimated by measuring the area growth over time for each aggregate.

3. Theoretical background

3.1. Acoustic forces

Forces acting on particles in an acoustic resonator have been studied under different conditions and for different goals. The origin of acoustic forces generated by ultrasonic standing waves has been extensively exploited [16–20]. Depending on the experimental conditions, some of those forces can be generated and quantified. The most studied acoustic force is the PRF (primary radiation force), which is the force generated by an ultrasonic

standing wave occurring between the walls of a resonator [19–21]. In the case of a closed fluid-filled chamber, resonance is obtained when its thickness is equal to: $w = N\lambda/2$ where N is the number of nodes in the chamber and λ is the ultrasound wavelength. The acoustic force F_{ac} drives particles towards the nodes or antinodes depending on their acoustic properties. $F_{ac} = Vk\tilde{A}\,\langle E_{ac}\rangle \sin(2kx)$, where V is the particle volume, $k = 2\pi/\lambda$ is the wave number, $\tilde{A} = [3(\rho_p - \rho_f)/(2\rho_p + \rho_f) - \left(c_p^2\rho_p/c_f^2\rho f\right)]$ is the acoustic contrast factor, where c_p and c_f are the sound speeds of the particles and the fluid respectively, and $\langle E_{ac}\rangle$ is the average acoustic energy density [17,18]. It is well known that the PRF appears as a second order of the Navier–Stokes equation [18,24,25]. The order of magnitude of the acoustic force is really low ($\sim 10^{-9}$ N) but high enough for influencing micron sized particles [26–28], cells [12], lipids [29] or even bacteria [28].

A number of other primary and secondary acoustic forces have also been described, namely: the primary and secondary Bjerknes forces [19,20,22,23], the secondary interparticle force [21] and the force generated by the transversal component of the PRF [19]; the latter is considered to be the force influencing the aggregation process. Several reports have demonstrated that all of the forces mentioned above are at least two orders of magnitude smaller than the axial component of the primary force [20,30,31]. Nevertheless, when particles reach the nodal plane the axial net force is zero, thus unveiling the transversal forces leading to the initiation of aggregation.

The transversal migration of particles in the nodal plane is due to a complex coupling between forces generated by the non-homogeneity energy field distribution in the chamber and the transversal PRF originated by the imperfections of the resonator (for instance, the parallelism of the resonator walls and the lateral walls vibrations). The particle transversal force is therefore difficult to predict; nevertheless, by measuring the particle transversal velocity we can estimate the mean transversal force F_{Tr}, by considering that it is balanced by the Stokes' force F_s, such that: $F_{Tr} - F_s = 0$, where $F_s = 3\pi\eta\, d\, v_{Tr}$, with d being the particle diameter, η the dynamic viscosity and v_{Tr} the transversal velocity at the levitation plane. The complexity of the interactions of those forces makes the aggregation process difficult to control. It has been reported [15] that 2-D or 3-D aggregate configurations can be controlled by the initial concentration of cells, however in the current study we shall demonstrate that pulsed ultrasound introduces new control parameters.

3.2. Controlling the aggregation process

The aggregation process starts when isolated particles in levitation converge towards a specific point, where the acoustic energy is maximal. In order to generate the transversal migration, the resonance frequency must be carefully tuned. In our resonator, levitation of cancer cells was obtained at all frequencies in the range of 2.1 and 2.4 MHz but the optimal aggregation started when the frequency was 2.13 MHz, at which frequency, the aggregation process occurred very fast. On the other hand, when the frequency was close but not at the optimal resonance frequency, several small aggregates were formed at different positions in the levitation plane. For instance, for cancer cells, operated at the aggregation frequency (2.13 MHz) and at 10 V_{p-p} amplitude, within 10 s the aggregate reached its maximum size, as we will demonstrate in the experimental section below. The resonance is thus very specific for every resonator. We also clarify that there is no detectable increase in the resonator temperature over 1 h of continuous ultrasound exposure that could result in a change in the resonance frequency, as previously shown by Bazou et al. [8].

One way of controlling the aggregation velocity is by tuning the resonance frequency. However, in this case, particle velocities change rapidly at resonance, resulting in poor reproducibility and a wide range of stable velocities. The second parameter that could be used for controlling the aggregation is the force amplitude indicated by the transducer voltage. We have observed that by varying the amplitude, all the acoustic forces are modified but not in the same extent. We observed that it is difficult and challenging to predict and establish the relationship between the modified amplitude and the resultant aggregation velocity; this aspect will be illustrated in the discussion.

3.3. Pulsed ultrasound and aggregation

Pulsed ultrasound in the range of 0.1–10 MHz is used in several applications only with progressive waves [32–35], while working in pulsed regime with standing waves remains very rare or never done. Our experimental approach of pulsed ultrasound consists of generating groups of pulses (one pulse is one period) at a certain repetition frequency (Fig. 2). For instance, at 2 MHz, one pulse lasts for 500 ns; we typically use 100 periods, lasting t_{on} = 0.5 ms, separated by t_{off} = 1 ms repetition time. This means that for one experiment lasting 1 min, each *on-off* cycle lasts t_{cycle} = 1.05 ms, leading to 57,143 *on-off* cycles during the experiment. The total time at which the force is *on* will then be ~2.86 s, i.e. ~5% of the total time. For reasons of clarity, we introduce a parameter, the *pulse mode factor* $P_{mf} = t_{on}/t_{cycle}$. For the conditions reported above P_{mf} = 0.05.

In order to apply pulsed ultrasound in our resonator we had to consider the number of pulses needed for establishing a standing wave. Thus, for a parallel-plate resonator filled with distilled water, an ultrasound pulse has to cross the 250 μm thickness of the resonator at a sound speed of around 1500 m/s. The time needed for a wave to be reflected is $t_s \sim 330$ ns, therefore, with a few pulses a standing wave is generated. Several parameters also need to be taken into consideration when employing pulsed ultrasound for particle and cell aggregation: *(i) The number of pulses* should be high enough for generating a standing wave which lasts sufficiently for particles and cells to reach their terminal velocity. The terminal velocity is given by the well known relationship: $u(t) = u_0[1 - \exp(-t/\tau)]$ where u_0 is the terminal velocity, and τ is the relaxation time obtained by solving the equation of motion: $F_{Tr} + F_s = \rho_p V\, du/dt$. The value of the acoustic force F_{Tr} is unknown and there is no relationship that includes the complex coupling between the transversal acoustic forces implied in the aggregation process. We can estimate the relaxation time if we consider that F_{Tr} is two orders of magnitude smaller than the PRF as mentioned before. Nevertheless, as a theoretical study of the acoustic forces in a resonator is beyond the scope of this study, the relaxation time can be estimated by solving the motion equation for the ratio $[u(t)/u_0]$ that does not depend on the field force. Thus, the relaxation time is given by: $\tau = \rho_p\, d^2/18\eta$. For 10 μm latex particles, ρ_p = 1.05 g/cm^{3}and $\tau \sim 300$ ns to compare to 500 ns of an ultrasonic period. The same analysis and a similar result can be

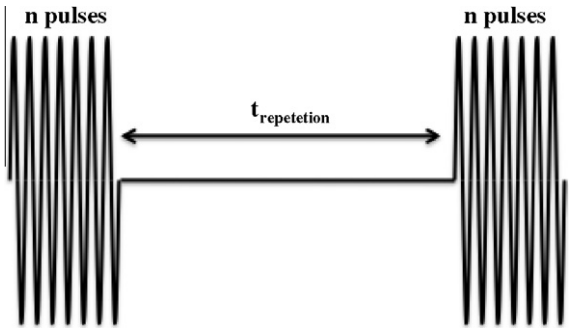

Fig. 2. Pulsed ultrasound technique, n pulses of time 1/frequency, separated by a repetition time.

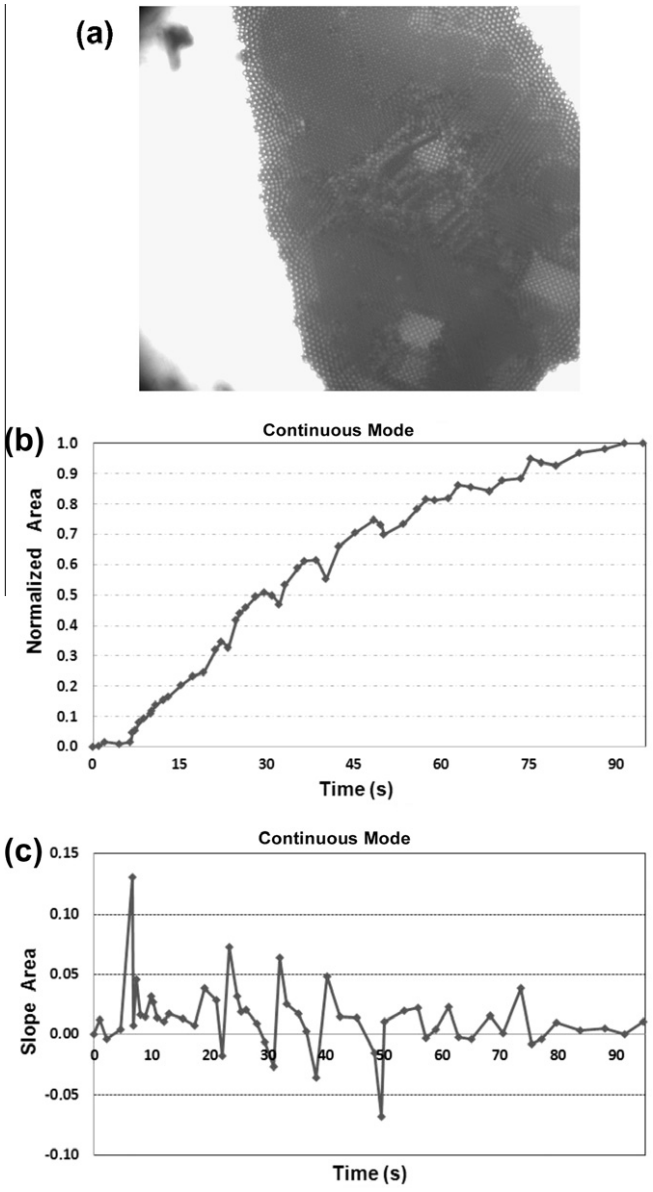

Fig. 3. (a) Aggregate (3-D) of 15 μm latex particles produced in continuous mode of operation. Normalized aggregate, (b) area and (c) rate vs. time in continuous mode.

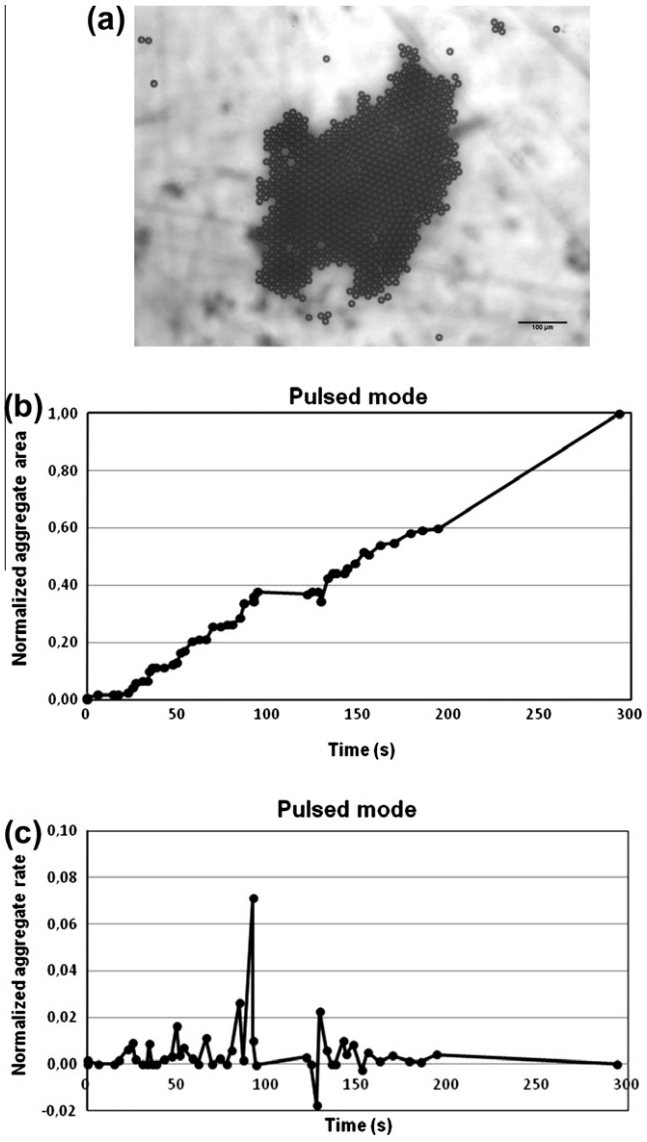

Fig. 4. (a) Aggregate (2-D) of 15 μm latex particles produced in pulsed mode at 250 pulses and repetition frequency 5 kHz. Normalized aggregate, (b) area and (c) rate vs time.

employed to estimate the time needed for a particle having an initial velocity u_0 to stop after the field force is switched off. Therefore, we can neglect the relaxation time when a minimum of 10 pulses is emitted, thereby reducing transient and retardation effects. We shall then consider that when the acoustic field is on, particles immediately move with a constant velocity, whereas when the acoustic field is off, particles instantly stop traveling. *(ii)The pulse repetition frequency* should be as well high enough in order to prevent particle sedimentation and to maintain particles or cells at the nodal plane. We shall consider the limit of the allowed settling distance as one particle radius. For example, a 10 μm latex particle has a sedimentation velocity $u_0 \sim 3$ μm/s, thus the repetition frequency should not be less than 0.6 Hz. Nevertheless, it is known that the sedimentation of an aggregate of particles is much faster than that of a single particle. We have experimentally determined that the minimum repetition frequency for preventing particle aggregate sedimentation is about 1 kHz. A more sophisticated analysis about the time needed for a particle to sediment could be made by taking into consideration the quality factor (Q-factor) [36]. This factor takes into consideration the energy dissipation and the relaxation time of the bulk. We consider that an in-depth analysis of the Q-factor is beyond the scope of this study as (i) we are interested in the motion of particles with respect to the fluid, and (ii) in pulsed mode, even though the aggregation is slowed down as it is demonstrated in this study, it is not inhibited by insufficient acoustic relaxation related to a low Q-factor.

One of our motivations for employing pulsed ultrasound, other than to control the aggregation process is to avoid transducer heating; a minimum number of pulses fulfill this requirement. In addition, a minimum number of pulses allow us to increase the acoustic force by increasing the voltage, thereby reducing the risk of transducer damage. In turn, the risk of liquid heating is also reduced, keeping the thermodynamic and physicochemical properties of the suspension as stable as possible.

By using pulsed mode ultrasound we can modify the aggregation velocity by controlling the number of pulses and the repetition frequency. In fact, we assume that in continuous mode particles and cells have the maximum transversal velocity at the nodal plane, while in pulsed mode they slow down in a controlled way.

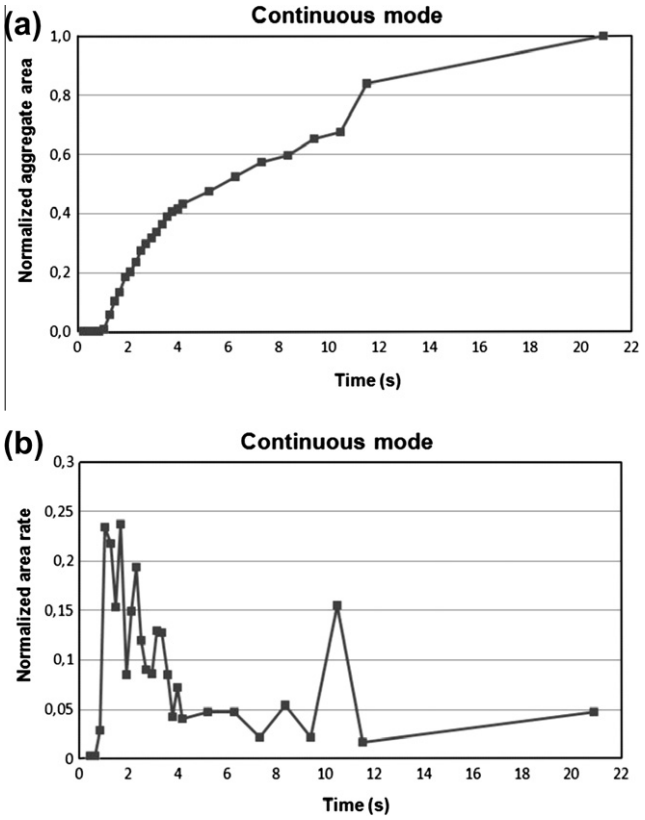

Fig. 5. Normalized aggregate (a) area and (b) rate of 10 μm latex particles vs time in continuous mode.

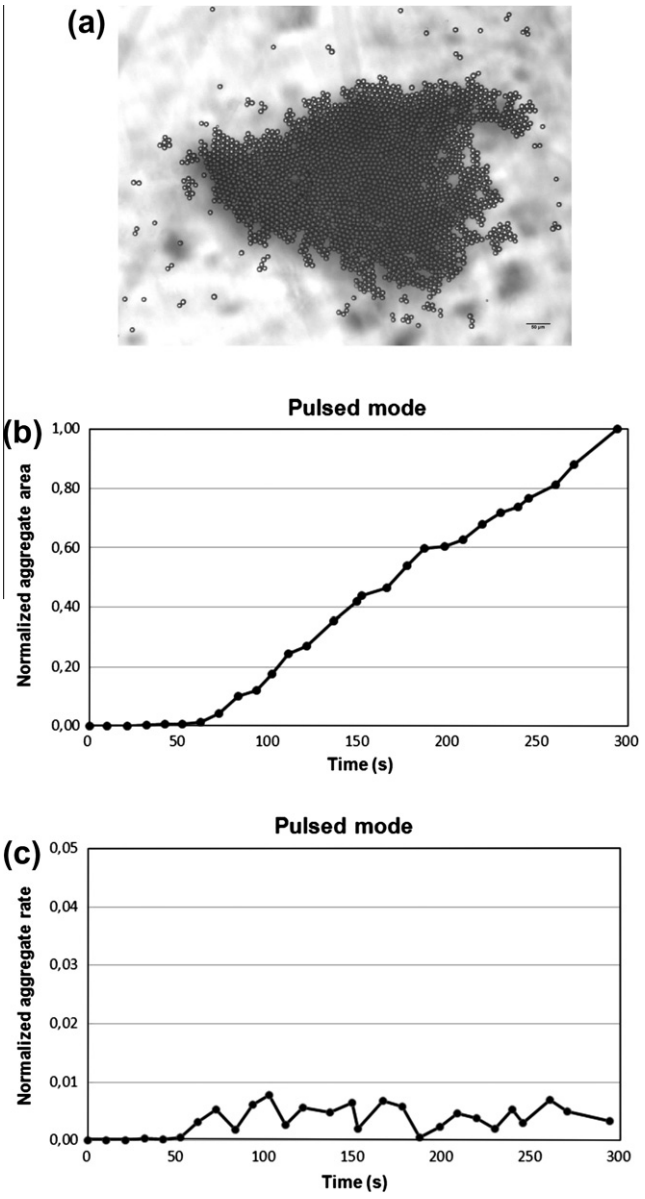

Fig. 6. (a) Aggregate (2-D) of 10 μm latex particles obtained in pulsed mode; 100 pulses and repetition frequency 4 kHz. Normalized aggregate (b) area and (c) rate vs time.

4. Experimental results

4.1. Pulsed acoustic field force

Initially, particles or cells were injected in the resonator where they homogeneously filled the chamber of volume 45 μl. The flow was then stopped, particles settled down and then the acoustic field was turned on. Because the main objective of our study was to introduce a new way of controlling the aggregation process by using pulsed ultrasound, we varied the number of pulses and the repetition frequency while keeping the other parameters constant. The initial experimental conditions were determined, including the aggregation frequency, the transducer voltage and the cell and particle concentration. Even though the optimum resonance frequency was established under continuous operation mode (continuous ultrasound), we considered that in pulsed mode this frequency was also optimal for levitation and aggregation. The transducer vibration has the maximum amplitude at the resonance frequency (the transducer vibration amplitude is a few nm and the vibration velocity a few cm/s) but the energy is not uniformly distributed and has a maximum intensity at the center. The Bernoulli force generated by this effect, as well as by other imperfections of the resonator, acts on particles driving them towards the maximum energy zone, thus leading to the generation of a single aggregate. The fact that in pulsed mode a single aggregate was also observed indicates that the resonance frequency does not change with respect to continuous mode.

In order to estimate the minimum number of pulses needed for maintaining one aggregate in levitation, it is important to distinguish the different properties of latex particles and cells including their sedimentation behavior in an acoustic field. In the case of particles (which are supposed to be only in hydrodynamic interaction), when the acoustic force is switched off, a 2-D or 3-D aggregate composed of tens or hundred of particles formed at the nodal plane, is immediately disrupted and settles down. Hydrodynamic lubrication interactions can keep particles in relatively close contact, therefore sedimentation of the disrupted aggregate occurs much faster than that of a single particle. We have to note that the resonator is a closed system therefore the aggregate is in batch sedimentation. Cell aggregate sedimentation is more unpredictable as cells are not rigid; they have physiological interactions [37,38] and in many cases they are polydisperse. We have observed that when the acoustic force is switched off, a cell aggregate has a very low sedimentation rate, much slower than that of an equivalent aggregate of particles. Furthermore, the cell aggregate does not fall as a consolidated regular shaped body due to cell–cell interactions, but more like a folded sheet.

Our first aim was to find the number of pulses necessary for keeping the aggregate construct unchanged and in levitation. For

10 and 15 μm latex particle aggregates, a minimum of 100 pulses was required, while at lower pulses aggregates disrupted and sediment. Sedimentation was also observed when the repetition frequency was smaller than 1 kHz irrespective of the number of pulses. In addition, 100 pulses were enough for maintaining particles in levitation but not for aggregation. In contrast, when cells were employed, the minimum number of pulses required for aggregation was 50. Even though the exact acoustic energy distribution was not determined, the aggregate shape and maximum size (~2 mm diameter) were highly reproducible. When the aggregate was reaching the maximum size, only a few particles remained at the edges of the resonator and converged very slowly to join the aggregate, but the size was not relevant in our case. In fact, our aim was to demonstrate that pulsed ultrasound generates 2D aggregates, whereas at the same conditions continuous ultrasound generates 3D aggregates. Therefore, in all experiments we aimed at forming aggregates of similar sizes (maximum diameter~2 mm).

4.2. Particle aggregates

We made an estimation of the transversal acoustic force responsible for aggregation, by measuring (using the software: http://www.cabrillo.edu/~dbrown/tracker/) the migration velocity of a particle at the focusing plane in continuous and in pulsed mode at the resonance frequency of 2.13 MHz. In continuous mode, single 10 μm and 15 μm latex particles had average transversal velocities of $u_{Tr10} = 2 \times 10^{-5}$ m/s (at 13.8 V_{p-p}) and $u_{Tr15} = 1.3 \times 10^{-5}$ m/s (at 16 V_{p-p}) respectively. The respective average transversal forces are $F_{Tr} = 1.8 \times 10^{-12}$ N and 2×10^{-11} N; these values are as indicated before, at least two orders of magnitude smaller than the PRF. Fig. 3a shows a 3-D aggregate of 15 μm latex particles formed in continuous mode. The normalized particle aggregate area grows monotonically with time showing area fluctuations (Fig. 3b). The aggregation process was completed in 18 s. Fig. 3c (normalized area growth rate vs time) shows the fluctuations close to zero; the stronger fluctuation appears by 7 s. The resultant aggregate formed is 3-D. When pulsed ultrasound was employed for 15 μm particles, at 250 pulses and 2 kHz repetition frequency, the average particle velocity was $u_{Tr15\ pulsed} \sim 3.5 \times 10^{-6}$ m/s, corresponding to a transversal acoustic force $F_{Tr} \sim 2 \times 10^{-13}$ N; the latter being much smaller than that obtained in continuous mode. A 2-D aggregate was formed (Fig. 4a). The area increased linearly with time (Fig. 4b), and the fluctuations were much smaller than those observed in continuous mode. The normalized area growth rate shows very small fluctuations (close to zero) (Fig. 4c).

3-D and 2-D aggregates of 10 μm latex particles, in continuous mode and in pulsed mode at 100 pulses and 4 kHz repetition frequency were also generated. The particle velocity in pulsed mode was of the order of $u_{Tr10\ pulsed} \sim 4 \times 10^{-6}$ m/s, much smaller than in continuous mode, corresponding to a transversal force $F_{Tr} \sim 4 \times 10^{-13}$ N. We ended the aggregation in pulsed mode after 300 s when the aggregate was about 2 mm in diameter. Fig. 5a and b shows the curves of the normalized growth and the normalized growth rate versus time. Features analogous to those of 15 μm particles are observed. Nevertheless, the normalized area growth in continuous mode (Fig. 5a) showed an initial rapid increase (for the first 4 s), and then decreased to finally becoming linear. The area growth rate fluctuations (Fig. 5b), peaked within one second during the aggregation process, followed by a smooth decrease; these features were more pronounced for 10 μm than for 15 μm particles. In pulsed mode, a 2-D aggregate was obtained (Fig. 6a), the growth rate was linear (Fig. 6b) and the fluctuations of the growth rate were negligible compared to those in continuous mode (Fig 6c).

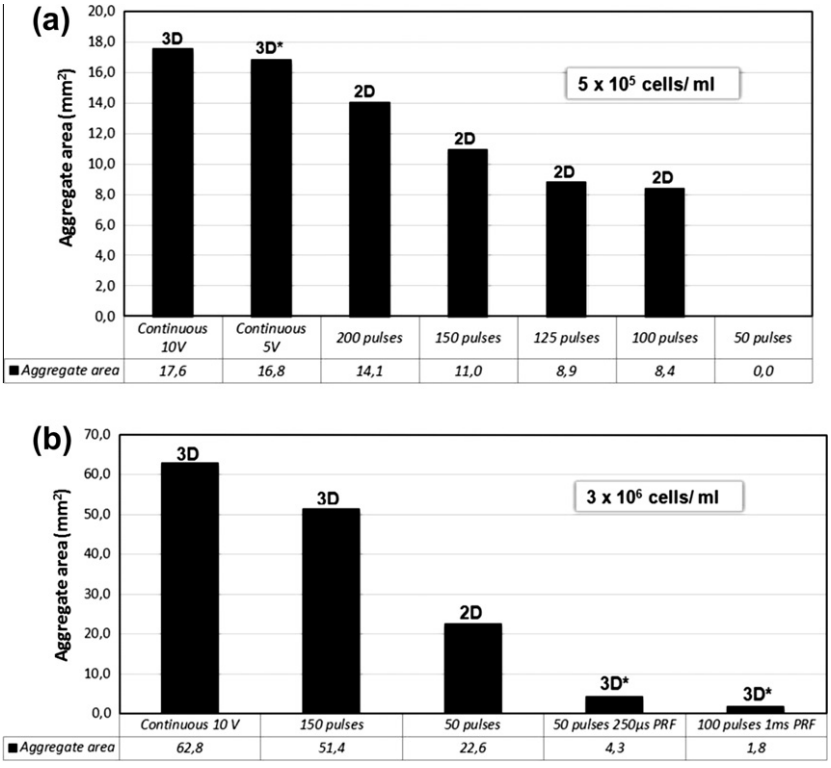

Fig. 7. Cell aggregate area measurements produced at (a) low (5×10^5 cells/ml) and (b) high (3×10^6 cells/ml) cell concentrations in continuous and pulse mode (50–200 pulses). The final cell aggregate architecture (2D vs 3D) and the pulse repetition frequency are also indicated. Asterisks indicate that the aggregate settle down.

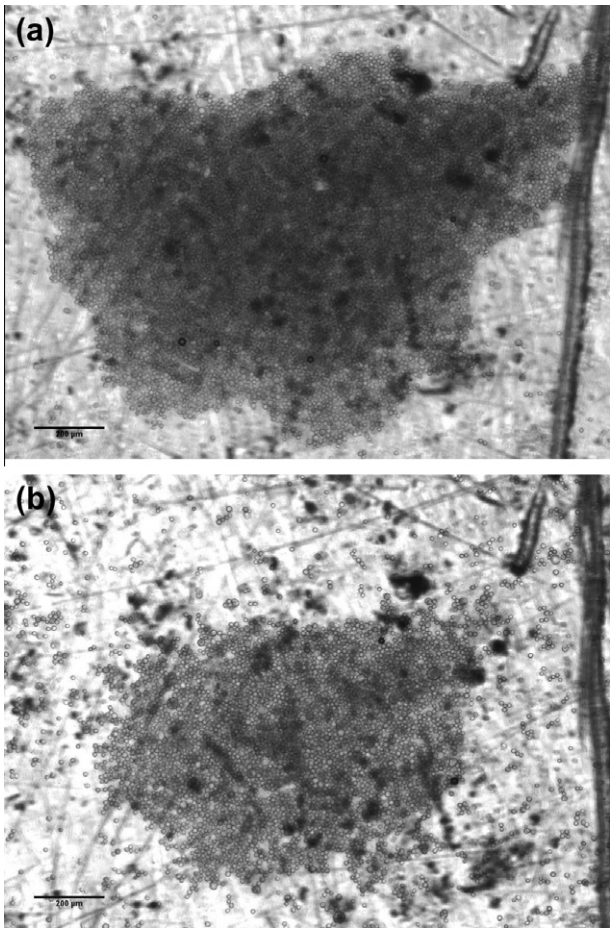

Fig. 8. Representative Caco2 cell aggregates (concentration 3×10^6 cells/ml) produced in (a) continuous and (b) pulsed mode, 50 pulses and repetition frequency 4 MHz.

4.3. Cells aggregates

For cell aggregation, different experimental parameters were varied including the cell concentration, number of pulses, repetition time and voltage. The typical cell size was 20 μm and the typical velocities were 223 μm/s in continuous mode and 147 μm/s in pulsed mode, corresponding to acoustic forces of $\sim 12 \times 10^{-11}$ N and $\sim 5.5 \times 10^{-11}$ N respectively. The histograms in Fig. 7a and b shows all the parameters and the conditions where 3-D and 2-D aggregates were generated. Representative 3-D and 2-D cell aggregates are shown in Fig. 8a and b under continuous and pulsed ultrasound. The results of the growth rate and the growth rate fluctuations are depicted in Fig. 9a and b respectively. In continuous mode, the cell aggregate growth rate followed the same pattern as that for 10 μm particle aggregates; a rapid increase of the area in the first second followed by a linear growth. In contrast, in pulsed mode the growth rate was slower and followed a linear pattern. This holds true for all the pulsed ultrasound conditions used here. The growth rate fluctuations in continuous mode showed an initial peak and then decreased to converge with the curves obtained for the different pulsed ultrasound conditions; peaks in pulsed mode curves were rarely observed and were still much smaller than those observed in continuous mode.

5. Discussion

In this study we reported for the first time the use of pulsed ultrasound for generating programmed 2-D and 3-D particle and cell aggregates. Initially, we demonstrated how pulsed ultrasound can control particle and cell aggregation. As demonstrated in the experimental section, the aggregation rate is reduced when pulsed ultrasound is employed. The pulse mode factor for 15 and 10 μm particles: $P_{mf15} = 0.19$ and $P_{mf10} = 0.16$ indicates that the acoustic force was applied during the 19% and 16% of the total experimental time respectively. By considering that particles have a constant transversal velocity and by taking into account that the drag force is proportional to the velocity, we can compare P_{mf} to the velocity

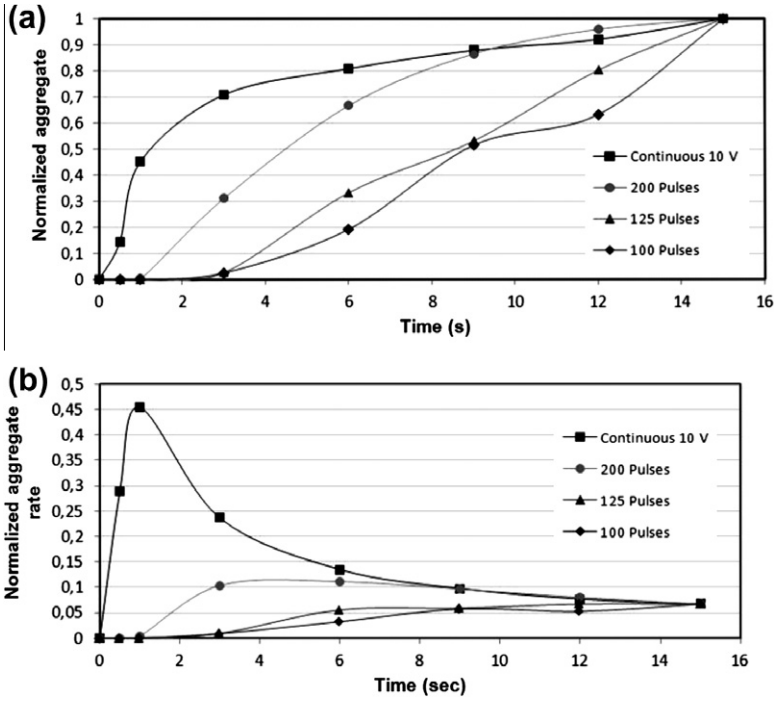

Fig. 9. Normalized aggregate area and rate vs time of Caco2 cells (3×10^6 ml) in (a) continuous and (b) pulsed mode.

ratio: $u_{pulsed}/u_{continuous}$, being 0.24 for 15 μm and 0.2 for 10 μm particles, not very different from their respective pulsed mode factor. This result suggests that the inertial effects, i.e. the time needed for reaching the terminal velocity and the relaxation of the maximal amplitude related to the Q-factor, do not significantly influence the aggregation process in pulsed mode. In the opposite event the values for the velocity ratio would be smaller than the P_{mf}. We note that the considerations made here concern typical velocities; an analytical statistical study that determines the velocity distributions would be required for thoroughly exploiting the aggregation process in pulsed mode.

The fact that in pulsed mode the aggregation is slower than in continuous mode does not directly imply that lower growth rates entail a higher probability of obtaining 2-D than 3-D aggregates; in fact, the initial particle or cell concentration needs to be taken into consideration. It is worth noting that in continuous mode during the aggregation process, almost all particles reached the focusing plane before aggregating (only a few particles joined the aggregate from the bottom of the resonator, and their contribution to the 3D structure was negligible), whereas in pulsed mode, all particles started aggregating at the focusing plane.

Our experiments showed that when the aggregate was growing, the momentum transmitted by incoming particles gave rise to the rearrangements of particles and cells, indicating that the pressure distribution in the aggregate was modified. When the pressure was high enough, particles or layers started to overlap, mostly in the central part of the aggregate, leading to area growth rate fluctuations as depicted in Figs. 3a and 7a. As in those experiments only few particles joined the aggregate from elsewhere other than from the levitation plane, we conclude that the overlapping of the particle and cell layers were generated by the increasing pressure of incoming particles, thus determining the transition from 2-D to 3-D aggregates. Experiments with particles clearly showed layer overlapping (Fig. 3a), while aggregates of cells showed rather darker layers (Fig. 8a).The aggregation process showed that the fluctuations in the aggregate area coincided with the overlapping of layers. We observed that these fluctuations disappeared in pulsed ultrasound where only 2-D aggregates were formed. In Fig. 4c (pulsed mode, 15 μm particles), we observed one big fluctuation, but still smaller than those during continuous mode. In fact, in this case we observed, a small aggregate reaching the main aggregate hence generating a great pressure and a strong particle rearrangement; the aggregate was nevertheless 2-D (Fig. 4a).

This new method is developed with the aim to generate controlled cell constructs. When cells were employed, even though the area fluctuations were visible, the process did not show rapid fluctuations. It is important to note that cells are more elastic than particles, thus initially, compaction of the aggregates occured with increasing pressure prior to the formation of cell layers. The curve of the growth rate variation in continuous ultrasound is depicted in Fig. 7a. The curve shows a maximum analogous to that shown for 10 μm particles, suggesting that a maximum in the growth rate time variation could indicate the formation of a 3D structure. When cells are employed, the aggregate does not grow linearly with time. The elastic properties of the cells as well as their polydispersity could account for this effect. The aggregation dynamics need to be revisited and thoroughly studied in the light of this new pulsed ultrasound approach that allows careful control of various aggregation parameters.

Finally, the histograms in Fig. 5a and b indicate that the size of the cell aggregates is a function of the number of pulses employed for both concentrations studied. 2D constructs of different sizes can be formed with suspensions of very different initial cell concentrations; for example, 5×10^5 cells/ml at 200 pulses generates smaller aggregates than 3×10^6 cells/ml at 50 pulses. Regardless of the initial concentration, the pulsed ultrasound technique allows 3D or 2D aggregates to be formed. It is therefore evident that pulsed ultrasound introduces new parameters for controlling the aggregation process in ultrasonic standing waves resonators.

5.1. Effect of the amplitude

It is interesting to compare the possibility of generating 2-D aggregates by reducing the amplitude of the acoustic force, i.e. by reducing the voltage. Lower amplitude implies weaker acoustic forces. We performed experiments with 15 μm latex particles (0.1% solids in water). By reducing the intensity to 60, 40 and 30% of the maximum amplitude of 15 V, we observed, as expected, an increase in the duration of the aggregation time. At 60% the aggregate was still 3-D. At 40% (Fig. 10a) the aggregate was mostly 2-D, as it was difficult to distinguish whether all particles were at the same plane at the centre of the aggregate. At 30% (Fig. 10b) the aggregate was 2-D but at the center a concave shape showed that the aggregate was not in plane. At lower amplitudes, no aggregation was possible. We also observed that the aggregation time was double the aggregation time in pulsed mode. Finally, by comparing the 2-D aggregates obtained at reduced amplitude and in pulsed mode (Fig. 4a) we can see that in pulsed mode the aggregate is plane and regular. Based on these observations, we consider that reducing the amplitude in order to control aggregation, it is difficult to get a precise amplitude to generate the optimum or required 2-D aggregate.

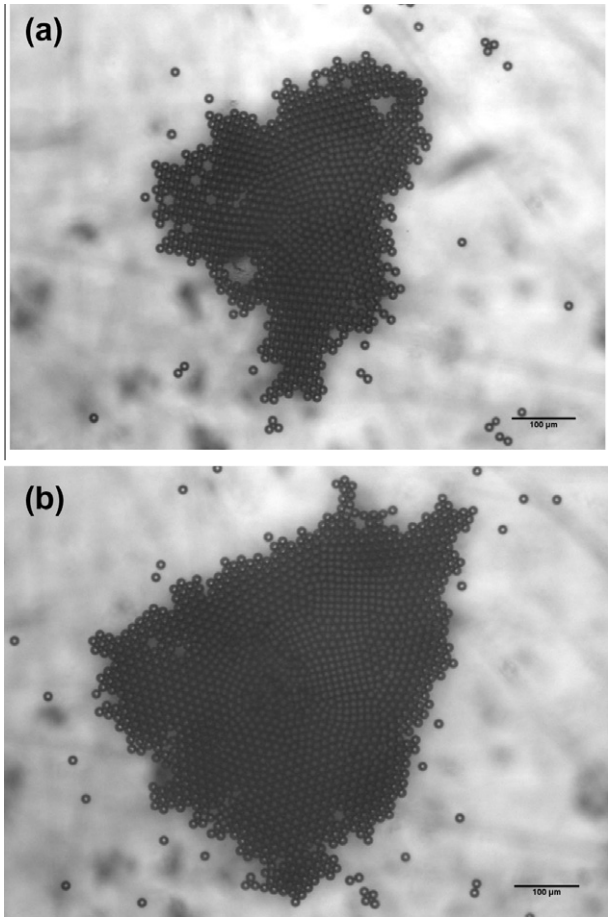

Fig. 10. 2-D aggregates of 15 μm particles obtained in continuous mode at different amplitudes: (a) 6 V_{p-p} and (b) 4.5 V_{p-p} (maximum voltage 15 V). In both cases the aggregates look like 2-D but at the center particles are unfocused, aggregates are not in plane. At higher amplitudes the aggregate is 3-D, while at lower amplitudes no aggregation is possible.

6. Conclusion

We presented for the first time the use of pulsed ultrasound for the generation of 2-D or 3-D particle or cell aggregates in a controlled manner. The use of pulsed ultrasound offers several advantages in relation to continuous ultrasound including: (a) reduced transducer heating, (b) increased acoustic force through employment of a minimum number of pulses that results in rapid yet controlled particle or cell aggregation without adversely affecting the cells, (c) reduced liquid/cell media heating thus maintaining constant the thermodynamic and physicochemical properties of the suspension and (d) the architecture of the resultant aggregate can be modified irrespective of the initial particle or cell concentration.

Acknowledgements

The authors wish to acknowledge to the Ulysses International program France-Ireland. A.C. acknowledges the financial support BDI from CNES-CNRS France.

References

[1] C.M. Lin, Y.S. Lai, H.P. Liu, C.Y. Chen, A.M. Wo, Trapping of bioparticles via microvortices in a microfluidic device for bioassay applications, Analytical Chemistry 80 (2008) 8937–8945.
[2] S.K. Mohanty, K.S. Mohanty, M.W. Berns, Manipulation of mammalian cells using a single-fiber optical microbeam, Journal of Biomedical Optics 13 (2008) 054049.
[3] C. Bustamante, Y.R. Chemla, J.R. Moffitt, High-resolution dual-trap optical tweezers with differential detection: an introduction, Cold Spring Harbor Protocols 10 (2009) (pdb.top60).
[4] L.S. Jang, P.H. Huang, K.C. Lan, Single-cell trapping utilizing negative dielectrophoretic quadrupole and microwell electrodes, Biosensors and Bioelectronics 24 (2009) 3637–3644.
[5] R.S. Thomas, H. Morgan, N.G. Green, Negative DEP traps for single cell immobilization, Lab on a Chip 9 (2009) 1534–1540.
[6] J.H. Koschwanez, R.H. Carlson, D.R. Meldrum, Easily fabricated magnetic traps for single-cell applications, Review of Scientific Instruments 78 (2007) 044301.
[7] W. Liu, N. Dechev, I.G. Foulds, R. Burke, A. Parameswaran, E.J. Park, A novel permalloy based magnetic single cell micro array, Lab on a Chip 9 (2009) 2381–2390.
[8] D. Bazou, L.A. Kuznetsova, W.T. Coakley, Physical environment of 2-D animal cell aggregates formed in a short pathlength ultrasound standing wave trap, Ultrasound in Medicine and Biology 31 (2005) 423–430.
[9] M. Evander, L. Johansson, T. Lilliehorn, J. Piskur, M. Lindvall, S. Johansson, M. Almqvist, T. Laurell, J. Nilsson, Noninvasive acoustic cell trapping in a microfluidic perfusion system for online bioassays, Analytical Chemistry 79 (2007) 2984–2991.
[10] S. Oberti, A. Neild, J. Dual, Manipulation of micrometer sized particles within a micromachined fluidic device to form two-dimensional patterns using ultrasound, The Journal of the Acoustical Society of America 121 (2007) 778–785.
[11] D.H. Kim, A. Haake, Y. Sun, A.P. Neild, J.E. Ihm, J. Dual, J.A. Hubbell, B.K. Ju, B.J. Nelson, High-throughput cell manipulation using ultrasound fields, Engineering in medicine and biology society IEEE Conference 4 (2004) 2571–2574.
[12] D. Bazou, G.A. Foster, J.R. Ralphs, W.T. Coakley, Molecularadhesion development in a neural cell monolayer forming in an ultrasound trap, Molecular Membrane Biology 22 (2005) 229–240.
[13] W.T. Coakley, D. Bazou, J. Morgan, G.A. Foster, C.W. Archer, K. Powell, K.A. Borthwick, C. Twomey, J. Bishop, Cell–cell contact and membrane spreading in an ultrasound trap, Colloids and Surfaces B: Biointerfaces 34 (2003) 221–230.
[14] J. Liu, L.A. Kuznetsova, G.O. Edwards, J. Xu, M. Ma, W.M. Purcell, S.K. Jackson, W.T. Coakley, Functional three-dimensional HepG2 aggregate cultures generated from an ultrasound trap: comparison with HepG2 spheroids, Journal of Cellular Biochemistry 102 (2007) 1180–1189.
[15] D. Bazou, W.T. Coakley, A.J. Hayes, S.K. Jackson, Long-term viability and proliferation of alginate-encapsulated 3-D HepG2 aggregates formed in an ultrasound trap, Toxicology in Vitro 22 (2008) 1321–1331.
[16] L.V. King, On the acoustic radiation pressure on spheres, Proceedings of the Royal Society of London, Series A: Mathematical and Physical Sciences 147 (1934) 212–240.
[17] K. Yosioka, Y. Kawasima, Acoustic radiation pressure on a compressible sphere, Acta Acoustica 5 (1955) 167–173.
[18] L.P. G'orkov, On the forces acting on a small particle in an acoustical field in an ideal fluid, Soviet Physics Doklady 6 (9) (1962) 773–775.
[19] G. Whitworth, M.A. Grundy, W.T. Coakley, Transport and harvesting of suspended particles using modulated ultrasound, Ultrasonics 29 (1991) 439–444.
[20] S.M. Woodside, B.D. Browen, J.M. Piret, Measurement of ultrasonic forces for particle-liquid separations, AICHE Journal 43 (1997) 1727–1736.
[21] J.J. Hawkes, D. Barrow, W.T. Coakley, Microparticle manipulation in millimeter scale ultrasonic standing wave chambers, Ultrasonics 36 (1998) 925–931.
[22] S.M. Woodside, B.D. Browen, J.M. Piret, M. Gröschl, E. Benes, B.D. Bowen, Acoustic force distribution in resonators for ultrasonic particle separation, AICHE Journal 44 (1998) 1976–1984.
[23] M.A.H. Weiser, R.E. Apfel, E.A. Neppiras, Interparticle forces on red cell in a standing wave field, Acta Acustica 56 (1984) 114–119.
[24] B.T. Chu, R.E. Apfel, Acoustic radiation pressure produced by a beam of sound, Journal of Acoustic Society of America 72 (6) (1982) 1673–1687.
[25] H. Bruus, Theoretical Microfluidics, Oxford University Press, 2008.
[26] G. Whitworth, W.T. Coakley, Particle column formation in a stationary ultrasonic field, Journal of the acoustical society of America 91 (1) (1992) 79–85.
[27] C. Ratier, M. Hoyos, Acoustical Programming in Step-Splitt flow lateral transport thin fractionation, Analytical Chemistry 82 (4) (2010) 1318–1325.
[28] J.J. Hawkes, W.T. Coakley, Force field particle filter, combining ultrasound standing waves and laminar flow, Sensors and Actuators B: Chemical 75 (3) (2001) 213–222.
[29] F. Petersson, A. Nilsson, C. Holm, H. Jönssonc, T. Laurell, Separation of lipidsfrombloodutilizingultrasonic standing waves in microfluidicchannels, The Analyst 129 (2004) 938–943.
[30] J.F. Spengler, W.T. Coakley, K.T. Christensen, Microstreaming effects on particle concentration in an ultrasonic standing wave, AICHE Journal 49 (2003) 2773–2782.
[31] L.A. Crum, Bjerknes forces on bubbles in a stationary sound field, Journal of the Acoustical Society of America 57 (1975) 1363–1370.
[32] T.A. Krouskop, D.R. Dougherty, F.S. Vinson, A pulsed doppler ultrasonic system for making noninvasive measurements of the mechanical properties of soft tissue, Journal of Rehabilitation Research and Development 24 (2) (1987) 1–8.
[33] M. Hoyos, J.C. Bacri, J. Martin, D. Salin, A study of the sedimentation of noncolloidal bidisperse, concentrated suspensions by an acoustic technique, Physics of Fluids 6 (12) (1994) 3809–3817.
[34] Y. Takeda, Velocity profile measurement by ultrasonic doppler method, Experimental Methods in Thermal and Fluid Science 10 (4) (1995) 444–453.
[35] D.R. Sisan, N. Mujica, W.A. Tillotson, Y.M. Huang, W. Dorland, A.B. Hassam, T.M. Antonsen, D.P. Lathrop, Experimental observation and characterization of the magnetorotational instability, Physical Review Letters 93 (11) (2004) 1–4.
[36] M. Gröshl, Ultrasonic separation of suspended particles – Part I: fundamentals, Acustica Actaacustica 84 (1998) 432–447.
[37] W.T. Coakley, D. Bazou, J. Morgan, G.A. Foster, C.W. Archer, K. Powell, K.A.J. Borthwick, C. Twomey, J. Bishop, Cell–cell contact and membrane spreading in an ultrasound trap, Colloids and Surfaces B: Biointerfaces 34 (2004) 221–230.
[38] D. Bazou, G.P. Dowthwaite, I.M. Khan, C.W. Archer, J.R. Ralphs, W.T. Coakley, Gap junctional intercellular communication and cytoskeletal organization in chondrocytes in suspension in an ultrasound trap, Molecular Membrane Biology 23 (2) (2006) 195–205.

Appendix B

Experimental Study on Inter-Particle Acoustic Forces

Experimental study on inter-particle acoustic forces

Anna Garcia-Sabaté [a)b)]
Department of Applied Physics, Universitat Politècnica de Catalunya (BarcelonaTech) - Esteve Terrades 5, 08860 Castelldefels (Barcelona), Spain

Angélica Castro
Ecole Supérieure de Physique et Chimie Industrielles (ParisTech), Laboratoire de Physique et Mécanique des Milieux Hétérogènes, UMR 7636 CNRS, 10 Rue Vauquelin, 75231 Paris Cedex 05, France

Mauricio Hoyos
Ecole Supérieure de Physique et Chimie Industrielles (ParisTech), Laboratoire de Physique et Mécanique des Milieux Hétérogènes, UMR 7636 CNRS, 10 Rue Vauquelin, 75231 Paris Cedex 05, France

Ricard González-Cinca
Department of Applied Physics, Universitat Politècnica de Catalunya (BarcelonaTech) - Esteve Terrades 5, 08860 Castelldefels (Barcelona), Spain

[a)] Also at: Ecole Supérieure de Physique et Chimie Industrielles (ParisTech), Laboratoire de Physique et Mécanique des Milieux Hétérogènes, UMR 7636 CNRS, 10 Rue Vauquelin, 75231 Paris Cedex 05, France
[b)] e-mail: anna.garcia@fa.upc.edu

Abstract

A method for the experimental measurement of inter-particle forces (secondary Bjerknes force) generated by the action of an acoustic field in a resonator micro-channel is presented. The acoustic radiation force created by an ultrasonic standing wave moves suspended particles towards the pressure nodes and induces particle oscillations. Once particles are in the levitation plane, transverse and secondary Bjerknes forces become important. Experiments were carried out in a resonator filled with a suspension composed of water and latex particles of different size (5 to 15 μm) at different concentrations. Ultrasounds were generated by means of a 2.5 MHz nominal frequency transducer. For the first time the acoustic force generated by oscillating particles acting on other particles has been measured, and the critical interaction distance in various cases has been determined.

I. INTRODUCTION

Almost two centuries ago, Faraday pointed out that particles and bubbles undergo different forces when an acoustic field is applied [1]. Since then, many studies have been carried out involving different aspects of the phenomenon, such as the observation of particle aggregation [2], early theoretical analysis [3], mathematical analysis of pulsating air bubbles [4], or the development of a rigorous analytical expression for the acoustic radiation pressure on spheres [5]. Except for Bjerknes' work, these studies were mainly focused on the effects of the primary sound field on spherical objects without analyzing any secondary forces. More recently, pioneering studies on the interaction forces between particles in an acoustic field were carried out focusing on rigid spheres [6], and on bubbles (secondary Bjerknes force) [7].

Research on bubbles and solid particles in acoustic fields developed in parallel for a long time. Weiser et al. [8] contributed in the field of inter-particle forces taking into account for the first time the secondary Bjerknes force (usually described for bubbles) in the study of the interaction between two compressible solid spheres. Many authors have studied, both experimentally and theoretically, the secondary Bjerknes force on bubbles ever since [9–13]. Although some research works on secondary forces on particles have been reported [14, 15], the magnitude of these forces has not been determined experimentally.

We present an experimental study on the force between elastic solid particles in an acoustic field. A theoretical review of the forces acting on a particle in an acoustic field is presented in Section . In Section we present the experimental setup and procedure. The data analysis technique to determine the magnitude of the inter-particle forces, as well as the results obtained from the study of different cases are presented in Section .

II. BACKGROUND

The force generated by an external acoustic field acting on bubbles, drops or particles, without considering the interaction between neighboring objects, is known as the primary acoustic force. Yosioka and Kawasima [16] and Gor'kov [17] calculated the acoustic radiation pressure on a compressible sphere giving rise to the primary acoustic force for plane standing waves. In the direction of propagation of the wave, this force is given by:

$$F_z = 4\pi R^3 E_{ac} k G \sin(2kz), \tag{1}$$

where R is the radius, E_{ac} is the average acoustic energy density (sum of the time-averaged kinetic and potential energy densities), k is the wave number, z is the distance from the nearest pressure antinode, and G is the acoustic contrast factor defined as:

$$G = 1 - \frac{\beta_p}{\beta_f} + \frac{3(\rho_p - \rho_f)}{2\rho_p + \rho_f}, \tag{2}$$

where β is the compressibility, ρ is the density, and subscripts p and f correspond to particle and fluid, respectively. For $G < 0$ (generally the case of gas bubbles), particles move to the pressure antinodes by the action of the primary acoustic force. However, if particles are denser than the surrounding fluid ($G > 0$), they are driven to the pressure nodes.

Standing waves with a non-uniform amplitude (due to diffraction effects or non-uniform performance of the transducer) generate energy gradients in the system which affect the movement of particles in a levitation plane perpendicular to the direction of propagation of the wave. In this case, a transverse component of the primary acoustic force has to be considered [17]:

$$F_{xy} = \frac{4}{3}\pi R^3 \nabla E_{ac} \left(\frac{3(\rho_p - \rho_f)}{2\rho_p + \rho_f} \cos^2(kz) - \left(1 - \frac{\beta_p}{\beta_f}\right) \sin^2(kz) \right). \quad (3)$$

The transverse component of the primary acoustic force moves particles towards the regions of maximum acoustic energy. Since the axial component scales with E_{ac} and the transverse component scales with the gradient of E_{ac}, the axial component is often at least one order of magnitude larger than the transverse one.

Bubbles under the effects of a standing wave pulsate due to the positive and negative cycles of the wave. These pulsations coupled to the non-zero average pressure of the acoustic field cause the motion of the bubbles. The corresponding translational forces are the so-called Bjerknes forces. From the general expression of the time-averaged Bjerknes force $F_B = -\langle V(t) \nabla P_a \rangle$ (where $V(t)$ is the volume of the bubble at time t, and ∇P_a is the pressure gradient of the applied field), the primary and secondary Bjerknes forces (due to the external acoustic field and to the acoustic field generated by neighboring bubbles, respectively) can be obtained by specifying the field. When the pressure gradient of the applied acoustic field is included in the equation, the primary Bjerknes force averaged over an acoustic cycle is obtained:

$$F_{PB} = -\frac{4\pi f}{3} k P_a \cos(kz) \int_0^T R(t)^3 \sin(\omega t) dt, \quad (4)$$

where P_a is the pressure of the primary acoustic field, f and ω being the linear and angular frequency, respectively.

Pulsating bubbles generate a secondary acoustic field, which makes bubbles to attract or repel each other. Expressions for the secondary Bjerknes force are usually given as a

function of the change in volume of the particle or bubble [7, 8, 18], which is very difficult to estimate. An alternative expression taking into account the compressibility of the spheres can be written as [19]:

$$F_{SB} = -\frac{2\pi\rho_f}{9}(\beta_f \omega P_a)^2 \left(1 - \frac{\beta_{p1}}{\beta_f}\right)\left(1 - \frac{\beta_{p2}}{\beta_f}\right)\frac{R_{p1}^3 R_{p2}^3}{d^2} \tag{5}$$

where R_{p1} and R_{p2} denote the radius each particle taking part in the process, and d is the inter-particle distance.

The interaction force between two rigid spheres oscillating in an acoustic field can also to be considered. Two different expressions for this force are given in Weiser et al. [8] depending on the angle yield between a straight line connecting the particles and the direction of the propagating field. The force between two spheres with equal radii lined up in the direction of propagation of the sound field is attractive and given by:

$$F_r = \frac{4\pi(\rho_p - \rho_f)^2 v_{ac}^2 R_p^6}{3\rho_f d^4}, \tag{6}$$

where v_{ac} is the velocity (assumed uniform) of the incident acoustic wave at the position of the spheres. When particles are lined up perpendicular to the wave propagation, the force is attractive and given by:

$$F_r = -\frac{2\pi(\rho_p - \rho_f)^2 v_{ac}^2 R_p^6}{3\rho_f d^4} \tag{7}$$

The forces acting on a particle in an acoustic field are illustrated in Fig. 1.

Table 1 shows the orders of magnitude of these forces considering polystyrene particles of 10μm diameter in water and a frequency of 2.830 MHz. The axial and transverse acoustic

	Force	Plane of Action	Described for	Magnitude (N)
Primary Acoustic Field	Axial Acoustic Force F_z	Axial	Particles	10^{-11}
	Primary Bjerknes Force F_{PB}	Axial	Bubbles	10^{-5}
	Transverse Acoustic Force F_{xy}	Transversal	Particles	10^{-13}
Secondary Acoustic Field	Secondary Bjerknes Force F_{SB}	Transversal	Particles and Bubbles	$10^{-13}/10^{-5}$
	Force Between Two Rigid Spheres F_r	Transversal	Particles	10^{-14}

Table 1: Orders of magnitude of the acoustic forces acting on a pair of particles/bubbles of radius $R = 5\mu$m separated 20 µm.

forces have obtained considering $E_{ac} = 18\text{J/m}^3$ ([15]). In order to determine F_{PB} and F_{SB} the following expression for the acoustic pressure have been used ([18]):

$$P_a = c_a\sqrt{4\rho_f E_{ac}}, \tag{8}$$

where c_a is the speed of sound in the fluid and ρ_0 is the the density of the medium. Finally, the relation $E_{ac} = (\rho_f v_{ac}^2)/2$ is used to obtain $v_{ac} = 18.9$ cm/s in order to determine F_r.

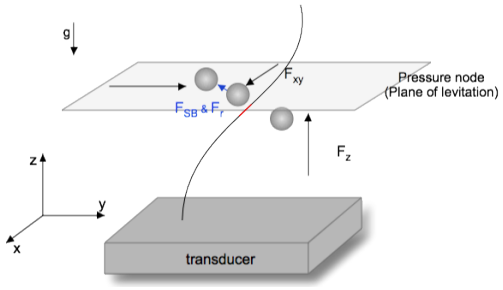

Figure 1: Acoustic forces acting on a pair of particles.

III. EXPERIMENTAL SETUP AND PROCEDURE

A scheme of the experimental setup is shown in Fig. 2. Experiments were carried out in a Hele-Shaw cell with an inner channel of thickness 250μm. The cell is a resonator made of a glass plate separated from a stainless steal plate by means of Mylar spacers. A rectangular (10mm×20mm) piezoelectric transducer (PZ27 Ferroperm Piezoceramics, Denmark) with a nominal frequency of 2.5MHz was glued with conductive epoxy (Chemtronics ITW, USA) to the stainless steal plate. The transducer was excited in each test by a function generator (Tabor Electronics WW1072, Israel) whose signal was amplified by a voltage amplifier (Tabor Electronics 9250, Israel) with 10x fixed gain, which was also connected to a digital oscilloscope (ISO-TECH IDS 8064, Hanan-Israel). A pressure node was created approximately at the center of the channel. The channel was observed through a reflective microscope (Zeiss Axiotech Vario 100HD), using 50x (Olympus SLMPlan) and 20x (PL Nachet LD) objectives. A camera (Moticam 2000) was mounted on the microscope through a 0.5x objective and connected to a computer.

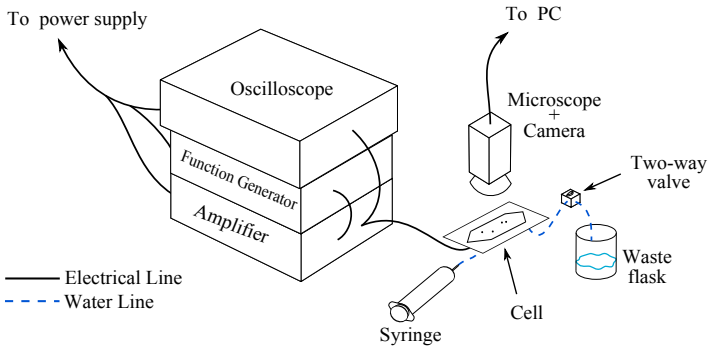

Figure 2: Experimental setup.

Different solution volumes (5ml, 10ml and 30ml) composed of water and latex particles

were injected in the channel by means of a syringe. A two-way valve was placed at the cell outlet to ensure stationary conditions inside the cell during the experiments, and to flush the suspension to a waste flask after each test. The channel was initially cleaned with a solution of soap and deionized water. In special cases, when a more thorough cleaning was needed, ethanol 76% was injected. Deionized water was used to rinse and fill up the channel. Once the channel was full of water, the resonance frequency of the system was determined. Fig. 3 (where V_{osc} is the voltage measured by the oscilloscope, and V_{FG} is the voltage at the output of the amplifier) shows the amplitude obtained at different frequencies between 2.0MHz and 3.5MHz. The highest peak corresponds to the resonance frequency, which is the optimal one to levitate particles, although it is not necessarily the optimal one for aggregation.

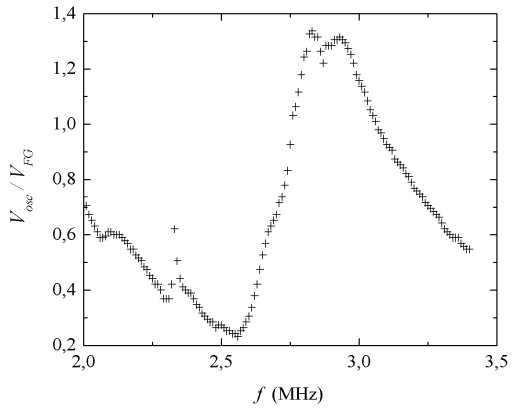

Figure 3: Amplitude response of the transducer at different frequencies.

Monodispersed latex beads (Micromod - Rostock, Warnemunde Germany) of different diameter (5µm, 7µm, 10µm and 15µm) were diluted in deionized water at different concentrations and injected into the channel. Once particles were injected, the two way valve

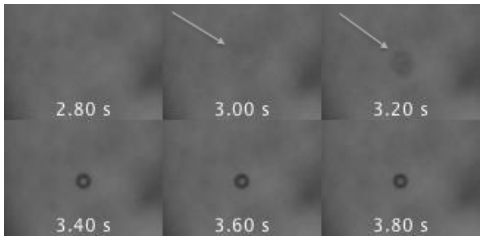

Figure 4: Particle levitation due to the axial force.

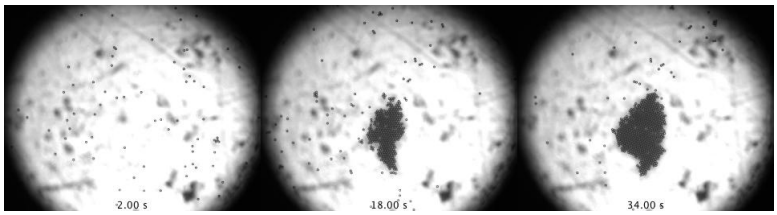

Figure 5: Particle aggregation at the plane of levitation due to transverse forces.

was closed and particles were let to sediment for some minutes. Afterwards, the ultrasound generation system was turned on at the desired frequency and videos were recorded by the camera through the microscope.

Fig. 4 illustrates the particle movement towards the plane of levitation due to the action of the acoustic axial force when the ultrasound generation system is turned on. Once in this plane, particles tend to form aggregates under the action of transverse forces (Fig. 5).

The films recorded in each test were saved in gray-scale and processed by means of the open-source software Fiji (ImageJ) [20]. In order to obtain the position of the particles at each frame, we used the plug-in MTrack2. This plug-in needs a threshold stack to properly track the particles, hence it was necessary to process the video before using the tracking

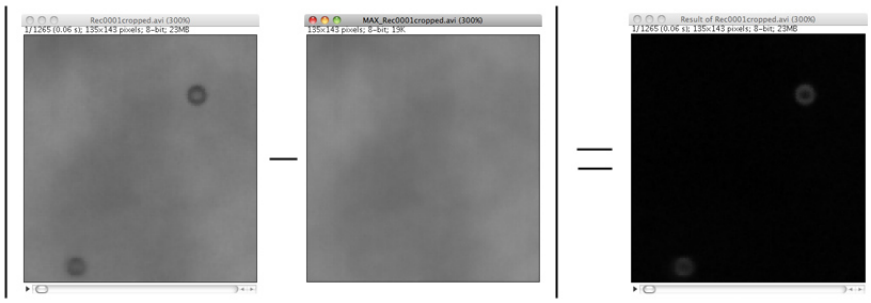

Figure 6: Resulting stack from the image calculator.

plugin. A z-projection of the maximum intensity pixels was obtained and substracted from the entire stack using the image calculator (Fig. 6). A threshold stack was obtained and used for tracking the position of the particles frame by frame.

IV. RESULTS AND DISCUSSION

A. Data analysis method

More than 100 films were recorded by the camera, 9 of which containing analysable cases. These cases (17 in total) show two particles approaching each other in the levitation plane due to the effects of the transverse acoustic force and the secondary Bjerknes force. The low number of analysable cases can be explained by the fact that the secondary Bjerknes force is considerably weaker than the transverse acoustic force. Thus, the cases where the effects of the secondary Bjerknes force can be observed are difficult to identify. In addition, the field of view of the microscope through which the channel was observed only allowed the observation of a limited number of cases.

F_{SB} could not be measured directly since direct measurements of the acoustic pressure

inside the channel cannot be made. Therefore, an indirect method based on the balance of forces acting on a particle in the plane of levitation was considered. The force balance can be expressed as:

$$\left(\rho_p V_0 + \frac{\rho_f V_0}{2}\right)\frac{dv}{dt} = F_{xy} + F_D + F_{SB}, \tag{9}$$

where V_0 is the static particle volume, v is the particle velocity, and F_D is the drag force. Since the Reynolds number in the channel is small, Stoke's drag can be considered:

$$F_D = -6\pi\mu R v, \tag{10}$$

where μ is the dynamic viscosity.

Since particle position and velocity can be obtained at each video frame, Eq. 9 contains two unknown terms, F_{xy} and F_{SB}. In order to determine these forces, we need to identify the regions where each force is acting. This identification can be carried out from the analysis of the time evolution of the particle velocity. We observed in the selected films that the dynamics of two particles moving closely suffered an abrupt change at a critical distance between particles, d_c. At this point, a change in velocity and sometimes in direction (approaching each other) was observed in both particles. We consider that this change in the dynamics is the evidence of the effects of F_{SB}.

To accurately determine in each case the time t_{dc} at which particles are at a distance d_c, the velocity of each particle was obtained for a few seconds. In most of the cases the particles were accelerating, which added some difficulty to determine the time at which d_c was reached. In order to avoid the problem we only considered the cases where one of the

particles was moving at a constant velocity before aggregating. Figs. 7(a) and 7(b) show the particle trajectories and velocity profiles, respectively, of one of this cases. We consider that particles are at the critical distance d_c when the particle moving at constant velocity (Particle 1) undergoes a change (usually a velocity increase) that lasts until the aggregation of both particles. Dotted line in Fig. 7(b) shows the time at which d_c is reached.

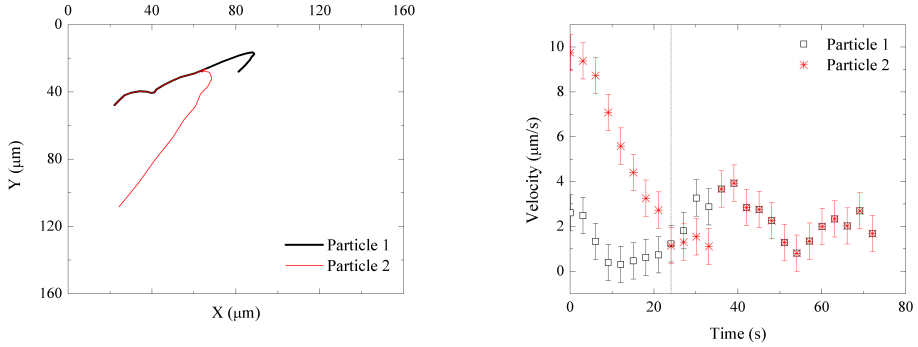

(a) (b)

Figure 7: (a) Trajectories, and (b) velocity profile of two 5μm particles. Dotted line shows the time at which d_c is reached.

Just before d_c, the velocity of Particle 1 is approximately constant and thus $\frac{dv}{dt} \approx 0$, and since F_{SB} is weak enough to be neglected, $F_{xy} = F_D$. Therefore, we can calculate F_{xy} from the mean velocity obtained along the period during which it is considered constant. Assuming that F_{xy} does not change significatively just after d_c is reached, F_{SB} can be determined from the new value of the velocity of Particle 1 with Eq. 9. Since F_{SB} is the same for both particles, F_{xy} of Particle 2 can also be calculated. Finally, once F_{SB} is known, P_a can be calculated from Eq. 5.

B. Particle dynamics

Among the seventeen selected cases, only in four of them a particle moving at constant speed was observed. The following subsections describe the dynamics of the pairs of particles under a given frequency of the external acoustic field in the four cases.

1. 5μm particles and 2.830MHz.

Figs. 7(a) and 7(b) show the particle trajectories and velocity in the plane of levitation, respectively. The closest third particle to the point of aggregation of the pair of particles was approximately at 250µm. From Fig. 7(b) we obtain $t_{dc} \approx 22s$. During the $10s$ before t_{dc} Particle 1 is moving at an approximately constant velocity, while Particle 2 is moving towards Particle 1 in a decelerated movement. After t_{dc} both particles accelerate towards each other. The attractive secondary Bjerknes force measured in this case is 6.78×10^{-14}N.

2. 7.5μm particles and 2.830MHz.

Figs. 8(a) and 8(b) show the particle trajectories in the plane of levitation and the velocity evolution in time, respectively. In the instants just after $t_{dc} \approx 7s$, velocity of Particle 1 slightly increases while Particle 2 reaches a steady state. The pair of particles aggregates at $t \approx 17$s. Right after the aggregation of the two particles, three new particles appeared in the field of view, finally forming a 5-particle aggregate. The secondary Bjerknes force obtained for the initial pair of particles is 7.02×10^{-14}N.

3. 5μm particles and 2.866MHz.

The aggregation of six particles was observed at the point where the pair of particles aggregated just before their aggregation took place. The larger aggregate immediately moved to another point of aggregation with higher acoustic energy. Figs. 9(a) and 9(b) show the particle trajectories (the dashed trajectory corresponds to the path covered by Particle

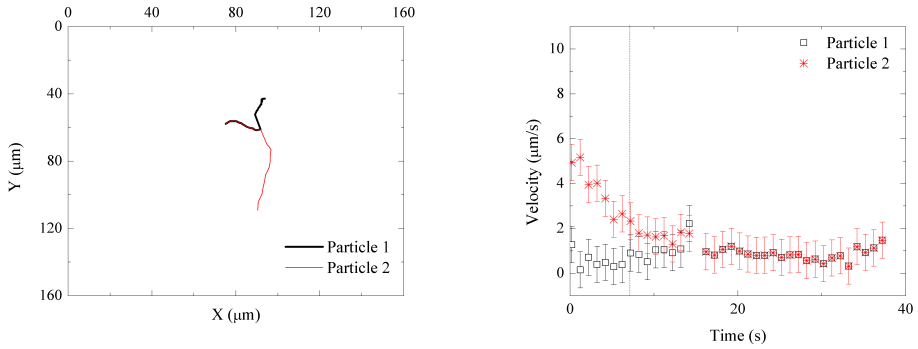

(a) (b)

Figure 8: (a) Trajectories, and (b) velocity profile of two 7.5μm particles. Dotted line shows the time at which d_c is reached.

1 before Particle 2 was tracked) in the plane of levitation and the velocity, respectively. Particle 1 entered the field of view at a high velocity and rapidly decelerated when it reached the region of aggregation. Particle 2 entered a few seconds later with a velocity similar to the velocity of Particle 1. After $t_{dc} \approx 126s$, Particle 1 accelerated and changed its trajectory before aggregating with Particle 2. Once the aggregate was formed, it accelerated towards the region with higher acoustic energy. The measured secondary Bjerknes force was 5.07×10^{-14}N.

4. 3.5μm and 5μm particles and 2.830MHz.

Figs. 10(a) and 10(b) show the particle trajectories in the plane of levitation and the velocity evolution in time, respectively. In this case, Particle 1 remained approximately at the same position throughout the whole process. Other particles were observed close to the point of aggregation, and an aggregate was created at 100μm. Particle 2 entered the field of view with a decelerating movement, while velocity of Particle 1 slightly decreased and the

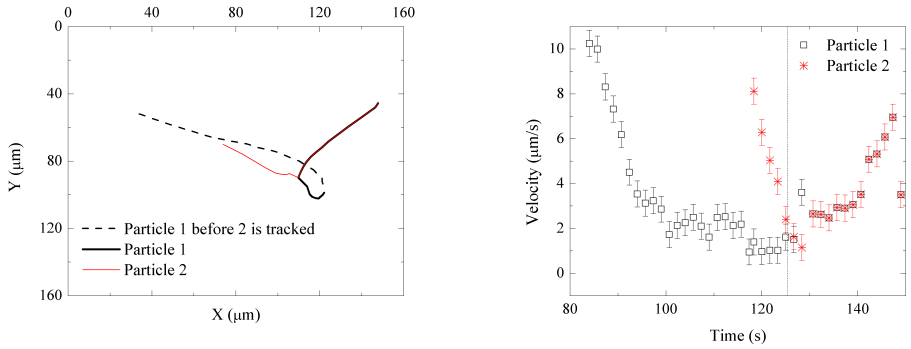

(a) (b)

Figure 9: (a) Trajectories, and (b) velocity profile of two 5μm particles. Dotted line shows the time at which d_c is reached.

particle remained almost quiescent from $t = 18$s The determination of the critical distance in this case is less clear than in the previous ones. Some differences can be observed in the dynamics of both particles from $t_{dc} = 26s$ since the velocity of Particle 2 kept around 2μm/s, while Particle 1 slightly accelerated. The value of the secondary Bjerknes force measured in this case was 2.49×10^{-14}N.

C. Secondary Bjerknes force

Table 2 shows the critical distance as well as the transverse and secondary Bjerknes forces measured in Section for the four considered cases. The acoustic pressure obtained from Eq. 5 and the acoustic energy calculated with Eq. 8 are also shown. The values of F_{xy} and F_{SB} at the critical distance obtained in each case are compatible with the expected values shown in Table 1. Moreover, when comparing the two cases with particles of 5μm, F_{SB} is larger in the case of smaller d_c, in accordance with Eq. 5.

The different values obtained for the acoustic pressure and energy can be explained by

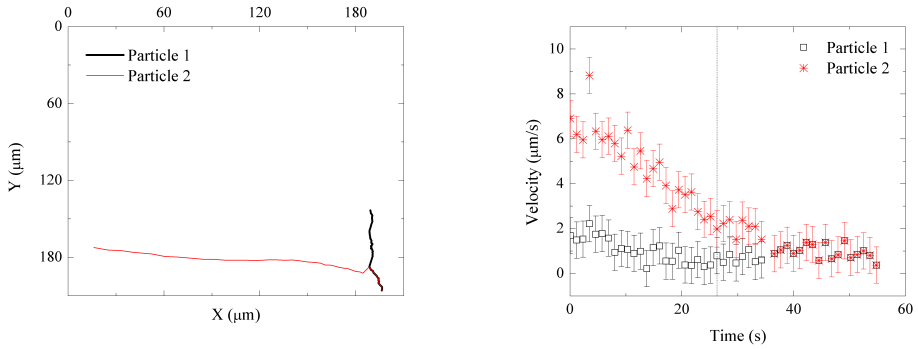

(a) (b)

Figure 10: (a) Trajectories, and (b) velocity profile of 3.5μm and 5μm particles. Dotted line shows the time at which d_c is reached.

Particle size	d_c (μm)	F_{xy} (N)	F_{SB} (N)	P_a (Pa)	E_{ac} (J/m^3)
5μm	24.1	4.75×10^{-14}	6.78×10^{-14}	3.92×10^{5}	17.10
7.5μm	39.2	5.75×10^{-14}	7.02×10^{-14}	1.92×10^{5}	4.09
5μm	24.4	1.01×10^{-13}	5.07×10^{-14}	3.38×10^{5}	12.70
5μm/3.5μm	23.1	4.90×10^{-14}	2.49×10^{-14}	3.88×10^{5}	16.70

Table 2: Critical distance, forces, acoustic pressure and acoustic energy obtained in each case analyzed.

the fact that each case was carried out under different experimental conditions. Therefore, the particle attraction and aggregation took place in regions of the levitation plane with different values of the acoustic energy density. Nevertheless, the range of values of the acoustic energy is very similar to the one reported by Woodside et al. [15] (13-18J/m^3). The order of magnitude of the values of the Secondary Bjerknes force is within the theoretically predicted range. Moreover, one can observe from Table 2 that the pair of largest particles (7.5μm) generates the largest F_{SB}, while, for same size pairs of particles, the largest F_{SB} is generated at the shortest d_c, as predicted by Eq. 5.

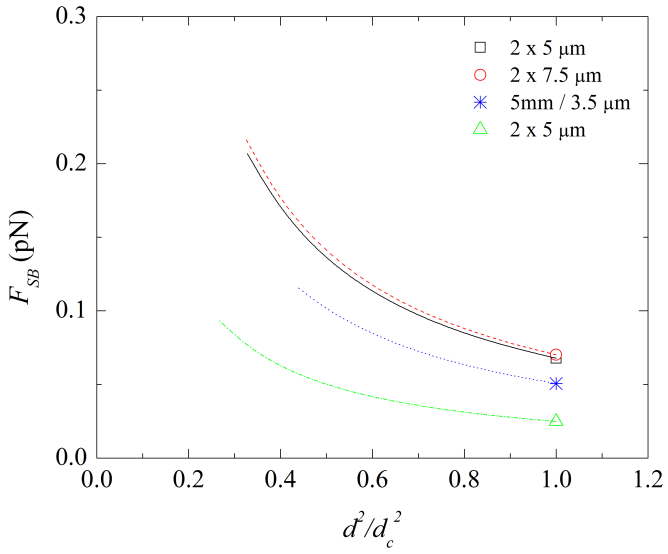

Figure 11: Secondary Bjerknes force as a function of the square of the dimensionless distance between particles.

Assuming that the region where particles move after reaching d_c does not contain significant variations of the acoustic pressure, Eq. 5 is used to predict the value of the force until the pair of particles aggregates. Fig. 11 shows the computed secondary Bjerknes force as a function of the dimensionless distance between particles. The values of the force are within the theoretically predicted range.

Fig. 12 shows the distance between particles normalized by the diameter as a function of the time normalized by the time between t_{dc} and the particles aggregation, t_f. The four cases analyzed present a smooth evolution of the length ratio with time. The ratio turns out to be smaller in the case of larger particles, even though they start interacting at larger distances than small particles do.

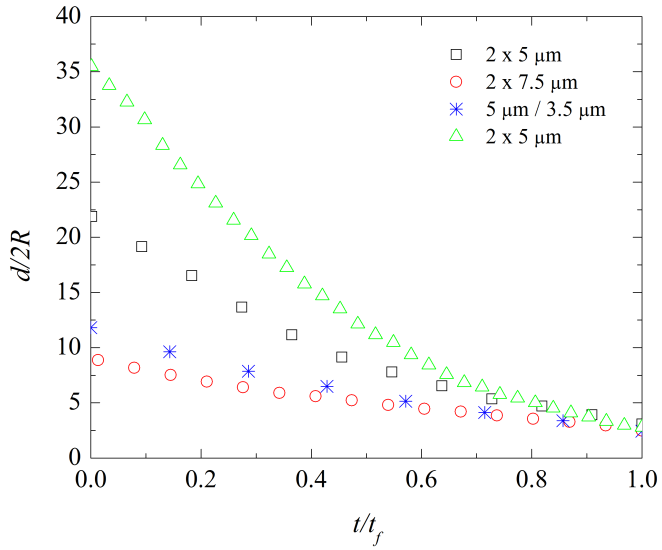

Figure 12: Distance between particles normalized by the particle diameter as a function of the time normalized by the time between t_{dc} and the particles aggregation.

V. CONCLUSIONS

We have presented a method to experimentally determine the transverse force on particles in an acoustic field as well as the Secondary Bjerknes force between elastic solid particles. The methodology also provides and indirect measurement of the acoustic pressure. We have applied the method in selected cases where particles levitated in a plane perpendicular to the direction of the acoustic field. The magnitude of the forces obtained is consistent with the theoretical predictions. The work presented here is the first experimental determination of the Secondary Bjerknes force between solid particles.

VI. ACKNOWLEDGEMENTS

A. G-S. is indebted to the *Laboratoire de Physique et Mécanique des Milieux Hétérogènes,*

Appendix C

Hydrodynamic focusing

Contrarily to the SPLITT device, the step-Splitt allow the construction of channels with one or several inlets and outlets according to separation requirements. Here, we present a s-SPLITT device of 3 inlets and 1outlet where particles of 10 μm diameter were focused hydrodynamically, Figure C.1.

Particles were observed *in situ* by Digital Holographic Microscope (DHM), with partially coherent illumination. Details about the DMH can be found in [77] and references cited herein [1].

The holographic reconstruction of each image has been undertaken by solving the 2D Kirchhoff-Fresnel diffraction equation. Figure C.2 presents the holograms obtained before and after the image processing procedure. The example in figure C.2 is the superposition of ten holograms recorded at equally spaced times during one run. We observe out of focus particles with diffraction rings, the microscope was focus at the mid channel thickness.

The modification of the flow inlets: the sample and the carrier fluid, allows the modification of the particle layer. Observations done at the same point in the thickness confirmed that modification, as show Figure C.3.

Experiments were done to test the homogeneity of the particle layer thickness at the width of the device (Figure C.4a). Also, it is possible to modify the thickness of the particle layer as show Figure C.4b.

[1] The holographic microscope is composed of a Mach-Zehnder interferometer using a 626nm wavelength laser beam. This microscope allows observations in 3D time evolution configuration of particles in a window of $300 \times 400 mm^2$. The holograms are composed of diffraction patterns recorded in a CCD camera operating at 24 images per seconds during 25 seconds, for a total of 600 images for each experiment.

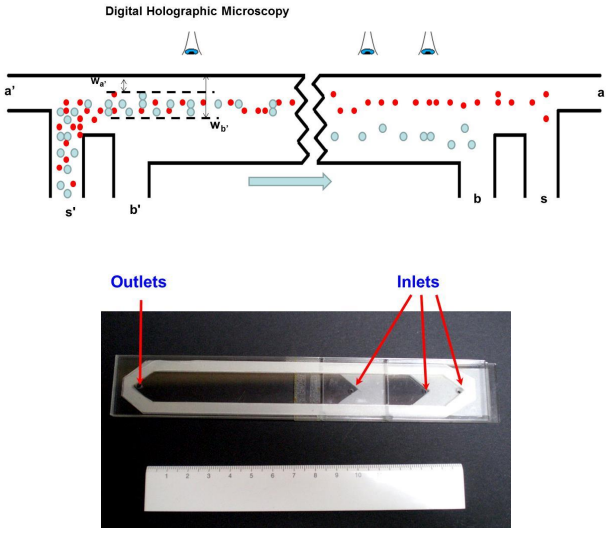

Figure C.1 3 inlets-3 outlets s-SPLITT and scheme of observation *in situ* of the device by holographic microscope. 3 inlets-1 outlet s-SPLITT

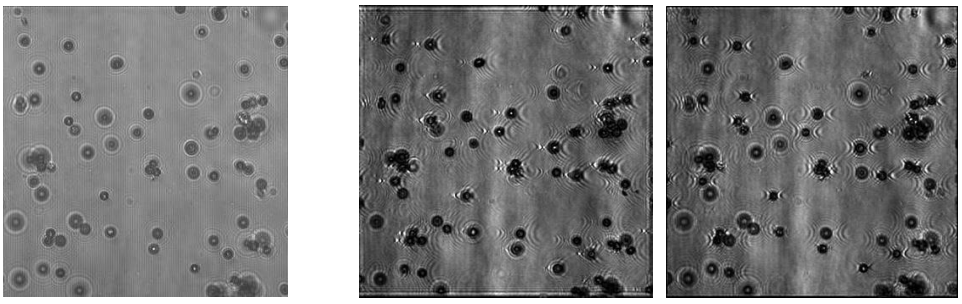

Figure C.2 Holographic focusing of 10 μm latex beads in the s-SPLITT. Left: Image of an hologram obtained by *in situ* observation throughout the thickness of the channel. If the particle is focused on the plane of observation, it can be identified by a central white dot. Otherwise, particles have concentric rings. Right: Reconstructed image showed at the left obtained at two different planes where between those reconstruction there is a difference of approximately 100μm.

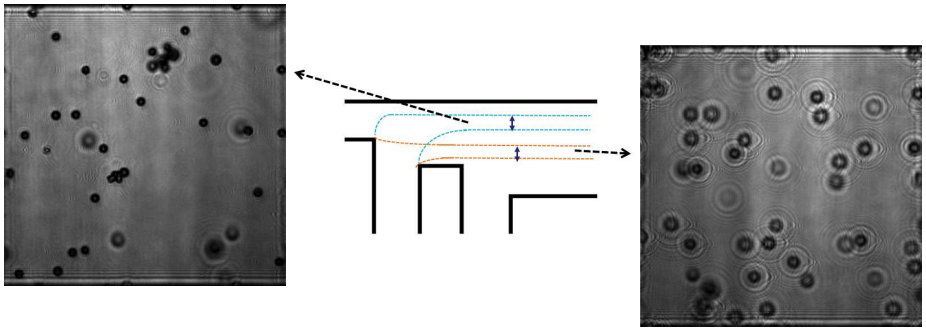

Figure C.3 Flow modification determines the position of the particle layer on the thickness. Blue-dot lines show a thickness, the same as the yellow-dot lines.

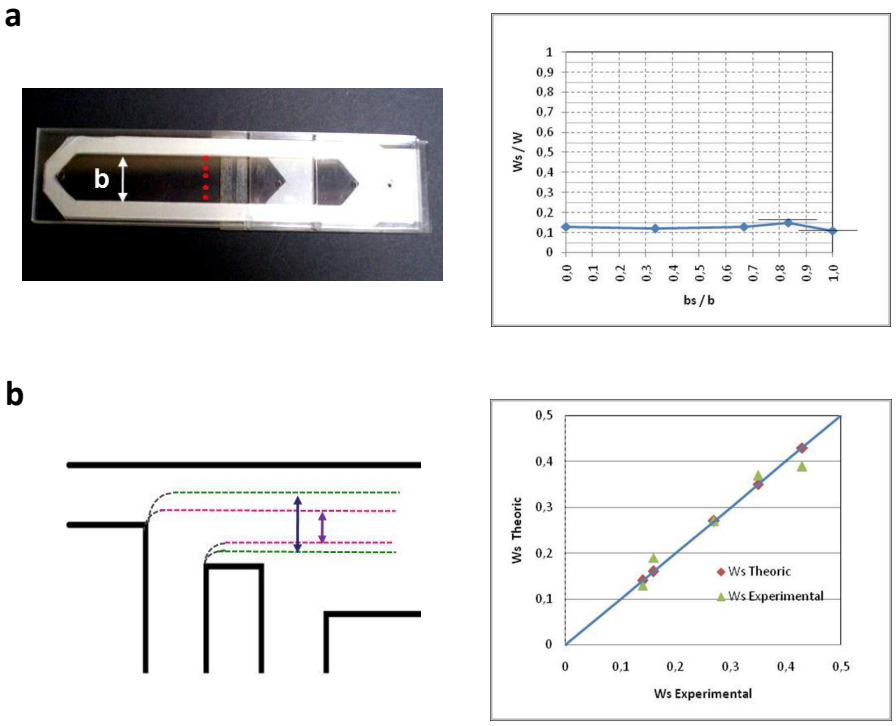

Figure C.4 a. Scheme of the observations made at the width of the channel; the curve show the normalized layer thickness at the normalized witdh where there is not big modifications of the layer. b) Particle layer modification. The curve at the righy show the contrast between experimental and theoretical values of the layer thickness.

Appendix D

Controlling the Acoustic Streaming by Pulsed Ultrasounds

Ultrasonics 53 (2013) 70–76

Contents lists available at SciVerse ScienceDirect

Ultrasonics

journal homepage: www.elsevier.com/locate/ultras

Controlling the acoustic streaming by pulsed ultrasounds

Mauricio Hoyos *, Angélica Castro

Laboratoire de Physique et Mécanique des Milieux Hétérogènes, UMR7636 CNRS, Ecole Supérieure de Physique et Chimie Industrielles, ESPCI, 10 rue Vauquelin, 75231 Paris Cedex 05, France

ARTICLE INFO

Article history:
Received 2 November 2011
Received in revised form 29 March 2012
Accepted 30 March 2012
Available online 11 April 2012

Keywords:
Acoustic streaming
Pulsed ultrasound
Standing waves

ABSTRACT

We propose a technique based on pulsed ultrasounds for controlling, reducing to a minimum observable value the acoustic streaming in closed ultrasonic standing wave fluidic resonators. By modifying the number of pulses and the repetition time it is possible to reduce the velocity of the acoustic streaming with respect to the velocity generated by the continuous ultrasound mode of operation. The acoustic streaming is observed at the nodal plane where a suspension of 800 nm latex particles was focused by primary radiation force. A mixture of 800 nm and 15 μm latex particles has been also used for showing that the acoustic streaming is hardly reduced while primary and secondary forces continue to operate. The parameter we call "pulse mode factor" i.e. the time of applied ultrasound divided by the duty cycle, is found to be the adequate parameter that controls the acoustic streaming. We demonstrate that pulsed ultrasound is more efficient for controlling the acoustic streaming than the variation of the amplitude of the standing waves.

© 2012 Elsevier B.V. All rights reserved.

1. Introduction

Particle manipulation by using ultrasonic standing waves (USWs) in microfluidic devices is ubiquitous in bioseparations, characterization and analysis of micron-sized species. A great number of publications have been highlighted the utility of USW by showing how particles, cells, bacteria and other non-colloidal materials can be affected by acoustic radiation forces in very different manners [1–10]. Primary radiation forces generate levitation of species at the nodal plane in a resonator; inhomogeneity of the transversal energy distribution and non-idealities in geometry of the resonator may lead particles to agglutinate at the nodal plane [10–12]. Secondary Bjerknes forces may keep aggregates consolidated and stable [13,14]. Finally, acoustic streaming may generate clumps and recirculation of particles at nodal planes [15–19]. Aggregation of cancer cells for instance, can be generated in cylindrical resonators in order to study physiological cell interactions [20]. Acoustic focusing in microfluidic channels allows generating separations in function of size and acoustic impedance [3,5,10] and acoustic levitation has demonstrated the possibility of enhancing spore capture into an immune-coated surface [21].

It is well known that species bigger than 2–3 μm are easily trapped by an USW namely, can be focused at the nodal plane of the standing wave and kept closely immobile [22]; isolated particles, as well as 2D and 3D aggregates, can be kept in stable levitation [23]. When species become smaller than ~1 μm, Brownian agitation becomes not negligible and acoustic and thermodynamic forces enter in competition for establishing a steady state after a relaxation time. Nevertheless, the well-known phenomenon called acoustic streaming (AS), in this study we are dealing with Rayleigh streaming [19,24], becomes visible when a suspension is composed of sub-micronic particles, thus displacements of fluid may drag the species over the whole volume of the resonator modifying thereby the thermodynamic equilibrium. Several works have been devoted to the observation and description of the acoustic streaming in microfluidic devices [15,25–27].

AS is always present when the acoustic radiation pressure generated by USW is operating, but primary radiation forces veil it when micron-sized species are manipulated. Several works have visualized the AS by using particle image velocimetry, (PIV) [15,27,28], showing that the flow velocity generated by the streaming is strong enough for making the manipulation of sub-micronic species extremely difficult. Manipulation means generating relative displacements between particles and the surrounding fluid under the action of ultrasonic radiation forces in order to induce separations, aggregation or other transport processes. It has been observed that AS concentrates sub-micronic particles in stream-lines forming clumps, leading to configurations that may depend on the acoustic energy distribution, but also on the competition between radiation forces and diffusion [27].

In this work, we experimentally demonstrate the possibility of controlling the AS by using a pulsed ultrasound technique. Thus, species in Brownian motion can be focused close to a nodal plane in a resonator generating a steady concentration profile, and at the same time, AS can be systematically reduced to a minimum

* Corresponding author.
E-mail address: hoyos@pmmh.espci.fr (M. Hoyos).

0041-624X/$ - see front matter © 2012 Elsevier B.V. All rights reserved.
http://dx.doi.org/10.1016/j.ultras.2012.03.015

detectable, keeping secondary forces strong enough for generating aggregates of micron-sized species. We demonstrate in this study that the pulsed ultrasound is more efficient for controlling the acoustic streaming than the technique consisting in reducing the amplitude of the acoustic waves. By using the technique we propose, new applications in colloid sciences requiring aggregation and separation should be possible.

2. Acoustic streaming and sub-micronic species

The term streaming generally describes the flow induced by any force acting upon a fluid and dominated by its fluctuating velocity components. The AS is induced by the non-uniformity of the acoustic field and/or by the energy dissipation at the boundary layer at the vicinity of the interface fluid–solid wall of the resonator. The AS is so far a well understood non-linear phenomenon; many papers and books have been thoroughly reviewed the different types of streaming and analyzed its effects in particle and cell manipulation [18,19,27,29,30]. The AS may be visualized using μPIV taking sub-micronic particles as seeds following the streamlines [31–34]. AS in microfluidic channels has been visualized with flow velocities spanning from tenths to hundreds of μm/s [15,27]. It has been demonstrated that micron-sized particles, cells and even bacteria [35] can be trapped by primary radiation forces, but are not affected by the streaming. Let's note that the acoustic primary force and the streaming force are proportional in theory because both are proportional to the acoustic energy density [15,36], but the relationship between them is difficult to establish experimentally, for that purpose, a thorough study beyond of this work would need to be conducted.

3. Pulsed ultrasound technique

We have recently demonstrated that micron-sized species $d \geqslant 10$ μm, latex particles and cancer cells, can be manipulated by using pulsed ultrasounds [37]. We demonstrated that the aggregation rate and the configuration 3D or 2D could be controlled in a very precise way. In that aggregation process the AS was not playing any roll even though the observed weak rotation or vibration of a whole aggregate could be attributed to the AS. Pulsed ultrasound technique consists on sending a group of N of pulses or periods denoted by $T_p = N/f$, with f the driven frequency, separated by repetition time T_r. Therefore, species undergoing the optimum or maximum force migrate at a maximum velocity during short periods T_p separated by times of rest T_r called, leading to an average velocity smaller than that corresponding to continuous mode ultrasound.

4. Experimental section

4.1. Experimental set-up

Experiments have been conducted in two different chambers in order to show that the control of the streaming is independent of the resonator geometry. The first ultrasonic resonator UR1, was a Hele-Shaw cell of 4 cm length, 5 mm wide and 280 μm thickness, composed of 2 mm thick stainless steel plate and 1 mm glass plate separated by a polyimide Kapton® tape spacer assembled in sandwich with neoprene glue. The second ultrasonic resonator UR2, was a cylinder of 5 mm diameter and 180 μm thickness composed of a 2 mm stainless steel plate and 180 μm thick glass slide, separated by polyimide Kapton® tape. The transducer was glued with conductive epoxy (Chemtronics ITW, Kennesaw GA, USA) behind the metal plate in both chambers. Ultrasounds have been generated by 100 MHz dual channel arbitrary wave generator (5062 Tabor Electronics, Israel), the signal was amplified by a dual differential wide band 100 MHz amplifier (9250 Tabor Electronics, Israel) and the signal was visualized with a digital storage oscilloscope (IDS 8064 60 MHz ISOTECh, Hanan–Israel). We employed 800 nm latex particles (Fluorescent particles, Polysciences Inc., Warrington PA, USA) of concentration less than 0.1%; some experiments have been performed with a mixture 800 nm and 15 μm latex particles (Micromod Rostock-Warnermunde, Germany). All the experiments have been performed in steady state. The suspension has been observed by a reflecting Olympus epi-fluorescence microscope with magnifications 10X and 20X, provided with a high resolution camera DCU223 M ThorLabs (Hans-Brocker, Dachau Germany) and recorded in a PC computer.

4.2. Experimental results and discussion

We perform several experiments in both resonators: UR1 parallel plate channel at resonance frequency 2.63 MHz, and UR2 cylindrical shape at resonance frequency 4.12 MHz. The maximum amplitude applied in both resonators was $13V_{p-p}$. Both resonators present one pressure node close to the mid distance between the walls.

4.2.1. Evidence of the acoustic streaming control

The acoustic streaming was first studied in UR1 device. When the acoustic was off, 800 nm particles showing Brownian motion, were initially distributed in the whole channel thickness. Once the acoustics applied, the nano-metric-sized particles were both, focused by the primary radiation force around the nodal plane and dragged out by the AS. After a period of relaxation, a quasi-steady state was observed into the microscope field of view, which was 210×157 μm^2 at 10X magnification. The quasi-steady state was identified when the streaming velocity and the thickness of the layer formed by focused particles reached constant values; that relaxation time was estimated less than 45 s in our specific experimental conditions. The focus of the microscope in the thickness was fixed at the nodal plane, previously determined by the equilibrium position reached by 15 μm latex particles when the ultrasounds were acting at maximum amplitude. The concentration profile showed an apparent higher nanometric particle concentration at the nodal plane. We determined the layer thickness by fixing the positions of the firsts and the last particles with the focus of the microscope. The precision of the measurement was relatively low in continuous mode at maximum amplitude because of the presence of the AS. We reach better precision in pulsed and continuous modes when the AS was the minimum observable; we shall discuss this aspect later on.

Structures already reported [26,27] have also been observed in our resonator namely, the agglutination of particles and recirculation forming stretched clouds, as shown in Fig. 1. These structures more or less stable have been formed several minutes after the acoustic force was applied. The meaning of "stable" is that the structure remains more or less unchanged even though particles continue to move agglutinating and following the streamlines in closed trajectories. The explanation of those structures is related to the energy distribution in the resonator and on other resonances generated by geometrical factors [38]. We fixed the observation zone where the particle flux was roughly constant and the streaming velocity throughout the horizontal plane did not vary more than 20%; the streaming velocity considered was an average of particle velocities determined at three different points in the plane field of view. Let's note that when ultrasounds were turned off, the flow stops instantly while when the acoustics was turned on, the streaming takes some seconds to be established. The AS characteristic velocity has been determined by tracking both, individual particles and small aggregates composed of a few particles,

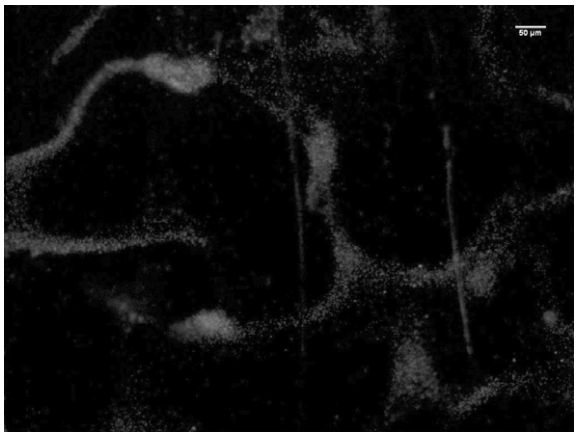

Fig. 1. Acoustic streaming patterns of 800 nm fluorescent particles, magnification 5X, observed at the resonator in continuous regime after 2 min.

by using the freeware software Tracker [39]. Individual particles have been tracked when the microscope was operating in fluorescence mode.

The first experiment was to measure the characteristic streaming velocity $v_{s,\max}$, in continuous mode at maximum applied voltage. An example of tracking particles is depicted in Fig. 2 where a superposition of three images shows the displacement of a small aggregate composed of a few 800 nm particles during 7 s. The average streaming velocity in that example, was $v_{s,\max} = 15$ μm/s. It is worth noting that in many cases colloidal aggregates formed during the process, of diameter bigger than ~10 μm, have been found moving at slower velocity than the bulk flow, till 30% of the streaming velocity. This is an important finding because a relative velocity between an object, in this case a colloidal aggregate and the surrounding fluid, means that the object could be manipulated by acoustics as done with rigid particles. We shall refer to this aspect in the last section.

In order to study the influence of pulsed ultrasound on AS we performed experiments measuring the streaming velocity of nano-metric-sized particle velocity, at different number of pulses T_p i.e. time of acoustic "on" and different repetition time T_r i.e. time of acoustic "off". In Fig. 3 is depicted the normalized streaming velocity $v_s/v_{s,\max}$ in pulsed mode in function of the number of pulses N for three different repetition frequencies $f_r = 1/T_r = 1.9$, 2.5 and 4.3 kHz. The curves show the separated influence of the time "on" and "off" on the streaming velocity. At fixed repetition frequency, v_s is a monotonously increasing function of the time of applied ultrasounds, and at fixed number of pulses v_s is an increasing function of the repetition frequency. This trend was expected, in fact, we assume that in mode "acoustic on" particles move at constant velocity during the time T_p corresponding to the maximum streaming velocity $v_{s,\max}$ and in "acoustic off" particles stop instantly. These curves show that we have two useful parameters for controlling the AS in complementary manner. The following experiments have been performed in order to demonstrate that pulsed ultrasound allows diminishing the streaming in the resonator without inhibiting the possibility of manipulating micron-sized objects like particles or cells. Nevertheless, before referring to latter experiments, it is worthwhile to compare the pulsed mode of operation applied for reducing the streaming, to the technique of reducing the amplitude that should produce the same effect.

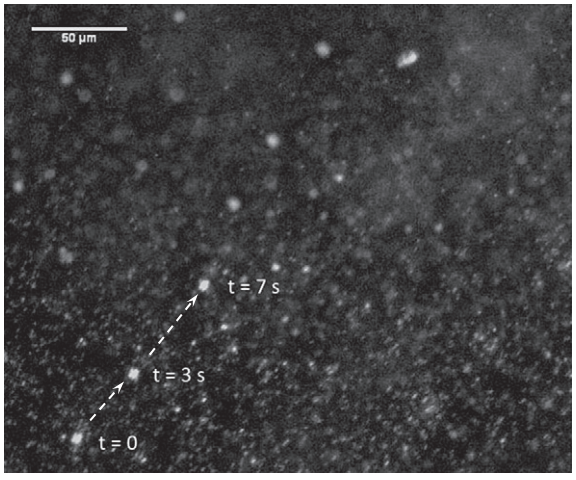

Fig. 2. Superimposed images of an aggregate of 800 nm particles at the levitation plane (magnification 10X), at three different moments of the migration under continuous regime. The streaming velocity was vs ~15 μm/s.

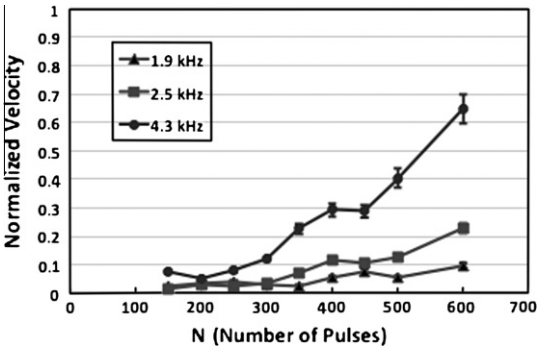

Fig. 3. Relationship of the normalized streaming velocity and the number of pulses using three different repetition frequencies.

4.2.2. Comparison between pulsed and continuous regimes

Other way of controlling the AS is to modify in continuous mode the wave amplitude, given in V_{p-p}. Experiments performed in UR1 device with 800 nm particles show as expected, the streaming velocity increasing with the amplitude. Nevertheless, in order to compare continuous and pulsed modes, we need to find common variables. On the one hand, it is known that the acoustic energy is proportional to the square of the amplitude [40]. On the other hand, the streaming velocity is proportional to the energy according to the relationship [15]: $v_s = 3\pi/32\,[v_o/c_o]^2 y_l f$ with y_l the levitation plane distance from the bottom wall of the resonator, c_o the sound speed in the fluid and f the frequency; v_o is the amplitude of the ultrasonic velocity related to acoustic energy density by the relationship: $\langle E_{ac}\rangle = 1/2\rho_0 v_o^2$ [15]. We see therefore that the streaming velocity becomes proportional to the average energy density. The maximum streaming velocity $v_{s,\max}$ is the velocity at the maximum voltage and proportional to the maximum energy density $<E_{ac,\max}>$. It follows that $v_s/v_c = \langle E_{ac}\rangle/\langle E_{ac,\max}\rangle = (V_{p-p}/V_{p-p,\max})^2$.

In pulsed mode, we can make the hypothesis that the average particle velocity during one cycle is $v_s = v_{s,\max}\, T_p/(T_p + T_r) = v_c\, P_{mf}$, where $1/(T_p + T_r)$ is the duty cycle, and P_{mf} we called pulse mode factor [37]. Let's note that in continuous mode $P_{mf} = 1$, and $P_{mf} = 0$ when the acoustic is "off". Being proportional to the streaming velocity, P_{mf} becomes thereby proportional to the mean energy density $\langle E_{ac}\rangle$. It follows that, $v_s/v_{s,\max} = \langle E_{ac}\rangle/\langle E_{ac,\max}\rangle = P_{mf}/P_{mf,\max} = P_{mf,}$ with $P_{mf,\max} = 1$. Pulsed and continuous regimes are compared in Fig. 4. In this figure, we subtracted the velocity measured when the acoustic was off, that was 2.14 μm/s higher than the characteristic velocity related to Brownian motion estimated

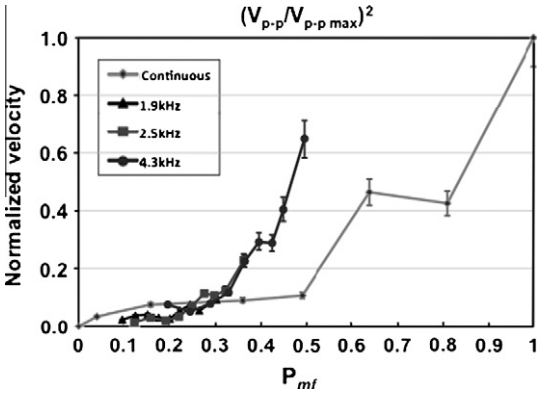

Fig. 4. Relationships between normalized streaming velocities in function of the pulse mode factor in pulsed regime, and of normalized acoustic amplitude square in continuous regime $(V_{p-p}/V_{p-p,max})^2$ and P_{mf} are equivalent.

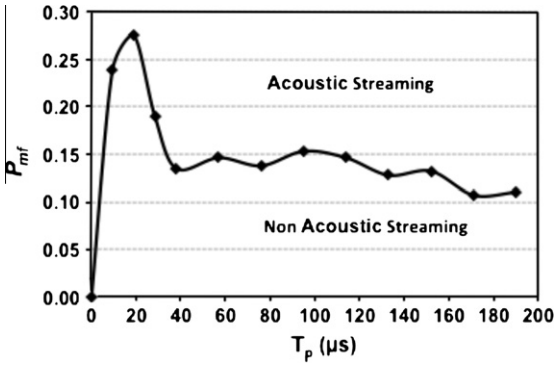

Fig. 5. Acoustic streaming threshold obtained in pulsed mode. Each experimental condition is represented as the relationship between the pulsed mode factor and the time of pulses.

to 1 μm/s. The latter value was obtained by calculating the diffusion coefficient $D = kT/3\pi\eta d \sim 5.5 \times 10^9$ cm^2/s; $d = 800$ nm, k is the Boltzmann constant, T the absolute temperature, and the diffusion length l in a time $t = 1$ s given by $l = (2Dt)^{1/2} \sim 1$ μm. Remaining currents due to defects in horizontality of the chamber and other thermal effects account for this minimum streaming.

If both regimes were equivalent, curves in Fig. 4 should coincide. We surprisingly find that they diverge as the energy density increases. It is interesting to analyze first the curve of pulsed mode. We observe that all points join the same master curve that tell us that P_{mf} is a good parameter to use for controlling the AS. Nevertheless, the curve that should be linear according to the assumptions made before, is rather close to a power law. We don't have a clear explanation of these effects, we might suppose that in reality inertial effects could generate micro-streaming in pulsed mode inducing this non-linearity. Instead, varying the amplitude just reduces the streaming velocity without any other superimposed effect.

The curve corresponding to the modification of the amplitude can be divided in two tendencies, one of constant lower values of the streaming velocity and the other not clearly linearly increasing as predicted by the theory. The divergence in both behaviors shows that for generating the same acoustic streaming velocity it is necessary less energy in pulse mode than in continuous mode. We find this result remarkable because this indicates that pulse mode seems to be a more efficient way of applying ultrasound in resonators. Less energy implies also less heat dissipation that is a good advantage when ultrasounds need to be applied for long periods. A consequence of this result is also that in pulsed mode we cannot determine the energy density by measuring the acoustic streaming velocity using the relationship [15] $v_s = 3\pi f \langle E_{ac} \rangle y_l / 16 \rho_0 c_o^2$ valid only for the system operating in continuous mode. To establish the corresponding relationship in pulsed regime needs a thorough study beyond the scope of this work that is rather focused in validating the pulsed mode for allowing manipulating micron-sized and likely sub-micron-sized species without detrimental effects generated by the AS.

4.2.3. Note about the threshold of the acoustic streaming

A series of experiments aiming to find the conditions in pulsed ultrasound under which the AS was reduced to a minimum have been performed in UR1. The procedure was to use continuous mode for focusing the 800 nm latex particles at the nodal plane and generating AS, then we switched to pulsed mode to systematically vary the number of pulses and the repetition frequency. We thus visually determine the conditions at which the streaming stops or is reduced to the minimum observable, $v_s < 2.5$ μm/s. In Fig. 5 is depicted P_{mf} vs T_p. Two regions are highlighted, above the curve the acoustic streaming is observed and under the curve the acoustic streaming is negligible. Higher values of T_p, corresponding in our experiment to 50 pulses, seem not vary too much around an average value $P_{mf} \sim 0.12$. This value depends on the ultrasonic frequency and probably on the geometry of the resonator; values obtained in UR2, operated at 4.2 MHz have similar behavior around $P_{mf} \sim 0.1$. The curve in Fig. 5 presents a maximum around a T_p corresponding 25 pulses. We don't have any explanation to this behavior that could be associated an inertial effect; a thorough investigation will be conducted about this trend. Curve in Fig. 5 allows thereby optimize the parameters to be used in pulsed mode for controlling the streaming.

4.2.4. Pulsed ultrasound and radiation forces

4.2.4.1. Primary radiation force. The object of this study was not only to find an efficient way of controlling the AS but also to be able to reduce it by keeping the primary and the secondary radiation forces strong enough to manipulate on the one hand non-colloidal particles and on the other hand to explore the possibility of manipulating sub-micron-sized particles. We compare the capability of the resonator to focus colloidal particles at the nodal plane in continuous and pulsed mode in conditions of minimum streaming velocity. Several experiments have been conducted with 800 nm latex particles. After the injection of the suspension in the chamber with the acoustic field off, particles were distributed in the entire thickness. After a few seconds when the suspension reached a stationary state, the acoustic field was applied generating migration of particles toward the node. Measurements of the layer thickness have been done after a relaxation time of 45 s which was the time taken by the suspension to reach the new stationary state. The layer thickness around the acoustic focusing plane was obtained by locating the position of the firsts and the lasts particles at the focus of the microscope; values obtained gave a maximum thickness and not the more reliable measure that would be a mean value of the concentration profile. This determination needs to introduce more elaborated image techniques. We needed only a rough measure of the thickness for comparing both methods. In continuous mode as expected, the layer thickness was observed to increase when the amplitude was decreased. The variations were from 70 to 80 μm at maximum amplitude ($13V_{p-p}$), to 180–190 μm at minimum amplitude ($4.2V_{p-p}$). Let's recall that the chamber was $w = 280$ μm thick, making the layer to occupy about $\sim 0.7w$. In pulsed mode, at $P_{mf} \sim 0.15$, when the streaming velocity was the minimum, the layer thickness was 100–110 μm occupying about $\sim 0.3w$, much smaller than that in continuous mode. This result clearly shows that the primary radiation force is stronger in pulsed mode than in continuous mode at the threshold. This result

is qualitatively in agreement with that suggested in Fig. 4 where stronger acoustic forces are generated in pulsed mode for equivalent average amplitudes, with respect to continuous mode.

4.2.4.2. Secondary radiation force. In order to test the capability of the resonator to keep primary and secondary radiation forces strong enough for generating particle levitation and aggregation, we performed experiments using a 15 μm and 800 nm mixture of latex particles in UR2 resonator; let's note that UR2 is a cylindrical resonator optimized for generating aggregates at the center. The first test consisted in operating the resonator in continuous mode to produce an aggregate of 15 μm particles. A sequence of four images where the aggregate in levitation is surrounded by 800 nm colloidal particles is showed in Fig. 6. Images in Fig. 7a and b separated of 17 s show the evidence of the coexistence between a stable aggregate and the AS. The pattern formed by the smaller particles evolves showing a cloud approaching the aggregate. Images in Fig. 6c and d, shows an aggregate of three particles reaching the main aggregate pushed by secondary radiation forces at a velocity much higher than that of the AS. The aggregate is at stable position and is not affected by the streaming. Experiments with the mixture allowed visualizing the fact that if we were interested only in aggregation of micron-sized species, we might neglect the AS. The experiment followed by switching the system to pulsed mode at 100 pulses and repetition frequency of 6.5 kHz. Levitation was very quick but a little slower that in continuous mode at the threshold. A stationary state is observed in Fig. 7a, and b that show images at 34 s time interval. We also observe that the configuration of colloidal particles around the aggregate remains stable, the aggregate was focused at the same plane as in continuous mode. Analogue experiments performed in continuous regime at the threshold of the streaming, showed that the levitation time was longer than that in pulsed mode. In this case the levitation time was more than one second, and the aggregate did not levitate consolidated as was observed in pulsed mode. This result indicates that primary radiation force is stronger in pulsed mode than in continuous mode at the threshold as previously stated based on particle layer thickness.

The last experiment concerned secondary forces. We measured the velocity of individual 15 μm particles aggregating in continuous and pulsed regimes at the threshold of the streaming. The constant velocity is the result of the equilibrium established between Stokes' drag force and secondary radiation forces responsible of the aggregation at the nodal plane. We limited our research to determine some characteristic velocities at different positions at the nodal plane. We measured 5 velocities for each mode and in average we found that velocities in pulsed mode reach till 35 μm/s, while in continuous regime at the threshold, the velocities were <5 μm/s. This result clearly demonstrates that secondary forces are also stronger in pulsed mode than in continuous mode at the threshold of the streaming.

Finally, we tracked a ~10 μm aggregate of 800 nm particles in pulsed mode at the threshold of the AS. Fig. 8 is a superposition of two images separated by 7 min. The velocity of the aggregate was 0.6 μm/s while the velocity of individual particles was ~2.5 μm/s. This relative velocity is related to the acoustic trapping of the aggregate by acoustic forces. This result demonstrates that colloidal aggregates could be manipulated by ultrasounds in pulsed regime.

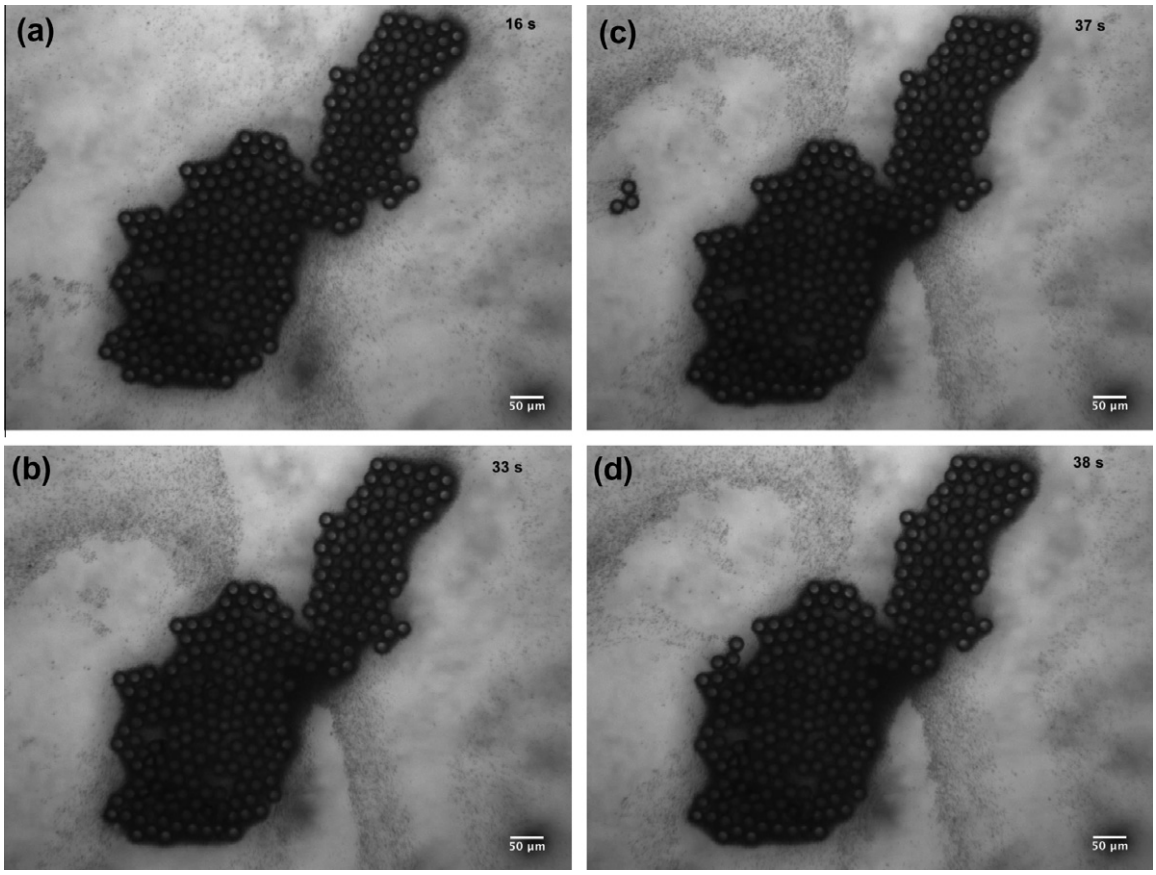

Fig. 6. Images of the acoustic streaming in continuous regime observed (20X) at different times of a mixture of 0.8 and 15 μm latex beads at the levitation plane. (a) and (b): streaming around a 15 μm particle aggregate. (c) and (d): a small aggregate join the big one.

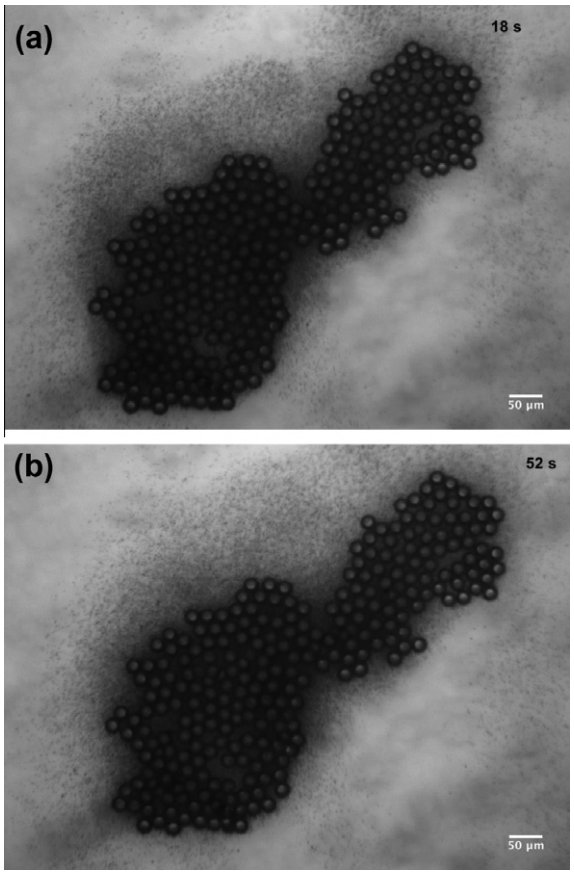

Fig. 7. Images of 0.8 μm particles around a 15 μm particles aggregate obtained in pulsed regime, at the threshold of the streaming, at different times (34 s interval) at the levitation plane (20X). The distribution of smaller particles remains unchanged.

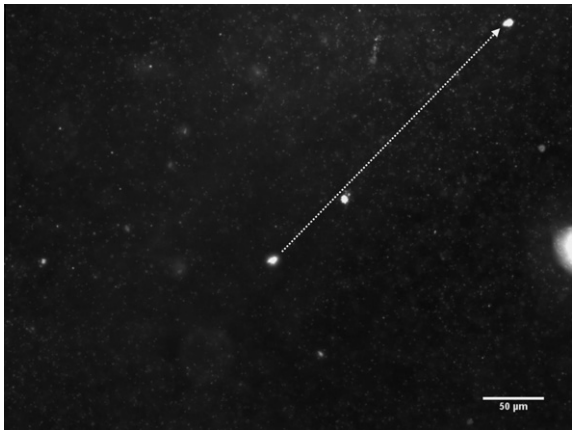

Fig. 8. Superimposed images (10X) separated by 7 min of an aggregate of 800 nm particles, migrating at the levitation plane in pulsed regime at the threshold of the streaming. Aggregate velocity ~0.75 μm/s while the streaming velocity is: ~2.5 μm/s.

5. Conclusion

In this experimental work we demonstrated the possibility of controlling the Acoustic Streaming in an USW fluidic resonator by using a pulsed ultrasound technique. We found that the AS could be reduced and likely stopped by adequately adjusting the number of pulses and the repetition frequency. The pulsed mode factor i.e. the time of pulses times the duty cycle, allows determining the parameters to be used for controlling the AS. The streaming velocity does not increase linearly with the pulse mode factor as predicted, but much faster as a power-like law; pulsed regime being more efficient in generating streaming than the amplitude of the wave. Finally, we demonstrated that secondary acoustic forces affect aggregates of nano-metric-sized particles opening thereby new perspectives in manipulation of colloidal species by ultrasonic standing waves.

Acknowledgment

The authors acknowledge the CNES "Aide à la recherché grant". A.C was supported by CNES-CNRS fellowship.

References

[1] M. Groschl, Ultrasonic separation of suspended particles. Part III: Applications in biotechnology, Acustica Acta Acustica 84 (5) (1998) 815–822.
[2] M. Evander, L. Johansson, T. Lilliehorn, J. Piskur, M. Lindvall, S. Johansson, M. Almqvist, T. Laurell, J. Nilsson, Noninvasive acoustic cell trapping in a microfluidic perfusion system for online bioassays, Analytical Chemistry 79 (2007) 2984–2991.
[3] C. Ratier, M. Hoyos, Acoustical programming in step-splitt flow lateral transport thin fractionation, Analytical Chemistry 82 (4) (2010) 1318–1325.
[4] J.J. Hawkes, W.T. Coakley, Force field particle filter, combining ultrasound standing waves and laminar flow, Sensors and Actuators B: Chemical 75 (3) (2001) 213–222.
[5] F. Petersson, A. Nilsson, C. Holm, H. Jönssonc, T. Laurell, Separation of lipids from blood utilizing ultrasonic standing waves in microfluidic channels, The Analyst 129 (2004) 938–943.
[6] R.J. Townsend, M. Hill, N.R. Harris, M.B. McDonnell, Performance of a quarter-wavelength particle concentrator, Ultrasonics 48 (2008) 515–520.
[7] G.D. Pangu, D.L. Feke, Dropplet transport and coalescence kinetics in emulsions subjected to acoustic fields, Ultrasonics (2007), http://dx.doi.org/10.1016/j.ultras.2007.03.004.
[8] J.J. Hawkes, M.S. Limaye, W.T. Coakley, Filtration of bacteria and yeast by ultrasound-enhanced sedimentation, Journal of Applied Microbiology 82 (1997) 39–47.
[9] W.T. Coakley, G. Whitworth, M.A. Grundy, R.K. Gould, R. Allman, Ultrasonic manipulation of particles and cells, Bioseparation 4 (1994) 73–83.
[10] S.M. Woodside, B.D. Browen, J.M. Piret, Measurement of ultrasonic forces for particle-liquid separations, AICHE Journal 43 (1997) 1727–1736.
[11] G. Whitworth, W.T. Coakley, Particle column formation in a stationary ultrasound field, The Journal of the Acoustical Society of America 91 (1) (1992) 79–85.
[12] D. Bazou, L.A. Kuznetsova, W.T. Coakley, Physical environment of 2-D animal cell aggregates formed in a short pathlength ultrasound standing wave trap, Ultrasound in Medicine and Biology 31 (2005) 423–430.
[13] L.A. Crum, Bjerknes forces on bubbles in a stationary sound field, The Journal of the Acoustical Society of America 57 (1975) 1363–1370.
[14] M.A.H. Weiser, R.E. Apfel, E.A. Neppiras, Interparticle forces on red cell in a standing wave field, Acta Acustica 56 (1984) 114–119.
[15] J.F. Spengler, W.T. Coakley, K.T. Christensen, Microstreaming effects on particle concentration in an ultrasonic standing wave, AICHE Journal 49 (2003) 2773–2782.
[16] J.F. Spengler, M. Jekel, Ultrasound conditioning of suspensions – studies of streaming influence on particle aggregation on a lab and pilot plant scale, Ultrasonics 38 (2000) 624–628.
[17] W.T. Coakley, J.J. Hawkes, M.A. Sobanski, C.M. Cousins, J. Spengler, Analytical scale ultrasonic standing wave manipulation of cells and microparticles, Ultrasonics 38 (2000) 638–641.
[18] W.L. Nyborg, Acoustic streaming due to attenuated plane waves, The Journal of the Acoustical Society of America 25 (1) (1953) 68–75.
[19] N. Riley, Steady streaming, Annual Revisions in Fluid Mechanics 33 (2001) 43–65.
[20] W.T. Coakley, D. Bazou, J. Morgan, G.A. Foster, C.W. Archer, K. Powell, K.A. Borthwick, C. Twomey, J. Bishop, Cell-cell contact and membrane spreading in an ultrasound trap, Colloids and Surfaces B: Biointerfaces 34 (2003) 221–230.
[21] S.P. Martin, R.J. Townsend, L.A. Kuznetsova, K.A.J. Borthwick, M. Hill, M.B. McDonnell, W.T. Coakley, Spore and micro-particle capture on an immunosensor surface in an ultrasonic standing wave system, Biosensors and Bioelectronics 21 (2005) 758–767.
[22] W.T. Coakley, Ultrasonic separations in analytical biotechnology, TIBTECH 15 (December) (1997) 506–511.
[23] D. Bazou, L.A. Kuznetsova, W.T. Coakley, Physical environment of 2-D animal cell aggregates formed in a short pathlength ultrasound standing wave trap, Ultrasound in Medicine and Biology 31 (3) (2005) 423–430.
[24] J. Lighthill, Acoustic streaming, Journal of Sound and Vibration 61 (3) (1978) 391–418.

[25] H. Mitome, The mechanism of generation of acoustic streaming, Electronics and Communications in Japan 81 (3) (1998) 1614–1620.
[26] H. Mitome, Ultrasonic levitation and accompanying acoustic steaming, Japanese Journal of Applied Physics 28 (1988) 146–148.
[27] L.A. Kutznetsova, S.P. Martin, W.T. Coakley, Sub-micron particle behavior and capture at an immune-sensor surface in an ultrasonic standing wave, Biosensors and Bioelectronics 21 (2005) 940–948.
[28] V. Frenkel, R. Gurka, A. Liberzon, U. Shavit, E. Kimmel, Preliminary investigations induced acoustic streaming using particle image velocimetry, Ultrasonics 39 (2001) 153–156.
[29] J.W.S. Rayleigh, The Theory of Sound, vol. 2, Dover, New York, 1945.
[30] Q. Wan, Beam Vibration Induced Acoustic Streaming: A Numerical and Theoretical Analysis, VDM, Verlag, June 5, 2009.
[31] G. Zauhar, H.C. Starrit, F.A. Duck, Studies of acoustic streaming in biological fluids with an ultrasound Doppler technique, The British Journal of Radiology 71 (1998) 297–302.
[32] O. Dron, J.L. Aider, M. Hoyos, C. Ratier, Micro-particle image velocimetry of acoustic focusing particles, Microfluidics and Nanofluidics 7 (2009) 857–867.
[33] J.J. Hawkes, W.T. Coakley, Force field particle filter, combining ultrasound standing waves and laminar flow, Sensors and Actuators B 75 (2001) 213–222.
[34] J.J. Hawkes, R.W. Barber, D.R. Emerson, W.T. Coakley, Continuous cell washing and mixing driven by an ultrasound standing wave within a microfluidic channel, Lab on a Chip 4 (2004) 446–452.
[35] A. Sobanski, C.R. Tucker, N.E. Thomas, W.T. Coakley, Sub-micron particle manipulation in an ultrasonic standing wave: applications in detection of clinically important biomolecules, Bioseparation 9 (6) (2000) 351–357.
[36] K. Yoshioka, Y. Kawasima, Acoustic radiation pressure on acompressible sphere, Acustica 5 (1955) 167–173.
[37] D. Bazou, A. Castro, M. Hoyos, Controlled Cell Aggregation in a Pulsed Acoustic Field, Ultrasonics, in press.
[38] G. Whitworth, W.T. Coakley, Particle column formation in a stationary ultrasound field, The Journal of the Acoustical Society of America 91 (1) (1992) 79–85.
[39] http://www.cabrillo.edu/~dbrown/tracker/.
[40] R. Barnkob, P. Augustsson, T. Laurell, H. Bruus, Measuring the local pressure amplitude in microchannel acoustophoresis, Lab Chip 10 (2010) 563–570.

Appendix E

Autonomous Motion of Metallic Microrods Propelled by Ultrasound

Autonomous Motion of Metallic Microrods Propelled by Ultrasound

Wei Wang,[†] Luz Angelica Castro,[‡] Mauricio Hoyos,[‡,*] and Thomas E. Mallouk[†,*]

[†]Department of Chemistry, The Pennsylvania State University, University Park, Pennsylvania 16802, United States and [‡]Laboratoire de Physique et Mécanique des Milieux Hétérogènes, UMR7636 CNRS, UMPC, ESPCI, 10 rue Vauquelin, 75005 Paris, France

ABSTRACT Autonomously moving micro-objects, or micromotors, have attracted the attention of the scientific community over the past decade, but the incompatibility of phoretic motors with solutions of high ionic strength and the use of toxic fuels have limited their applications in biologically relevant media. In this letter we demonstrate that ultrasonic standing waves in the MHz frequency range can levitate, propel, rotate, align, and assemble metallic microrods (2 μm long and 330 nm diameter) in water as well as in solutions of high ionic strength. Metallic rods levitated to the midpoint plane of a cylindrical cell when the ultrasonic frequency was tuned to create a vertical standing wave. Fast axial motion of metallic microrods at ~200 μm/s was observed at the resonant frequency using continuous or pulsed ultrasound. Segmented metal rods (AuRu or AuPt) were propelled unidirectionally with one end (Ru or Pt, respectively) consistently forward. A self-acoustophoresis mechanism based on the shape asymmetry of the metallic rods is proposed to explain this axial propulsion. Metallic rods also aligned and self-assembled into long spinning chains, which in the case of bimetallic rods had a head-to-tail alternating structure. These chains formed ring or streak patterns in the levitation plane. The diameter or distance between streaks was roughly half the wavelength of the ultrasonic excitation. The ultrasonically driven movement of metallic rods was insensitive to the addition of salt to the solution, opening the possibility of driving and controlling metallic micromotors in biologically relevant media using ultrasound.

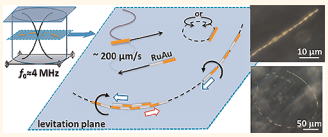

KEYWORDS: ultrasonic standing wave · metallic microrod · autonomous motors · self-assembly · self-acoustophoresis

Synthetic micromotors are an emerging class of micromachines.[1−3] The micromotors studied so far have been driven by a variety of mechanisms, including electrochemical decomposition of chemical fuels,[4−9] magnetic fields,[10−15] magnetic interactions between particles,[16] electric fields,[17,18] light,[19−22] bubble-driven propulsion,[23−26] polymerization,[27] and diffusiophoresis.[21,28,29] Micromotors fall into two classes: they can be propelled by external (*e.g.*, electric or magnetic) fields, and therefore move in concert with each other, or they can be propelled by local conversion of energy and move autonomously. Autonomous micromotors display fascinating biomimetic behavior that includes transport of cargo,[30−33] chemotaxis,[34] swarming, and predator−prey interactions,[21,35] and they have been studied for possible applications in bioanalytical sensing and microfluidics.[9,36−38] However, for motors that can move autonomously, there are issues that limit their practical utility in biological environments. Many catalytic micromotor systems rely on the use of toxic hydrogen peroxide (H_2O_2) or hydrazine derivatives as the fuel.[7−9,23−26,30−33] In addition, the high ionic strength of biological fluids is incompatible with propulsion mechanisms based on electrophoresis and diffusiophoresis.[5,8,10,11,17,24,26,29] While external electric and magnetic fields can be used to drive micro-objects in biological media, the resulting motion is not autonomous. Given the current strong interest in microrobotics for medical diagnostics, drug delivery, and minimally invasive surgeries, there continues to be a need for a biocompatible energy transduction mechanism that can power autonomous micromotors.[1,39,40]

Acoustic energy is an interesting candidate for driving micromotors in fluids, including biological media. Medical applications of sound waves at high frequency, such as ultrasonography, have been developed for decades and are widely used.[41] High frequency sound waves, in particular in the MHz regime, have minimal deleterious effects on biological systems.[42,43] Not only are sound waves in this frequency range safe, they are also a powerful tool for manipulating microparticles. Built upon the experimental discoveries of the acoustic collection of small suspended particles in the early 19th century by Kundt and Lehman,[44] and subsequent theoretical work,[45−47] the understanding of the ultrasonic standing wave and technological advancements in ultrasonic transducers have made more advanced manipulation of suspended microparticles possible.[48−56] For example, suspended microscale spherical particles can be aligned into 1-D lines,[49,50,55] 2-D arrays, and more complicated patterns.[48,52]

* Address correspondence to hoyos@pmmh.espci.fr, tem5@psu.edu.

Received for review March 24, 2012 and accepted May 25, 2012.

Published online May 25, 2012
10.1021/nn301312z

© 2012 American Chemical Society

The 3-D manipulation of microparticles has also been achieved by using the appropriate experimental geometry.[56] This kind of positioning, regardless of its dimensionality (1-, 2-, or 3-D) or how the acoustic field is applied (surface acoustic wave or bulk acoustic wave), is usually considered to be the result of collecting microparticles at the nodes of ultrasonic standing waves, and the motion of the particles is driven by a pressure gradient. Acoustic levitation and streaming are also commonly observed during these experiments. They can be attributed to the primary acoustic radiation force and to steady-state fluid flow caused by the variation of the acoustic field, respectively.[53,57] Another interesting aspect of research in this field is the ability to align high aspect ratio particles, such as rods and tubes,[58−60] and to rotate particles by using acoustic fields.[61,62] However research in this area has so far been limited and autonomous microrod propulsion has not been reported.

Here we describe experiments in which ultrasonic acoustic waves can propel metallic rods in fast (~200 μm/s) axial directional motion as well as in fast in-plane rotation. Additionally, we have observed the formation of ring and streak patterns by metal rods and the assembly of metallic rods and spheres into well-aligned chains, as well as their rotation. The key findings of these experiments are as follows: (1) metallic rods, particularly polar metallic rods, behave differently in acoustic fields than polymer spheres or rods; (2) shape asymmetry drives motion along the axis of the metallic rod, a mechanism we tentatively call self-acoustophoresis; and (3) the presence of metallic rods at the edge of a ring or streak pattern in the nodal plane induces strong vortices in the fluid, which causes the rods to spin and results in their self-assembly into chains.

RESULTS AND DISCUSSION

Experiments were conducted using a homemade cylindrical cell, as illustrated in Figure 1, and videos were taken with an optical microscope (see Supporting Information). Particle motion in the cell was typically observed in dark field.

The conditions for forming a standing wave in this cell are described by eq 1,

$$h = \frac{1}{2}n\lambda = \frac{1}{2}n\frac{c}{f}, \quad n = 1, 2, 3... \qquad (1)$$

where h is the cell height (acoustic path length) and c is the speed of sound in the medium (deionized water, c = 1492 m/s). The cell was designed to have a height of 180 μm. For the simplest case where n = 1, the resonance frequency is calculated from (1) to be 4.1 MHz, and at that frequency a nodal plane forms at the center of the cell where the acoustic pressure is at its minimum (Figure 1, inset). Preliminary experiments indicated a resonant frequency of about 3.7 MHz.

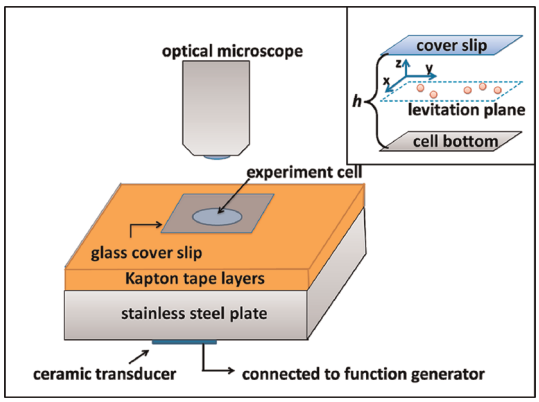

Figure 1. Cylindrical ultrasonic cell. The transducer was mounted on a steel plate at the bottom of the cell. Inset: Illustration of the cell cross-section when the acoustic field is applied. The particles are shown in the levitation plane. The cell height, *h*, is defined as the distance between the top coverslip and the bottom wall of the cell.

Therefore sine waves with a frequency of 3.7 MHz and output amplitude of 10 $V_{p\text{-}p}$ (a output power of 23.97 dBm, or 249.5 mW) were typically used as the starting point for experiments, and both parameters were varied continuously. Experiments were also done in pulse mode, where the acoustic power was delivered at the same instantaneous power and frequency, but in trains of pulses. A number of pulses N was delivered over a period of time T_p, where $T_p = N/f$ and f is the frequency. These pulse trains were separated by a repetition time T_r. The *duty cycle D* is defined by $D = T_p/(T_p + T_r)$.[63] The number of pulses N was varied between 150 and 800, and the pulse repetition rate ($1/(T_p + T_r)$) was varied from 1 to 4 kHz. This is illustrated in Figure S12 (see Supporting Information).

Spherical Polystyrene Particles. Experiments were first conducted with polystyrene microspheres (470 nm and 2 μm diameter) to gain an understanding of the motion of spherical particles in the cylindrical acoustic cell. FESEM images of the polystyrene particles are shown in the Supporting Information (Figure S1 and S2). In the absence of ultrasound, colloidal particles suspended in the cell showed ordinary Brownian motion (Supporting Information video S1, part 1), and there was little evidence of interparticle or particle−substrate (steel plate) interactions at the particle densities used. Upon application of bulk acoustic waves at 3.7 MHz, the polystyrene particles levitated into the nodal plane (also called the levitation plane), as evidenced by the fast upward motion of all the particles from the bottom of the cell. The origin of the levitation force is well-known in the acoustics literature, and is generally attributed to the primary acoustic radiation force exerted on particles by sound propagation perpendicular to the substrate.[64] Since the acoustic pressure is at its minimum in the nodal plane, particles are trapped in that plane. The frequency range for levitating particles was between 3.5 and

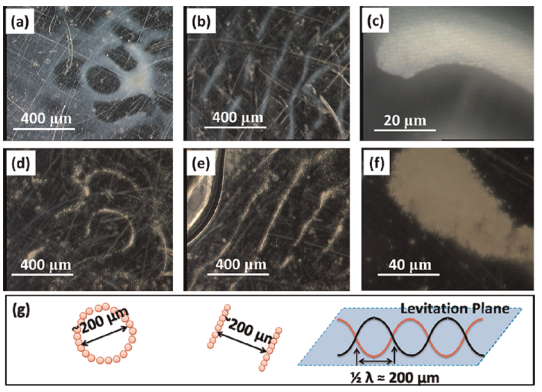

Figure 2. Typical patterns formed by polystyrene (PS) tracer particles in the nodal plane in a 3.7 MHz acoustic field. (a−c) ring patterns, streak patterns, and a dense aggregate formed by 470 nm diameter PS particles, respectively. (d−f) the same types of patterns formed by 2 μm diameter PS particles. In these dark field images, the particles appear bright and the background is dark. (g) Cartoons showing the dimensions of the formed patterns as well as the nodes.

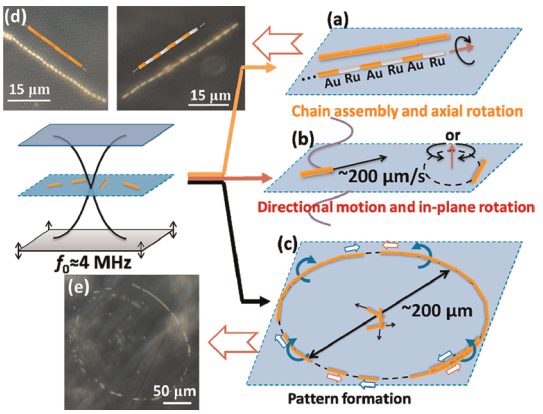

Figure 3. (a)-(c): Illustration of the kinds of motion (axial directional motion, in-plane rotation, chain assembly and axial spinning and pattern formation, especially ring patterns) of metal microrods in a 3.7 MHz acoustic field. AuRu rods (gold−silvery color in dark field) showed similar behavior to the Au rods, except that they moved with their Ru ends (the silvery end in the image) forward and aligned head-to-tail into chains. (d) and (e): Dark field images of typical chain structures and ring patterns formed by Au and AuRu rods. Note that the cartoons superimposed on (d) are intended to show the alignment of the rods and are not to scale or in proportion to the aspect ratio of the Au or AuRu rods.

4 MHz, which was close to the calculated $n = 1$ resonant frequency of the cell. When frequencies below or beyond that range were used, the particles remained at the bottom of the cell. Turning off the acoustic excitation resulted in sinking of the levitated particles.

Once in the nodal plane, both small (470 nm) and large (2 μm) spherical polystyrene particles showed acoustic streaming. At certain frequencies, within seconds to minutes, the particles formed circular or linear aggregates (termed ring and streak patterns, respectively, in the discussion below), as shown in Supporting Information video S2 and Figure 2. It was hard to predict or control the shapes of these aggregates, although varying the frequency could lead to the transformation from streak patterns to ring patterns, or *vice versa*. The collection of particles in patterns in the nodal plane of a bulk acoustic field has been reported before and is generally considered to be due to the variation of the acoustic field in the lateral directions.[57,65] Such variations can arise from near field effects or from higher dimensional acoustic modes.[66,67] Although the origin of these variations is not known in the present case, it appears that the particles follow the acoustic energy distribution in the nodal plane.

The ring diameters and distances between streaks were typically in the range of 200 μm, which corresponds to half the wavelength of the sound wave at the driving frequency. This indicates a correlation between the patterns and the acoustic nodal structures in the plane (Figure 2g). Although sharp resonance patterns are difficult to obtain in the nodal plane because of scattering and reflection of acoustic waves, under certain conditions localized nodal patterns can be formed, and that explains the ring and streak patterns that formed at certain frequencies. One can draw a comparison between the patterns seen in Figure 2 to nodal patterns formed by sand on a Chladni plate, which collects mobile particles at the acoustic nodes.[68] Similarly, 2-D alignment of particles into rings and other more complicated structures has been experimentally demonstrated and theoretically modeled.[52] It is worth noting that once the polymer microparticles were collected and aligned into rings or streaks, they showed only acoustic streaming with no evidence of powered rotation or directional motion in either the levitation plane or the vertical direction.

Metallic Microrods. Suspensions of metallic microrods showed interesting differences from polymer spheres under the same conditions. In these experiments, the rods were typically 1−3 μm long and 300 nm in diameter. FESEM images of the metal rods are included in the Supporting Information. The rods were made of a single metal component (Au, Ru, or Pt) or were axially segmented (AuRu or AuPt, with the two ends being different metals). Au, Ru, and Pt rods behaved almost identically to each other, and this was also true for AuRu and AuPt bimetallic rods. Therefore for the convenience of the discussion, we focus on pure Au and axially segmented AuRu rods. When the acoustic field was turned on, the rods levitated (Supporting Information Video S2, part 1) and ring and/or streak patterns were formed (Supporting Information Video S2, part 5−7), similar to those of polymer tracer particles. However a number of new behaviors (illustrated and summarized in Figure 3), including powered autonomous motion, were also observed.

Once in the levitation plane the metallic rods showed axial directional motion (Figure 3b) at speeds as high as ~200 μm/s, as can be seen in Supporting

Information Video S2, part 2. The directional motion of a few AuRu rods at the resonant frequency was tracked, and the trajectory is plotted in Supporting Information Figure S10. It is important to note that this motion was not driven simply by fluid convection, as rods that were near each other in the fluid moved autonomously in different directions. Varying the amplitude of the acoustic wave can lead to faster or slower rod speed. The speed was a function of both the location of the rods in the levitation plane and the frequency of the acoustic wave. For example, at a driving frequency of 3.776 MHz, the rods near the cell center showed very fast axial motion as well as in plane rotation (Supporting Information Video S2, part 3), while rods near the edge of the cell showed much slower motion. Therefore we identify 3.776 MHz as the resonance frequency for the cell center. It is important to note that even a slight deviation (a few kHz, about 1% of the frequency) away from the resonant frequency dramatically decreased the intensity of the rod motion. However tuning the frequency away from resonance for the cell center brought other parts in the cell into resonance and induced rapid movement of metal rods in those locations. Representative observations of this motion are shown in Supporting Information Video S2, part 2. Although we could not distinguish in the optical microscope which end was moving forward for single component metal rods, the two ends of the bimetallic rods had clear optical contrast in dark field, from which we could infer that they were propelled with one end consistently forward. For example, in the case of AuRu rods, the directional motion was always with the Ru end (which appears silvery in the dark field) leading. This suggests that the asymmetry of composition or shape of the metal rods can lead to directional motion.

Directional motion of metal rods occurred everywhere in the levitation plane, even where rods were aggregated into ring or streak patterns (Figure 3c). As noted above, the metallic rods when levitated into the nodal plane also formed ring and streak patterns. However unlike the polymer spheres, which showed only acoustic streaming within these patterns, metallic rods moved along the edges of these patterns and particularly for the ring patterns orbited the center of the ring, with different rods orbiting clockwise and counter-clockwise. This indicates that the propulsion of the metallic rods in the acoustic field is independent of their aggregation into rings or streaks; that is, the aggregation of the rods into patterns did not stop their directional motion or change their direction. Additionally, the metallic rods not only formed a dense ring pattern, as polystyrene particles did, but also populated the inside of the ring, forming many concentric and less dense rings in which chains of rods orbited the center (see Figure 3e and Supporting Information Video S2, part 5). At the centers of these rings, there was a smaller number of metal rods showing limited directional motion. As noted above for the case of polystyrene particles, the aggregation of metal rods into defined structures in the levitation plane can be attributed to the distribution of the acoustic energy in that plane.

Within the rings or streaks formed by metallic rods we observed another unique behavior that was not seen with spherical polymer particles. The metal rods and their aggregates rotated rapidly about the axis of the rods and the spindle axis of the rod-shaped aggregates, respectively, as is illustrated in Figure 3a. In contrast, for 470 nm and 2 μm diameter polymer spheres, we observed the aggregation of particles into patterns, but no axial rotation. Owing to the instrumental limitation of the camera used to record the videos (30 frames per second), the rotation speed of the metal rods or aggregates could not be accurately measured. At present, this motion is not completely understood, but it has been reported that ultrasound irradiating metal particles and cylinders in suspension can excite elastic surface waves, or Rayleigh waves, at frequencies spanning from kilohertz to megahertz depending on the nature of the metal.[69] Depending on the angle of the incident wave, in this case the standing wave in the levitation plane, the surface waves can have a helical shape with respect to the rod axis.[70] We hypothesize that the helical surface waves can drive the rotation of the metal rods, which in turn creates a vortex through hydrodynamic drag. It may also cause the in-plane rotation of metallic rods noted above (Figure 3b and Supporting Information Video S2, part 3), since in that case the incident wave is in the vertical direction, not in the levitation plane as it is for rods rotating axially. It is important to note that Rayleigh waves are also present in the case of spheres, generating rotation by interaction with incident standing waves. This will help explain the chaining and rotation of gold microspheres, which will be discussed below. This effect was seen only for metallic particles and not for polymer particles, presumably because the elastic waves in polymers are dampened much more effectively because of the higher compressibility of polymers.

For ring patterns, the vortices always pointed to the inside of the ring in the sense that fluid was driven into the ring from above and out from below, regardless of which direction the rods were moving or where they were observed on the ring. This toroidal motion can be seen in Supporting Information Video S2, part 6. This uniform flow pattern around the ring, concurrent with the axial movement of rods around the ring, indicates that the generation of vortices and the axial propulsion of the metal rods have two distinct mechanisms and can be decoupled.

To examine more closely the fluid flow induced by the spinning metal rods as well as to study the interaction between the metal rods and passive tracer

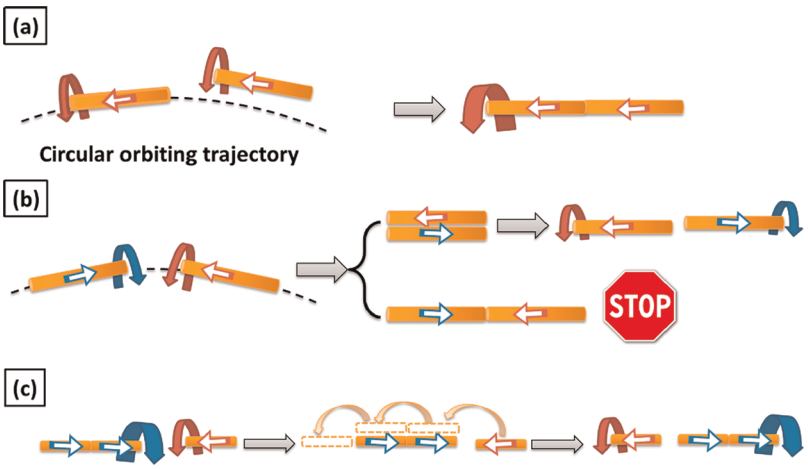

Figure 4. Illustration of chain assembly and directional motion of metal rods along the chains: (a) two metal rods moving in the same direction along the ring interacts and form a spinning doublet. (b) two metal rods moving in opposite directions either brush against each other or meet each other head-to-head (much less likely to occur); (c) when a metal microrod meets a chain moving in the opposite direction, the rod brushes against the chain and the two parties continue separately.

particles, we mixed metal rods with 470 nm polystyrene particles (see Supporting Information Video S3). The tracer particles were readily trapped by the vortex formed around the metal rods once the ring or streak patterns were established, and they were observed to orbit around the rod spindle axis. The hydrodynamic drag of the vortex extended many rod diameters into the fluid, and the vortex tended to become stronger as the spinning bundle increased in length and diameter. The motion of tracer particles in this experiment also confirmed the toroidal fluid pumping into and out of the ring.

The vortices generated by the metal rods lead to the self-assembly of the rods into chains, as illustrated in Figure 3(a) and (d), and in Video S2, part 4 as well as Video S4, part 5. The chaining occurred exclusively in the ring and streak patterns, and is believed to result (as described below) from a combination of several attractive and repulsive forces. Once two metal rods align, they continue to assemble with other rods, individual or chains, and form long chains. Interestingly, when two chains (or rods) traveling in opposite directions meet each other, they do not interfere with each other's motion or assemble into growing chains. Instead they spiral around each other and continue in their original direction of motion; these directions are opposite along the chain axis, because all the rods are confined by the vortex drag force. This illustrates the strong integrity of the self-assembled chain structures. Figure 4 schematically illustrates the self-assembly and interactions of chains formed by metal rods.

We also observed polar chains formed by AuRu bimetallic rods (Figure 3a,d). Each polar rod in these chains points in the same direction so that the chain has an AuRu|AuRu|AuRu|... structure. This head-to-tail assembly is not particularly surprising considering that the bimetallic rods always move with the same end forward (*e.g.*, the Ru end for AuRu rods), and only rods moving in the same direction can align into chains. As noted above, chains moving in opposite directions eventually pass each other without coalescing into a single chain.

Metallic Spheres and Polymeric Rods. To better understand the effects of different materials and shapes in the ultrasonic field, we conducted control experiments with polymer (polypyrrole) rods and gold microspheres. The behavior of these particles is summarized briefly in Table 1.

To summarize the results collected in the table, metal rods induced strong vortices when aligned and also showed strong axial directional motion, whereas spherical metal particles induced vortices but only rarely showed directional motion, which was possibly a consequence of some small shape asymmetry. Polymer particles, regardless of their shape, did not show directional motion or induce strong vortices. This supports the hypothesis that material and shape are important in inducing strong vortices and directional motion. In addition, the fact that polymer rods showed no directional motion but weak axial rotation when aligned supports the hypothesis that axial rotation and directional motion are distinct behaviors that arise from different effects in the acoustic field.

Among the kinds of motion described above, axial propulsion is particularly interesting because it opens up the possibility of powering autonomous movement in a variety of media that are compatible with ultrasound. The speed of axial propulsion can be altered by changing the amplitude and the frequency of continuously applied acoustic energy. Another way to change the activity of the acoustic motors, and to estimate the magnitude of forces that cause levitation, chain formation, and axial motion, is by using pulsed ultrasound. Pulsed-mode experiments were carried

TABLE 1. Summary of Behaviors of Different Samples in an Acoustic Field

sample	pattern formation[a]	directional motion	particle alignment into chains[c]	aggregate spinning
polymer spheres	yes	no	no, particles were loosely aligned into narrow aggregates	no
polymer rods	yes	no	no, particles were loosely aligned into narrow bands	yes, but weak
metallic spheres	yes	some did[b]	yes, with clear attraction between particles	yes, fast
metallic rods	yes	yes	yes, very regular chains were formed, clear attraction between particles observed	yes, fast

[a] Patterns formed by either polymer or metallic microparticles in an acoustic field are generally rings, streaks, or dense aggregates. [b] A small percentage of gold microspheres showed fast directional motion in an acoustic field. It is likely that these gold particles were not perfectly spherical (as can be seen in Supporting Information, Figure S3), and that their asymmetric shapes induced directional motion as in the case of gold rods. [c] See Supporting Information, Figure S11.

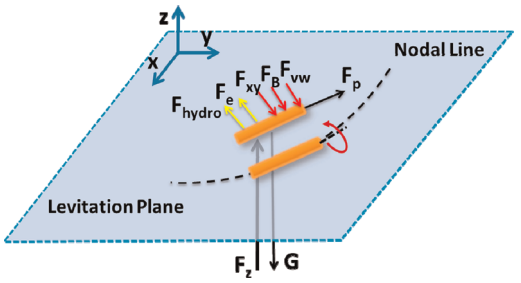

Figure 5. Illustration of the forces experienced by a metal rod in an acoustic field during self-assembly into chains. Red and yellow colors denote forces that bring the rods closer and push them apart, respectively. F_z, the primary radiation force in the z direction; G, the gravitational force; F_p, the propulsion force; F_{hydro}, the hydrodynamic force from the vortex; F_e, the electrostatic force; F_{xy}, the transverse component of the primary radiation force in the levitation plane; F_B, the Bjerknes force; F_{VW}, the van der Waals force.

out at the same frequency and amplitude as in the continuous experiments. The threshold for levitating rods at the onset of rotating motion was at a duty cycle of $D_0 = 0.04$, which translates to a 1 kHz pulse repetition rate and $N = 150$. By choosing different combinations of T_r and T_p, and therefore different D, it was possible to observe the onset of different kinds of movement. For example at a high D, which means a larger T_p and smaller T_r, metal rods levitate and show strong rotation. However when D is lowered, the activity of the rods decreased until at the threshold D_0 the rods maintained levitation but showed little rotation. A duty cycle below the threshold D_0 results in destabilization and sinking of the rods back to the bottom of the cell. Supporting Information, video S5 demonstrates a pulse mode experiment with metal rods at a small pulse repetition rate.

Discussion of Forces at Work. The results from the pulsed-mode experiments help to quantify the forces at work in the different motions of the metal rods, especially the self-assembly into spinning chains (Figure 5). First, there is a primary radiation force (PRF) in the z direction (F_z) that levitates the rods and pushes them into the nodal plane at the center of the cell. Below the threshold duty cycle of $D_0 = 0.04$, metal rods were no longer levitated and began to sink. At this power, the levitation force balances the gravitational force (G), which is approximately 0.027 pN for 2 μm $\times$ 300 nm gold rods. Therefore, for experiments carried out with continuous ultrasound at the same instantaneous power, the levitation force in the z direction can be estimated to be $1/D_0 \times 0.027$ pN = 0.75 pN.

There is also a transverse component of that primary radiation force acting on the rods in the xy levitation plane (F_{xy}), which pushes them into nodal lines and forms the streak and ring patterns in the levitation/nodal plane. At low Reynolds numbers ($\sim 10^{-4} - 10^{-5}$ for microrods moving at a few μm/s), this force is equal to the hydrodynamic drag force, which can be estimated from eq 2.

$$F_{drag} = \frac{2\pi\mu L}{\ln\left(\frac{2L}{R}\right) - 0.72} v \qquad (2)$$

where μ is the dynamic viscosity of water, L is the length of the rods (2 μm), R is the radius (150 nm), and v is the velocity of the rods that are being pushed to the nodal lines, which is as $\sim$5 μm/s as seen in the video clips. From eq 2, the drag force calculated to be $\sim$0.025 pN, which equals to the transverse primary radiation force F_{xy}. The 1–2 orders of magnitude difference between the primary radiation force in the z direction (0.75 pN) and the xy direction (0.025 pN) is consistent with previous experiments in similar geometries.[71]

The force that propels the metal rods along their axis (F_p) can also be estimated from eq 2, only in this case the velocity v can be as high as 200 μm/s, which corresponds to a force of 0.98 pN. This force is about 2 orders of magnitude stronger than F_{xy} and is comparable to the primary radiation force in the z direction F_z. This suggests the axial propulsion of the metal microrods arises primarily from scattering of acoustic waves traveling in the z-direction. A more detailed discussion on the axial propulsion will be provided in the following section.

It is well-known that for two particles in the same nodal plane there exists an attractive force between the particles that arises from the reflected wave from one particle acting on the other. This is known as the secondary radiation force, also called the Bjerknes force (F_B). Woodside *et al.* measured the Bjerknes force relative to the primary radiation force in the z direction for two 5.1 μm radius polystyrene particles and found that the maximum F_B is approximately 2 orders of magnitude weaker than the maximum F_z.[65] Using their

experiment as a guideline we estimate the average Bjerknes force between two metal rods to be the order of 10^{-2} pN, which is similar to the transverse component of the primary radiation force F_{xy}. We note that F_B scales as $1/D^2$, where D is the distance between the particles. Therefore as the rods get closer to each other they experience a stronger F_B.

Another attractive force is the van der Waals force (F_{VW}), which is significant only at short-range. By approximating the particles as 1 μm diameter gold spheres, we estimate F_{VW} on the order of 10^{-2} pN at $D = 1$ μm from

$$F_{VW} = \frac{AR}{12D^2} \quad (3)$$

Here A is the Hamaker constant for gold (3.0×10^{-19} J), R is the radius of the particle (500 nm), and D is the distance between the particles. Since F_{VW} is on the same order of F_B, they play similar roles in bringing two rods together when they are relatively close.

For metal rods that have a negative zeta potential in water, there is additionally a longer-range electrostatic repulsive force (F_e). As detailed below, we compared the behavior of the metal rods in pure water and in solutions of high ionic strength in which the electrostatic attraction should be screened at distances greater than tens of nanometers. Because the behavior was similar in the two media, it appears that the effect of electrostatic repulsion in the chain assembly process is negligible.

Considering the magnitude and direction of these forces, we present the following scenario for the self-assembly of metal rods: two rods moving near the nodal line are pushed by the transverse primary radiation force (F_{xy}) so that they align on the nodal line, preferentially into one line so each rod is at the pressure minimum. When rods align within a distance of a few micrometers, the attractive Bjerknes (F_B) and van der Waals (F_{VW}) forces cause them to accelerate toward each other and form a chain. The spiral trajectory of the rods moving together and eventually connecting to form a spinning chain on the nodal line, as shown in Supporting Information, Video S2 part 4, is a combination of the axially forward motion of the incoming rod and its circular revolution around the chain.

Mechanism of Axial Rod Propulsion. At present, the axial motion of the metallic rods is not understood quantitatively, but some mechanisms can be eliminated based on control experiments. One of these is self-electrophoresis, which is one of the most important mechanisms for catalytic microparticle propulsion in the presence of chemical fuels such as H_2O_2.[72,73] Because the generation of H_2O_2 in water by ultrasound has been reported,[74] it is conceivable that H_2O_2 generated at the rod surface could contribute to axial motion. However three experimental observations argue compellingly against this mechanism in the present case. The first one is that single-component rods, such as Au and Ru, showed comparable directional motion to bimetallic AuRu rods; the former do not show fast chemically powered movement in H_2O_2 solutions, whereas the latter do. The second observation is that AuRu moved with the Ru end forward when powered by ultrasound and in the opposite direction when powered by H_2O_2.[72] We observed that these rods reversed their direction when an acoustic field was applied to a rod suspension in 5% H_2O_2 solution, indicating different mechanisms with and without the acoustic field. It is also well-known that even low concentrations of salts inhibit the self-electrophoretic movement of catalytic micromotors in H_2O_2.[8] However, we observed identical behavior when the acoustic experiments were conducted in 1, 10, or 100 μM $NaNO_3$ solutions, while the catalytic motors showed significantly decreased activity in 100 μM $NaNO_3$. We also found that the activity of levitated metal rods in ultrasound was not significantly affected in a phosphate buffer saline (PBS) solution diluted 1:1 with water. The latter experiment illustrates the promise of using ultrasonic propulsion of metal rods in a biological environment.

A more plausible mechanism for the directional motion of metal rods in an acoustic field is based on the shape asymmetry of the rods. Nanorods prepared

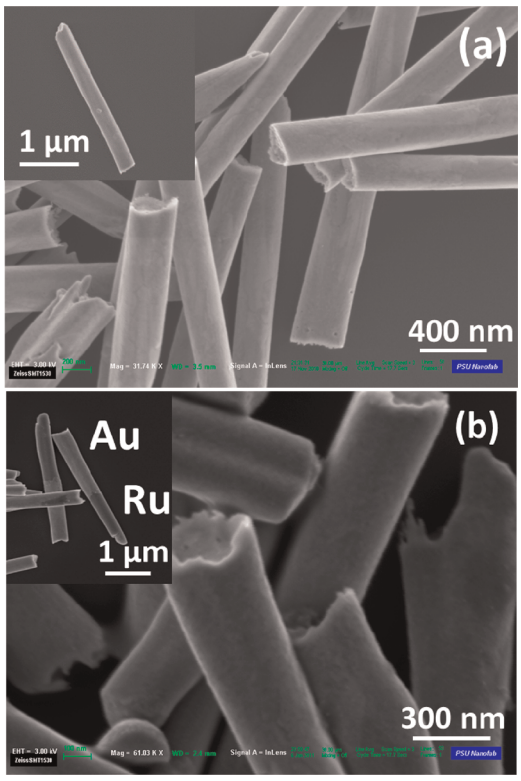

Figure 6. Electron micrographs of Au (a) and AuRu (b) rods used in the ultrasonic propulsion experiments. For AuRu rods, the Au end is clearly concave and there is also some incidence of rod branching at the Au end. The Ru end is usually pointed or flat. Au rods typically have one concave end and one pointed or flat end.

by template electrodeposition typically have a concave or convex end instead of perfectly flat end. The pores in which the nanorods are grown are small enough that the rod−wall interaction can lead to preferential growth along the wall. The unevenness of the surface on the rod end is made more complex by the kinetics of the metal deposition, since fast growth (high current density) produces rougher deposits while slower deposition tends to produce a smoother end surface.[75,76] Field emission SEM images of the metal rods that were used in the acoustic experiments (Figure 6 and FESEM images in the Supporting Information) showed that regardless of the metals used, one end of the rod was always markedly concave while the other end was slightly convex to flat (Ru), fairly flat (Pt) or quite rugged (Au). The end where it was always concave was identified as the end grown immediately after deposition of the sacrificial silver layer, which is typically the first step in electrodepositing nanowires in AAO membranes.

The asymmetric shape of the metal rods can lead to an asymmetric distribution of the acoustic pressure from the scattering of the incident acoustic waves at the metal surface. The scattering of acoustic waves from concave shapes concentrates energy near the curvature, whereas convex shapes scatter radially and weaken the energy density near the curvature. Therefore asymmetric shapes result in an uneven distribution of acoustic pressures in the fluid that is stronger at the concave end (Au end in AuRu rods), propelling the rods with the other end (Ru) consistently forward. It is important to note that many studies have been made about scattering of acoustic waves by cylinders at $ka > 1$ (where k is the wavenumber and a is the cylinder diameter),[70,77] and only a few of them focus on cases where $ka \ll 1$,[78,79] which is the case in the present experiments.

The locally induced pressure gradient propels the metal rods in a similar way as the acoustic pressure gradient moves particles, a phenomenon sometimes called acoustophoresis.[48,80] Since the pressure gradient is generated locally and affects only the individual rods, we use the term self-acoustophoresis to describe this mechanism. We also examined AuPt bimetallic rods and the same mechanism could be applied to explain their direction of motion. Although we cannot identify which end leads the directional motion of single-component metal rods, the same concave features were found on those rods, and therefore their motion can be explained by the same mechanism.

To further investigate this mechanism, we fabricated PtAu wires by electrodepositing Pt before Au segment. Rods made this way had a concave end at the Pt end, as shown in Supporting Information, Figure S4b. In this case, some of the PtAu rods moved with the Pt end forward while others moved with the Au end forward. The reversal of direction of some of the rods supports the hypothesis that the concave feature at the end of the rods is responsible for axial propulsion.

Finally, for ultrasonically propelled micromotors to be useful in biological environments, it is important to evaluate whether the power level is harmful to tissues or cells. The output power from the function generator in a typical experiment is 250 mW. A fraction of this power is transmitted to the sample cell (0.2 cm^2), and the rest is dissipated by the much larger steel plate (20 cm^2) that is coupled to the transducer. While we have not quantified the power density inside the fluid cell, the upper limit is 250 mW/0.2 cm^2 = 1.25 W/cm^2. That power level is intermediate between that of therapeutic ultrasound (several W/cm^2 or higher) and diagnostic ultrasound (740 mW/cm^2, the maximum ultrasonic power level allowed by FDA for diagnostic purposes).[81,82] Because the configuration of our transducer and cell are not yet optimized, it seems reasonable to conclude that fast propulsion of metallic micromotors will be possible within the power limits of diagnostic ultrasound.

CONCLUSIONS

We have demonstrated that MHz frequency acoustic waves can propel, align, rotate, and assemble metallic microrods in water. Control experiments with polymer particles and metal spheres lend support to the hypothesis that shape and material play a critical role in the directional motion and the generation of strong vortices along the axis of aligned metal rods. The fact that axial movement and chain assembly/spinning were observed independently of each other in experiments with metal and polymer rods indicates that the two kinds of movement are caused by distinct effects. On the basis of observations with template-grown homogeneous and bimetallic nanorods, it is likely that shape asymmetry, specifically the curvature at the ends of the microrods, leads to the directional motion by a self-acoustophoresis mechanism. The significance of this finding lies in the possibility of driving and controlling micromachines in biologically relevant environments using ultrasound.

MATERIALS AND METHODS

Sample Preparation. Polystyrene microspheres of 470 nm were purchased from Polybead (cat. no. 07763, amino-functionalized). Polystyrene microspheres of 2 μm were purchased from Polysciences (cat. no. 18327, carboxylate-functionalized). Gold microparticles (AuMP, 0.8−1.5 μm, 99.96+ %) were purchased from Alfa Aesar. The synthetic procedure for growing microrods was adapted from previous reports.[72,83−85] Anodic alumina membranes (AAO, purchased from Whatman Inc., 200 nm pore size) were used as the template for the electrodeposition of

metals. The metal plating solutions were purchased from Technic Inc. and were used as received. A 5 nm length of Cr and 350 nm of Ag were evaporated by using a Kurt Lesker Lab-18 electron beam evaporator on the back side of the AAO membrane (branched side) to serve as the working electrode. A Pt coil was used as the counter electrode. For the deposition of Ag, Au, or Pt, a two-electrode system was generally used with the Pt coil serving as the pseudoreference electrode. In this case, current was controlled to be constant. For the deposition of Ru and polypyrrole, a three electrode system with Ag/AgCl in 3 M NaCl as the reference electrode was used, and rods were grown at constant potential. In a typical deposition procedure, a $\sim$10 μm silver segment was first deposited into the AAO membrane as the sacrificial layer. Then segments of metals (or polymers) of interest were grown. The lengths of the segments were controlled by monitoring the charge passed. The plating conditions for Ag, Au, and Pt were -1.77, -1.24, and -1.77 mA/cm^2, respectively. Ru and polypyrrole were deposited at a constant potential of -0.65 V and $+0.7$ V *vs* Ag/AgCl, respectively. Note that at the potential to deposit polypyrrole, silver is oxidized and dissolved, and therefore in this case a short gold plug was plated in the membrane instead of silver sacrificial layer. Multisegment nanowires were made by replacing the plating solution without disassembling the plating cell, with a rinsing step in between. After the electrodeposition step the membrane was thoroughly rinsed with DI water and dried, and usually one-half of the membrane was soaked sequentially in 1:1 v/v HNO_3 and 0.5 M NaOH to dissolve the silver and the alumina membrane, respectively. After that the wires were sonicated and washed in DI water several times until the pH was neutral. The nanowire suspension obtained from this procedure had a number density of around 1×10^9/mL.

A PBS buffer solution was made by dissolving 1 bag of commercially available BupH phosphate buffered saline pack (Thermo Scientific, no. 1890535) in 500 mL of DI water. The resulting solution contains 0.1 M phosphate and 0.15 M NaCl, and has a pH value of 7.2.

Acoustic Experiments. The acoustic experiment was conducted using a homemade cylindrical cell. The cell was made by applying three layers of polyimide Kapton tape (50 μm thickness per layer), with a circular hole of 5 mm diameter cut in the center, on a piece of stainless steel plate (45 mm $\times$ 45 mm $\times$ 1 mm). A ceramic transducer PZ26 (Ferroperm, Kvistgard, Denmark) was attached by conductive epoxy glue (Chemtronics ITW, Kennesaw GA, USA) to the back of the metal plate to generate acoustic waves in the thickness mode. The transducer was connected to a function generator that outputted sine waves (5062 Tabor Electronics, Israel), and the signal was amplified if necessary by a dual differential wide band 100 MHz amplifier (9250 Tabor Electronics, Israel). The signal was visualized with a digital storage oscilloscope (IDS 8064 60 MHz ISOTECH, Hanan, Israel). In a typical experiment, 30 μL of colloidal particle suspension was added to the cell, which was then covered by a square glass coverslip which served as the sound reflector. In the case of metal rods, the suspension normally had a number density of approximately 1×10^8 mL^{-1}. Video recording was started at the same time the function generator signal output was turned on. An Olympus BX60 M optical microscope and a commercial video capturing bundle (Dazzle Video Creator Plus) were used for observing the particles and recording videos.

Tracking of Particles in an Acoustic Field. The method of tracking the motors was based on our previous work on catalytic nanomotors.[72] Videos of the metal rods were captured at 30 frames per second. The video was then loaded with PhysMo 2, an open source tracking software (PhysMo—Video Motion Analysis Package, http://physmo.sf.net), and the coordinates of the metal rods as a function of time were recorded. Further data analysis was done in Microsoft Excel 2010. Rod speed was calculated by dividing the displacement of the rod center between two frames by the time interval (0.033 s), then taking the average of the speed over the selected tracking period. The tracking was repeated with multiple wires to ensure statistically robust results. An example of the tracking results and trajectories of six AuRu rods at the resonance frequency (3.700 MHz) are shown in Supporting Information, Figure S10.

Conflict of Interest: The authors declare no competing financial interest.

Acknowledgment. We thank Profs. Jay Maynard, Vincent Crespi, and Tony Jun Huang for helpful discussions. Work at Penn State was supported by the National Science Foundation under MRSEC Grant DMR-0802404. M.H. and A.C. acknowledge the financial support BDI from CNES-CNRS and Aide à la Recherche Grant CNES-France. Analytical instrumentation used in this work was supported by the Pennsylvania State University Materials Research Institute Nanofabrication Laboratory under National Science Foundation Cooperative Agreement No. ECS-0335765.

Supporting Information Available: FESEM images of microparticles, representative tracking results of AuRu microrods in an acoustic field, optical images of chains formed in four different experiments, and videos of particle movement in acoustic fields. This material is available free of charge *via* the Internet at http://pubs.acs.org.

REFERENCES AND NOTES

1. Mirkovic, T.; Zacharia, N. S.; Scholes, G. D.; Ozin, G. A. Fuel for Thought: Chemically Powered Nanomotors Out-Swim Nature's Flagellated Bacteria. *ACS Nano* **2010**, *4*, 1782–1789.
2. Wang, J.; Manesh, K. M. Motion Control at the Nanoscale. *Small* **2010**, *6*, 338–345.
3. Mallouk, T. E.; Sen, A. Powering Nanorobots. *Sci. Am.* **2009**, 72–77.
4. Liu, R.; Sen, A. Autonomous Nanomotor Based on Copper−Platinum Segmented Nanobattery. *J. Am. Chem. Soc.* **2011**, *133*, 20064–20067.
5. Pantarotto, D.; Browne, W. R.; Feringa, B. L. Autonomous Propulsion of Carbon Nanotubes Powered by a Multienzyme Ensemble. *Chem. Commun. (Cambridge)* **2008**, 1533–5.
6. Mano, N.; Heller, A. Bioelectrochemical Propulsion. *J. Am. Chem. Soc.* **2005**, *127*, 11574–11575.
7. Kline, T. R.; Paxton, W. F.; Mallouk, T. E.; Sen, A. Catalytic Nanomotors: Remote-Controlled Autonomous Movement of Striped Metallic Nanorods. *Angew. Chem.* **2005**, *117*, 754–756.
8. Paxton, W. F.; Baker, P. T.; Kline, T. R.; Wang, Y.; Mallouk, T. E.; Sen, A. Catalytically Induced Electrokinetics for Motors and Micropumps. *J. Am. Chem. Soc.* **2006**, *128*, 14881–14888.
9. Wu, J.; Balasubramanian, S.; Kagan, D.; Manesh, K. M.; Campuzano, S.; Wang, J. Motion-Based DNA Detection Using Catalytic Nanomotors. *Nat. Commun.* **2010**, *1*, 36.
10. Zhang, L.; Abbott, J. J.; Dong, L.; Peyer, K. E.; Kratochvil, B. E.; Zhang, H.; Bergeles, C.; Nelson, B. J. Characterizing the Swimming Properties of Artificial Bacterial Flagella. *Nano Lett.* **2009**, *9*, 3663–3667.
11. Ghosh, A.; Fischer, P. Controlled Propulsion of Artificial Magnetic Nanostructured Propellers. *Nano Lett.* **2009**, *9*, 2243–2245.
12. Tottori, S.; Zhang, L.; Qiu, F.; Krawczyk, K. K.; Franco-Obregon, A.; Nelson, B. J. Magnetic Helical Micromachines: Fabrication, Controlled Swimming, and Cargo Transport. *Adv. Mater.* **2012**, *24*, 811–816.
13. Gao, W.; Sattayasamitsathit, S.; Manesh, K. M.; Weihs, D.; Wang, J. Magnetically Powered Flexible Metal Nanowire Motors. *J. Am. Chem. Soc.* **2010**, *132*, 14403–14405.
14. Dreyfus, R.; Baudry, J.; Roper, M. L.; Fermigier, M.; Stone, H. A.; Bibette, J. Microscopic Artificial Swimmers. *Nature* **2005**, *437*, 862–865.
15. Zhang, L.; Petit, T.; Lu, Y.; Kratochvil, B. E.; Peyer, K. E.; Pei, R.; Lou, J.; Nelson, B. J. Controlled Propulsion and Cargo Transport of Rotating Nickel Nanowires near a Patterned Solid Surface. *ACS Nano* **2010**, *4*, 6228–6234.
16. Ogrin, F. Y.; Petrov, P. G.; Winlove, C. P. Ferromagnetic Microswimmers. *Phys. Rev. Lett.* **2008**, *100*, 218102.
17. Calvo-Marzal, P.; Sattayasamitsathit, S.; Balasubramanian, S.; Windmiller, J. R.; Dao, C.; Wang, J. Propulsion of Nanowire Diodes. *Chem. Commun.* **2010**, *46*, 1623–1624.

18. Chang, S. T.; Paunov, V. N.; Petsev, D. N.; Velev, O. D. Remotely Powered Self-Propelling Particles and Micropumps Based on Miniature Diodes. *Nat. Mater.* **2007**, *6*, 235–240.
19. Hong, Y.; Diaz, M.; Córdova-Figueroa, U. M.; Sen, A. Light-Driven Titanium-Dioxide-Based Reversible Microfireworks and Micromotor/Micropump Systems. *Adv. Funct. Mater.* **2010**, *20*, 1568–1576.
20. Liu, M.; Zentgraf, T.; Liu, Y.; Bartal, G.; Zhang, X. Light-Driven Nanoscale Plasmonic Motors. *Nat. Nanotechnol.* **2010**, *5*, 570–573.
21. Ibele, M.; Mallouk, T. E.; Sen, A. Schooling Behavior of Light-Powered Autonomous Micromotors in Water. *Angew. Chem., Int. Ed.* **2009**, *48*, 3308–3312.
22. Abid, J. P.; Frigoli, M.; Pansu, R.; Szeftel, J.; Zyss, J.; Larpent, C.; Brasselet, S. Light-Driven Directed Motion of Azobenzene-Coated Polymer Nanoparticles in an Aqueous Medium. *Langmuir* **2011**, *27*, 7967–71.
23. Stock, C.; Heureux, N.; Browne, W. R.; Feringa, B. L. Autonomous Movement of Silica and Glass Micro-objects Based on a Catalytic Molecular Propulsion System. *Chem.—Eur. J.* **2008**, *14*, 3146–3153.
24. Gibbs, J. G.; Zhao, Y. P. Autonomously Motile Catalytic Nanomotors by Bubble Propulsion. *Appl. Phys. Lett.* **2009**, *94*, 163104–3.
25. Solovev, A. A.; Mei, Y.; Bermúdez Ureña, E.; Huang, G.; Schmidt, O. G. Catalytic Microtubular Jet Engines Self-Propelled by Accumulated Gas Bubbles. *Small* **2009**, *5*, 1688–1692.
26. Gao, W.; Sattayasamitsathit, S.; Orozco, J.; Wang, J. Highly Efficient Catalytic Microengines: Template Electrosynthesis of Polyaniline/Platinum Microtubes. *J. Am. Chem. Soc.* **2011**, *133*, 11862–11864.
27. Pavlick, R. A.; Sengupta, S.; McFadden, T.; Zhang, H.; Sen, A. A Polymerization-Powered Motor. *Angew. Chem., Int. Ed.* **2011**, *50*, 9374–9377.
28. Golestanian, R.; Liverpool, T. B.; Ajdari, A. Propulsion of a Molecular Machine by Asymmetric Distribution of Reaction Products. *Phys. Rev. Lett.* **2005**, *94*, 220801.
29. Howse, J. R.; Jones, R. A. L.; Ryan, A. J.; Gough, T.; Vafabakhsh, R.; Golestanian, R. Self-Motile Colloidal Particles: From Directed Propulsion to Random Walk. *Phys. Rev. Lett.* **2007**, *99*, 048102.
30. Campuzano, S.; Orozco, J.; Kagan, D.; Guix, M.; Gao, W.; Sattayasamitsathit, S.; Claussen, J. C.; Merkoçi, A.; Wang, J. Bacterial Isolation by Lectin-Modified Microengines. *Nano Lett.* **2011**, *12*, 396–401.
31. Sundararajan, S.; Lammert, P. E.; Zudans, A. W.; Crespi, V. H.; Sen, A. Catalytic Motors for Transport of Colloidal Cargo. *Nano Lett.* **2008**, *8*, 1271–1276.
32. Balasubramanian, S.; Kagan, D.; Jack Hu, C.-M.; Campuzano, S.; Lobo-Castañon, M. J.; Lim, N.; Kang, D. Y.; Zimmerman, M.; Zhang, L.; Wang, J. Micromachine-Enabled Capture and Isolation of Cancer Cells in Complex Media. *Angew. Chem., Int. Ed.* **2011**, *50*, 4161–4164.
33. Burdick, J.; Laocharoensuk, R.; Wheat, P. M.; Posner, J. D.; Wang, J. Synthetic Nanomotors in Microchannel Networks: Directional Microchip Motion and Controlled Manipulation of Cargo. *J. Am. Chem. Soc.* **2008**, *130*, 8164–8165.
34. Hong, Y.; Blackman, N. M. K.; Kopp, N. D.; Sen, A.; Velegol, D. Chemotaxis of Nonbiological Colloidal Rods. *Phys. Rev. Lett.* **2007**, *99*, 178103.
35. Kagan, D.; Balasubramanian, S.; Wang, J. Chemically Triggered Swarming of Gold Microparticles. *Angew. Chem., Int. Ed.* **2011**, *50*, 503–506.
36. Campuzano, S.; Kagan, D.; Orozco, J.; Wang, J. Motion-Driven Sensing and Biosensing Using Electrochemically Propelled Nanomotors. *Analyst* **2011**, *136*, 4621–4630.
37. Jun, I.-K.; Hess, H. A Biomimetic, Self-Pumping Membrane. *Adv. Mater.* **2010**, *22*, 4823–4825.
38. Zhang, H.; Yeung, K.; Robbins, J. S.; Pavlick, R. A.; Wu, M.; Liu, R.; Sen, A.; Phillips, S. T. Self-Powered Microscale Pumps Based on Analyte-Initiated Depolymerization Reactions. *Angew. Chem., Int. Ed.* **2012**, *51*, 2400–2404.
39. Ozin, G. A.; Manners, I.; Fournier-Bidoz, S.; Arsenault, A. Dream Nanomachines. *Adv. Mater.* **2005**, *17*, 3011–3018.
40. Ebbens, S. J.; Howse, J. R. In Pursuit of Propulsion at the Nanoscale. *Soft Matter* **2010**, *6*, 726.
41. Erikson, K. R.; Fry, F. J.; Jones, J. P. Ultrasound in Medicine—A Review. *IEEE Trans. Sonics Ultrasonics* **1974**, *21*, 144–170.
42. Ziskin, M. C.; Petitti, D. B. Epidemiology of Human Exposure to Ultrasound: A Critical Review. *Ultrasound Med. Biol.* **1988**, *14*, 91–96.
43. Litvak, E.; Foster, K. R.; Repacholi, M. H. Health and Safety Implications of Exposure to Electromagnetic Fields in the Frequency Range 300 Hz to 10 MHz. *Bioelectromagnetics* **2002**, *23*, 68–82.
44. Kundt, A.; Lehman, O. Longitudinal Vibrations and Acoustic Figures in Cylindrical Columns of Liquids. *Annal Phys.* **1874**, 1.
45. King, L. V. On the Acoustic Radiation Pressure on Spheres. *Proc R. Soc., London* **1934**, *a147*, 212–40.
46. Rayleigh, J. W. On the Pressure of Vibrations. *Philos. Mag.* **1902**, *3*, 338–46.
47. Yosioka, K.; Kawasima, Y. Acoustic Radiation Pressure on a Compressible Sphere. *Acustica* **1955**, *5*, 167–73.
48. Shi, J.; Ahmed, D.; Mao, X.; Lin, S.-C. S.; Lawit, A.; Huang, T. J. Acoustic Tweezers: Patterning Cells and Microparticles Using Standing Surface Acoustic Waves (SSAW). *Lab Chip* **2009**, *9*, 2890–2895.
49. Wood, C. D.; Evans, S. D.; Cunningham, J. E.; O'Rorke, R.; Walti, C.; Davies, A. G. Alignment of Particles in Microfluidic Systems Using Standing Surface Acoustic Waves. *Appl. Phys. Lett.* **2008**, *92*, 044104.
50. Haake, A.; Dual, J. Contactless Micromanipulation of Small Particles by an Ultrasound Field Excited by a Vibrating Body. *J. Acoust. Soc. Am.* **2005**, *117*, 2752–2760.
51. Lee, W.; Amini, H.; Stone, H. A.; Di Carlo, D. Dynamic Self-Assembly and Control of Microfluidic Particle Crystals. *Proc. Natl. Acad. Sci. U.S.A.* **2010**, *107*, 22413–22418.
52. Oberti, S.; Neild, A.; Dual, J. Manipulation of Micrometer Sized Particles within a Micromachined Fluidic Device to Form Two-Dimensional Patterns Using Ultrasound. *J. Acoust. Soc. Am.* **2007**, *121*, 778–785.
53. Friend, J.; Yeo, L. Y. Microscale Acoustofluidics: Microfluidics Driven *via* Acoustics and Ultrasonics. *Rev. Mod. Phys.* **2011**, *83*, 647–704.
54. Wang, Z.; Zhe, J. Recent Advances in Particle and Droplet Manipulation for Lab-on-a-Chip Devices Based on Surface Acoustic Waves. *Lab Chip* **2011**, *11*, 1280–1285.
55. Oberti, S.; Möller, D.; Neild, A.; Dual, J.; Beyeler, F.; Nelson, B. J.; Gutmann, S. Strategies for Single Particle Manipulation Using Acoustic and Flow Fields. *Ultrasonics* **2010**, *50*, 247–257.
56. Shi, J.; Yazdi, S.; Steven Lin, S.-C.; Ding, X.; Chiang, I. K.; Sharp, K.; Huang, T. J. Three-Dimensional Continuous Particle Focusing in a Microfluidic Channel *via* Standing Surface Acoustic Waves (SSAW). *Lab Chip* **2011**, *11*, 2319–2324.
57. Martyn Hill, N. R. H., Ultrasonic Particle Manipulation. In *Microfluidic Technologies for Miniaturized Analysis Systems*; Steffen Hardt, F. S., Ed.; Springer: New York, 2007; pp 357−392.
58. Lim, W. P.; Yao, K.; Chen, Y. Alignment of Carbon Nanotubes by Acoustic Manipulation in a Fluidic Medium. *J. Phys. Chem. C* **2007**, *111*, 16802–16807.
59. Kong, X. H.; Deneke, C.; Schmidt, H.; Thurmer, D. J.; Ji, H. X.; Bauer, M.; Schmidt, O. G. Surface Acoustic Wave Mediated Dielectrophoretic Alignment of Rolled-up Microtubes in Microfluidic Systems. *Appl. Phys. Lett.* **2010**, *96*, 134105.
60. Smorodin, T.; Beierlein, U.; Ebbecke, J.; Wixforth, A. Surface-Acoustic-Wave-Enhanced Alignment of Thiolated Carbon Nanotubes on Gold Electrodes. *Small* **2005**, *1*, 1188–1190.
61. Shilton, R. J.; Glass, N. R.; Chan, P.; Yeo, L. Y.; Friend, J. R. Rotational Microfluidic Motor for on-Chip Microcentrifugation. *Appl. Phys. Lett.* **2011**, 98.
62. Hu, J.; Tay, C.; Cai, Y.; Du, J. Controlled Rotation of Sound-Trapped Small Particles by an Acoustic Needle. *Appl. Phys. Lett.* **2005**, *87*, 094104.
63. Bazou, D.; Castro, A.; Hoyos, M., Controlled Cell Aggregation in a Pulsed Acoustic Field. *Ultrasonics* in press.

64. Lierke, E. G. Acoustic Levitation—A Comprehensive Survey of Principles and Applications. *Acustica* **1996**, *82*, 220–237.
65. Woodside, S. M.; Bowen, B. D.; Piret, J. M. Measurement of Ultrasonic Forces for Particle−Liquid Separations. *AIChE J.* **1997**, *43*, 1727–1736.
66. Townsend, R. J.; Hill, M.; Harris, N. R.; White, N. M. Investigation of Two-Dimensional Acoustic Resonant Modes in a Particle Separator. *Ultrasonics* **2006**, *44*), e467–71.
67. Lilliehorn, T.; Simu, U.; Nilsson, M.; Almqvist, M.; Stepinski, T.; Laurell, T.; Nilsson, J.; Johansson, S. Trapping of Microparticles in the near Field of an Ultrasonic Transducer. *Ultrasonics* **2005**, *43*, 293–303.
68. Jensen, H. C. Production of Chladni Figures on Vibrating Plates Using Continuous Excitation. *Am. J. Phys* **1955**, *23*, 503–505.
69. Hobæk, H.; Nesse, T. L., Scattering from Spheres and Cylinders—Revisited. In *29th Scandinavian Symposium of Physical Acoustics*; Norwegian Physical Society: Oslo, Norway, 2006.
70. Bao, X.-L.; Cao, H.; Uberall, H. Resonances and Surface Waves in the Scattering of an Obliquely Incident Acoustic Field by an Infinite Elastic Cylinder. *J. Acoust. Soc. Am.* **1990**, *87*, 106–110.
71. Spengler, J. F.; Coakley, W. T.; Christensen, K. T. Microstreaming Effects on Particle Concentration in an Ultrasonic Standing Wave. *AIChE J.* **2003**, *49*, 2773–2782.
72. Wang, Y.; Hernandez, R. M.; Bartlett, D. J.; Bingham, J. M.; Kline, T. R.; Sen, A.; Mallouk, T. E. Bipolar Electrochemical Mechanism for the Propulsion of Catalytic Nanomotors in Hydrogen Peroxide Solutions. *Langmuir* **2006**, *22*, 10451–10456.
73. Moran, J. L.; Posner, J. D. Electrokinetic Locomotion Due to Reaction-Induced Charge Auto-Electrophoresis. *J. Fluid Mech.* **2011**, *680*, 31–66.
74. Anbar, M.; Pecht, I. On the Sonochemical Formation of Hydrogen Peroxide in Water. *J. Phys. Chem.* **1964**, *68*, 352–355.
75. Banholzer, M. J.; Li, S.; Ketter, J. B.; Rozkiewicz, D. I.; Schatz, G. C.; Mirkin, C. A. Electrochemical Approach to and the Physical Consequences of Preparing Nanostructures from Gold Nanorods with Smooth Ends. *J. Phys. Chem. C* **2008**, *112*, 15729–15734.
76. DaSilva, M.; Schneider, M. M.; Wood, D. S.; Kim, B.-J.; Stach, E. A.; Sands, T. D. The Use of Polyethyleneimine To Control the Growth-Front Morphology of Electrochemically Deposited Gold Nanowires for Engineered Nanogap Electrodes. *Small* **2009**, *5*, 2387–2391.
77. Ye, Z. A Novel Approach to Sound Scattering by Cylinders of Finite Length. *J. Acoust. Soc. Am.* **1997**, *102*, 877–884.
78. Honarvar, F.; Enjilela, E.; Sinclair, A. N. Correlation between Helical Surface Waves and Guided Modes of an Infinite Immersed Elastic Cylinder. *Ultrasonics* **2011**, *51*, 238–244.
79. Mitri, F. G. Acoustic Backscattering Enhancements Resulting from the Interaction of an Obliquely Incident Plane Wave with an Infinite Cylinder. *Ultrasonics* **2010**, *50*, 675–682.
80. Lenshof, A.; Magnusson, C.; Laurell, T. Acoustofluidics 8: Applications of Acoustophoresis in Continuous Flow Microsystems. *Lab Chip* **2012**, *12*, 1210–1223.
81. Khandpur, R. S. *Handbook of Biomedical Instrumentation*; McGraw-Hill Professional: New Delhi, India, 2003.
82. Barnett, S. B.; Ter Haar, G. R.; Ziskin, M. C.; Rott, H.-D.; Duck, F. A.; Maeda, K. International Recommendations and Guidelines for the Safe Use of Diagnostic Ultrasound in Medicine. *Ultrasound Med. Biol.* **2000**, *26*, 355–366.
83. Hernández, R. M.; Richter, L.; Semancik, S.; Stranick, S.; Mallouk, T. E. Template Fabrication of Protein-Functionalized Gold−Polypyrrole−Gold Segmented Nanowires. *Chem. Mater.* **2004**, *16*, 3431–3438.
84. Kline, T. R.; Tian, M.; Wang, J.; Sen, A.; Chan, M. W. H.; Mallouk, T. E. Template-Grown Metal Nanowires. *Inorg. Chem.* **2006**, *45*, 7555–7565.
85. Mbindyo, J. K. N.; Mallouk, T. E.; Mattzela, J. B.; Kratochvilova, I.; Razavi, B.; Jackson, T. N.; Mayer, T. S. Template Synthesis of Metal Nanowires Containing Monolayer Molecular Junctions. *J. Am. Chem. Soc.* **2002**, *124*, 4020–4026.

Appendix F

Steering Acoustically Propelled Nanowire Motors towards Cells in a Biologically Compatible Environment using Magnetic Fields

Steering Acoustically Propelled Nanowire Motors towards Cells in a Biologically Compatible Environment using Magnetic Fields

*Suzanne Ahmed,[1] Wei Wang,[1] Lamar O. Mair,[6,6b] Robert D. Fraleigh,[2] Sixing Li,[3,5] Luz Angelica Castro,[7] Mauricio Hoyos,[7] Tony Jun Huang,[4] and Thomas E. Mallouk[1,3]**

Departments of [1]Chemistry, [2]Physics, [3]Biochemistry and Molecular Biology, [4]Engineering Science and Mechanics, and [5]Cell and Developmental Biology Graduate Program, The Pennsylvania State University, University Park, PA 16802 USA

[6] Center for Nanoscale Science and Technology, National Institute of Standard and Technology, 100 Bureau Drive, Stop 6200, Gaithersburg, MD 20899 USA

[6b]Maryland Nanocenter, University of Maryland, College Park, MD 20742 USA

[7]Laboratoire de Physique et Mécanique des Milieux Hétérogènes,UMR7636 CNRS, UMPC, ESPCI,10 rue Vauquelin, 75005 Paris, France

ABSTRACT: The recent discovery of fuel-free propulsion of nanomotors using acoustic energy has provided a new avenue for using nanomotors in biocompatible media. Crucial to the application of nanomotors in biosensing and biomedical applications is the ability to

remotely control and steer them towards targets of interest such as specific cells and tissues. We demonstrate *in vitro* magnetic steering of acoustically powered nanorod motors in a biologically compatible environment. Steering was accomplished by incorporating (40 ± 5) nm thick nickel stripes into the electrochemically grown nanowires. An external magnetic field of 15 mT to 40 mT was used to orient the motors, which were acoustically propelled along their long axes. In the absence of a magnetic field, (300 ± 30) nm diameter, (4.3 ± 0.2) μm long nanowires with (40 ± 5) nm thick magnetic stripes exhibit the same self-acoustophoretic behavior, including pattern formation into concentric nanowire circles, aligned spinning chains and autonomous axial motion, as their non-magnetic counterparts. In a magnetic field these wires and their paths are oriented as evidenced by their comparatively linear trajectories. Coordinated motion of multiple motors and targeting of individual motors towards HeLa cells with micron-level precision was demonstrated (End of Abstract).

Research into the propulsion and control of nano- and microscale motors has grown steadily over the past decade. [1-10] Research in this field has been largely driven by potential applications in biosensing and biomedicine.[11-16] The recent discovery of the propulsion of nanomotors using acoustic energy has provided a new avenue to the use of nanomotors in biocompatible media.[17-18] Self-acoustophoretic nanowire motors are especially attractive as they are fuel-free and hence allow continuous propulsion that is not limited by the supply of fuel. They are operated in a frequency and power range that is biologically safe.[17,19-20] The power density used in these experiments is (13 ± 1) mW/cm^2 which is well below the FDA limit of 740 mW/cm^2 for diagnostic ultrasound.[19-20] The self-acoustophoretic mechanism also allows one to change the nanomotor speed easily by adjusting the applied power.[21-26] In order to take full advantage of ultrasonically propelled motors one must be able to direct and guide their motion towards targets of interest such as cells and tissues. Here we demonstrate that remote steering and targeting of acoustically powered motors is possible by using externally applied magnetic fields. As in previous reports of magnetically oriented autonomous nanomotors, a magnetic segment was incorporated into the nanowires.[27-29] A ferromagnetic nickel stripe was electrochemically grown between diamagnetic Au and Ru segments, as shown in Figure 1, and it responded to a weak external magnetic field that could be oriented to define the motor's path in two dimensions.

It should be noted that uncertainties in these measurements derive primarily from experiment to experiment distributions. Measurement error for each of the measured values was less than 5 % of the reported uncertainty, and all representations of uncertainty are given as one standard deviation.

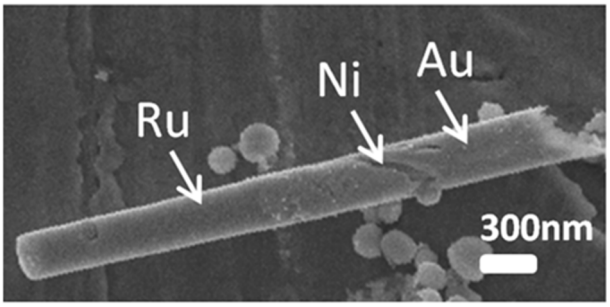

Figure 1. A representative FE-SEM image of the Au-Ni-Ru nanowire motors.

Behavior of Nanomotors in Static Magnetic Fields. When excited by ultrasonic standing waves near the resonant frequency of the cylindrical cell (3.77 ± 0.01 MHz), nanowires with (40 ± 5) nm thick magnetic stripes exhibited the same behavior as their non-magnetic counterparts, including levitation to the midpoint of the cell, pattern formation into concentric nanowire circles, alignment into spinning chains, and autonomous axial motion.[17] The polar alignment of Au-Ni-Ru wires in spinning chains at the acoustic nodal lines, with the ruthenium ends leading, was also consistent earlier observations with non-magnetic Au-Ru nanorods. The average speed of the wires did not change with application of a static magnetic field: speeds of (26 ± 12) μm/s and (26 ± 18) μm/s were observed, without and with the field, respectively (the resulting Reynolds number is approximately (1 ± 0.8) × 10^{-4}). These values are based on 46 measurements of wires with an applied magnetic field and 120 measurements of wires with no applied field. The positional measurement error was less than 0.3 μm and thus the distribution in speed derives primarily from wire to wire speed variation. However, the pattern of movement changed markedly, as shown in Figure 2. In the absence of magnetic field, wire trajectories followed loops (possibly from slight bending of the wires, asymmetry in the wire end shape, and/or localized acoustic streaming) and also contained random turns, but in the magnetic field they followed straight line trajectories. In the static field (applied parallel to the y axis in Figure 2) the majority of the wires align with their long axis oriented perpendicular to the applied field (along the x axis in Figure 2). The range of

angles observed between the direction of movement and the applied field can be explained by the fact that the Ni stripes in the wires in general were not perfectly perpendicular to the wire axis (Figure 1). These static field experiments were conducted at a constant field of (40 ± 1) mT by placing a NdFeB magnet (6.60 ± 0.03) cm from the active area of the acoustic cell.

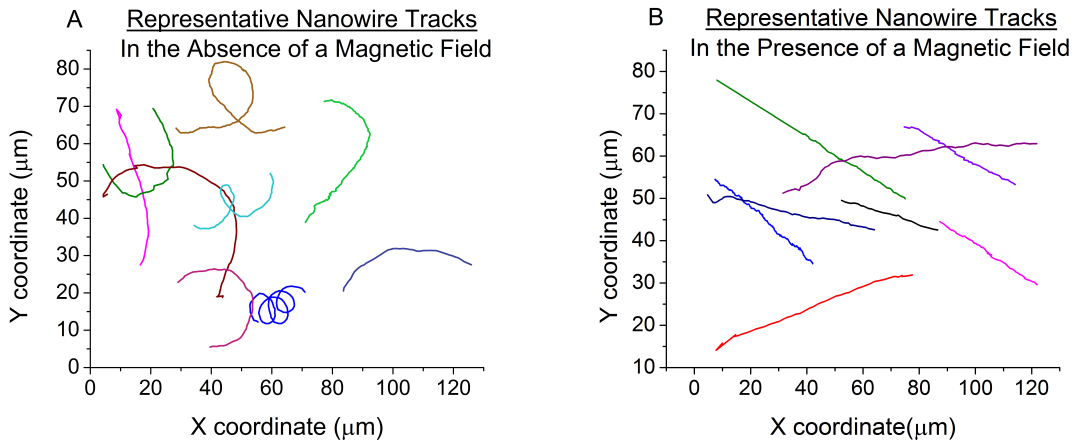

Figure 2. Representative nanowire tracks plotted from the x and y coordinates obtained from tracking nanowires, the bottom left of the screen is defined as the origin. (A) Representative tracks in the absence and (B) in the presence of a magnetic field; field direction is indicated by the arrow.

This field strength applied a maximum torque of (2 ± 0.5) × 10^{-16} $N \cdot m$ on the nanowires within the cell as calculated from equation (1):

$$\tau = \mu \times B \qquad (1)$$

where τ is the torque, μ is the magnetic dipole moment of the wire (6.5 ± 0.5) × 10^{-15} A·m^2 as determined by ensemble superconductong quantum interference device (SQUID) magnetometry measurements (Figure 3), and B is the field strength of the aligning magnet. From this value, the energy required to turn the nanowire through 90° (i.e., to align the long axis parallel to the field) is approximately 2 × 10^{-16} J, which is much greater than the thermal energy $k_BT \approx 4 \times 10^{-21}$ J.

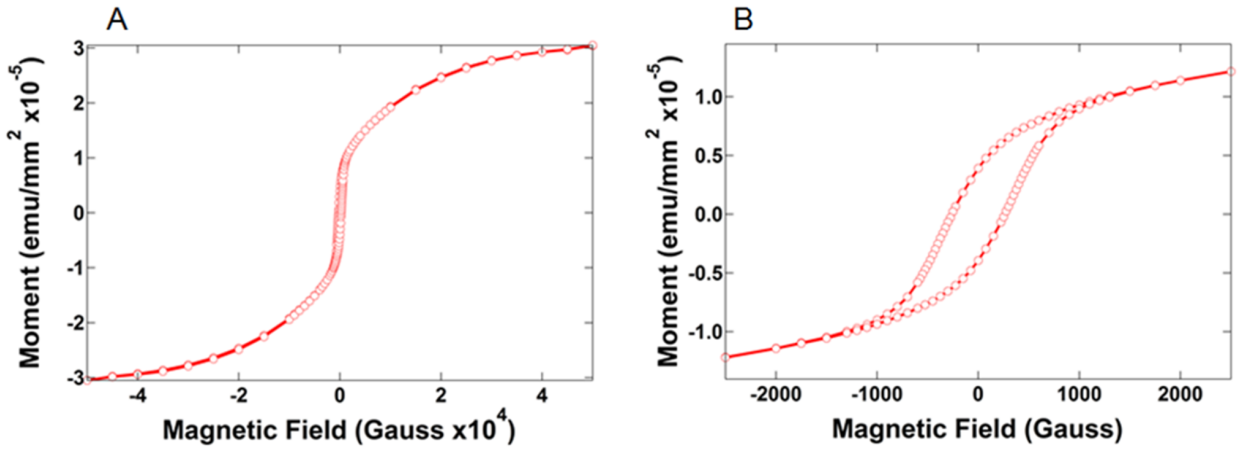

Figure 3. SQUID magnetometry measurements. (a) Magnetization of a Au-Ni-Ru nanowire sample from -5 to 5T showing the saturation magnetization used to calculate the magnetic dipole moment of the wires. (b) Zoomed in hysteresis curve from -2500G to 2500G showing the ferromagnetic character of the nanowire sample.

In the low Reynolds number limit, the acoustic propulsion force on the wires is equal to the drag force experienced by the wires. The axial propulsion force on the wires from scattering of ultrasonic waves was determined from the Stokes drag equation (2) to be (2 ± 0.1) pN for wires traveling at 25 μm/s.

$$F_{drag} = \frac{2\pi\eta L}{\ln\left(\frac{L}{R}\right) - 0.72} v \qquad (2)$$

Here η is the dynamic viscosity of water at 293 K, L is the length of the wire, R is its radius and v its velocity.[29] In contrast, the axial propulsion force on the nanowires due to the magnetic field was negligible as evidenced by the fact that there is no change in the speed of the wires before and after the application of the field. This is to be expected as the magnetic field was essentially uniform over the 100 μm to 200 μm length scale under view.[27]

Magnetic Steering. Using handheld magnets at a distance of 1 cm to 1.5 cm, which apply a (15 ± 1) mT to (30 ± 1) mT field at the sample location, it was possible to reversibly disrupt

patterns, such as spinning chains that are formed in the acoustic field, by reorienting the wires perpendicular to the chain. The applied field could also steer autonomously moving wires that were traveling as fast (170 ± 10) μm/s. The disruption of pattern formation can be seen in Figure 3 and Video S1 in Supporting Information.

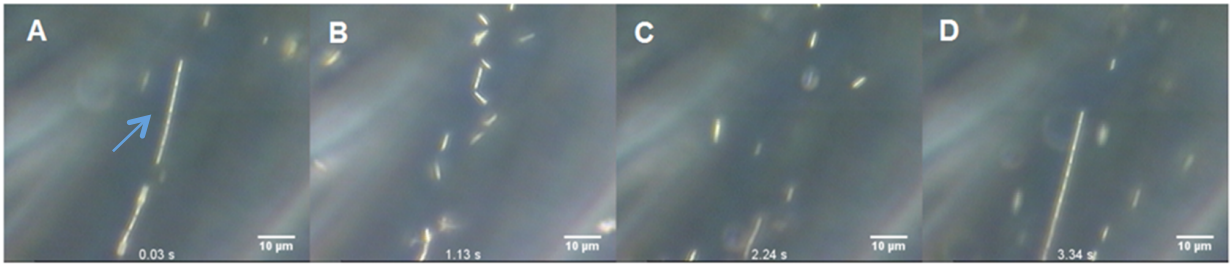

Figure 4. (a) Nanowire motors within an acoustic cell assemble at nodal lines, eventually forming patterns such as spinning chains. (b) Upon the application of an oscillating magnetic field the chain is rapidly disrupted and the nanowire motors follow varying trajectories not confined to the nodal lines. (c, d) Upon the removal of the field the chain re-organizes. Times of frames (a-d) are indicated. (Video S1 in Supporting Information).

Magnetic steering was demonstrated with nanowire motors moving at axial speeds ranging from (8 ± 3) μm/s to (170 ± 10) μm/s. This is illustrated by the ensemble motion of wires, which could be directed to move in concert as shown in Fig. 4. The autonomous nature of the acoustically propelled motion was retained when the magnetic field was applied. The top panel of Fig. 4 illustrates the magnetic steering of groups of motors that were initially traveling in approximately the same direction and then taken through a series of turns by re-orienting the external field. The bottom panel of Figure 4 shows the effect of the field on wires traveling in opposite directions. These wires are also re-oriented in the field, but in opposite directions, and were also made to take multiple sharp U-turns.

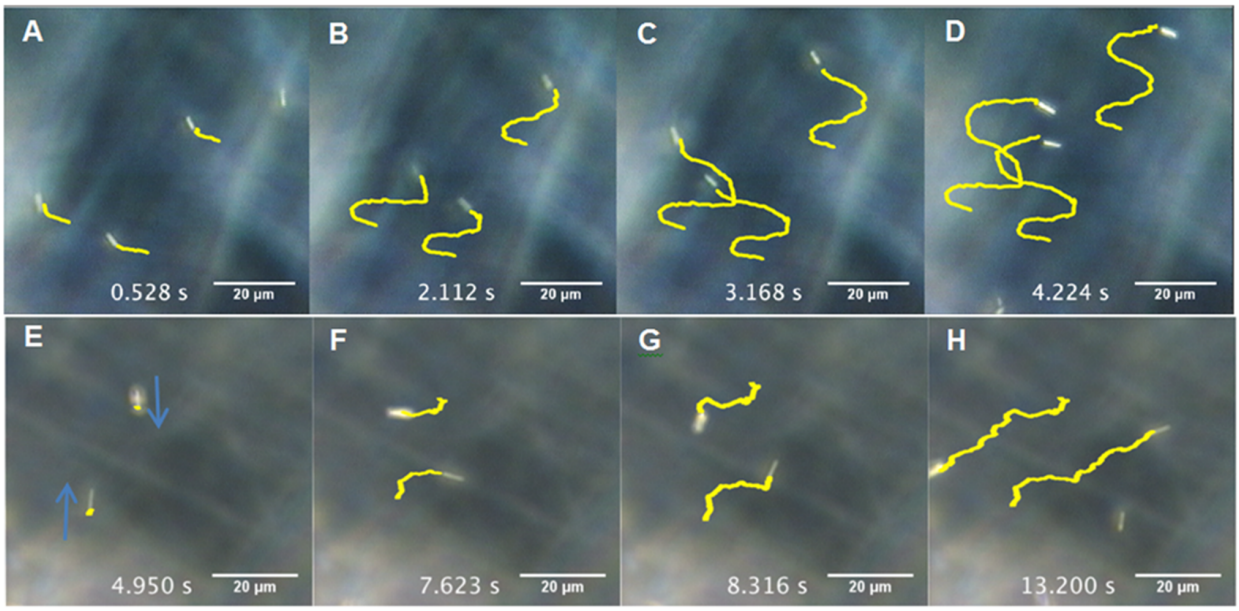

Figure 5. Top panel: Steered ensemble motion of wires moving at (25 ± 5) μm/s, showing (a) earlier and (b) later times in the trajectory. Yellow tracking lines are superimposed on the final frame of the video. The wires undergo multiple guided U-turns (Videos S2 and S3 in Supporting Information). Times of frames (a-d) are indicated. **Bottom panel:** Autonomous steering of motors moving at (8 ± 3) μm/s. Times of frames (e-h) are indicated and arrows show initial direction of motion in (e) and consequent guided sharp U-turns (f-h). (Video S4 in Supporting Information).

Cell Targeting Experiments. For possible bioanalytical and biomedical applications, it is important to show that acoustically powered nanomotors can be steered in a biocompatible environment. Here we demonstrate the magnetic steering of nanomotors towards live HeLa cells in an aqueous phosphate buffer. Nanomotors were mixed with HeLa cells and placed into the acoustic cell. Cell viability tests showed no significant degradation after 20 min exposure to acoustic excitation at the power levels used in the steering experiments (see Supporting Information). In Video S5 (see Supporting Information) one nanomotor was selected and guided towards a cell. At the start of the video (Video S5), in order to

demonstrate directional control, the wire was taken through multiple 180º turns before guiding it towards the targeted cell. It was possible to steer nanowire motors towards cells that were adjacent in aggregates and hence only microns apart. Targeting of a single nanowire towards an individual cell, and an approximately 90º turn of a group of nanowires into a group of cells, are illustrated in Figure 5. Nanowire targeting toward cells was successfully repeated multiple times to ensure the robustness of the technique.

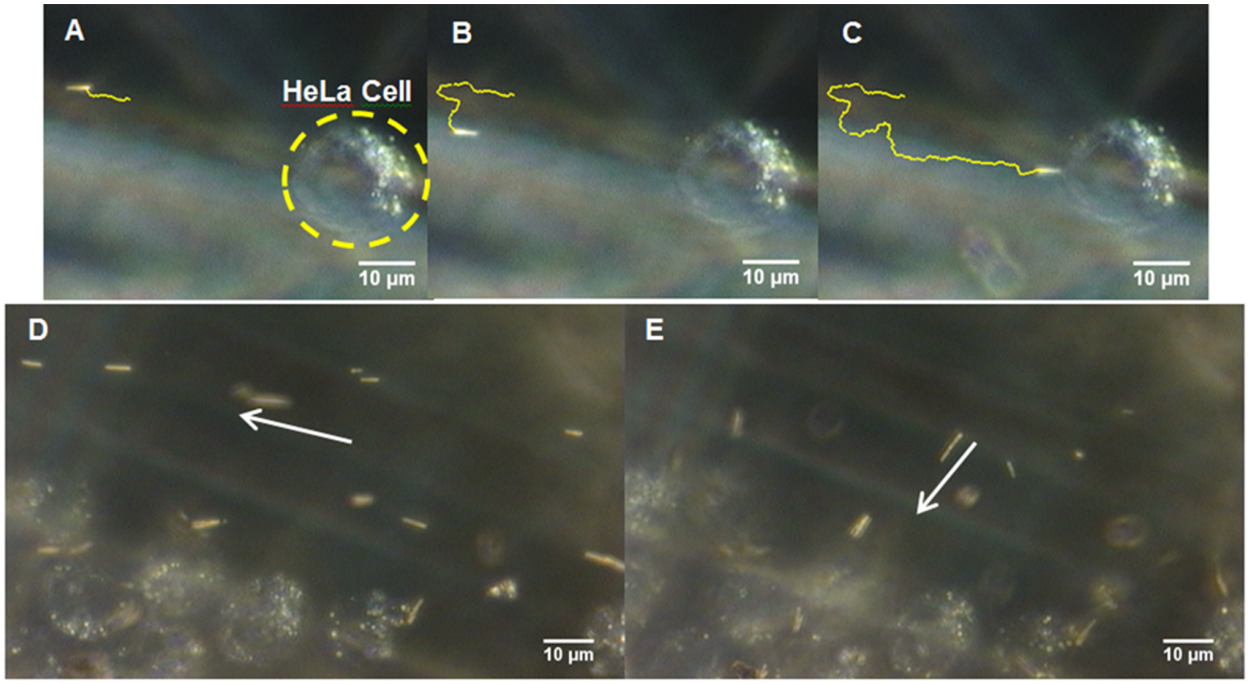

Figure 6. **Top panel**: (a-c) Nanomotor targeting towards a HeLa cell. Nanowires were guided to make multiple U-turns to demonstrate control before being steered towards the live cell. (see Video S5 of Supporting Information). **Bottom panel**: (d) Nanowires are moving parallel to a group of cells, with their direction indicated by the arrow. (e) By turning the external field, nanowires are magnetically steered through an approximately 90º turn towards the cells. (Video S6 of Supporting Information)

These experiments have demonstrated that it is possible to suppress random motion and exert relatively fine control over the steering of acoustically propelled nanomotors using a weak external magnetic field. Both the propulsion and steering of these motors can be

carried out in biocompatible buffers, as evidenced by steering of motors towards live cells in these media.

Methods. *Nanowire growth and characterization*. Bimetallic and trimetallic nanowires were grown electrochemically using commercial anodic aluminum oxide (AAO) membranes (Whatman Inc., nominal pore diameter 200 nm) as templates. Segmented gold-nickel-ruthenium wires were made by sequentially changing the plating solution within an electrochemical cell. A two-electrode electrochemical cell was used for the plating of silver, nickel and gold.[31] A silver layer evaporated onto the AAO membrane served as the cathode and a platinum wire as the anode. Ruthenium was plated in a three electrode cell with an additional Ag/AgCl electrode serving as the reference electrode. A thin gold adhesion layer was deposited between the nickel and ruthenium segments to prevent nanowire fragmentation during release. Gold and ruthenium deposition was conducted under conditions identical to those used previously in order to yield wires with similar morphological and shape asymmetry.[17] Nickel was deposited at a constant current density of 0.7 mA/cm^2 for 3 min.

The lengths of the nickel segments were (40 ± 5) nm, smaller than a single magnetic domain which is typically ≈150 nm, and also smaller than the diameter of the nanorod. This ensured that the easy axis and hence the direction of magnetization was approximately perpendicular to the nanowire long axis.[27,32-33] In this arrangement the motors can be steered with a magnetic field in the plane of the acoustic cell; the field applies substantial torque but minimal axial force to the nanowire. In the static field experiments described above, the majority of the wires align with their long axis oriented perpendicularly (along the x axis in Figure 2) to the applied field (the y axis direction in Figure 2).

The magnetic properties of the nanowires were characterized using SQUID magnetometry. The magnetic susceptibility of a 7 mm^2 portion of the template with embedded wires was

measured at 5 K from 5 T to -5 T. A background measurement of a control sample containing gold-ruthenium wires grown under identical conditions, but without the nickel segment, was made for subtraction from the sample measurement. The magnetic dipole moment per wire (μ) was determined by dividing the total saturation magnetization of the sample by the number of wires contained within it and was determined to be approximately $(6.5 \pm 0.5) \times 10^{-15}$ A· m^2. This value was used to determine the torque on the wires in the applied magnetic fields (Eqn. 1).

Acoustic propulsion experiments. The cylindrical acoustic cell with a height of (180 ± 10) μm and a diameter of (5.0 ± 0.1) mm has been described in an earlier work, and was used in all experiments.[17] The solution in the cell was excited by a piezoelectric disc transducer (1 mm thick) affixed to the center of a stainless steel plate (4.2 cm × 4.2 cm × 1 mm). Kapton tape was applied to the opposite side of the steel plate, and a hole punched in the center of the tape defined the cell. A glass microscope cover slip was placed on the cell during the experiments as a reflector to set up a standing wave. The resonant frequency of the cell center was (3.77 ± 0.01) MHz. Experiments were conducted on wires in the levitation plane at the midpoint of the cell at frequencies close to the resonance frequency. The voltage had a peak to peak value of 10 V and was applied using a waveform generator.

The behavior of the acoustically propelled nanowire motors in the presence of a static magnetic field was studied and compared to their behavior in the absence of a magnetic field. A cylindrical NbFeB magnet (2.50 ± 0.01) cm in diameter and (7.60 ± 0.01) cm in length was held in the plane of the cell at a fixed distance to maintain a constant field strength at the sample. The strength of the applied magnetic field was measured using a digital DC gaussmeter. The average speed for 46 and 120 wires was determined with the magnetic field on and off, respectively. For steering experiments, hand held magnets were used. The external magnetic field was applied using six rectangular FeNbB magnets (2.5 cm × 2.5 cm ×

0.625 cm) in the plane of the cell, at a distance of 1 cm to 1.5 cm from the wires. The strength of the applied magnetic field was measured using a digital DC gaussmeter.

Nanowire motion was tracked using the open access program Video Spot Tracker (http://cismm.cs.unc.edu/downloads/?dl_cat=3) both in the presence and absence of a magnetic field. Videos of nanomotor motion were taken at 500 × magnification at a frame rate of 30 s^{-1}.

For cell targeting experiments, living human cervical cancer cells (HeLa cells) were used. The cells were used within one day of culture and stored refrigerated in a phosphate buffer solution that is 0.1 M phosphate, 0.15 M NaCl at a pH of 7.2. Details of cell growth and cell viability tests can be found in Supporting Information.

Acknowledgments

We thank Prof. Nitin Samarth for helpful discussions and for use of the SQUID magnetometer. This work was supported by the National Science Foundation under MRSEC grant DMR-0802404. Analytical instrumentation used in this work was supported by the Pennsylvania State University Materials Research Institute Nanofabrication Laboratory under National Science Foundation Cooperative Agreement No. ECS-0335765. The tracking software Video Spot Tracker was developed at the CISMM at the University of North Carolina at Chapel Hill, supported by the NIH NIBIB (NIH 5-P41-RR02170). LOM acknowledges support under the Cooperative Research Agreement between the University of Maryland and the National Institute of Standards and Technology Center for Nanoscale Science and Technology, Award 70ANB10H193, through the University of Maryland.

Supporting Information

Videos illustrating acoustic propulsion and magnetic steering, a description of the cell viability test, and cell viability data. This material is available free of charge via the Internet at http://pubs.acs.org.

Corresponding Author

*Email: tem5@psu.edu

Notes

The authors declare no competing financial interests.

Disclaimer

Certain commercial equipment, instruments, or materials are identified in this paper to foster understanding. Such identification does not imply recommendation or endorsement by the National Institute of Standards and Technology, nor does it imply that the materials or equipment identified are necessarily the best available for the purpose.

References

(1) Mallouk, T.; Sen, A. Powering Nanorobots. Scientific American 2009, 300, 72–77.

(2) Ozin, G. A.; Manners, I.; Fournier-Bidoz, S.; Arsenault, A., Dream Nanomachines. Adv. Mater. 2005, 17, 3011-3018.

(3) Fournier-Bidoz, S.; Arsenault, A. C.; Manners, I.; Ozin, G. A., Synthetic self-propelled nanorotors. Chem. Commun. 2005, 441-443.

(4) Mirkovic, T.; Zacharia, N. S.; Scholes, G. D.; Ozin, G. A., Nanolocomotion - Catalytic Nanomotors and Nanorotors. Small 2010, 6 (2), 159-167.

(5) Gibbs, J. G.; Zhao, Y. P., Design and characterization of rotational multicomponent catalytic nanomotors. Small 2009, 5 (20), 2304-8.

(6) Gibbs, J.; Zhao, Y., Catalytic nanomotors: fabrication, mechanism, and applications. Frontiers of Materials Science 2011, 5 (1), 25-39.

(7) Sengupta, S.; Ibele, M. E.; Sen, A., Fantastic Voyage: Designing Self-Powered Nanorobots. Angew Chem Int Edit 2012, 51, 8434-8445.

(8) Fischer, P.; Ghosh, A., Magnetically actuated propulsion at low Reynolds numbers: towards nanoscale control. Nanoscale 2011, 3, 557-563.

(9) Agarwal, A. ; Hess ,H. , Molecular motors as components of future medical devices and engineered materials", Journal of Nanotechnology in Engineering and Medicine 2009,1(1),011005.

(10) Wang, J.; Manesh, K. M., Motion control at the nanoscale. Small 2010, 6, 338-345.

(11) Hess, H. ; Jaeger, L., Nanobiotechnology. Current Opinion in Biotechnology 2010, 21,373-375.

(12) Qin, L. D.; Banholzer, M. J.; Xu, X. Y.; Huang, L.; Mirkin, C. A., Rational design and synthesis of catalytically driven nanorotors. J. Am. Chem. Soc. 2007, 129, 14870-14871.

(13) Nelson, B. J.; Kaliakatsos, I. K.; Abbott, J. J., Microrobots for Minimally Invasive Medicine. Annual Review of Biomedical Engineering 2010, 12, 55-85.

(14) Solovev, A. A.; Xi, W.; Gracias, D. H.; Harazim, S. M.; Deneke, C.; Sanchez, S.; Schmidt, O. G., Self-Propelled Nanotools. ACS Nano 2012, 6 (2), 1751-1756.

(15) Sanchez, S.; Pumera, M., Nanorobots: the ultimate wireless self-propelled sensing and actuating devices. Chem Asian J 2009, 4, 1402-10.

(16) Wang, J.; Gao, W., Nano/Microscale Motors: Biomedical Opportunities and Challenges. ACS Nano 2012, 6, 5745-5751.

(17) Wang, W.; Castro, L. A.; Hoyos, M.; Mallouk, T. E. Autonomous Motion of Metallic Microrods Propelled by Ultrasound. ACS Nano 2012, 1-30.

(18) Kagan, D.; Benchimol, M. J.; Claussen, J. C.; Chuluun-Erdene, E.; Esener, S.; Wang, J., Acoustic Droplet Vaporization and Propulsion of Perfluorocarbon-Loaded Microbullets for Targeted Tissue Penetration and Deformation. Angew Chem Int Edit 2012, 51, 7519-7522.

(19) Barnett, S. B.; Ter Haar, G. R.; Ziskin, M. C.; Rott, H.-D.; Duck, F. A.; Maeda, K., International recommendations and guidelines for the safe use of diagnostic ultrasound in medicine. Ultrasound in Medicine & Biology 2000, 26 (3), 355-366.

(20) Wang, W. Understanding the propulsion and assembly of autonomous nano- and micromotors powered by chemical gradients and ultrasound. Ph.D. thesis. The Pennsylvania State University 2013.

(21) Bruus, H. Acoustofluidics 7: The acoustic radiation force on small particles. Lab Chip 2012, 12, 1578-86.

(22) Lenshof, A.; Magnusson, C.; Laurell, T., Acoustofluidics 8: Applications of acoustophoresis in continuous flow microsystems. Lab Chip 2012, 12, 1210-1223.

(23) Friend, J.; Yeo, L. Y., Microscale acoustofluidics: Microfluidics driven via acoustics and ultrasonics. Rev Mod Phys 2011, 83, 647-704.

(24) Ding, X. Y.; Lin, S. C. S.; Kiraly, B.; Yue, H. J.; Li, S. X.; Chiang, I. K.; Shi, J. J.; Benkovic, S. J.; Huang, T. J., On-chip manipulation of single microparticles, cells, and organisms using surface acoustic waves. P Natl Acad Sci USA 2012, 109, 11105-11109.

(25) Shi, J.; Ahmed, D.; Mao, X.; Lin, S.-C. S.; Lawit, A.; Huang, T. J., Acoustic tweezers: patterning cells and microparticles using standing surface acoustic waves (SSAW). Lab Chip 2009, 9 (20), 2890-2895.

(26) Chen, Y.; Ding, X.; Steven Lin, S.-C.; Yang, S.; Huang, P.-H.; Nama, N.; Zhao, Y.; Nawaz, A. A.; Guo, F.; Wang, W.; Gu, Y.; Mallouk, T. E.; Huang, T. J., Tunable Nanowire Patterning Using Standing Surface Acoustic Waves. ACS Nano 2013, 7 (4), 3306-3314.

(27) Kline, T. R.; Paxton, W. F.; Mallouk, T. E.; Sen, A., Catalytic nanomotors: remote-controlled autonomous movement of striped metallic nanorods. Angew Chem Int Ed Engl 2005, 44, 744-6.

(28) Solovev, A. A.; Sanchez, S.; Pumera, M.; Mei, Y. F.; Schmidt, O. G., Magnetic Control of Tubular Catalytic Microbots for the Transport, Assembly, and Delivery of Micro-objects. Adv. Funct. Mater. 2010, 20, 2430-2435.

(29) Garcia-Gradilla,V.; Orozco, J.; Sattayasamitsathit, S.; Soto,F.; Kuralay,F.; Pourazary, A.; Katzenberg, A.; Gao, W.; Shen, Y.; Wang, J. Fucntionalized Ultrasound-Propelled Magnetically Guided Nanomotors: Toward Practical Biomedical Applications. ACS Nano. (2013) ASAP DOI: 10.1021/nn403851v.

(30) Happel, J.; Brenner, H. Low Reynolds Number Hydrodynamics; Prentice Hall: Englewood Cliffs, NJ, 1965; eq 5-11.52.

(31) Kline, T. R.; Tian, M.; Wang, J.; Sen, A.; Chan, M. W. H.; Mallouk, T. E., Template-Grown Metal Nanowires. Inorg. Chem. 2006, 45, 7555-7565.

(32) Love, J. C.; Urbach, A. R.; Prentiss, M. G.; Whitesides, G. M. Three-dimensional self-assembly of metallic rods with submicron diameters using magnetic interactions. J. Am. Chem. Soc 2003, 125, 12696-7.

(33) Wei, M.S.; Chou, S.Y. Size effects on switching field of isolated and interactive arrays of nanoscale single-domain Ni bars fabricated using electron beam nanolithography. J. Appl. Phys. 1994,76,6679-6681.

TOC graphic

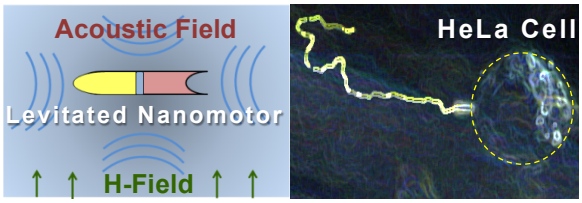

Bibliography

[1] Mikkel Settnes Lasse Mejling Andersen, Anders Nysteen. Forces acting on microparticles in acoustofluidic systems, 2009.

[2] MT Pigott and RC Strum. Observed onset of acoustic streaming. *The Journal of the Acoustical Society of America*, 41:662, 1967.

[3] Yanyan Liu and Junhui Hu. Trapping of particles by the leakage of a standing wave ultrasonic field. *Journal of Applied Physics*, 106(3):034903, 2009. ISSN 00218979. doi: 10.1063/1.3169517. URL `http://link.aip.org/link/JAPIAU/v106/i3/p034903/s1&Agg=doi`.

[4] Vincent Vandaele, Pierre Lambert, and Alain Delchambre. Non contact handling in microassembly: Acoustical levitation. *Precision engineering*, 29(4):491–505, 2005.

[5] Martyn Hill, Rosemary J Townsend, and Nicholas R Harris. Modelling for the robust design of layered resonators for ultrasonic particle manipulation. *Ultrasonics*, 48(6): 521–528, 2008.

[6] John Calvin Giddings. *Unified separation science*. Wiley New York etc, 1991.

[7] Dorra Salhi. *Séparation hydrodynamique des particules par la technique de SPLITT*. PhD thesis, Université Paris 6, 2006.

[8] Natacha Callens. *Développement, étude expérimentale et visualisation par holographie digitale de mini-séparateurs fluidiques (STEP-SPLITT) en vue de la séparation d'objets de taille micrométrique./Development, experimental study and visualization by digital holography of mini fluidic separators (STEP-SPLITT) in order to separate micron-size species.* PhD thesis, 2005.

[9] Claire Ratier and Mauricio Hoyos. Acoustic programming in step-split-flow lateral-transport thin fractionation. *Analytical chemistry*, 82(4):1318–25, February 2010. ISSN 1520-6882. doi: 10.1021/ac902357b. URL `http://www.ncbi.nlm.nih.gov/pubmed/20099837`.

[10] Claire Ratier. *Etude et realisation dún dispositif de séparation acoustique et de son application á des objets biologiques*. PhD thesis, University Paris 7, Denis Diderot, 2009.

[11] Mikael Evander and Johan Nilsson. Acoustofluidics 20: applications in acoustic trapping. *Lab on a chip*, 12(22):4667–76, November 2012. ISSN 1473-0189. doi: 10.1039/c2lc40999b. URL http://www.ncbi.nlm.nih.gov/pubmed/23047553.

[12] A Lenshof, M Evander, T Laurell, and J Nilsson. Acoustofluidics 5: Building microfluidic acoustic resonators. *Lab Chip*, 12(4):684–95, February 2012. ISSN 1473-0189. doi: 10.1039/c1lc20996e. URL http://www.ncbi.nlm.nih.gov/pubmed/22246532http://xlink.rsc.org/?doi=c1lc20996e.

[13] Andreas Nilsson, Filip Petersson, Henrik Jönsson, and Thomas Laurell. Acoustic control of suspended particles in micro fluidic chips. *Lab on a chip*, 4(2):131–5, April 2004. ISSN 1473-0197. doi: 10.1039/b313493h. URL http://www.ncbi.nlm.nih.gov/pubmed/15052353.

[14] AA Doinikov. Acoustic radiation forces : classical theory and recent advances. *Recent Res Devel Acoustics*, 661(2):39–67, 2003. URL http://www.researchgate.net/publication/235345891_Acoustic_radiation_forces_Classical_theory_and_recent_advances/file/32bfe51138bda0459b.pdf.

[15] Armen Sarvazyan, Oleg V Rudenko, and Wesley L Nyborg. Biomedical applications of radiation force of ultrasound: historical roots and physical basis. *Ultrasound in medicine & biology*, 36(9):1379–94, September 2010. ISSN 1879-291X. doi: 10.1016/j.ultrasmedbio.2010.05.015. URL http://www.ncbi.nlm.nih.gov/pubmed/20800165.

[16] L. V. King. On the Acoustic Radiation Pressure on Spheres. *Proceedings of the Royal Society A: Mathematical, Physical and Engineering Sciences*, 147(861):212–240, November 1934. ISSN 1364-5021. doi: 10.1098/rspa.1934.0215. URL http://rspa.royalsocietypublishing.org/cgi/doi/10.1098/rspa.1934.0215.

[17] K. Yosioka and Y. Kawasima. Acoustic radiation pressure on a compressible sphere. *Acustica*, 5(3):167–173, 1955.

[18] LP Gor'Kov. On the forces acting on a small particle in an acoustical field in an ideal fluid. 6:773, 1962.

[19] Henrik Bruus. *Theoretical microfluidics*, volume 18. Oxford University Press, 2008.

[20] Henrik Bruus. Acoustofluidics 10: scaling laws in acoustophoresis. *Lab on a Chip*, 12(9):1578–1586, 2012.

[21] Rune Barnkob and Per Augustsson. Acoustic radiation-and streaming-induced microparticle velocities determined by micro-PIV in an ultrasound symmetry plane. *arXiv*, (d), 2012. URL http://arxiv.org/abs/1208.6534.

[22] J Nilsson, M Evander, B Hammarström, and T Laurell. Review of cell and particle trapping in microfluidic systems. *Analytica chimica acta*, 649(2):141–57, September 2009. ISSN 1873-4324. doi: 10.1016/j.aca.2009.07.017. URL http://www.ncbi.nlm.nih.gov/pubmed/19699390.

[23] Zenon I. Mandralis and Donald L. Feke. Fractionation of suspensions using synchronized ultrasonic and flow fields. *AIChE Journal*, 39(2):197–206, February 1993. ISSN 0001-1541. doi: 10.1002/aic.690390202. URL http://doi.wiley.com/10.1002/aic.690390202.

[24] Despina Bazou, George a Foster, James R Ralphs, and W Terence Coakley. Molecular adhesion development in a neural cell monolayer forming in an ultrasound trap. *Molecular membrane biology*, 22(3):229–40, 2005. ISSN 0968-7688. doi: 10.1080/09687860500093396. URL http://www.ncbi.nlm.nih.gov/pubmed/16096265.

[25] G. Whitworth, MA Grundy, and WT Coakley. Transport and harvesting of suspended particles using modulated ultrasound. *Ultrasonics*, 29(6):439–444, 1991.

[26] Despina Bazou, W.Terence Coakley, Keith M. Meek, Ming Yang, and Duc T. Pham. Characterisation of the morphology of 2-D particle aggregates in different electrolyte concentrations in an ultrasound trap. *Colloids and Surfaces A: Physicochemical and Engineering Aspects*, 243(1-3):97–104, August 2004. ISSN 09277757. doi: 10.1016/j.colsurfa.2004.04.075. URL http://linkinghub.elsevier.com/retrieve/pii/S0927775704003115.

[27] JJ Hawkes and MJ Long. Ultrasonic deposition of cells on a surface. *Biosensors*, 19:1021–1028, 2004. doi: 10.1016/j.bios.2003.10.003. URL http://www.sciencedirect.com/science/article/pii/S0956566303003579.

[28] PL Marston and DB Thiessen. Manipulation of fluid objects with acoustic radiation pressure. *Annals of the New York Academy of Science*, 1027:414–34, November 2004. ISSN 0077-8923. doi: 10.1196/annals.1324.034. URL http://www.ncbi.nlm.nih.gov/pubmed/15644372http://onlinelibrary.wiley.com/doi/10.1196/annals.1324.034/full.

[29] Larisa a Kuznetsova and W Terence Coakley. Applications of ultrasound streaming and radiation force in biosensors. *Biosensors & bioelectronics*, 22(8):1567–1577, March 2007. ISSN 0956-5663. doi: 10.1016/j.bios.2006.08.023. URL http://www.ncbi.nlm.nih.gov/pubmed/16979887.

[30] SM Woodside, BD Bowen, and JM Piret. Measurement of ultrasonic forces for particle–liquid separations. *AIChE journal*, 43(July):1727–1736, 1997. URL http://onlinelibrary.wiley.com/doi/10.1002/aic.690430710/abstract.

[31] Thomas Laurell, Filip Petersson, and Andreas Nilsson. Chip integrated strategies for acoustic separation and manipulation of cells and particles. *Chemical Society reviews*, 36(3):492–506, March 2007. ISSN 0306-0012. doi: 10.1039/b601326k. URL http://www.ncbi.nlm.nih.gov/pubmed/17325788.

[32] A A Doinikov and S T Zavtrak. Radiation forces between two bubbles in a compressible liquid. *Journal of Acoustic Society of America*, 102(3):1424–1431, 1997.

[33] Rune Barnkob. *Acoustofluidics in microsystems : investigation of resonances.* PhD thesis, 2009.

[34] Rune Barnkob. Acoustofluidics in microsystems: investigation of resonances. Master's thesis, DTU Nanotech, Department of Micro and Nano technology, 2009.

[35] Henrik Bruus. Acoustofluidics 2: Perturbation theory and ultrasound resonance modes. *Lab on a Chip*, 12(1):20–8, January 2012. ISSN 1473-0189. doi: 10.1039/c1lc20770a. URL http://www.ncbi.nlm.nih.gov/pubmed/22105715http://pubs.rsc.org/en/content/articlehtml/2012/lc/c1lc20770a.

[36] S I R Jamfb Lighthill. ACOUSTIC STREAMING. *Journal of sound and vibration*, 61(3):391–418, 1978.

[37] Kenneth D. Frampton, Shawn E. Martin, and Keith Minor. The scaling of acoustic streaming for application in micro-fluidic devices. *Applied Acoustics*, 64(7):681–692, July 2003. ISSN 0003682X. doi: 10.1016/S0003-682X(03)00005-7. URL http://linkinghub.elsevier.com/retrieve/pii/S0003682X03000057.

[38] Lord Rayleigh. On the circulation of air observed in Kundt's tubes, and on some allied acoustical problems. *Philosophical Transactions of the Royal Society of London*, pages 1–21, 1884. doi: 10.1098/rstl.1884.0002. URL http://www.jstor.org/stable/10.2307/109434.

[39] Martin Wiklund, Roy Green, and Mathias Ohlin. Acoustofluidics 14: Applications of acoustic streaming in microfluidic devices. *Lab on a Chip*, 12(14):2438–51, July 2012. ISSN 1473-0189. doi: 10.1039/c2lc40203c. URL http://www.ncbi.nlm.nih.gov/pubmed/22688253http://pubs.rsc.org/en/content/articlehtml/2012/lc/c2lc40203c.

[40] Larisa a. Kuznetsova and W. Terence Coakley. Microparticle concentration in short path length ultrasonic resonators: Roles of radiation pressure and acoustic streaming. *The Journal of the Acoustical Society of America*, 116(4):1956, 2004. ISSN 00014966. doi: 10.1121/1.1785831. URL http://link.aip.org/link/JASMAN/v116/i4/p1956/s1&Agg=doi.

[41] Johannes F. Spengler and W. Terence Coakley. Ultrasonic Trap To Monitor Morphology and Stability of Developing Microparticle Aggregates. *Langmuir*, 19(9):3635–3642, April 2003. ISSN 0743-7463. doi: 10.1021/la026798c. URL http://pubs.acs.org/doi/abs/10.1021/la026798c.

[42] J F Spengler, M Jekel, K T Christensen, R J Adrian, J J Hawkes, and W T Coakley. Observation of yeast cell movement and aggregation in a small-scale MHz-ultrasonic standing wave field. *Bioseparation*, 9(6):329–41, January 2000. URL http://www.ncbi.nlm.nih.gov/pubmed/11518236.

[43] W T Coakley. Ultrasonic separations in analytical biotechnology. *Trends in biotechnology*, 15(12):506–11, December 1997. ISSN 0167-7799. URL http://www.ncbi.nlm.nih.gov/pubmed/9418305.

[44] R J Townsend, M Hill, N R Harris, and N M White. Modelling of particle paths passing through an ultrasonic standing wave. *Ultrasonics*, 42(1-9):319–24, April 2004. ISSN 0041-624X. doi: 10.1016/j.ultras.2004.01.025. URL http://www.ncbi.nlm.nih.gov/pubmed/15047305.

[45] Gautam D. Pangu and Donald L. Feke. Acoustically aided separation of oil droplets from aqueous emulsions. *Chemical Engineering Science*, 59(15):3183–3193, August 2004. ISSN 00092509. doi: 10.1016/j.ces.2004.03.038. URL http://linkinghub.elsevier.com/retrieve/pii/S0009250904002891.

[46] Mikael Evander, Linda Johansson, Tobias Lilliehorn, Jure Piskur, Magnus Lindvall, Stefan Johansson, Monica Almqvist, Thomas Laurell, and Johan Nilsson. Noninvasive acoustic cell trapping in a microfluidic perfusion system for online bioassays. *Analytical chemistry*, 79(7):2984–91, April 2007. ISSN 0003-2700. doi: 10.1021/ac061576v. URL http://www.ncbi.nlm.nih.gov/pubmed/17313183.

[47] Despina Bazou, Larisa a Kuznetsova, and W Terence Coakley. Physical enviroment of 2-D animal cell aggregates formed in a short pathlength ultrasound standing wave trap. *Ultrasound in medicine & biology*, 31(3):423–30, March 2005. ISSN 0301-5629. doi: 10.1016/j.ultrasmedbio.2004.12.007. URL http://www.ncbi.nlm.nih.gov/pubmed/15749566.

[48] D Bazou, W T Coakley, A J Hayes, and S K Jackson. Long-term viability and proliferation of alginate-encapsulated 3-D HepG2 aggregates formed in an ultrasound trap. *Toxicology in Vitro*, 22:1321–1331, 2008. doi: 10.1016/j.tiv.2008.03.014.

[49] Athanasia E Christakou, Mathias Ohlin, Bruno Vanherberghen, Mohammad Ali Khorshidi, Nadir Kadri, Thomas Frisk, Martin Wiklund, and Björn Onfelt. Live cell imaging in a micro-array of acoustic traps facilitates quantification of natural killer cell heterogeneity. *Integrative biology : quantitative biosciences from nano to macro*, 5(4):712–9, March 2013. ISSN 1757-9708. doi: 10.1039/c3ib20253d. URL http://www.ncbi.nlm.nih.gov/pubmed/23435966.

[50] WT Coakley, D Bazou, and J Morgan. Cell–cell contact and membrane spreading in an ultrasound trap. *Colloids and Surfaces B*, 34 (4):221–30, April 2004. ISSN 0927-7765. doi: 10.1016/j.colsurfb.2004.01.002. URL http://www.ncbi.nlm.nih.gov/pubmed/15261061http://www.sciencedirect.com/science/article/pii/S0927776504000244.

[51] Despina Bazou. Biochemical properties of encapsulated high-density 3-D HepG2 aggregates formed in an ultrasound trap for application in hepatotoxicity studies : Biochemical responses of encapsulated 3-D HepG2 aggregates. *Cell biology and toxicology*, 26(2):127–41, April 2010. ISSN 1573-6822. doi: 10.1007/s10565-009-9123-0. URL http://www.ncbi.nlm.nih.gov/pubmed/19306066.

[52] Rune Barnkob, Per Augustsson, Thomas Laurell, and Henrik Bruus. Measuring the local pressure amplitude in microchannel acoustophoresis. *Lab on a chip*, 10 (5):563–570, March 2010. ISSN 1473-0197. doi: 10.1039/b920376a. URL http://www.ncbi.nlm.nih.gov/pubmed/20162231.

[53] LA Kuznetsova and Despina Bazou. Multiple three-dimensional mammalian cell aggregates formed away from solid substrata in ultrasound standing waves. *Biotechnology*, 25(3):834–841, 2009. doi: 10.1021/bp.164. URL http://onlinelibrary.wiley.com/doi/10.1002/btpr.164/full.

[54] Terence Coakley and Despina Bazou. Particle and cell manipulation by radiation forces in ultrasound standing waves. *Bubble and particle dynamics in acoustic fields: modern trends and applications*, 2005.

[55] Anna Garcia Sabaté et al. Experimental study of inter-particle acoustic forces. Master's thesis, 2012.

[56] Xiaoyu Zheng and Robert E Apfel. Acoustic interaction forces between two fluids shepres in an acoustic field. *Journal of Acoustic Society of America*, 97(4):2218–2226, 1995.

[57] MAH Weiser, RE Apfel, and EA Neppiras. Interparticle forces on red cells in a standing wave field. *Acustica*, 56(2):114–119, 1984.

[58] Robert E Apfel. Acoustically induced square law forces and some speculations about gravitation. *Am. J. Phys*, 56(8):8, 1988.

[59] CB Fuh, MN Myers, and JC Giddings. Analytical SPLITT fractionation: rapid particle size analysis and measurement of oversized particles. *Analytical Chemistry*, (10): 3125–3132, 1992. URL http://pubs.acs.org/doi/abs/10.1021/ac00048a010.

[60] Natacha Callens, Mauricio Hoyos, Pascal Kurowski, and Carlo S Iorio. Particle sorting in a mini step-split-flow thin channel: influence of hydrodynamic shear on transversal migration. *Analytical chemistry*, 80(13):4866–75, July 2008. ISSN 1520-6882. doi: 10.1021/ac702579g. URL http://www.ncbi.nlm.nih.gov/pubmed/18512948.

[61] J Calvin Giddings. Optimization of transport-driven continuous splitt fractionation. *Separation science and technology*, 27(11):1489–1504, 1992.

[62] C Contado and M Hoyos. Splitt cell analytical separation of silica particles. nonspecific crossover effects: Does the shear-induced diffusion play a role? *Chromatographia*, 65(7-8):453–462, 2007.

[63] JF Spengler, WT Coakley, and KT Christensen. Microstreaming effects on particle concentration in an ultrasonic standing wave. *AIChE journal*, 49(11): 2773–2782, 2003. URL http://onlinelibrary.wiley.com/doi/10.1002/aic.690491110/abstract.

[64] Hideto Mitome. The Mechanism of Generation of Acoustic Streaming. In *Electronics and communications in JApan*, volume 81, pages 1–8, 1998.

[65] Jens a.D. Jensen, Pawel Pocwiardowski, Per O.Å. Persson, Lars Hultman, and Per Mø ller. Acoustic streaming enhanced electrodeposition of nickel. *Chemical Physics Letters*, 368(5-6):732–737, January 2003. ISSN 00092614. doi: 10.1016/S0009-2614(02)01917-6. URL http://linkinghub.elsevier.com/retrieve/pii/S0009261402019176.

[66] Martin Wiklund. Acoustofluidics 12: Biocompatibility and cell viability in microfluidic acoustic resonators. *Lab on a Chip*, 12(11):2018–28, May 2012. ISSN 1473-0189. doi: 10.1039/c2lc40201g. URL http://www.ncbi.nlm.nih.gov/pubmed/22562376http://pubs.rsc.org/en/content/articlehtml/2012/lc/c2lc40201g.

[67] Helen Mulvana, Sandy Cochran, and Martyn Hill. Ultrasound assisted particle and cell manipulation on-chip. *Advanced drug delivery reviews*, pages 1–11, July 2013. ISSN 1872-8294. doi: 10.1016/j.addr.2013.07.016. URL http://www.ncbi.nlm.nih.gov/pubmed/23906935.

[68] Lisa Clarke, Andrew Edwards, and Elizabeth Graham. Acoustic streaming: an in vitro study. *Ultrasound in medicine & biology*, 30(4):559–62, April 2004. ISSN 0301-5629. doi: 10.1016/j.ultrasmedbio.2004.01.007. URL http://www.ncbi.nlm.nih.gov/pubmed/15121259.

[69] G Zauhar, H C Starritt, and F a Duck. Studies of acoustic streaming in biological fluids with an ultrasound Doppler technique. *The British journal of radiology*, 71 (843):297–302, March 1998. ISSN 0007-1285. URL http://www.ncbi.nlm.nih.gov/pubmed/9616239.

[70] Jeremy J Hawkes and W Terence Coakley. Force field particle filter, combining ultrasound standing waves and laminar flow. *Sensors and Actuators B: Chemical*, 75:213–222, 2001.

[71] Gastón Miño, Thomas E. Mallouk, Thierry Darnige, Mauricio Hoyos, Jeremi Dauchet, Jocelyn Dunstan, Rodrigo Soto, Yang Wang, Annie Rousselet, and Eric Clement. Enhanced Diffusion due to Active Swimmers at a Solid Surface. *Physical Review Letters*, 106(4):048102, January 2011. ISSN 0031-9007. doi: 10.1103/PhysRevLett.106.048102. URL http://link.aps.org/doi/10.1103/PhysRevLett.106.048102.

[72] J J Hawkes, D Barrow, and W T Coakley. Microparticle manipulation in millimetre scale ultrasonic standing wave chambers. *Ultrasonics*, 36(9):925–31, August 1998. ISSN 0041-624X. URL http://www.ncbi.nlm.nih.gov/pubmed/9735860.

[73] Shahrzad Yazdi and Arezoo M. Ardekani. Bacterial aggregation and biofilm formation in a vortical flow. *Biomicrofluidics*, 6(4):044114, 2012. ISSN 19321058. doi: 10.1063/1.4771407. URL http://link.aip.org/link/BIOMGB/v6/i4/p044114/s1&Agg=doi.

[74] Wei Wang, Luz Angelica Castro, Mauricio Hoyos, Thomas E Mallouk, and Wang E T Al. Autonomous Motion of Metallic Microrods Propelled by Ultrasound. *ACS Nano*, (7):6122–6132, 2012.

[75] Dirk van Swaay and Andrew DeMello. Microfluidic methods for forming liposomes. *Lab on a chip*, 13(5):752–67, March 2013. ISSN 1473-0189. doi: 10.1039/c2lc41121k. URL http://www.ncbi.nlm.nih.gov/pubmed/23291662.

[76] Joseph Wang and Wei Gao. Nano/Microscale motors: biomedical opportunities and challenges. *ACS nano*, 6(7):5745–51, July 2012. ISSN 1936-086X. doi: 10.1021/nn3028997. URL http://www.ncbi.nlm.nih.gov/pubmed/22770233.

[77] Frank Dubois, Maria-Luisa Novella Requena, Christophe Minetti, Olivier Monnom, and Eric Istasse. Partial spatial coherence effects in digital holographic microscopy with a laser source. *Applied optics*, 43(5):1131–1139, 2004.